Correlated electro-optical and TEM studies on single III-N nanowire heterostructures

Maria Spies

Communauté
UNIVERSITÉ Grenoble Alpes

THÈSE

Pour obtenir le grade de

DOCTEUR DE LA COMMUNAUTE UNIVERSITE GRENOBLE ALPES

Spécialité : **NANOPHYSIQUE**

Arrêté ministériel : 25 mai 2016

Présentée par

Maria SPIES

Thèse dirigée par **Bruno Gayral**
et codirigée par **Martien I. den Hertog** et **Eva Monroy**

préparée au sein du **Laboratoire Institut Néel**
dans **l'École Doctorale de Physique**

Études électro-optiques et TEM corrélées sur nanofils hétérostructurés III-N uniques

Correlated electro-optical and TEM studies on single III-N nanowire heterostructures

Thèse soutenue publiquement le **17 octobre 2019**
devant le jury composé de :

Monsieur Lorenzo Rigutti
Maître de Conférences, Université de Rouen Normandie, Rapporteur
Monsieur Tobias Voß
Professeur, Technische Universität Braunschweig, Rapporteur
Monsieur Fernando Calle
Professeur, Universidad Politécnica de Madrid, Examinateur
Monsieur Julien Pernot
Professeur, Université Grenoble Alpes, Président
Monsieur Helge Weman
Professeur, Norwegian University of Science and Technology, Examinateur

Acknowledgements

First and foremost I want to thank my three supervisors. Each of them has been - and remains to be - an enormous inspiration for me. Working with you on a daily basis has been exciting, encouraging, uplifting, even fun (!) and gave me the possibility to grow as a scientist and as a human being. I feel honored to have been able to work with three such competent and experienced scientists of different fields and having been able to learn from all of them. Being able to work with not one, or two but with three such scientists made a whole plethora of knowledge available to me, be it scientific, strategic or diplomatic, which was and is very useful. I very much appreciate having been able to knock on their office doors with questions, results, ideas, being blocked, confused, worried, excited or enthousiastic. The availability and enthousiasm I was met with were generous and have helped me through the easier and the harder parts of this project. I also want to thank them for an excellent collaboration between each other that made this work possible. The three of them are considerate, concise and cooperative which makes working together and discussing enjoyable and constructive.

Specifically, I am thankful to Martien whose considerate way of working with others and her enthousiasm - which just might be boundless - for collaborating, for results, experiments and getting things done I appreciate. Her unfailing interest, drive to understand, and optimistic attitude are encouraging and inspiring.

I am thankful to Eva working with whom is just an incredibly uplifting experience. I appreciate how easy it is to approach her. I'm thakful for the support I have received, for her dedication, her initative when data is pointing in all directions, for the confidence, that trends in data will be found and explained, and of course for the contagious enthousiasm.

I am thankful to Bruno whose realism, down-to-earth estimations and thorough scientific understanding are refreshing and insightful. I appreciate having gotten to discuss experiments, results, explanations, paper and thesis writing strategies with him, and of course having the small office lectures. I appreciate the unwavering optimistic scepticism about experiments and the support I have received.

I also thank the three of them for sending me to workshops and numerous conferences. Each time it turns out that there's a whole world out there, which skyrocketed my motivation regularly.

In also discussing my future possibilities they gave me insights into their different perspectives allowing me to see several aspects of the new chapter which is in front of me. I hope that our paths meet again in the future and until then your enthousiasm, help, support and insight will be missed. If one, two or all three of them offer you a PhD position, take it !

I thank the Pheliqs lab, and the NPSC group in INAC/ IRIG in CEA Grenoble, and the PLUM, and MRS group in Institut Néel Grenoble, for welcoming me. I am thankful for the funding of the PEM pôle of Université de Grenoble-Alpes for the CopTon project which made this PhD project possible.

And because three supervisors aren't really enough, there is :

Jonas ! Who I'm thankful to for introducing me to my project and teaching me the first months how to do the TEM grid fabrication, nanowire contacting, electrical measurements, spectral response, power dependence measurements, and introducing me to nextnano simulations … For continually being interested in the project, later even from Berlin, and always being ready to loan his brain power to the project for a moment of discussion, and making good, relevant remarks.

I thank Akhil as well for growing nice nanowires, that are thin, little coalesced and have awesome heterostrucutres. And the growers of the group of Prof. Martin Eickhoff in Gießen (now Bremen) for providing the very useful nanowires with a superlattice.

I also thank Jakub who as a Master's student started off the project together with Jonas before I arrived. And Zahra who joined in my last year, who will continue the fabrication and whose smiles and enthousiasm are contagious.

Furthermore I'd like to thank Houssaine, my office mate for nearly two years, for being easy to talk to, open, an enthousiastic, positive nature, someone I could discuss fabrication with among other things, for little office mate breaks, cracking walnuts and having tea with fresh ginger together.

And here is the point now of thanking people I didn't directly work with, or not at all, for making the short three years in Grenoble interesting, enjoyable, even worthwhile. And as the mobility of people in Grenoble is way too high, let me just mention the last few ones, such as skiing and snowboarding adventures with Joachim - there's a creek under this ?, Kimon - even on the way to L2A the E_g of AlN seems ~6 eV, Jorge - that's less than 30% inclination, and other adventures with Cindy – pizza ?, Nathaniel – tea ?, immeasurable support and confidence while writing and transitionig out of CEA by Alberto, Farsane for having a contagious motivation, Tim for being motivated and suggesting an awesome bivouac at an (in)opportune moment, Kathi for being there and supportive, Anna for being easy to be around and fun, Alain for being surprising and simply awesome and those who I'm forgetting or whose paths have taken new directions. Thanks also to the older generation of PhDs, some of which I hadn't even met before, that were encouraging even at times and willing to share their different post-PhD experiences with me, giving me information and new perspectives on what my outlook is after the completion of this project.

Table of Contents

1. Context and Motivation

In this chapter a brief introduction to the historical developments, the context, the state of the art at the beginning of the project, the target of the project, as well as an overview of the organization of the manuscript are given.

1.1. Historical context

The III-nitride system has played a major role in the development of semiconductor applications[1]. The earliest applications are based on planar thin film designs. These evolved to incorporating planar heterostructures to make use of quantum confinement. These heterostructure were then increasingly employed in the engineering of nano-object such as nanowires (NW).

The developments leading up to the first commercial LED have been done in Japan. Showing p-type conduction for the first time, Amano et al.[2] showed a strong near band edge emission of around 370 nm (violet) in 1989 in a GaN p-n junction. In 1991 Nakamura et al.[3] showed the first high-power blue emission (430 nm) from Mg:GaN/Si:GaN p-n junction with an output power of 42 μW, an external quantum efficiency (EQE) of 0.18% and a full width half maximum (FWHM) of the emission peak of 55 nm. The addition of InGaN and AlGaN layers lead to a raise in the output power, eventually leading to the InGaN/AlGaN double heterostructure LED by Nakamura et al.[4] with EQE of 5.4%, 3 mW output power and a FWHM of 70 nm. An increase of the In content allowed first green and yellow LED emissions. Adding a yellow phosphor onto the blue LED gave rise to the white light LED, where the first had an EQE of 3.5% and an output power of 1mW. These developments further manifested in the application of LED structures in displays.

Optically pumped stimulated emission from GaN was shown as early as 1971[5]. Nakamura showed the first laser diode based on an InGaN multiple quantum well (MQW) system in 1996[6,7]. Stimulated emission at room temperature was observed at 410 nm under pulsed conditions above a threshold current density of 8 kA/cm^2. In the same year this was extended to continuous wave (CW) excitation and temperatures of up to 233 K[8].

Planar III-nitride systems have also been successful in their applications as surface acoustic wave devices, for UV photodetection (as photoconductors and photodiodes) and as transistors, most notably the high electron mobility transistor (HEMT).

Regarding photodetectors, the first high-quality UV photoconductor made of GaN/AlN was demonstrated by Khan et al.[9] as early as 1992. The device displayed a spectral responsivity from 365 nm to 200 nm with peak responsivity of 1000 A/W and a linear dependence on incident optical power over 5 orders of magnitude. These studies have been extended to AlGaN and AlGaN/AlN conductors with similar spectral response range and lower responsivities[10,11]. A drawback is the persistent photoconductivity on the order of hours.

UV photodiodes with relatively fast response times were demonstrated as early as 1997. The earliest AlGaN/GaN p-i-n photodiodes[12] demonstrated a maximum zero bias responsivity of 0.12 A/W at 364 nm which decreases by more than 3 orders of magnitude for wavelengths longer than 390 nm. Fast decay times of 12 and 29 ns were observed which proves useful for technical applications. A first n-/n+ GaN Schottky barrier detector[13] demonstrated 0.18 A/W responsivity and fast 118 ns of falltime, while a first GaN p-i-n diode array[14] demonstrated 0.11 A/W peak responsivity at 360 nm good visible rejection over 3−4 orders of magnitude.

These planar systems have evolved to incorporating heterostructures, potentially enabling quantum confinement. Quantum confinement has become a major topic in semiconductor physics and been extensively studied experimentally in the past decades. Structures, such as quantum wells (QWs) and quantum dots (QDs), are useful systems for the

experimental physicist (as well as the theoretical physicist) to study quantum mechanics and quantum optical phenomena on the fundamental level. The synthesis of these heterostructures has considerably contributed to the development and wide application of optoelectronic technology in the scientific, industrial, residential and recreational areas. Outside of optoelectronics, resonant tunneling diodes, high frequency power devices, and heterojunction bipolar transistors have been demonstrated.

Nowadays, an improved downscaling of on chip components, such as optical links in telecommunication is aimed for. The developments in the field of planar heterostructures made this development possible. The NW structure is a promising candidate for this downscaling.

NWs have drawn interest as a potential platform to study quantum phenomena as well. Strain relaxation and high surface sensitivity of these structures bring additional advantages. In the realm of photodetectors the transition from 2D to NWs brings, however, a sublinear dependence on impinging light and they are therefore less useful for the quantification of light intensity[15].

III-nitride structures are also contributing in the realm of rising quantum information technologies as single photon emitters. These supply indistinguishable photon pairs for entanglement and therewith encryption. The most efficient single photon emitters demonstrated so far are self-assembled InAs QD[16], due to the well-controlled epitaxy and the reproducibility of the devices. GaN QDs, however, have demonstrated single photon emission at room temperature[17].

To advance the research in this topic, the internal electric field in quantum confined structures needs to be studied in more detail. The NW structure is a likely candidate for such studies. The progress in microscopy makes a correlation of the structural properties with electrical and optical properties possible. The exploitation of the internal electric field through band engineering can be used to improve devices e.g. for the fabrication of on-chip sized photodetectors. The manipulation of the internal electric field by external bias can be used to further understand the complex nature of quantum confined structures.

1.2. State of the Art

Regarding GaN-based NW photodetectors, contacted n-i-n GaN NWs have been demonstrated by González-Posada et al.[18] and characterized in terms of their photodetection capabilities. Here, no heterostructure making use of the internal electric field was present. Rigutti et al.[19] were the first to demonstrate resonant tunneling transport through AlN barriers in a GaN NW which had better stability and reproducibility than double-barrier resonant tunneling diodes. Rigutti et al. likewise showed a NW UV detector incorporating a SL which improves the detection capabilities by making use of the internal electric field of the material[20]. The photosensitivity factor goes up to 5×10^2 when inserting the SL and the responsivity was reported to be 2×10^3 A/W. A first correlated microscopy study (electrical and structural properties) on contacted single GaN NWs had been done by Hertog et al.[21] with a NW containing a single AlN barrier. It was shown that the barrier blocked the current rendering it sensitive to the thickness of the GaN shell bypassing the barrier.

Regarding the emission properties of a single QD in a NW, at the beginning of this project, the luminescence of an axial wurtzite GaN QD embedded in AlN barriers in a GaN NW has been demonstrated and characterized optically by Renard et al.[22]. The influence of the QD size has been investigated[23,24]. A correlation with electrical properties, however, was not done. Room-temperature triggered single photon emission was first achieved by the group of Arakawa[17] in comparatively small and site-controlled QD in NWs. The autocorrelation function $g^{(2)}[0]$ at 300 K was as low as 0.13. The same group also demonstrated QDs in macrostep edges displaying a significant suppression (1 order of magnitude) of spectral diffusion effects compared to conventional QDs and record full-width half maxima (FWHM) of 87 μeV[25].

To further understand the internal electric field in a QD embedded in a NW correlated studies of the manipulation of this electric field are required. The manipulation of the internal electric field is interesting for quantum information technology applications. Müßener et al.[26] were the first to probe the internal electric field of a QD embedded in AlGaN barriers in a GaN NW and studying the optical (μPL) and electrical properties. A blue shift of the QD emission is observed for the application of an external electric field compensating the internal electric field in the structure. The electric field strength in the structure was extracted by correlation with numerical simulations.

1.3. Targets

The idea of this project is full correlation of optical, electrical and structural properties of GaN QDs embedded in a GaN NW, to better understand the electric field distribution, the band engineering opportunities, the influence of surface states, and the electric tunability of the QD emission. This study demands contacting a single NW containing QDs on an electron transparent and (scanning) transmission electron microscopy ((S)TEM) compatible chip. This chip will be used likewise for electrical measurements and optical microphotoluminescence measurements (μPL) in order to carry out multiple characterization techniques on the same single NW.

In the field of photodetectors, the goal of this project is to study the sublinearity of single NW photodetectors and the potential advantages of introducing a heterostructure in the device architecture.

1.4. Organization of the Manuscript

The manuscript is organized in seven chapters. Besides this context chapter, two chapters are introductory, three chapters are presenting and discussing experiments and results and the last chapter is drawing conclusions and giving perspectives for future studies.

Chapter 2 gives an introductory overview to III-nitride semiconductor physics, device design and heterostructuring. As a special case NWs are discussed. Photodetectors, standard figures of merit and the specific case of photodetectors are presented.

Chapter 3 is a brief introduction to the different methods employed throughout the project. It includes the growth of NW samples, TEM membrane fabrication, NW device fabrication, the electronic and optical characterization techniques and simulations with the nextnano[3] software.

The following two chapters concern studies of heterostructured single NW photodetectors. In chapter 4 a heterostructured GaN single NW structure displays bias-dependent spectral response that can be attributed to preferential active regions for the charge carrier collection when applying bias. The result is explained by correlation of the photocurrent measurements with scanning transmission electron microscopy observations of the same single NW, and semi-classical simulations of the strain and band structure in one and three dimensions.

In chapter 5 heterostructured GaN NW photodetectors behave linearly with the impinging optical power when the NW diameter is below a certain threshold. By semi-classical simulations and taking into account the structural information obtained by scanning transmission electron microscopy on the same single NWs, we are able to show that it corresponds to the total depletion of the NW stem due to the Fermi level pinning at the sidewalls.

In chapter 6 a GaN NW structure including a GaN quantum dot (QD) is shown to vary its QD emission as a function of the applied external bias. A blueshift of the emission with increasingly compensated internal electric field is observed. With increasing applied bias, an evolution of the recombining exciton to different charged states can be observed. By correlating the result with

scanning transmission electron microscopy information and doing semi-classical simulations an internal electric field was extracted.

Finally, in chapter 7 conclusions are drawn and perspectives given.

2. Introduction

In this chapter, an introductory overview to III-nitride semiconductor physics and device design is given. Structural, electronic and optical properties are discussed, as well as the possibility of implementing heterostructures. As a special case, NW structures are discussed at length. An important part of this chapter focuses on the physics of photodetectors and later more specifically on NW photodetectors. Standard figures of merit are introduced and discussed.

Parts of this introduction are published as a review on NW photodetectors based on wurtzite semiconductor heterostructures as Spies et al., Semicond. Sci. Technol. ***2019****, 34 (5), 053002.*[15]

2.1. Nitride Semiconductors

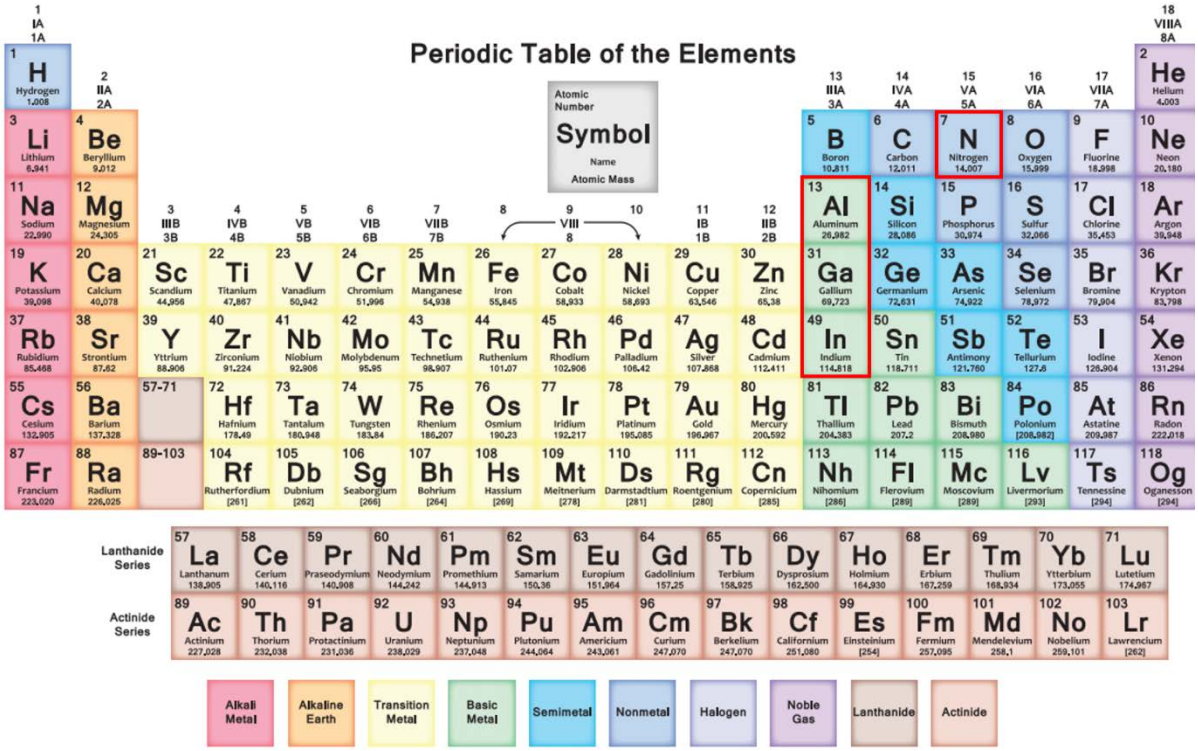

Figure 2.1. Periodic system of the elements. In red are indicated: the group III elements Ga, Al, In and the group V element N used in III-V semiconductor compounds. Modified from sciencenotes.org.

III-nitride semiconductors consist of group III metals Al, Ga and In and the group V element N. The atomic species involved are indicated in red in the periodic system of the elements in figure 2.1. This project focusses on GaN, AlN and their ternary alloy AlGaN.

2.1.1. Structural properties and spontaneous and piezoelectric polarization

III-V compounds can be synthesized in the zinc-blende (sphalerite) and the wurtzite crystal structure. Wurtzite is thermodynamically more stable and therewith occurs more often.

This project focuses on samples with wurtzite structure. Figure 2.2.(a) depicts the wurtzite lattice, which shows hexagonal symmetry. In such a lattice, directions and planes are described using four Miller-Bravais indices (hkil), where l is associated to the vertical axis of the hexagonal prism, and h, k, and i = −(h + k) are associated to vectors contained in the base of the prism, pointing to vertices of the hexagon that are separated by 120°. The c-[000$\bar{1}$], m-[1$\bar{1}$00] and a-

$[\bar{1}\bar{1}20]$ directions are indicated by arrows in figure 2.2.(a). The [0001] axis is considered positive when the vectors along the bonds between the group III atoms and the group V atoms along <0001> points from metal to N. Conventionally, (0001) crystals are called metal-polar and $(000\bar{1})$ crystal are called N-polar. A schematic of the significant tetrahedrons in the primitive cell can be seen in figure 2.3.

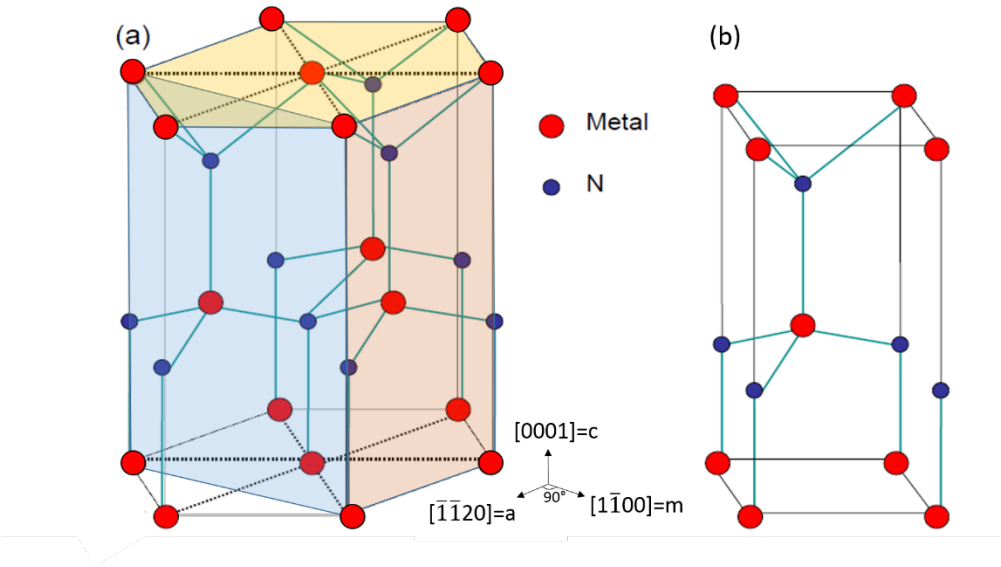

Figure 2.2.(a) Wurtzite crystal structure and (b) its primitive cell. Metal atoms are indicated in red, N atoms in blue. The nonpolar a-plane (blue), polar c-plane (yellow) and nonpolar m-plane (red) are indicated in (a). Modified from ref. [27].

The wurtzite unit cell is non-centrosymmetric, which results in materials with significant pyroelectric and piezoelectric properties. The difference in electronegativity between the two atomic species that constitute the lattice results in a displacement of the electrons of the bonds towards the more electronegative atom. The electric dipoles associated to the bonds are not mutually compensated due to the lack of symmetry of the crystal, which leads to a macroscopic spontaneous polarization field along the <0001> axis. The value of such polarization depends on the ideality of the crystal, the anion-cation bond length, and the electronegativity of the atoms involved. Therefore, it varies from one material to another (see table 2.1.).

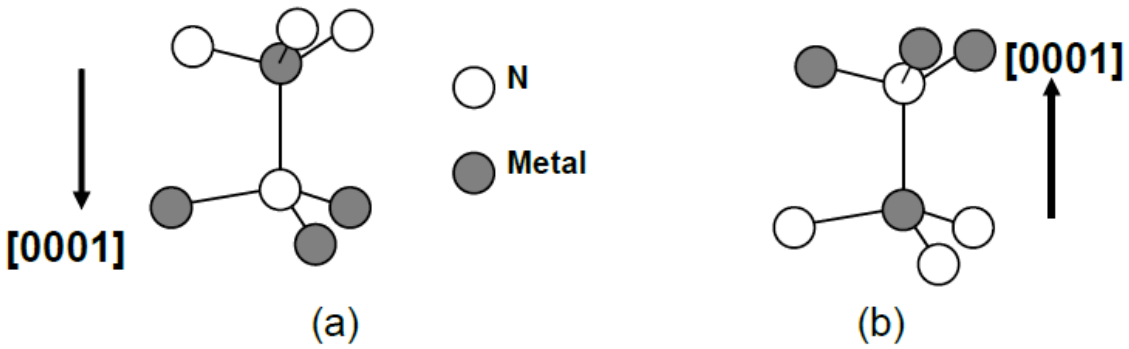

Figure 2.3.(a) N-polarity and (b) metal-polarity for structures grown along the c-axis of the wurtzite structure. Taken from ref. 27.

An additional polarization field can appear as a result of the lattice deformation due to misfit stress. Stress leads to a deformation of the crystal described by Hooke's law:

$$\sigma_{ij} = \sum_{kl} c_{ijkl}\varepsilon_{kl} \qquad (2.1)$$

where c_{ijkl} is the elastic tensor, and σ_{ij} and ε_{kl} represent the stress and strain, respectively. The presence of strain induces a polarization vector whose components are given by

$$\vec{P}_j = \sum_{kl} e_{jkl}\varepsilon_{kl} \qquad (2.2)$$

The terms c_{ijkl}, and e_{jkl} are transformed to c_{mn}, e_{jm} by replacing *m,n* = {*xx, yy, zz, yz, zx, xy*} with *m,n* = {1, 2, 3, 4, 5, 6}. Due to the crystallographic symmetry of the wurtzite structure, the only non-zero elastic constants are $c_{11} = c_{22}$, $c_{12} = c_{21}$, $c_{13} = c_{31} = c_{23} = c_{32}$, c_{33}, $c_{44} = c_{55}$, $c_{66} = (c_{11} - c_{21})/2$, and the non-zero piezoelectric constants are $e_{31} = e_{32}$, e_{33}, and $e_{15} = e_{24}$. The values of spontaneous polarization, elastic constants and piezoelectric constants of wurtzite GaN and AlN materials are presented in table 2.1, together with their lattice constants and energy bandgaps.

Parameters (units)	**Symbol**	**GaN**	**AlN**
Lattice constants (nm)	a	0.3189 [28]	0.3112 [28]
	c	0.5185 [28]	0.4982 [28]
Spontaneous polarization (C.m^{-2})	$\vec{P}_{SP}$	-0.034 [29]	-0.090 [29]
Piezoelectric constants (C.m^{-2})	e_{31}	-0.49 [30]	-0.60 [30]
	e_{33}	0.73 [30]	1.46 [30]
	e_{15}	-0.30 [31]	-0.48 [31]
Elastic constants (GPa)	c_{11}	390 [32]	396 [33]
	c_{12}	145 [32]	137 [33]
	c_{13}	106 [32]	108 [33]
	c_{33}	398 [32]	373 [33]
	c_{44}	105 [32]	116 [33]

Table 2.1. Lattice parameters, values for the spontaneous polarization, piezoelectric polarization and elastic constants are given for the III-V compounds of wurtzite GaN and AlN.

2.1.2. Electronic and optical properties

The electronic and optical properties are tightly linked and presented together in the following. The complex band structures of both wurtzite GaN and AlN are illustrated in figure 2.4.(a) and (b) respectively. The electronic band structure describes what energy ranges can be occupied by electrons in a crystalline material, according to the Schrödinger equation and assuming non-interacting electrons. It is represented as energy E as a function of wave vector k=(k_x, k_y, k_z). Considering the first Brillouin zone, which is a uniquely defined primitive cell in reciprocal space, we find critical points of high symmetry. It is illustrated in figure 2.4.(a). The Γ-point is the center of the Brillouin zone. A, H, K, L, M are other points of high symmetry within the hexagonal reciprocal space primitive cell. Using these, the energy distribution along the paths connecting these points within the reciprocal unit cell can be described, allowing a full description of all possible occupations in space. The energy bandgap of a semiconductor is a concept that can then be observed. It is defined as the difference between the highest energy of any point in the occupied valence bands and the lowest point in the unoccupied conduction bands. Should these points (not) superpose on the same point in reciprocal space the bandgap is called direct (indirect). III-N materials have a direct bandgap at the Γ-point, as can be seen in figure 2.4.(b,c).

Several numerical methods have been developed in order to calculate such electronic energy bands. The band structure of GaN in figure 2.4.(b) was calculated with the pseudo potential model and that for AlN given in (c), with the tight binding model. Other methods such as the nearly free electron approximation, density functional theory, muffin-tin approximation or Green's function methods also exist. In the following the k·p perturbation theory is employed as it requires only a few parameters, is commonly used for semiconductors and the parameters determined by experiment can be used as input. Generally, in the k·p model, the Bloch wave functions for solid lattice-ordered materials are used as solutions to the Schrödinger equation in order to describe the possible motions of the electrons within the reciprocal lattice and therewith in the Bravais lattice.

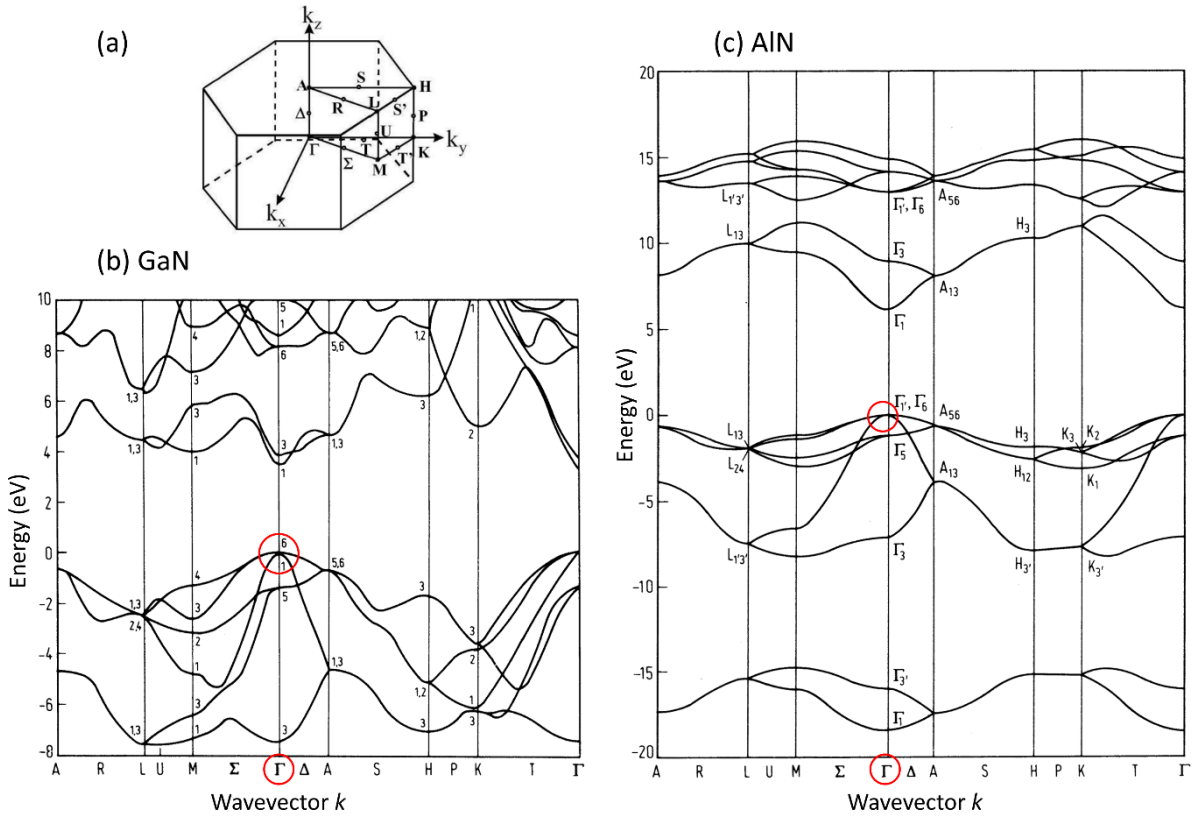

Figure 2.4.(a) First Brillouin zone of a wurtzite crystal[34]. Band structures of wurtzite (b) GaN[35] and (c)AlN[36].

What is important to note in the calculated band structures of wurtzite GaN and AlN is that there is a splitting of the valence band due to the crystal field (static electric field due to spontaneous polarization) and the spin-orbit coupling. These are called the A, B and C subbands or heavy hole (HH), light hole (LH) and crystal field hole (CH) respectively. These three bands are represented in more detail in figure 2.5. It is interesting to note that although the HH subband has a higher maximum than the LH subband for both the wurtzite GaN and AlN, the CH subband is lower than the other two in the case of GaN and higher than the other two in the case of AlN. Their behavior as a function of the wave vector components k_x and k_z is represented in figure 2.5.

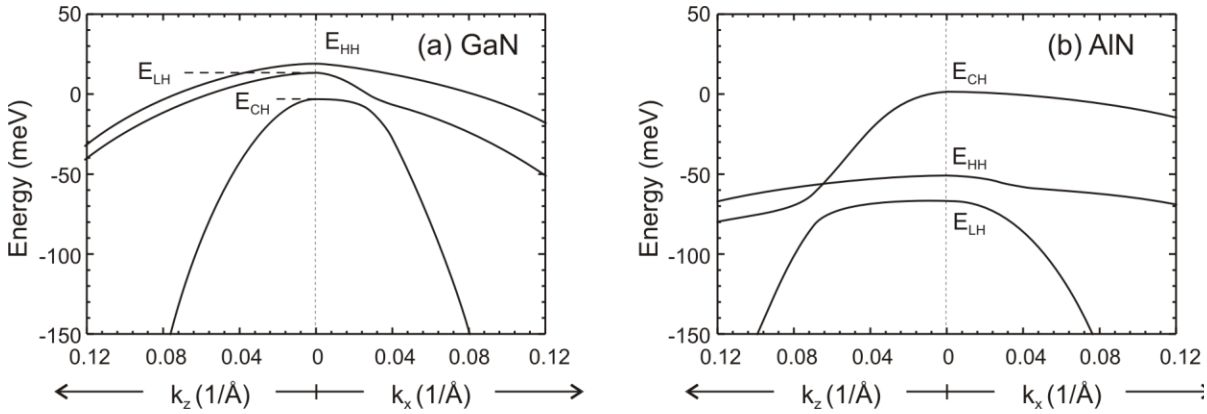

Figure 2.5. The energy levels of the non-degenerate valence band at the Γ-point in wurtzite (a) GaN and (b) AlN in the k_x and k_z direction in the reciprocal space: HH, LH and CH. Taken from ref. 37.

The band structure can be described by the effective mass approximation as it can be considered an electronic motion in the presence of a slowly varying perturbation. The band

structure is assumed to be parabolic at the Γ-point. In this configuration the motion of both holes and electrons can be expressed as the motion of a free particle having a modified mass, hence the effective mass m*. The Schrödinger equation can be solved with a one-electron Hamiltonian, neglecting electron-electron interactions and supposing a small electric field. The values of the bandgap, electron and hole effective mass and deformation potentials of the conduction and valence band for GaN and AlN are summarized in table 2.2.

Parameters (units)	**Symbol**	**GaN**	**AlN**
Bandgap (eV)	E_G	3.51 [28]	6.2 [28]
Electron effective mass (m_{e0})	m_e^*	0.2 [28]	0.3 [38]
Hole effective mass (m_{h0})	m_h^*	1.25 [39]	1.44 [40]
Varshni coefficient (meV/K)	α_V	0.909 [28]	1.999 [28]
Debye coefficient (K)	β_D	830 [28]	1429 [28]
Deformation potentials (eV): a_{cz} , a_{ct} = conduction band deformation potentials D_i = valence band deformation potentials	a_{cz}-D_1	-5.81 [41]	-4.3 [41]
	a_{ct}-D_2	-8.92 [41]	-12.1 [41]
	D_3	5.47 [41]	9.12 [41]
	D_4	-2.98 [41]	-3.79 [41]
	D_5	-2.82 [41]	-3.23 [41]

Table 2.2. The values of the bandgap, electron and hole effective mass, Varshni coefficient, Debye coefficient and deformation potentials of the conduction and valence band are given for GaN and AlN.

The bandgap of the ternary alloys is obtained by a quadratic interpolation of the energy of the corresponding binary compounds

$$E_g(x) = (1-x)E_g^A + xE_g^B - bx(1-x) \tag{2.3}$$

using bowing parameters b = 0.68 eV for AlGaN, b = 2.1 eV for InGaN and b = 4.4 eV for AlInN[42].

The temperature dependent lattice expansion and the electron-lattice interaction lead to a variation of the bandgap with temperature, which can be described with the empirically found Varshni law

$$E_g(T) = E_g(T = 0K) - \frac{\alpha_V T^2}{\beta_D + T} \tag{2.4}$$

where α_V is the Varshni coefficient and β_D is the Debye coefficient. Both coefficients are material specific and given in table 2.2.

2.2. III-Nitride Heterostructures

The III-nitride family of semiconductors opens up enormous opportunities of heterostructuring and band engineering as they form a continuous alloy system. A diagram of the bandgap of binary compounds as a function of their respective lattice parameters is given in figure 2.6.(a). It shows that a large range of bandgaps can be engineered by alloying AlN, GaN and InN while staying within a small range of lattice mismatch induced by different lattice parameters. The spectral range covers wavelengths from the infrared, via the visible to the ultraviolet. The conduction band offsets between binary compounds are represented in figure 2.6.(b). They are ≈ 1.8 eV for AlN/GaN [43] and ≈ 2.2 eV for GaN/InN[44].

All three of these materials have spontaneous polarization as outlined in chapter 2.1.1. whose value, however, differs from one another. Therefore, bringing two of these binary materials into contact leads to the formation of a charge sheet at the interface. The spatially separated positive or negative charges within a unit cell, that make up the dipole, are compensated by the same amount of opposite charge from the neighboring unit cell of the same polarization. If the neighboring unit cell however possesses a different polarization, i.e. a different dipole moment

within the unit cell, there is an over- or under-compensation, which is ultimately a charge sheet of excess carriers at the hetero-interface. The surplus of positive or negative charges is stationary at that point of the structure. These spontaneously formed charge sheets modify the band structure across the interface, which can be used in order to band engineer specific heterostructures. An example can be seen in figure 2.7., which presents the band profile of a GaN QW in an infinite GaN/AlN SL structure. Schematically, the unit cells of such a heterostructure are represented with a simplified dipole moment whose charge accumulations are represented symbolically by + and – signs. Comparing the simplified electron density distribution of neighboring dipoles of differing strength, the difference in charge becomes evident. The charge sheets are indicated in the band structure of the heterostructure. As a result of the electric field created by such a constellation the electron-hole pair is spatially separated: the electron (hole) wave function is attracted towards the positive (negative) charge sheet i.e. to the right (left) part of the well as indicated in figure 2.6.(c).

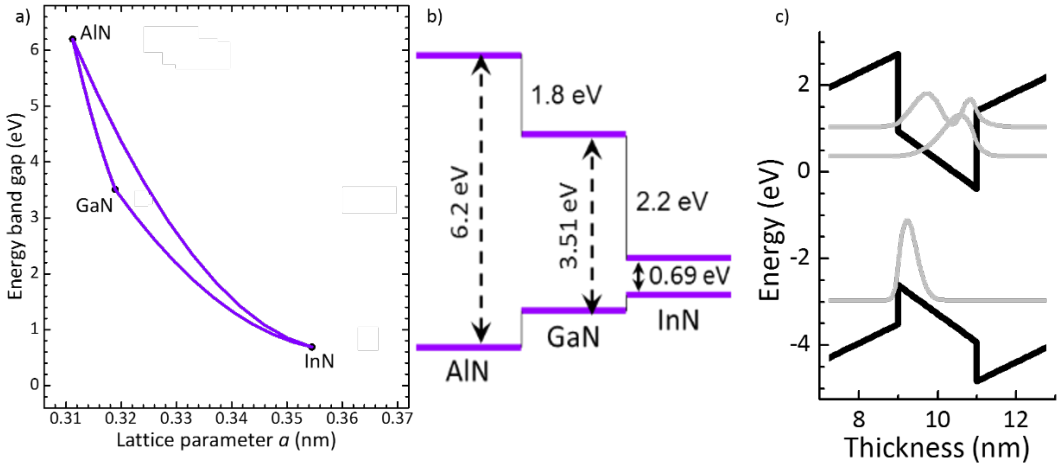

Figure 2.6.(a) Energy gap vs. lattice parameters of the III-V family, suggesting large heterostructuring opportunities. (b) Bandgap of GaN, AlN and InN and the respective conduction and valence band offsets between the binary compounds: ≈ 1.8 eV for AlN/GaN[43] and ≈ 2.2 eV for GaN/InN[44] (c) Band profile of a GaN quantum well in an infinite GaN/AlN (2.1 nm/3 nm) multi-QW system. In gray lines, squared wave functions associated to the first and second confined levels of electrons (e_1, e_2) and the first confined level of holes (h_1). The thickness of the structure increases into the +c direction.

The electric fields in such a heterostructure can be calculated as follows[45]. Assuming the electric displacement vector to be conserved we obtain

$$\epsilon_w \overrightarrow{E_w} - \epsilon_b \overrightarrow{E_b} = \overrightarrow{P_b} - \overrightarrow{P_w} \tag{2.5}$$

where ∈ is the dielectric constant, $\vec{E}$ the electric field, $\vec{P}$ the polarization of the well or the barrier. In a single QW between infinite barriers we assume that $\overrightarrow{E_b}$ goes to zero and we obtain

$$\vec{E}_w = \frac{(\vec{P}_b - \vec{P}_w)}{\epsilon_w} \tag{2.6}$$

The electric field in the QW can be on the order of 10 MV/cm. In the case of an infinite SL, we assume boundary conditions of

$$l_w \overrightarrow{E_W} + l_b \overrightarrow{E_b} = 0 \tag{2.7}$$

where l is the length of the well or barrier section. Therewith we obtain

$$\vec{E}_w = (\vec{P}_b - \vec{P}_w) \frac{l_b}{(\epsilon_b l_w + \epsilon_w l_b)} \tag{2.8}$$

The resulting separation of the electron and the hole wave function is already indicated schematically in figure 2.6.(c). Due to the electric field, the electron and hole wave functions get spatially separated. The overlap integral is therefore lower than in a symmetric well, decreasing the recombination probability. Additionally, the electron-hole transition is shifted towards lower energies (red shift). That is called the Quantum Confined Stark Effect (QCSE).

There are no polarization effects to be observed at the material interfaces if the structure is grown along a non-polar direction such as the m-plane ($1\bar{1}00$) or the a-plane ($11\bar{2}0$).

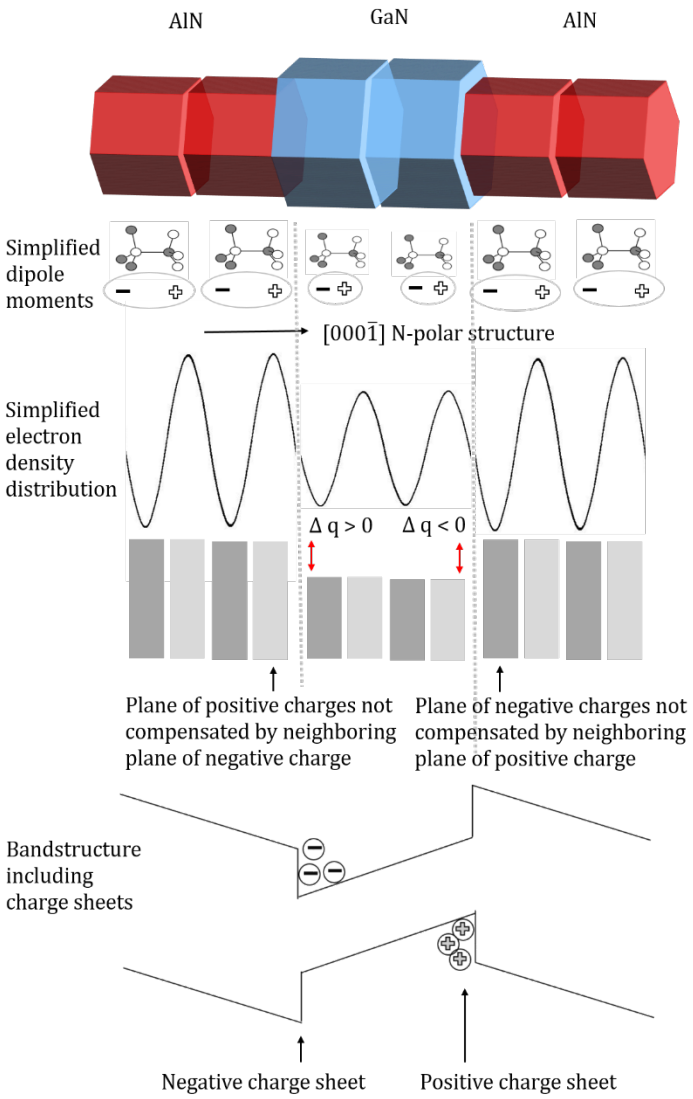

Figure 2.7. Simplified representation of a GaN QW embedded in an infinite GaN/AlN SL structure. In blue: hexagonal wurtzite unit cells of GaN, in red: of AlN. The value of the spontaneous polarization is higher in AlN than GaN, represented by larger dipoles (indicated by + and – signs) and larger electron density. The charge sheets arising due to the difference in spontaneous polarizations are indicated.

2.3. III-Nitride Nanowires

NWs are rod- or wire-shaped structures that have two of the three dimensions nanometer sized. That leads to interesting properties as, for instance, surface phenomena play an important role. Moreover, misfit strain can relax at the surfaces by deformation of the wire rather than by introduction of dislocations as it happens in 2D materials. Heterostructuring capabilities are in that way elevated beyond what is possible in 2D layers.

The growth of GaN NWs can be done on sapphire, Si, GaN or AlN. It takes place epitaxially matched to the substrate. It is called homoepitaxy if the growth material is the same as the substrate and heteroepitaxy if they are different materials. Switching of precursor fluxes allows for heterostructuring and doping.

The fabrication of vertically-aligned semiconductor NWs with an epitaxial relationship with the substrate was demonstrated using a variety of techniques, such as molecular beam epitaxy (MBE), metalorganic vapor phase epitaxy (MOVPE), chemical vapor deposition (CVD), thermal evaporation, or hydrothermal growth.

Independent of the growth technique, NWs can be obtained by several methods: (i) catalytic (or metal-seeded) growth, (ii) catalyst-free growth, (iii) selective area growth, and (iv) top-down fabrication.

i) In the case of *catalytic growth* metal particles are dispersed on a substrate by means of metal evaporation and annealing (random distribution) or lithography, metallization and lift-off (position-controlled arrays). By increasing the temperature and introducing the reactants in the growth chamber, the metal particle forms an alloy with one or more reactants. When the alloy supersaturation is high enough, the growth of the semiconductor NW starts by precipitation at the particle/substrate interface, and continues layer by layer. This growth mechanism is often referred to as VLS (vapor-liquid-solid)[46], and it is maybe the most successful method in synthesizing single-crystalline NWs. Figure 2.8. presents a schematic description of the method together with an example of growth of wurtzite GaAs NWs using gold as a catalyst[47]. As a mayor limitation, the catalyst may contaminate the NW, altering its optical or electrical properties. The most commonly used metal is gold, but other materials have been considered. The catalyst must be a good solvent for the targeted NW material, ideally forming a eutectic compound.
When the catalyst is a constituent of the NW (e.g. Ga for the synthesis of GaAs NWs), we speak about *self-catalyzed* or *self-seeded* growth[48,49]. The major advantage of a self-catalytic process is that it avoids contamination by foreign materials.

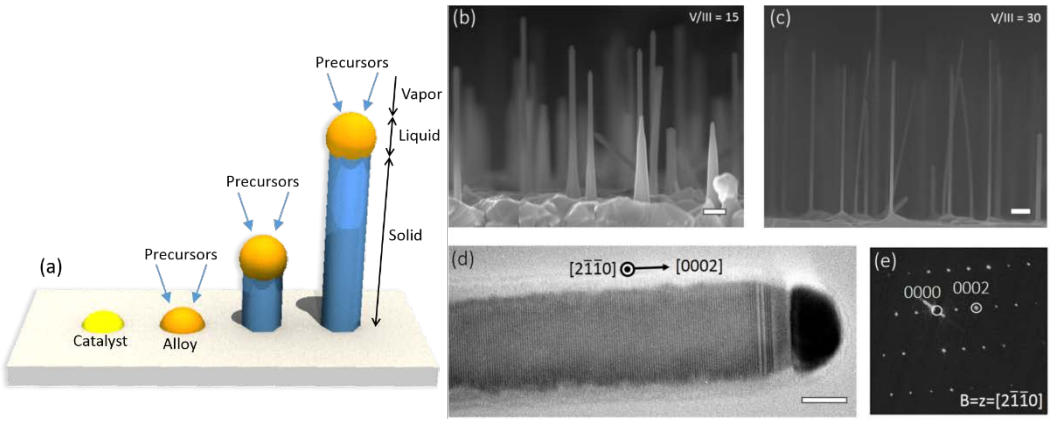

Figure 2.8.(a) Schematic description of the VLS growth method. (b,c) Scanning electron microscopy images of GaAs NWs grown by the VLS method using two different V/III beam-equivalent-pressure ratios. (d) Bright-field TEM image (scale bar corresponds to10 nm) of an individual GaAs NW from (c). The wire has wurtzite crystal structure, as shown on the electron diffraction pattern (e). The region directly below the gold particle features a 'cooling neck' with zinc-blende phase. Taken from ref. 47.

ii) Some materials do not require the presence of seed particles. The growth of NWs happens spontaneously under certain growth conditions. In this situation, we speak about *catalyst-free growth* or *vapor-solid growth mechanism*. For example, GaN NWs can be fabricated by plasma-assisted molecular beam epitaxy (PAMBE) under nitrogen-rich conditions[50–52]. Their strain-driven nucleation process is illustrated in figure 2.9. Likewise the synthesis of metal-oxide nanoribbons is possible by simply evaporating metal-oxide powders at high temperature[53].

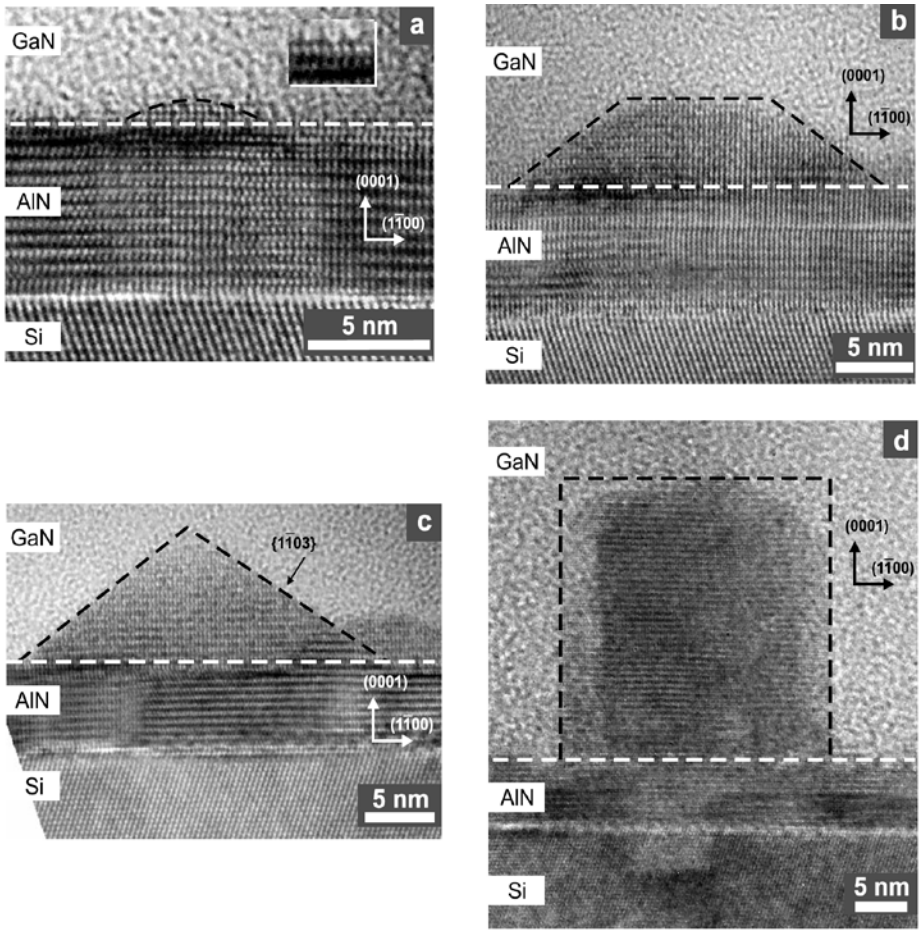

Figure 2.9. High-resolution transmission electron microscopy images illustrating the initial steps of the growth of GaN NWs on Si(111) using an AlN buffer layer by PAMBE. Images were taken after 6, 9, 10 and 15 min of GaN growth under nitrogen-rich conditions: (a) spherical cap-shaped island with an inset representing a high magnification of the first AlN monolayers at the interface, (b) truncated pyramid-shaped island, (c) full pyramid-shaped island, and (d) NW. The pyramid-shaped islands and the NW are hexahedral. All the shapes are outlined for the sake of clarity. Taken from ref. 52.

iii) *Selective area growth* refers to a situation where the substrate is partially masked so that the material only grows in the mask openings[54–58]. By tuning the growth conditions, nucleation is obtained only in the areas where the substrate is exposed. Growth can be highly anisotropic, so that the material grows in one direction only keeping the cross section defined by the mask. As an example, figure 2.10. shows GaN NWs generated by selective area growth on a GaN-on-Si(111) structure using a thin (5 nm) e-beam patterned Ti mask[59]. Growth was performed by PAMBE. In general, in a selective area growth process, the growth rate depends on the distance between mask apertures.

The selective area growth reduces the variations in NW size and length that are characteristic of self-organized processes. As a possible drawback, good selectivity between the mask and the nucleation sites requires relatively high temperature, which might in certain cases complicate the growth of heterostructures or ternary/quaternary alloys. Another issue to be kept in mind is that the NW length depends not only on the growth time and precursor fluxes, but also on the distance between mask apertures.

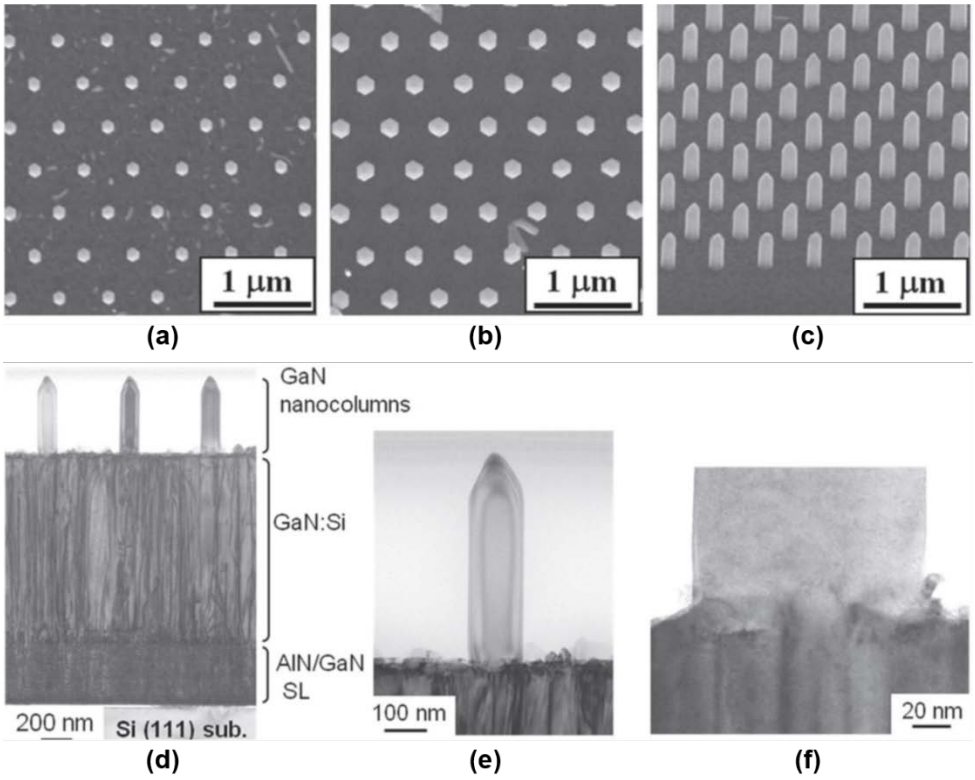

Figure 2.10. GaN NWs generated by selective area growth using a Ti mask. (a-c) Scanning electron microscopy images of a regular triangular-lattice array of GaN NWs with a 500 nm period. The wire diameters are (a) 122 nm, and (b,c) 170 nm. (d-f) Bright-field transmission electron microscopy images of the GaN NWs synthesized by selective area growth on a GaN-on-Si(111) structure. (d) View of the epitaxial layers including the Si substrate, an AlN/GaN superlattice (SL) buffer layer, a thick GaN layer and the GaN rods. (e) NW with a diameter of 122 nm. (f) Magnified image of the bottom of the NW in (e).Taken from ref. 59.

iv) Finally, it is also possible to fabricate NWs following a *top-down* approach, i.e. etching down an originally planar structure[60–62]. The etching pattern can be defined using electron lithography, nanoimprint or colloidal masking, for instance. Top-down NWs present better wire-to-wire homogeneity (even compared to selective area growth), and well controlled doping profile and heterostructure dimensions. This facilitates their integration into large-scale devices. However, in this process the critical thicknesses are determined by the two-dimensional growth, and the dislocations generated in the two-dimensional epitaxial growth remain in the patterned NW array. There is also a risk of structural damage during the plasma etching process, which might lead to a degradation of the optical properties. In some cases, damaged areas can be removed by wet etching, recovering the optical performance.
Figure 2.11. presents an example of GaN NWs obtained by a *top-down* approach[63]. In this case, the etch mask consisted of a monolayer of 3 μm diameter silica colloids that was self-assembled on the GaN surface in a Langmuir-Blodgett trough. GaN posts are then dry etched, which results in tapered rods. Finally, the etch-damaged areas are removed and the rods are thinned by anisotropic wet etching.

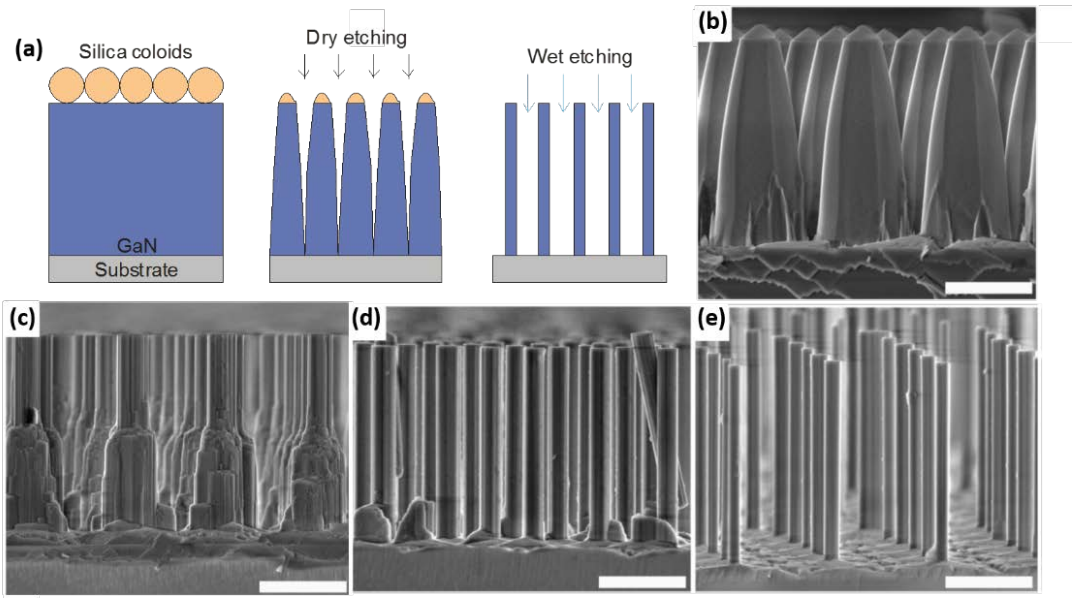

Figure 2.11.(a) Top-down fabrication process of GaN NWs using silica colloids as semi-periodic mask (b-e) Cross sectional SEM images showing dry-etched GaN posts transiting into GaN NWs (b) before wet etch, (c) after 2 hours, (d) after 6 hours and (e) after 9 hours from start of wet etch. All images have the same magnification. Scale bars are 2 µm. Taken from ref. 63.

When fabricating heterostructures, the polarity of the NW is particularly relevant, since it determines the direction of the polarization-induced electric fields. Self-assembled GaN NWs synthesized on sapphire substrates by metalorganic vapor phase epitaxy (MOVPE) grow along the <0001> polar axis and they present generally $\{1\bar{1}00\}$ sidewall facets and mixed polarity[64–66], with predominance of N polarity but with inversion domains contained in the wires. The predominance of N or Ga polarity depends on the substrate, substrate treatment and growth conditions. Thus, pencil-like Ga-polar NWs can be grown on non-nitridated sapphire under low precursor flows[67]. In the case of NWs obtained by selective area growth on sapphire, the core of the wires is generally N polar, and it is sometimes surrounded by a Ga-polar shell that nucleates on the opening rim[65]. Predominant Ga polarity is obtained by selective area growth on Si(111) substrates using AlN as nucleation layer[68].

In the case of GaN NWs grown by PAMBE, self-assembled NWs grow generally along the $[000\bar{1}]$ axis and present $\{1\bar{1}00\}$ sidewall facets. This is independent of the substrate (silicon, sapphire, graphene, SiC, …). It is also relatively common that the NWs contain inversion domains[69]. The more reliable method to obtain Ga-polar NWs by PAMBE is the selective area growth on Ga-polar GaN substrates using metallic or dielectric masks[70].

In summary, GaN NWs grow along the polar axis and present nonpolar, generally m-plane facets. This implies that axial heterostructures are affected by the polarization-related internal electric field, but this is not the case for core-shell heterostructures.

Doping is a further control parameter playing a big role. N-type doping in GaN NWs and 2D layers is easily achieved, as non-intentionally doped GaN is intrinsically n-type[71,72]. The electron density can however be further increased by incorporating either Si or Ge. These two elements are group IV and their thermodynamically more stable constellation is replacing the group III element Ga, leading to n-type doping. Historically, Si was employed. In NWs, however, Si migrates to the NW sidewalls[73] introducing inhomogeneous doping. In recent years Ge wasemployed in both 2D layers and NWs[74], introducing less distortion of the lattice than Si.

P-type doping in planar structures is done with Mg. In NWs, p-doping was demonstrated as early as 2003 (using CVD)[75]. The incorporation of Mg requires a large reduction of the growth

temperature which also leads to an increase of unwanted lateral growth on the NW sidewalls. It has also been demonstrated that its incorporation is not uniform. Nevertheless, NWs including a p-n junction were demonstrated as both radial (core-shell)[76] and axial junctions[77,78].

Similarly, there are two ways of heterostructuring a NW. One is a radial sequencing of the materials which results in core-shell structures, as described in figure 2.12.(a). The other is an axial sequencing of the materials which results in axial or so called dot-in-a-wire heterostructures, illustrated in figure 2.12.(b). The heterostructures employed for the detection of light are outlined in more detail in chapter 2.7., including the relevant references.

Figure 2.12. Schematic description of (a) radial (core-shell) and (b) axial NW heterostructures.

The application possibilities of GaN NWs are wide and have been explored extensively. One large group of applications is energy conversion. Here photoconductors[18,20,79,80], photodetectors[81], photovoltaics[82,83] and piezoelectric transducers[84,85] are important. This manuscript focuses on photodetectors. Similarly, NW light emitting diodes[86,87] and NW lasers[88] have been demonstrated. Furthermore, NW applications can be found in nanoelectronics. Single NW field effect transistors[71,89–92], single electron transistors[93,94] and resonant tunneling diodes[95,96] have been developed. The group of sensor applications[21,97] is another big group making use of the chemical robustness characteristic of GaN.

2.4. Photodetectors

Photodetectors are devices that function as sensors of electromagnetic radiation. Typically, semiconducting materials are employed in a configuration relying on the photoelectric effect. While the standard configuration consists of a p-n junction, other device designs are possible. Solar cells are likewise based on photodetectors. In the following, standard figures of merit are described that serve as a metric of comparison between devices.

2.4.1. Responsivity and gain

The main parameter allowing to quantify the performance of any photodetector is the responsivity (R_λ), which expresses the generated photocurrent (I_{ph}) per incident optical power (P_{opt}):

$$R_\lambda = \frac{I_{ph}}{P_{opt}} = \frac{I_{ph}}{\Phi_{ph} A_{opt}} \tag{2.9}$$

where Φ_{ph} is the incident photon flux density, and A_{opt} is the illuminated area of the detector. The expression for the responsivity can be further developed to take into account losses described with the help of the quantum efficiency and the gain. The quantum efficiency (η) quantifies the number of generated electron-hole pairs per incoming photon, whereas gain (g) refers to the number of actually detected electrons per generated electron-hole pair. Additionally, expressing the incident photon flux density in terms of the wavelength (λ) and natural constants, we obtain:

$$R_\lambda = \frac{I_{ph}}{\Phi_{ph} A_{opt}} = \eta g \frac{e\lambda}{hc} \tag{2.10}$$

where *e* is the fundamental charge, *h* is Planck's constant, and *c* the speed of light.

The concept of photoconductive gain deserves further analysis. The gain can be written as:

$$g = \frac{I_{ph}/e}{P_{opt}/\left(\frac{hc}{\lambda}\right)} \tag{2.11}$$

In a photoconductor, i.e. a biased detector that reacts to illumination by changing its conductivity, the photocurrent can be described as $I_{ph} = V_B \Delta G$, where V_B is the bias voltage and ΔG is the change in the conductance. In turn, ΔG can be expressed as:

$$\Delta G = \Delta\left(en\mu\frac{A}{l}\right) = \frac{e\mu}{l}(A\Delta n + n\Delta A) \tag{2.12}$$

with n being the number of charge carriers, μ the carrier mobility, A the cross-section of the conductance channel, and l its length. The term Δn describes a change of the number of charge carriers and is therefore linear with increasing incident optical power (note that $\Delta n = \eta\Phi_{ph}$). However, the term ΔA is accounting for changes in the cross-sectional area of the conductance channel which depends nonlinearly on the density of carriers and on the location of the Fermi level at the NW sidewalls. Note that equation 2.12 assumes no changes in the carrier mobility due to illumination.

2.4.2. Quantum efficiency, external and internal quantum efficiency, conversion efficiency

For a photovoltaic detector (device operated at zero bias), the quantum efficiency (η) is the ratio of extracted free charge carriers (electrons in the external circuit) to incident photons. We generally differentiate between external quantum efficiency (EQE), which considers all photons impinging on the device, and internal quantum efficiency (IQE), which considers only photons that are not reflected.

The quantum efficiency (η, EQE or IQE) is a function of the photon wavelength, hence it is generally expressed as a spectral function. It should be differentiated from the "conversion efficiency" or just "efficiency" that characterizes a solar cell. In this case, efficiency refers to the ratio of electrical energy extracted from the solar energy impinging onto the cell. This parameter measures not only the performance of the solar cell as a photon-to-electron converter, but also the adaptation of the spectral response to the solar spectrum. The conditions under which the solar cell efficiency is measured must be carefully controlled, e.g. terrestrial solar cells are measured under standard AM1.5 conditions (ISO 9845-1:1992) and at a cell temperature of 25°C (contrary to solar cells used in space, which are characterized using AM0 conditions).

2.4.3. Spectral selectivity

When the spectral selectivity is considered as a factor of merit, the use of direct bandgap materials is generally preferred. In the case of ultraviolet photodetectors, a spectral figure of merit is the ultraviolet-to-visible rejection ratio, which is calculated as the peak responsivity in the ultraviolet range divided by the responsivity at 400 nm.

The spectral selectivity can be enhanced by integrating the active region into a resonant optical cavity, forming what is called resonant-cavity-enhanced photodetectors[98]. In addition to the spectral selectivity, the optical cavity serves to enhance the device responsivity without increasing the size of the active region.

2.4.4. Detectivity

The minimum detectable optical power, i.e. the optical power that provides a signal-to-noise ratio equal to one, is called the noise equivalent power, *NEP*. The NEP can be calculated by dividing the detector noise current (I_N) by the responsivity. The detectivity, D, is defined as the inverse of the *NEP*:

$$D = \frac{1}{NEP} = \frac{R_\lambda}{I_N} \tag{2.13}$$

The parameter generally used to compare different photodetector systems is the specific detectivity D^* (in Jones = cm $Hz^{1/2}\,W^{-1}$), which is D corrected for the detector optical area and bandwidth (Δf):

$$D^* = \frac{R_\lambda}{I_N}\sqrt{A_{opt}\Delta f} \tag{2.14}$$

2.4.5. Time response and 3 dB bandwidth

To quantify the time response τ_r of a photodetector under pulsed illumination the rise or fall time between 10% and 90% of the maximum response value are commonly used. The rise and fall times depend, on the one hand, on the photodetector electrical time constant $\tau_{RC} = RC$, where R is the resistance and C the capacitance of the photodetector. On the other hand, the time response depends also on drift and diffusion processes. The drift component (τ_{drift}) accounts for the movement of charge carriers traversing space charge regions, whereas the diffusion component (τ_{diff}) describes the movement of charge carriers along charge-neutral regions. These components lead to

$$\tau_r = \sqrt{(2.2\tau_{RC})^2 + \tau_{drift}^2 + \tau_{diff}^2} \tag{2.15}$$

for the time response (where the 2.2 factor arises due to the 10-90% definition of the response time). A detailed description of the response time of semiconductor photodiodes can be found in ref. [99].

The 3 dB bandwidth (BW_{3dB}) is defined as the modulation frequency i.e. chopper frequency of the incident light when the responsivity decreases by 3 dB (= 0.707 times the low-frequency value). The bandwidth is related to the response time of the detector by approximately $\tau_r = 1/2\pi BW_{-3dB}$.

2.5. Nanowire Photodetectors

2.5.1. Light Coupling

Extracting the responsivity of NW photodetectors from the measurements of the photocurrent as a function of the irradiance is not evident, mostly due to the non-obvious definition of the photodetector optical area (A_{opt} in equation (2.9))[100–103]. When a NW (or a NW ensemble) is exposed to an incident photon flux density Φ_{ph}, precise calculation of the absorbed optical power, $P_{opt} = \Phi_{ph}A_{opt}$, requires understanding how a planar light wave interacts with the NWs, which is a function of the wavelength, and the NW shape and refractive index. In the case of a NW ensemble or an array, the density and arrangement of the NWs must also be taken into consideration.

Analytical investigations by Xu et al.[100] suggest that vertical NW arrays behave similarly to a concentrating lens or a parabolic mirror, due to the large refractive index contrast between the NWs and the surrounding environment. This optical concentration effect, depicted in figure

2.13.(a), results in an increase of the effectively absorbing cross-section. Following the analysis of Heiss et al.[101], we can define "absorption enhancement" as the ratio between the absorbed optical power and the optical power that impinges onto the geometric cross-section of the NW as

$$Absorption\ enhancement = \frac{A_{opt}}{A_{inc}} \tag{2.16}$$

where A_{inc} is the cross-section of the wire exposed to the incident light. In the case of a standing NW and a planar wave incident perpendicularly to the substrate, $A_{inc} = \pi r^2$, where r is the NW radius (approximation of the NW by a cylinder with circular cross section). As an example to illustrate the relevance of the difference between A_{opt} and A_{inc}, figure 2.13.(b) describes the variation of the absorption enhancement as a function of the NW diameter ($2r$) and the wavelength of the incident light in a single GaAs NW standing on a silicon substrate. Note that the enhancement can reach a factor of 70, i.e. the optical area can be 70 times the geometrical area. Evidently, such considerations apply as well, with respective modifications, to NWs lying horizontally on a substrate (or experiencing sideway illumination)[104,105].

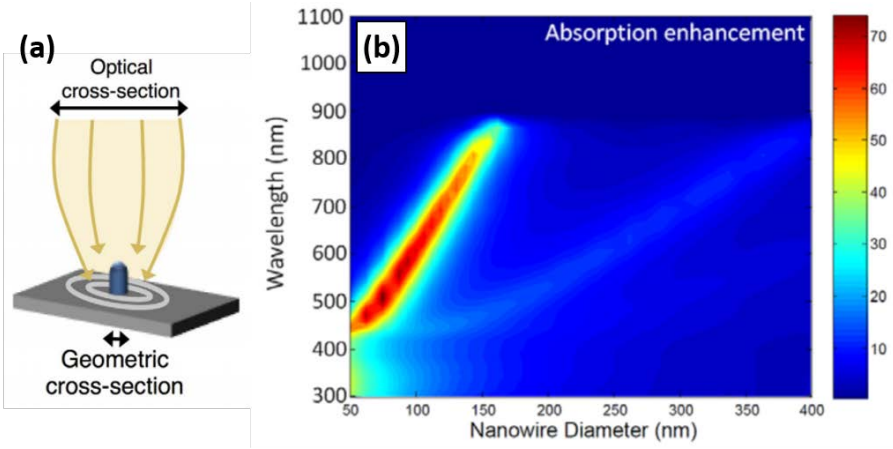

Figure 2.13. (a) Schematic of optical concentration in a nanostructure, illustrating the difference between optical area and geometrical area. Taken from ref. [100] *(b) Absorption enhancement in a single vertical GaAs NW standing on a silicon substrate, as a function of the NW diameter (2r). Taken from ref. 101.*

Due to the complexity of the calculation of A_{opt}, responsivity values in the case of single NW photodetectors are often obtained using the geometrical cross-section, A_{inc}. In this case, the responsivity values can be significantly over-estimated.

In the case of NW ensembles, theoretical works have studied the dependence of the light absorption on the diameter of the NWs, their geometry, and their geometrical arrangement on the substrate[103,106–109]. In particular, dense layers of randomly-spaced NWs are known to enhance light absorption thanks to multiple scattering, which reduces the specular reflectance[110].

2.5.2. Nanowire metal-semiconductor-metal photodetectors

Metal-semiconductor-metal photodetectors consist of a semiconducting material sandwiched between two metal contacts, which can be Ohmic or Schottky (rectifying)[111]. In general, a device with two Ohmic contacts behaves as a photoconductor, i.e. a resistor whose Ohmic value depends on the impinging light intensity. In the case of planar structures, photoconductors are slow (seconds) devices that operate under bias and can display extremely high values of responsivity, but their response is strongly sublinear with the optical power and they present problems of spectral selectivity since they are very sensitive to absorption below the semiconductor bandgap[111].

Replacement of one of the contacts by a Schottky contact results in the presence of a depletion region below the Schottky metallization which favors the collection of photogenerated carriers by drift transport. Typically, such devices react linearly to the incident irradiation, they do not present internal gain, and their speed is limited by resistance × capacitance (RC) factors. Schottky diodes can operate at zero bias, although applying negative bias on the Schottky contact increases the length of the depletion region resulting in higher responsivity and faster response (lower capacitance).

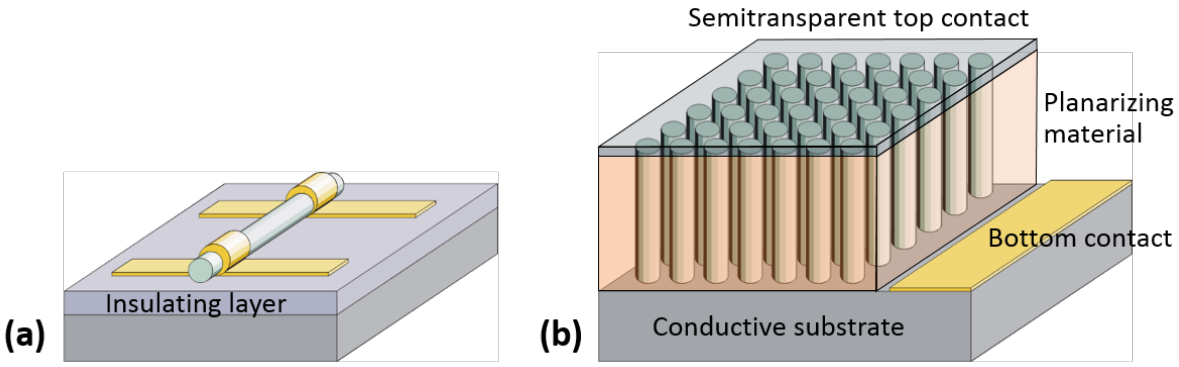

Figure 2.14. Schematic description of (a) a single-NW photodetector and (b) a NW ensemble photodetector.

If the two contacts are Schottky barriers, a situation of total depletion between the contacts may occur. In such a situation, the devices present space-charge-limited dark current and photogenerated carriers drift fast between the contacts. Generally, the photocurrent scales linearly with the optical power. Photodetection requires external bias, and gain might appear if the devices are operated at very high voltages.

Now that the different kinds of metal-semiconductor-metal detectors that can be implemented in planar geometries are introduced, we discuss below the results when such devices are fabricated using NWs. Single NW photodetectors can be fabricated by dispersion of NWs on an insulating substrate, followed by contacting using typically electron beam lithography, with the result described in the schematic in figure 2.14.(a). On the other hand, ensemble NW photodetectors consist of a layer of standing NWs which is planarized before contacting, as described in figure 2.14.(b). There are a number of publications on single NW photoconductors using a variety of wurtzite materials (GaN[18,79], AlN[112], InN[113], ZnO[114–117], ZnSe[118], ZnS[119], CdS[120,121], InP[122]).

2.5.3. Linearity and Responsivity

To identify the role of the NW on the photodetector performance, we will in the following focus on the properties of single NWs. In the case of single NW photoconductors, the variation of the photocurrent as a function of the incident optical power is often sublinear[18,114,115,123–127], as illustrated in figure 2.15.(b) for PAMBE-grown n-i-n (400 nm n-type Si-doped/ 400 nm undoped/ 400 nm n-type Si-doped) GaN NWs with the characteristics and measuring setup described in figure 2.16.[18].

Experimental results are often described with the relation

$$I_{ph} \propto P_{opt}^{\beta} \tag{2.17}$$

where the degree of linearity can be quantified with the exponent β. In the case of $\beta = 1$ the detected photocurrent is linear, whereas $\beta < 1$ describes a sublinear dependence. In the case of pulsed photocurrent measurements using a synchronous detecting system (light chopper and lock-in amplifier), increasing the chopping frequency leads to an improvement of the linearity (higher β)[18,128], as illustrated in figure 2.15.(b). However, in the case of GaN NWs, it was

demonstrated that the chopping frequency does not have any effect on the spectral response of the photodetector (see figure 2.15.(c)), in contrast to similar measurements on planar photoconductors[111].

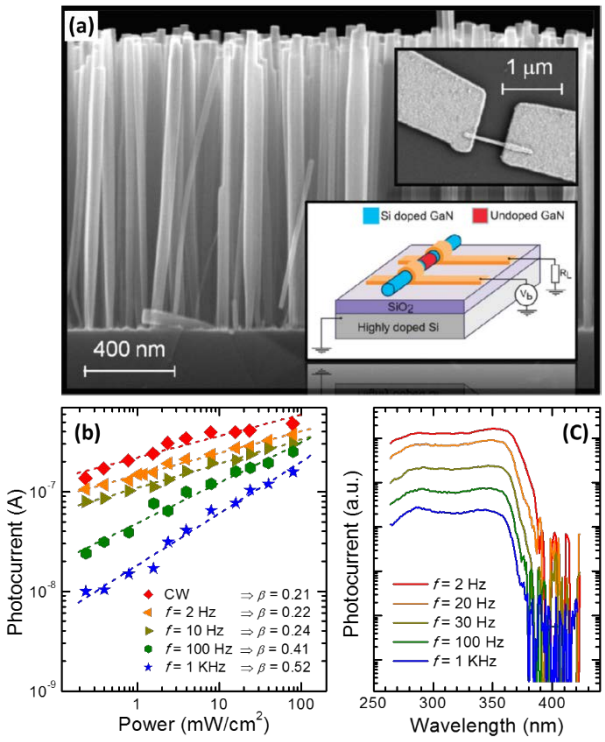

Figure 2.15. (a) Scanning electron microscopy image of n-i-n GaN NWs on a Si(111) substrate. Insets: Top panel is the top-view of a contacted single NW; bottom panel shows the measurement scheme for characterization of a single NW device. (b) Photocurrent variation from a single GaN NW as a function of the excitation power (λ = 244 nm) measured with a synchronous detection system at various light chopping frequencies. Dashed lines are fits to the relation $I_{ph} \propto P_{opt}^{\beta}$ using the values of β indicated in the legend. (c) Spectral response of a single GaN NW photodetector under 3 V bias measured at various light chopping frequencies. The spectra were corrected by the lamp intensity taking the measurements of the degree of linearity in (b) into account. Taken from ref. 18.

The nonlinearity of NW photodetectors, observed even in NWs that do not contain dislocations, stacking faults or inversion domains, suggests that the photoresponse is dominated by the redistribution of charge at the surface levels[18,80,115,129]. The surface states (mostly hole traps, with the exception of materials such as InN or InAs) determine the location of the Fermi level at the NW sidewalls, and generate a depletion region that propagates into the NW core (see figure 2.16.(a)). Illumination is known to modify the Fermi level pinning at the sidewalls[130], which results in a decrease of the depletion region depth and the corresponding enlargement of the diameter of the conductive core. This phenomena is sometimes called photogating effect[127,131], and it justifies the nonlinearity of the photocurrent via the second term of eq. (2.9)[18,132]. An additional contribution to the nonlinearity comes from an increase of the lifetime of photogenerated electrons due to the trapping of holes at surface states[73,79,129].

In this discussion, we have considered that the Fermi level pinning at the NW sidewalls originates an upwards band bending, hence pushing electrons towards the core of the wire. This is the case in NWs based on GaN, GaAs, ZnO, ZnS, CdS, etc. However, it is known that the use of materials like InAs[133–135] or InN[136–138] results in the opposite configuration: the Fermi level is pinned deep into the conduction band, and this originates an accumulation of electrons at the sidewalls.

There is a general agreement that NW photodetectors present high responsivity. However, the precise value of responsivity can depend on the optical power and on the light modulation

frequency. Therefore, it is important to indicate the degree of linearity of the detector, and the incident optical power for which the responsivity is measured. Furthermore, it is also imperative to indicate the optical area, A_{opt}, which is taken into account in the calculation (see discussion in section 2.5.1), to transmit a clear idea of the meaning of the responsivity value and allow comparative studies. Some authors prefer reporting gain instead of responsivity. Let us remind that gain and responsivity are linearly linked by eq. (2.10), and the quantum efficiency (η, number of photogenerated electrons per incident photon) is generally assumed to be unity. Keeping these considerations in mind, experimental values of gain in the range of 10^5-10^8 have been reported in single NW photodetectors based on ZnO[114,115], ZnS[139,140], ZnSe[118], GaN[18,126,141], InN[113], GaAs[125,142], or InAs[143]. In general, these high gain values can be attributed to the effect of light on the surface depletion region (i.e. on the conductive area of the device) and to the enhancement of the carrier lifetime due to the radial separation of photogenerated electrons and holes.

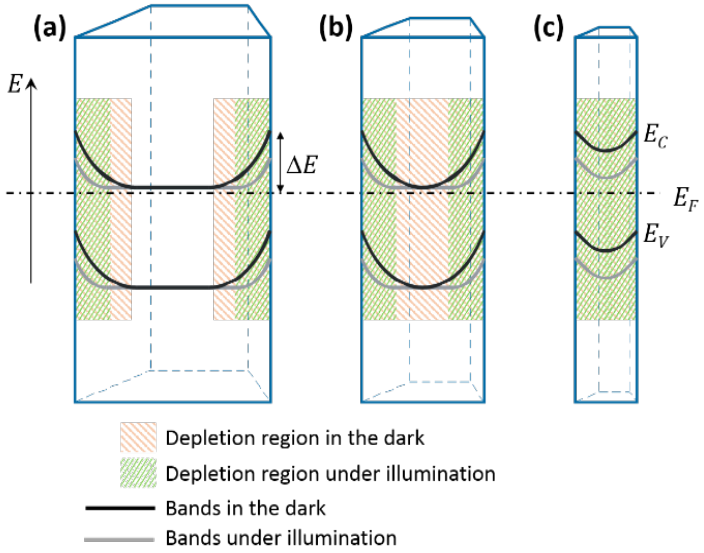

Figure 2.16. Schematic description of the conduction (E_C) and valence (E_V) band profile along the NW diameter in the dark (black) and under illumination (grey) for NWs that are (a) partially depleted, (b) at the threshold of full depletion in the dark, and (c) fully depleted. The dash-dotted line marks the Fermi level in the dark (E_F). In all the cases, the Fermi level is considered pinned at the NW sidewalls at an energy position $E_C - \Delta E$. Shadowed areas mark the depletion region in the dark and under illumination.

2.5.4. Time response

As described above, the radial separation of photogenerated electron and holes due to the surface band bending introduces a delay in the time response of NW photodetectors and photoconductors. When the light is switched off, the excess electrons in the NW conductive core have to overcome a potential barrier to recombine with the holes, located at the sidewalls. During the recombination process, the barrier height depends on the remaining carrier excess, so that the photocurrent decay can be strongly nonexponential[144]. As a result, the measured time response is a function of the incident optical power, with the response being faster for higher optical excitation. On the other hand, fully depleted NWs are responding faster than partially depleted wires[145], since the potential barrier for electron-hole recombination is lower in the former case, see figure 2.16.

It is important to note that the time response of NW metal-semiconductor-metal photodetectors (in the second to picosecond range, depending on the device architecture) is significantly faster than the persistent photoconductivity typically observed in planar photoresistors, where the photocurrent transients can be in the range of hours[111]. It was argued that the presence of deep defects such as oxygen vacancies in GaN might play a role on the

presence of persistent effects in NWs[129], but it is difficult to assess the relevance of such defects in comparison with the undeniable role of the surfaces and adsorbates. On the contrary, the excellent spectral selectivity of GaN NW photoconductors[18,114] testifies to the low point defect density in the NWs.

2.5.5. Effect of the Environment

As discussed above, the chemical environment can modify the energy location of the Fermi level at the NW sidewalls, with the subsequent effect on the dark current, responsivity/gain and time response. Therefore, these devices are particularly suitable for gas and chemical sensing. As an example, a comparison of the behavior of GaN, ZnO or InAs NW photodetectors in vacuum and in the air shows that the vacuum environment leads to higher dark current, higher responsivity and much slower photocurrent transient[21,81,114,143,145,146].

The influence of the surface on GaN 2D layers is well described by Foussekis et al.[147] and later in several works for GaN and ZnO NWs[114,127,130]. A remaining O_2 molecule from the environment may adsorb onto the NW surface via chemisorption. That involves capturing a free electron from the n-doped section of the material and forming a negatively charged ion at the surface. This pins the Fermi level and leads to an upward bending of the bands towards the surface in the n-type section. Upon UV exposure photogenerated holes migrate to the surface due to the bandbending. At the surface the negatively charged O_2 ion is neutralized and desorped. The desorbtion unpins the Fermi level which introduces a flattening of the bands and therewith an increased probability for the radiative recombination[79] of an electron hole pair. Underlining this, the PL intensity of GaN NWs in vacuum both at 10 K and at room temperature were shown to increase 2−5 times in intensity with continued UV illumination up to a level of saturation reached around 10 min after the start of the illumination[130]. Similarily, in air it has been shown that GaN nanocolumns at room temperature display a rising PL intensity within the first couple of seconds of UV illumination, going from 10% to 60% of its intensity in vacuum[148]. However, the intensity was observed to decay thereafter back to 10%. The depletion of the near-surface regions of the NW through the O_2 ions leads to smaller conduction channels for the photocurrent through the NW and therewith lower photocurrent. It is also possible that the photocurrent decreases due to recombination effects with the O_2 ions at the surface. Therefore the effect of O_2 may cause both decreased PL intensity and decreased photocurrent.

The sensitivity to the environment can be attenuated by inserting heavily doped regions in the NW[81], or by dielectric passivation of the surface[143].

2.5.6. Nature of the Contacts

Metal-semiconductor-metal NW photodetectors with two Ohmic contacts require bias, and they have high responsivity, often at the price of a slow response time. If one of the contacts is replaced by a Schottky contact, the dark current drops drastically as a result of the potential barrier at the metal-semiconductor interface. Under illumination, photogenerated electrons and holes are axially separated due to the electric field in the proximity of the Schottky contact. This allows operation at zero bias, which has motivated some authors to refer to these devices as “self-powered devices”[149]. The response time is shortened since transport under illumination is dominated by the drift of minority carriers towards the Schottky contact, and, in the absence of light, the current is quenched by the presence of the Schottky barrier. These processes have been demonstrated, for instance in ZnO NWs[150–153]. In contrast to planar Schottky photodiodes, devices based on NWs remain generally sublinear and with a millisecond time response, which is an indication of the relevance of surface phenomena in the process of carrier collection.

When both contacts are replaced by Schottky diodes, devices are generally referred as metal-semiconductor-metal photodiodes. In planar structures, the back-to-back Schottky

configuration is interesting to obtain total depletion between contacts. However, in the NW geometry, it is easier to obtain total depletion radially, via the sidewall surfaces, than axially, where very low residual doping levels would be required to get a Schottky depletion length comparable to the NW length. The use of two Schottky contacts results in a drastic decrease of the dark current, but the nominal symmetry of the device prevents zero-bias operation.

2.6. Nanowire p-n Junction Photodiodes

In p-n photodiodes, electrons and holes photogenerated near the junction drift in opposite directions due to the internal electric field in the space charge region. Similarly to Schottky photodiodes, p-n photodiodes can be operated at zero-bias, but speed and responsivity are enhanced when the junction is reverse biased, owing to the increase of the space charge region length. These devices are expected to display lower dark current than metal-semiconductor-metal photodetectors, since the junction behaves as a potential barrier that inhibits carrier transport in the dark. Furthermore, the capacitance associated to the depletion region of the p-n junction can be easily smaller than that of a Schottky photodiode, since the p-n potential barrier is approximately the semiconductor bandgap, generally larger than a Schottky barrier. Under zero-bias or reverse bias, p-n photodiodes react linearly to the incident optical power and present zero gain. Gain associated to impact-ionization phenomena (avalanche amplification) can appear when the devices are strongly reverse biased (several times the semiconductor bandgap). Gain can also occur under forward bias or in the case of reverse-biased junctions with important leakage current, since in these cases the response can be dominated by the photoconductor-like behavior of the conductive p and n type regions.

NW-based p-n photodiodes have been reported using a number of materials. In NW devices where both p and n regions are contained in the same NW, the arrangement can be radial [core-shell junction, as described in figure 2.17.(a), e.g. GaAs[154,155], GaAsP[156,157] or GaN[76]] or axial [as described in figure 2.17.(b), e.g. GaN[77,78], GaAs[158], or ZnO[159]]. The p-n junction can be implemented as a homojunction (both p- and n-doped zones are of the same material) or a heterojunction (p- and n-doped zones combine different materials). Homojunctions have the obvious advantage of avoiding any lattice mismatch, and therewith losses due to carrier recombination at structural defects at the junction. However, the doping levels can be limited by material or growth issues, e.g. it is difficult to obtain p-type ZnO or uniformly doped p-type GaN nanostructures. As alternative solutions, p-n photodiodes can be obtained by crossing two NWs [figure 2.17.(c)], one of them n-type and the other one p-type[118,153,160–164], branching[165–167] [figure 2.17(d)], or growing n(p)-type NWs on a p(n)-type substrate [figure 2.17(e), e.g. n-i-InP NWs on p-InP substrate[168], n-ZnO NWs on p-GaN substrate[169,170], p-ZnO NWs on n-ZnO substrates[171] or p-InGaAs NWs on n-GaAs substrate[172]].

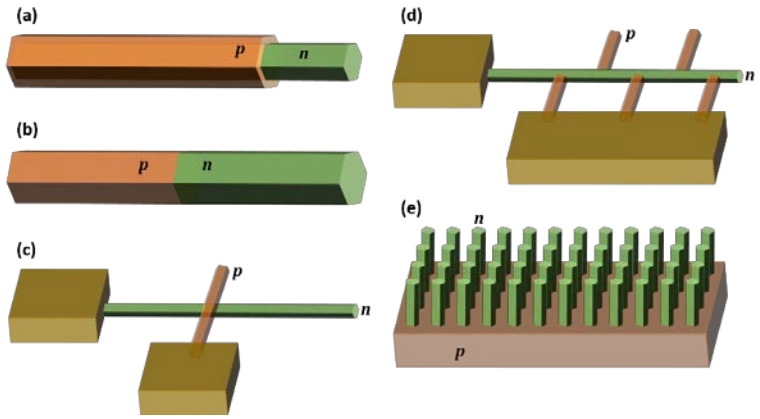

Figure 2.17. Schematic description of various p-n junction configurations involving NWs: (a) radial (core-shell), (b) axial, (c) crossing n and p NWs, (d) branched p-n junction, and n-type NWs on p-type substrate.

In the case of compound-semiconductor NWs, avalanche photodiodes have been demonstrated using a crossed n-CdS/p-Si heterojunction[160], an InP axial p-n junction incorporating an InAsP quantum dot[173] or an InAsP section (n^+-InP/n-InAsP/n-InP/p^+-InP, illustrated in figure 2.18.)[174], radial GaAs p-n junctions[175,176], and p-i-InGaAs NWs on n-GaAs substrates[177]. These devices are interesting for application in single-photon counting. For this purpose, semiconductor NWs offer advantages such as enhanced absorption due to optical resonance effects, elastic relaxation of the misfit strain in heterostructures, and compatibility with silicon technology. An additional advantage that was recently proposed is associated to the structure of a NW ensemble photodetector. Among the total amount of NWs constituting one photodiode, each avalanche event is confined in a single NW, which means that the avalanche volume and the number of filled traps can be drastically reduced. This leads to an extremely small afterpulsing probability compared to conventional single-photon avalanche photodetectors (SPADs). Farrell et al. have recently demonstrated NW-ensemble SPADs with a dark count rate below 10 Hz, due to reduced fill factor, with photon count rates of 7.8 MHz and timing jitter less than 113 ps[177].

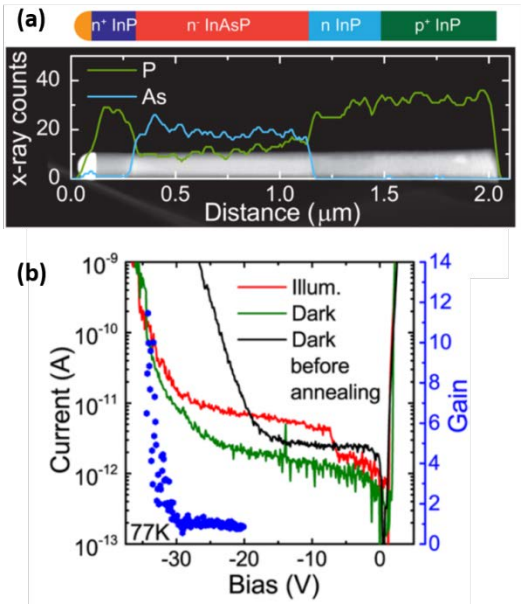

Figure 2.18. (a) Schematic of an InP/InAsP NW avalanche photodetector, along with energy-dispersive x-ray spectroscopy linescans superimposed on a transmission electron microscopy image. (b) Current-voltage characteristics and gain at 77 K of an InP/InAsP NW avalanche photodetector in the dark, before and after annealing, and after selective illumination of the InAsP absorption region. Taken from ref. 174.

2.7. Heterostructured Nanowire photodetectors

A heterostructure sequences a number of materials in a specific order to engineer the energy bands for certain purposes, e.g. charge carrier separation, quantum confinement, current blocking or tunneling. In the following different heterostructuring possibilities are outlined that are used in the design of photodetectors. While the two main types are radial and axial heterostructures, the difference between axial interband and axial intersubband structures are described in more detail.

2.7.1. Radial (core-shell) Nanowire photodetectors

The fabrication of core-shell NW heterostructures can obey several motivations:

i. To provide a *photoconductive NW with a passivating envelop* that improves its stability and reduces the effect of surface phenomena (e.g. surface recombination or chemical sensitivity). Examples of this application are GaAs/AlGaAs[178] or ZnO/ZrO_2[179] core/shell structures.

ii. To implement a *core-shell p-n junction photodetector*. In this case, the radial heterojunction is considered advantageous with respect to an axial heterojunction since the direction of light incidence is normal to the direction of charge separation. Therefore, this geometry provides short collection lengths (determined by the NW diameter, which is smaller than the carrier diffusion length) compatible with a large absorbing volume (determined by the NW length, which can be much longer than the absorption depth)[180]. As a result, the carrier collection efficiency can be improved without reducing the total absorption. However, in view of its application in solar cells, the radial heterojunction geometry complicates the implementation of tandem architectures considerably[181,182].

iii. To implement a *type-II heterostructure* which separates electrons and holes radially, thus increasing the carrier lifetime. Such type-II heterostructures have been proposed as an alternative to p-n junctions for the fabrication of solar cells[183]. Examples of type-II core/shell NW heterostructures are ZnO/ZnTe[184–186], ZnO/ZnSe[187–189], ZnO/ZnS[190,191] or ZnO/CdTe[192–195]. Note that the most stable crystallographic structure of ZnTe, ZnSe and ZnS is cubic zinc blende. As a result, an interesting feature in these kind of heterostructures is that the shell can present a different crystallographic structure than the wurtzite ZnO core. There is a significant dispersion in the values of band offsets in the literature[196–199].

2.7.1.1. Axial Nanowire Photodetectors

The incorporation of axial heterostructures in NW photodetectors may serve various purposes, e.g. designing quantum wells to tune the absorption spectrum or introducing a band bending leading to charge carrier separation. Within quantum wells, NW photodetectors can make use of either band-to-band transitions, whose energy depends on the semiconductor bandgap, or intersubband (ISB) transitions, i.e. transitions between confined electron states located within the conduction band or within the valence band. An ISB transition can occur only when there is an excess of electrons (if the transition involves conduction band states) or holes (if the transition involves valence band states). The ISB transition energy is determined by the size of the nanostructures and is independent of the semiconductor bandgap.

2.7.1.2. Interband Nanowire photodetectors

In the near-infrared spectral range, NW photodetectors incorporating axial heterostructures have been demonstrated using the InAs/InAsP[200] and InAsP/InP[173,201,202] material systems. As an outstanding result, InP NW photodetectors with a single InAsP well as light absorbing element demonstrated a quantum efficiency of 4%[201]. Under resonant excitation, the photocurrent scales linearly with the optical power and it is enhanced for light polarized parallel to the NW axis. These first results were promising for the development of photodetectors with subwavelength spatial resolution. In a second stage, a single InAsP well displaying photocurrent in the 963-1007 nm range was located in the avalanche multiplication region of a NW photodiode, which allowed the demonstration of single photon detection with a NW photodiode[173].

In the visible domain, a GaAs/GaP multi-quantum-well structure was used to tune the photocurrent spectral response of a GaP NW photodetector[203]. The presence of 15 periods of

GaAs/GaP (13 nm/ 15 nm) inserted in the i-region of a GaP p-i-n junction NW did not have a significant impact on the electrical behavior of the structure, but it red shifted the photocurrent spectral cutoff from 500 nm for pure GaP to 550 nm. In this case, an AlP shell was used to envelop the whole NW as a passivation method.

In the ultraviolet spectral range, selective photodetection is generally implemented using ZnO or GaN based NWs. These materials present strong polarization along the <0001> crystallographic axis, which is generally the growth axis of the NWs. At an axial heterointerface with a material of different polarization, the local charge distribution does not get compensated, which results in a fixed charge sheet located at the heterointerface. Such polarization-induced charge sheets modify significantly the band structure, e.g. generating an internal electric field in the quantum wells (see figure 2.6(c)], which leads to the separation of electron and hole wave functions. Therefore, the oscillator strength of the band-to-band optical transition decreases, and the transition energy decreases too. This is known as quantum confined Stark effect. Taking the polarization differences into consideration is hence critical to understand the performance of axial heterostructures.

The effect of inserting a 3.6-nm-thick AlN section into an n-i-n GaN single NW photodetector was studied by den Hertog et al.[21,204], with the results illustrated in figure 2.19. The NWs were synthesized catalyst-free by PAMBE under N-rich conditions. Structurally, the AlN insertion resulted also in the formation of an AlN shell that enveloped the GaN base of the NW. This thin (≈ 0.5 nm) AlN shell was in turn covered by a GaN shell with a thickness of 4-10 nm. These shells are due to the AlN and GaN radial deposition during growth. From the electrical viewpoint, the presence of the AlN insertion blocks the electron flow through the GaN core forcing a drop of the dark current by at least 3 orders of magnitude. The polarization difference between AlN and GaN results in an asymmetric potential profile that manifest in rectifying current-voltage characteristics in the dark, and zero-bias photoresponse under illumination. The insertion of the AlN barrier in the n-i-n GaN NW does not degrade the spectral selectivity of the structures. However, the GaN/AlN/GaN core/shell structure provides a parallel conduction path, i.e. the current can flow through the GaN outer shell, close to the NW sidewalls, as indicated in figure 2.19.(a). This surface conduction path increases the sensitivity of the photocurrent to the environment and in particular to the presence of oxygen [see figure 2.19.(d)], which can be interesting for the fabrication of chemical sensors, but it is undesirable in GaN/AlN photodetectors since it reduces the environmental stability and masks the advantages of the inserted heterostructure.

The presence of the GaN outer shell can be avoided by increasing the growth temperature. Axially heterostructured single NW photodetectors containing a wurtzite GaN/AlN SL without outer GaN shell were first demonstrated by Rigutti et al.[20] in 2010. PAMBE-grown NWs incorporating a stack of 20 AlN/GaN (2-3 nm/ 1-5 nm) quantum wells were considered. In comparison to NWs without any heterostructure, the insertion of the SL resulted in a reduction of the dark current that could reach 8 orders of magnitude (in the case of NWs without external GaN shell). The presence of the SL resulted also in an enhancement of the so-called photosensitivity factor (photocurrent divided by the dark current); however, the responsivity dropped significantly, going from 8-40×10^4 A/W to 100-2000 A/W at −1 V bias in NWs with the GaN/AlN SL (values corresponding to illumination with 5 mW/cm^2 of UV light at λ = 300 nm). Note that the responsivity was calculated assuming that the optical area is equal to the geometrical area of the NW. The spectral response is dominated by the GaN sections of the NW, but the spectral contribution from the GaN wells, located in the 450−400 nm spectral range, can be resolved in photocurrent spectroscopy measurements performed at room temperature. The photoresponse drops significantly with decreasing temperature, which demonstrate that photogenerated carrier extraction is thermally assisted.

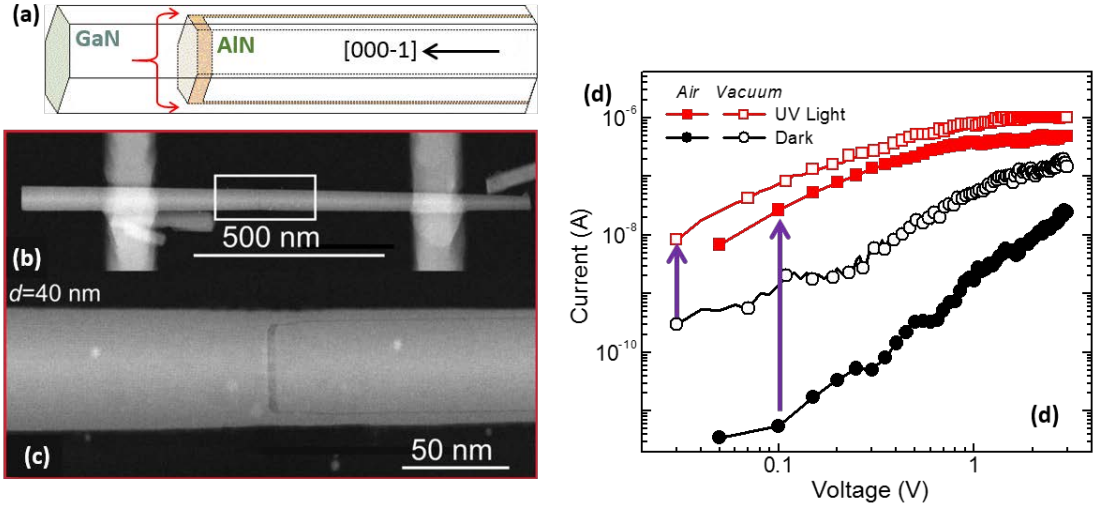

Figure 2.19. (a) Schematic description of the structure consisting of a GaN NW with an AlN axial insertion. The lateral growth during the deposition of the AlN and top GaN sections results in the formation of a GaN/AlN/GaN core/shell structure at the base of the NW. The current (red arrows) drifts towards the NW surface. (b) HAADF Scanning transmission electron microscopy image of a contacted NW and (c) magnified image of the AlN insertion. The AlN shell is visible in the image as a dark contrast. (d) Variation of the dark current and photocurrent as a function of the measurement atmosphere. The photocurrent is induced with illumination of ≈ 0.2 W/cm² of UV light (λ= 244 nm). Taken from ref. 204.

Using a GaN/AlN (2.7 nm/ 5.3 nm) SL without GaN outer shell (see figure 2.21.), Lähnemann et al.[128] showed a photocurrent that scaled sublinearly with the optical power. The spectral response clearly shows a sensitivity to wavelengths below 360–380 nm (cut-off associated to transitions to the first excited level in the quantum wells), and a rejection of longer wavelengths. Persistent photoconductivity is observed, with an initial decay time on the order of a few milliseconds, but it includes also slower components. Statistical measurements of dispersed NWs from the same wafer present a significant dispersion in the values of dark current (10^{-12} to 10^{-6} at +1 V bias) and photocurrent (10^{-9} to 10^{-2} A). This observation highlights the fact that conclusions should not be based on observations of only one or two NWs from a given sample. The dispersion is explained as due to the coalescence of NWs with displaced heterostructures, reducing the effective length of the heterostructure. As illustrated in figure 2.20.(d), lower dark currents correlate with higher photosensitivity factors, which is explained by a larger number of nanodisks contributing to the photocurrent.

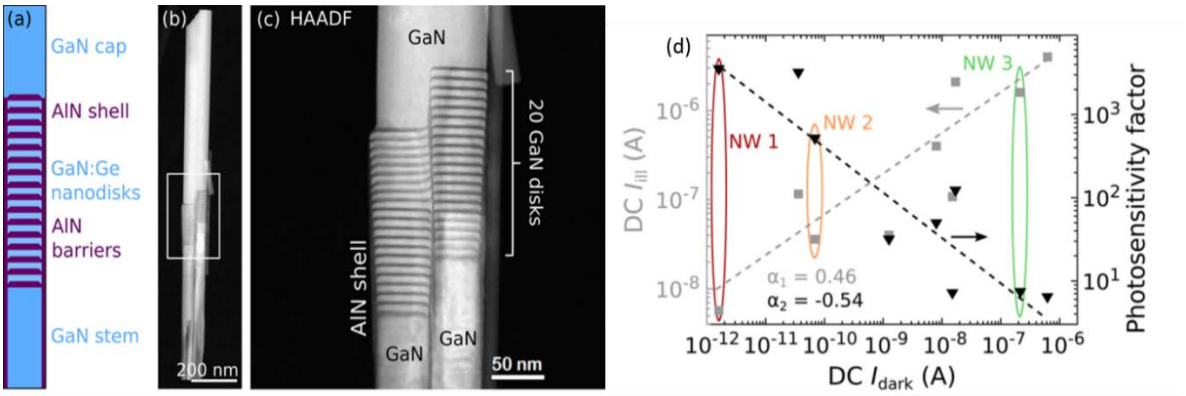

Figure 2.20.(a) Sketch of the NW structure under study. (b), (c) High angle annular dark field (HAADF) scanning transmission electron microscopy (STEM) images of two coalesced NWs with different magnification. The bright and dark gray areas correspond to GaN and AlN, respectively. (d) Photocurrent (I_{ill}) and photosensitivity factor (I_{ill}/I_{dark}) for different NWs plotted as a function of I_{dark}. Both I_{ill} and I_{dark} are measured at 1 V bias. The value of I_{ill} corresponds to an excitation density of ≈ 1 W/cm² (λ = 325 nm). Taken from ref. 128.

2.7.1.3. Intersubband Nanowire Photodetectors

Intersubband (ISB) devices rely on transitions between quantum-confined electron levels within the conduction band (or within the valence band) of semiconductor heterostructures. As the energy associated to such transitions is relatively small, the operation wavelengths of ISB devices are in the infrared (IR) spectral region, in the 1−50 μm range. ISB transitions are governed by a polarization selection rule: to interact, the incident radiation needs to have an electric field parallel to the direction of confinement in the heterostructure [transverse magnetic (TM) polarized light], i.e. there is no interaction with transverse-electric (TE) polarized light. A comprehensive introduction to ISB physics in quantum wells can be found in the works of Bastard[205] or Liu and Capasso[206]. Quantum cascade lasers[207] and quantum well infrared photodetectors (QWIPs)[208] are well-known illustrations of ISB devices.

In the 5−30 μm wavelength window, III-As based QWIPs can achieve picosecond response times, outperforming interband devices in terms of speed. GaN and ZnO materials open perspectives for room-temperature operation of ISB devices both in the near-IR (1−5 μm) and in the mid- to far-IR (5−30 μm) spectral ranges[209,210]. Even more importantly, they offer the opportunity to integrate NWs as active media, which represents the ultimate downscaling of devices incorporating quantum well SLs.

Following the trend of planar technologies, the logical choice of materials for NW ISB devices would be III-arsenides. In this line, the observation of resonant tunneling transport through quantum confined levels in an InP/InAs double-barrier NW heterostructure was already reported in 2002[211]. The current-voltage characteristics displayed negative differential resistance (NDR) with peak-to-valley ratios of up to 50:1 and current densities of 1 nA/μm^2 at low temperatures. However, the pronounced polytipism in III-As NWs has so far hindered the observation of ISB transitions in bottom-up GaAs-based heterostructured NWs (self-assembled or selectively nucleated).

In spite of these limitations, broadband ISB photodetectors were fabricated by planarization and contacting of an InP NW array containing an $InAs_{0.55}P_{0.45}$ quantum well[212–214]. The arrays were synthesized by selective area growth by MOVPE and planarization was performed by spin coating with photoresist S1818. The infrared response covered the 3-20 μm spectral range and was observed under normal incidence excitation. This was explained by the excitation of the longitudinal component of optical modes in the photonic crystal formed by the NW ensemble, combined with the non-symmetric potential profile of the wells, which are spontaneously formed during growth.

In the case of the wurtzite III-nitride material system, the lower density of structural defects in self-assembled NW heterostructures has made it possible to observe ISB transitions in the short- and mid-wavelength IR ranges[215–219]. Figure 2.21. presents the structural properties of a Ge-doped GaN/AlN NW heterostructure that displays ISB absorption around 1.5 μm, with the θ−2θ x-ray diffractogram being compared with that of a similar Si-doped structure, and those of planar layers with the same periodicity. In spite of the wire-to-wire inhomogeneities and the variations of tilt and twist in the NW ensemble, several satellites of the SL reflections are clearly resolved.

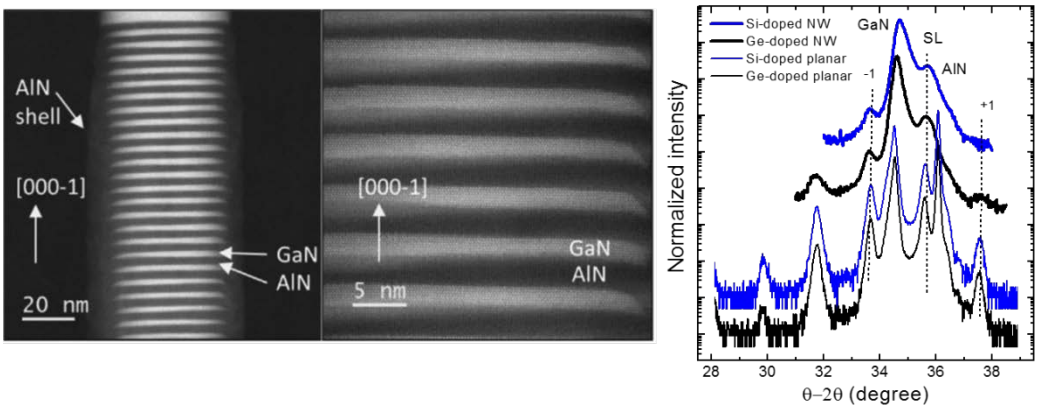

Figure 2.21. Top: High angle annular dark-field (HAADF) scanning transmission electron microscopy (STEM) images of a Ge-doped ([Ge] = 3×10^{19} cm^{-3}) GaN/AlN NW at two different magnifications. The heterostructure consists of 30 periods of Ge-doped GaN/AlN (2 nm/3 nm) quantum wells. Below the heterostructure, the GaN NW base is 800 nm long with a diameter of 60 nm, and the heterostructure is capped with 30 nm of GaN. Dark (bright) contrast corresponds to AlN (GaN). Bottom: High-resolution x-ray diffraction θ–2θ scan of the (0002) reflection of planar and NW GaN/AlN heterostructures, doped with Si or Ge. The diffractograms are normalized to the maximum of the GaN reflection and vertically shifted for clarity. The peak labeled SL corresponds to the main reflection of the GaN/AlN SL. Taken from ref. 218.

Figure 2.22. compares the ISB absorption observed in GaN/AlN NW and planar heterostructures, doped with Si and with Ge, with various doping levels. In the case of the GaN/AlN planar structures, ISB absorption around the 1.55 μm telecommunication wavelength is well documented in the literature[209]. The multi-Lorentzian-peak spectral profile observed in figures 2.22.(a) and (b) is due to in-plane thickness fluctuations in the quantum wells[220,221]. This structure is spectrally resolved because the linewidth of the transitions is smaller than the energetic difference associated to increasing the quantum well thickness by one monolayer. The blueshift and broadening of the ISB transition with doping is assigned to many-body effects, specifically exchange interactions and plasmon screening or depolarization[222].

In the case of these NW heterostructures, the TM-polarized absorption corresponds to the transition between the ground electron level of the GaN well and the first excited electron level associated to confinement along the growth axis (s-p_z). The spectral shape is rather Gaussian, due to the inhomogeneous distribution of well thickness/diameter from wire to wire and along the NWs. This prevents resolving monolayer thickness fluctuations in the axial direction, similar to observations in GaN/AlN quantum dots grown by the Stranski-Krastanov method[223]. Figure 2.22. presents the best result in the literature in terms of linewidth of ISB absorption in GaN NWs, with a full width at half maximum of 200 meV. When increasing the doping level, the absorption blueshifts due to many-body effects. However, the linewidths do not change significantly since they are not dominated by the interaction with ionized impurities but by structural inhomogeneities within the NW ensemble.

Resonant tunneling transport has also been demonstrated in single NWs containing GaN/AlN heterostructures[19,224]. In the case of a GaN/AlN double barrier in a single *n-i-n* GaN NW dispersed and contacted on SiO_2-on-silicon[224], features associated to NDR appeared at both negative and positive bias, and their location could be tuned by adjusting the electrostatic potential via a gate contact deposited on the back side of the silicon carrier wafer. In the case of multiple GaN/AlN wells[19], reproducible NDR associated to the electron tunneling through the quantum-confined electron states was also observed.

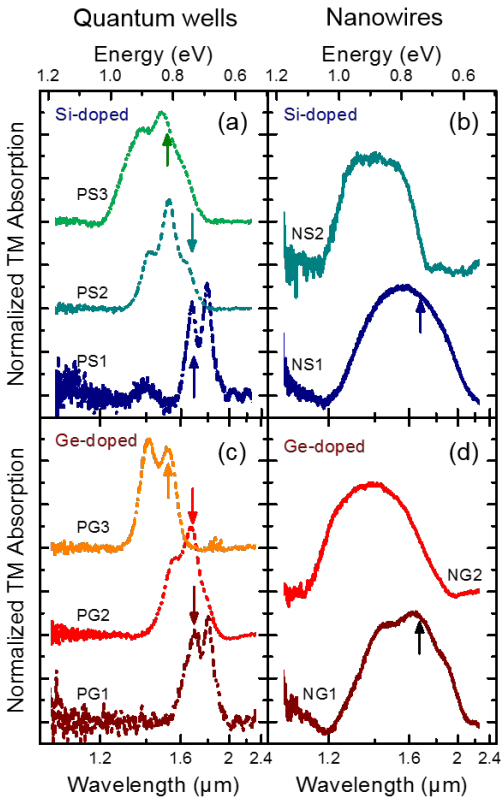

Figure 2.22. Room-temperature absorption spectra for TM-polarized light measured in (a) Si-doped planar heterostructures (PS1-PS3), (b) Si-doped NW heterostructures (NS1, NS2), (c) Ge-doped planar heterostructures (PG1-PG3), and (d) Ge-doped NW heterostructures (NG1, NG2). The nominal thickness of the heterostructures is 2 nm GaN / 3 nm AlN, repeated 30 times. Samples PS1-PS3 and NS1-NS2 are doped with Si in the GaN wells, with concentrations PS1, NS1: [Si] = 3×10^{19} cm^{-3}; PS2, NS2: [Si] = 1×10^{20} cm^{-3}; PS3: [Si] = 3×10^{20} cm^{-3}. Samples PG1-PG3 and NG1-NG2 are doped with Ge in the GaN wells, with concentrations PG1, NG1: [Ge] = 3×10^{19} cm^{-3}; PG2, NG2: [Ge] = 1×10^{20} cm^{-3}; PG3: [Ge] = 3×10^{20} cm^{-3}. The spectra are normalized to their maximum and vertically shifted for clarity. Theoretical values combining 1D nextnano³ and many-body calculations are indicated as arrows in (a), (c). Theoretical values from 3D nextnano3 calculations are indicated as arrows in (b), (d). Taken from ref. 217.

Using GaN/AlN (2 nm /3 nm) NW heterostructures with ISB absorption around 1.55 μm, a single NW QWIP was demonstrated[225]. The spectral response of the detector was obtained by measuring the photocurrent induced by various laser diodes operating at different wavelengths along the near-IR spectrum, as shown in figure 2.23. The response is maximum around 1.3−1.55 μm, which is consistent with ISB absorption from the first electron level in the wells to the first excited level associated to the confinement along the NW growth axis (e_1 to e_{2z}). Then, the response goes down at 1.0 μm and increases again at shorter wavelengths, which can be attributed to electron transitions to higher energy levels (e_{3z}, e_{4z}), theoretically predicted at 0.84 and 0.72 μm. Unlike the interband photocurrent (response to UV illumination in this case), the ISB photocurrent scales linearly with the incident optical power. This confirms that the ISB transitions are less sensitive to surface-related phenomena, as theoretically predicted[216]. The responsivity at 1.55 μm was estimated by assuming that the active area of the detector A_{opt} corresponded to the NW surface that was exposed to the laser, obtaining values of 0.6±0.1 A/W and 1.1±0.1 A/W when measuring at chopping frequencies of 647 and 162 Hz, respectively.

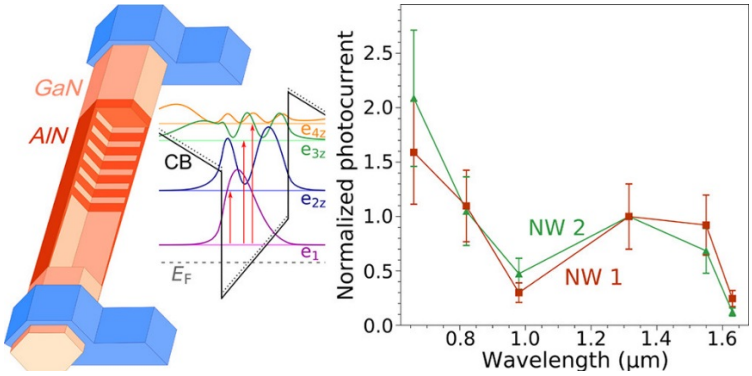

Figure 2.23. Schematic representation of the single-NW QWIP containing a GaN/AlN heterostructure. Conduction band (CB) diagram of one of the GaN wells in the heterostructure, indicating the grown electron level (e_1) and the excited levels associated to electron confinement along the growth axis (e_{2z}, e_{3z}, e_{4z}). The levels are represented with their respective squared wave functions. The horizontal dashed line represents the fermi level (E_F). On the right side, photocurrent as a function of the excitation wavelength measured in two different devices (NW 1 and NW 2). The spectra are normalized to the response at 1.3 μm. Taken from ref. 225.

2.8. Solar cells

One of the main challenges of our time is the evolution from energy systems based on fossil fuels towards a larger use of renewable resources. The deployment of solar cells is playing a crucial role in this energy transition. Huge research efforts are oriented to increase the solar cell power conversion efficiency, to increase the achievable "Watts per square meter" and therefore decrease the total system cost. Commercial solar cells are based on planar single junctions, whose efficiency is limited to about 33% according to the Shockley-Queisser theory[226,227]. In this context, NW junctions are attracting a lot of interest for the fabrication of solar cells[228–230] due to their increased lattice mismatch tolerance, which enables the implementation of tandem (multi-junction) solar cell designs with more flexibility than planar layers. Furthermore, the light concentration capabilities of NWs make it possible to reduce the amount of active material without degradation of the absorption. Finally, NWs are compatible with multiple substrates, such as silicon or flexible materials, which is interesting not only for large scale solar cells but also for the development of wearable devices. Due to the societal relevance of this research, we have decided to include this section to briefly review progress in this domain.

Various architectures have been considered for the fabrication of NW solar cells, namely radial and axial p-n junctions and radial type-II heterojunctions. So far, the efficiency of type-II heterojunctions is lower than that of p-n junction devices, and radial p-n junctions have shown relatively low open-circuit voltage, which points to a lower junction quality in comparison to axial junctions. As outstanding results, 11.1%[231] and 13.8%[232] conversion efficiencies were reported in 2013 by Eindhoven University of Technology and Lund University, respectively, both using axial-homojunction InP NW ensembles synthesized by localized growth in MOVPE using Au as a catalyst. In the same year, SunFlake A/S reported 10.2% conversion efficiency in a single-NW device consisting of a GaAsP radial homojunction (self-catalytic growth by MBE). In 2016, 15.3% conversion efficiency was reported by Sol Voltaics AB (spinoff company of Lund University) using an ensemble of axial homojunction GaAs NWs (localized growth by MOVPE using Au as a catalyst) with an AlGaAs shell for surface passivation[233]. Finally, 17.8% efficiency was reported by Eindhoven University of Technology (also in 2016) in a homojunction InP NW solar cell fabricated through the top-down method[234].

To optimize the performance of the solar cells, efforts on doping, surface passivation and fabrication technology are still required, and the introduction of this technology in the market will necessitate also a reduction of the fabrication costs. The implantation of NW tandem architectures, still in a very exploratory stage[235], might also lead to a breakthrough in terms of power conversion efficiency.

3. Methods

In this chapter a brief introduction to the different methods employed throughout this project is given. It includes the growth of NW samples using plasma assisted molecular beam epitaxy, the different steps of TEM membrane fabrication, NW device fabrication and all the characterization techniques used. These range from electron microscopy techniques such as scanning electron microscopy, electron beam induced current and transmission electron microscopy to electrical and photocurrent measurements, photoluminescence and simulations with the nextnano³ software.

3.1. Plasma-assisted Molecular Beam Epitaxy

All the NWs used for the PhD project were grown using plasma-assisted molecular beam epitaxy (PAMBE). MBE is an ultra-high vacuum (10^{-8}–10^{-12} mbar) crystal growth technique yielding high quality crystalline samples grown at a rate of 1 monolayer/s.

A schematic of the machine used at CEA-IRIG, Grenoble, France is depicted in figure 3.1.

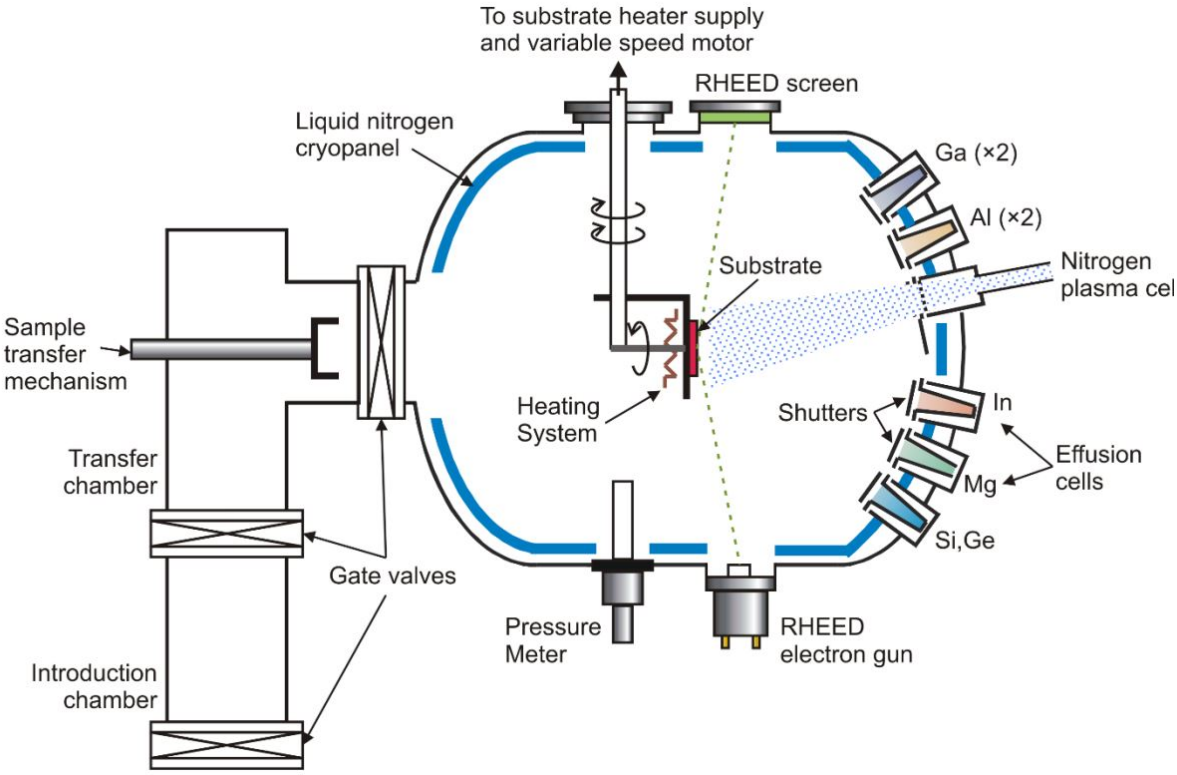

Figure 3.1. Schematic of the plasma-assisted MBE used in CEA-INAC/IRIG Grenoble. Taken from ref. 236.

The growth chamber is kept in ultra-high vacuum and its walls are kept at low temperature through liquid nitrogen cooling. Effusion cells (Ga, Al, Ge, Si) operated at controlled temperatures generate atomic flows into the reactor through thermal evaporation. Due to the ultra-high vacuum environment the emitted atoms have a mean free path longer than the distance to the substrate and it is therefore called a beam of the injected element. The PAMBE system for III-N materials is equipped with a radiofrequency plasma source that cracks high purity molecular N_2 into reactive mono-atomic N. In the center of the growth chamber, there is the molybdenum substrate holder, with the corresponding heating system and the possibility to rotate during the growth.

The crystal growth by PAMBE is governed by kinetics of the surface processes rather than thermal equilibrium. The modifiable growth parameters are the temperature of the substrate and

the effusion cells, the N flux and the N-cell radio-frequency power. The layer growth is monitored by reflection high energy electron diffraction (RHEED), which consist of an electron beam (acceleration voltage ~32 kV) impinging on the growing sample's surface at a grazing angle. The obtained diffraction pattern is a reciprocal space representation of the sample surface.

All NWs studied in this project were grown self-assembled in PAMBE on Si(111) substrates. In these conditions, the NWs tend to grow along the $[000\bar{1}]$ axis. The NWs studied in chapter 4 have been grown at Justus-Liebig-University in Gießen, Germany by Pascal Hille and Jörg Schörmann in the group of Prof. Martin Eickhoff. The growth was carried out in nitrogen-rich conditions, at a substrate temperature of 790°C. No AlN buffer layer was used. For the growth of Ge-doped GaN/AlN heterostructures, Al, Ga and Ge standard effusion cells were employed with beam equivalent pressures of $7x10^{-8}$, $1.5x10^{-7}$ and $1x10^{-10}$ mbar, respectively. The source of atomic nitrogen was operated at 300 W with a nitrogen flux of 1 sccm.

The NWs described in chapters 5 and 6 were grown in CEA-IRIG in Grenoble, France by Akhil Ajay and Eva Monroy. Here an AlN buffer layer was deposited in a 2-step growth process[237,238]: 1 nm deposited at 200°C substrate temperature followed by 8 nm deposited at 670°C. The growth rate of the NWs was 0.11 nm/s, and the substrate temperature was 810°C.

3.2. Processing and Membrane Fabrication

The processing comprises all the steps necessary to obtain contacted single NW on in-situ TEM grids starting from a Si wafer.

An approach to fabricate contacted nanostructures on a nitride membrane suitable for correlated in-situ TEM analysis was developed. UV laser lithography, reactive ion etching (RIE) and KOH wet etching are employed for the fabrication of such membranes. With the help of electron beam lithography nano-objects such as NWs can then be contacted on the membrane.

3.2.1. Choice of Wafer

To fabricate electron transparent in-situ TEM grids a 4" Si(100) wafer is used. It is 400 µm or 450 µm thick, heavily n-doped (As++) and has 200 nm of thermal SiO_2 on both sides. The thickness of the wafer should correspond to the acceptable sample thickness of the TEM sample holder. The n-doping avoids artefacts in optoelectronic measurements in the UV and IR range. A deposition of 40 nm of stoichiometric Si_3N_4 is performed on both sides of the wafer by low-pressure chemical vapor deposition by LioniX International. The thermal SiO_2 layer protects depositions on top of the Si_3N_4 layer (e.g. nano-objects and contacts) from short circuiting to the substrate. It may furthermore improve the quality of the subsequently deposited Si_3N_4. The thickness of the Si_3N_4 layer is chosen to give good high resolution TEM image quality combined with a relative robustness of the membranes. For TEM techniques requiring the studied sample to be suspended in vacuum, we have fabricated membranes including slits allowing to suspend nano-objects. In order to improve the membrane stability we augmented the Si_3N_4 layer to 200 nm.

The membrane fabrication steps are described in detail in the following and are illustrated in figure 3.2. The fabrication process is carried out on both sides of the wafer. In short: the membrane is defined by laser lithography into a photoresist on the backside of the wafer. The Si_3N_4 and SiO_2 layers are etched through the opened windows in the photoresist using RIE. If slits in the membranes are desired: a laser lithography on the front side is carried out, followed again by the same RIE steps. The wafer is then immersed in a KOH bath which etches the Si where it is exposed. In a last step a laser lithography is carried out on the front side of the wafer defining the metal contacts and any desired markers or labels.

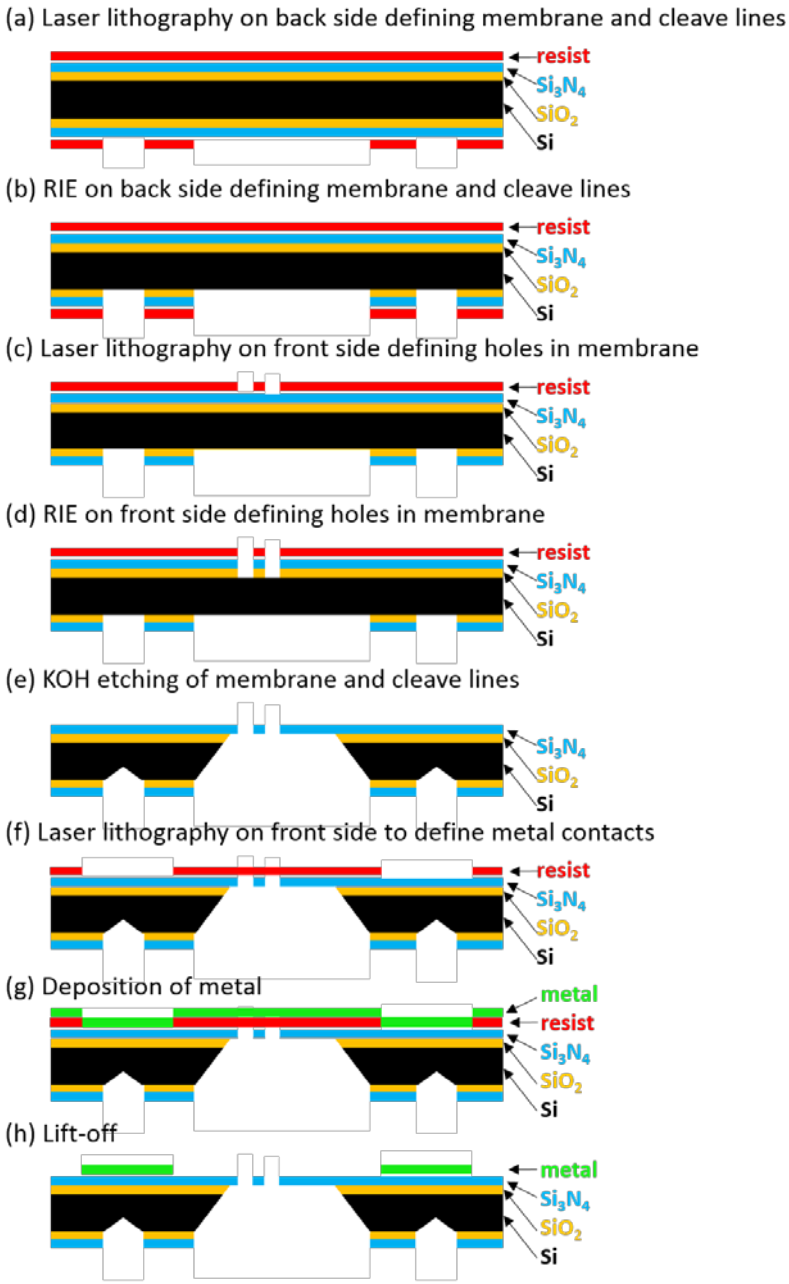

Figure 3.2. Cross-sectional view of the Si wafer during the different fabrication process steps. (a) The membrane and cleave lines are defined by laser lithography into a photoresist on the backside of the wafer. (b) The Si_3N_4 and SiO_2 layers are etched through the opened windows in the photoresist using RIE. (c) If slits in the membranes are desired: a laser lithography on the front side is carried out, (d) followed again by the same RIE steps. (e)The wafer is then immersed in a KOH bath which etches the Si. (f) In the last step a laser lithography is carried out on the front side of the wafer defining the metal contacts and any desired markers or labels. (g) The metal is then deposited and (h) lifted off.

3.2.2. Chip Design

The open source software KLayout can be used for the design of all features. Single chip dimensions of 3.1×3.7 mm^2 are chosen, to fit a DensSolutions double tilt six contacts heating/biasing TEM sample holder. These can be arranged e.g. in arrays of 4×4 membranes throughout the wafer. The top part of the chip serves as a space where the chip can be handled with tweezers or clamped mechanically. It was likewise chosen to add a chip label in the top left corner and marks for manual and automatic alignment in electron beam lithography in the center of the top part. Having alignment marks far from the membrane avoids accidental overexposure

of photoresist while aligning in electron beam lithography to contact nano-object. The membrane itself is below the center of the chip and laterally centered. Three contact pads of 0.35 mm width and up to 1.2 mm height are designed on both sides of the membrane and labeled. These have thin contact leads which connect to the membrane. On the membrane they are again labeled which is useful during TEM observation. Just off the corners of the membrane marks for fine alignment in electron beam lithography of contacting nano-objects are defined. On the membrane itself markers are drawn to help orientation on it.

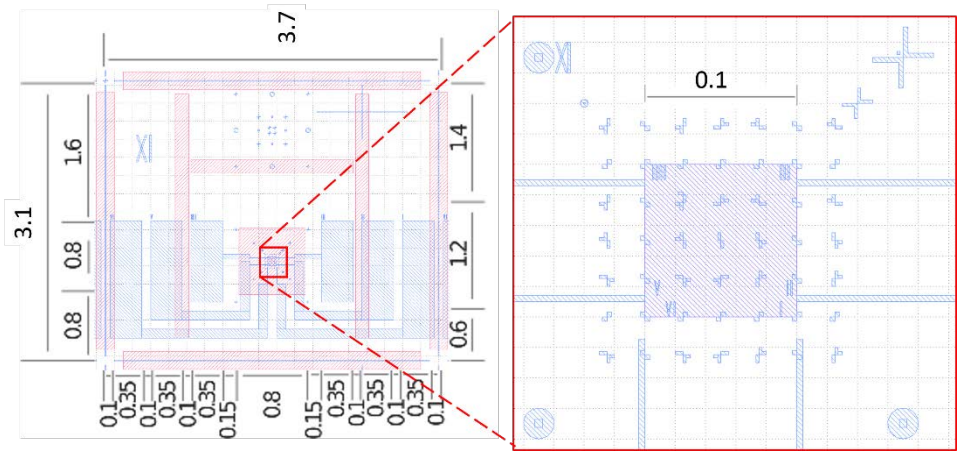

Figure 3.3.Individual chip design containing the in-situ TEM membrane (a) view of the whole chip including dimensions and the layers defined by laser lithography defined on the back side (in red: membrane and cleave lines) and the front side of the wafer (in blue: contacts, labels and markers). (b) Zoomed design of the membrane area. All dimensions are given in mm.

3.2.3. Defining the membrane by Laser Lithography

The Si_3N_4 membrane size is chosen to be 100×100 μm^2 for the 40 nm thick membranes. It is important to choose the window size small enough so that the membrane stays stable under the high voltage irradiation of the TEM. Thicker membranes support larger window sizes. For membranes of 200 nm Si_3N_4 layer thickness window sizes of 220×220 μm^2 are employed. The membrane window will later be etched through from the backside of the wafer. The employed wet etching process with KOH will etch along the Si {111} planes. As these planes make an angle of 54.47° with the {100} plane of the surface of the wafer, the desired window size needs to be adapted to this process. For a wafer thickness of 450 (400) µm, we define squares with lengths of 726 (786) µm to obtain window lengths of 100 (220) µm.

In the same step as defining the membranes, we also introduce cleave lines. These are useful for the handling of the individual chips once the fabrication process is concluded. We define lines of 200 µm thickness. Taking into account the angular etch direction, these will result in triangular grooves with a depth of around one third of the wafer thickness. It is important to maintain a minimum separation of 20 µm between different cleaving lines in order to not have overly unplanned etching at the intersections which renders the wafer fragile at that location.

In order to do the UV laser lithography step that defines the membranes and cleave lines (given in red in figure 3.3.) the following preparation is necessary. On both sides of the wafer the positive photoresist S1818 is spun (6000 rpm, 4000 r/s^2, 30 s) and baked (1 min at 115°C), see figure 3.2.(a). That results in 1.5 µm thickness of the photoresist. The side which has the resist heated twice is subsequently defined as the front side. Putting resist on the front side in these steps serves solely to protect it from potential scratches while positioning the wafer on a surface (for example during the laser lithography or RIE). It is of utmost importance to not scratch the Si_3N_4 layer, e.g. with the tip of tweezers, to avoid opening electrical current paths short-circuiting to the Si. We have developed a holder for the four-inch wafer that can be mounted on the spin-

coater to facilitate the spinning steps. The wafer is maintained in place by its weight and the rim of the holder. After the successful spinning of the photoresist on both sides, the UV laser lithography is performed on the back side of the wafer. A Heidelberg Instruments DWL 66_{FS} machine with a 405−410 nm diode laser is employed. The same write head is used for the different laser lithography steps. To have high resolution, write mode II is chosen which results in the focal length of 4 mm. The total laser power is 120 mW. By employing a single filter the irradiation power is reduced to 10%. Additionally, a dose of 45 is applied resulting in a final illumination percentage of 4.5% of the full diode power. The development of the irradiated photoresist is a 1 min bath in a 1:1 solution of Microdev and deionized water (DIW). The irradiated parts of the photoresist are dissolved leaving the wafer surface in these places unprotected by photoresist.

Then RIE is carried out on the backside (which is the same side the laser lithography was carried out beforehand) in order to etch the Si_3N_4 and SiO_2 layers in the places without remaining photoresist. An RIE PlasSys system was used. SF_6 and CHF_3 are employed respectively. The parameters used for RIE are summarized in table 3.1. Time of etching of the nitride layer is 1 min 30 sec (5min 45 sec) for the 40 nm (200nm) Si_3N_4 layer. The etching time for the 200 nm SiO_2 layer is 8 min and 45 sec. It is possible to replace this step by an ICP etch. Here an ICP machine by Oxford Instruments was employed. The Si_3N_4 etch consists of a gaseous mix of Ar (60 sccm), CHF_3 (41 sccm) and SF_6 (10 sccm) which is used for 1 min 20 sec. The SiO_2 etch is a gaseous mix of Ar (40 sccm), CHF_3 (40 sccm), O_2 (5 sccm) applied for 8 min. The wafer is cleaned in acetone and IPA to remove the photoresist and potential contaminations.

Etchant gas	**Power (W)**	**V_{bias} (V)**	**Pressure (sccm)**
SF_6	50	270	20
CHF_3	50	440	15

Table 3.1. Reactive ion etching (RIE) parameters used for etching Si_3N_4 and SiO_2 layers using SF_6 and CHF_3 respectively.

3.2.4. Defining the Slits by Laser Lithography

If the nano-object is desired to be suspended in vacuum it is possible to introduce slits in the membrane (see figure 3.4.(a)). Through drop casting or mechanical placement, the nano-object can then be installed across the slit and contacted on both ends on the membrane. These slits are likewise defined by laser lithography. The front side is prepared for the laser lithography with the same photoresist and spinning parameters as in the previous step. The wafer is subsequently mounted in the laser lithography machine. The laser lithography machine employed includes a camera mounted below the sample stage that allows alignment of the wafer using features on its backside. A cross-shaped marker in the middle of the wafer was defined in the previous laser lithography step and is now visible through the contrast between the Si of the marker and the surrounding Si_3N_4. On that feature the alignment is carried out. Specific attention has to be given to the minimization of a potential rotation of the wafer with respect to the desired pattern (the rotation should be below 3 mrad). Any misalignment here will evidently lead to a misalignment of the membranes with respect to the slits (see figure 3.4.(b)). The exposure of the front side photoresist is then performed defining the slits. After development and RIE etching with the same parameters as the first lithography step, the wafer is cleaned in acetone and IPA.

The slits can likewise be defined by an electron beam lithography technique such as the NanoBeam. It allows the definition of smaller features. The drawback is that alignment of the back side is not possible. This necessitates another laser lithography on the front side of the wafer followed by a metal deposition step and lift-off (described in the following) in order to define alignment marks useable in the electron beam lithography.

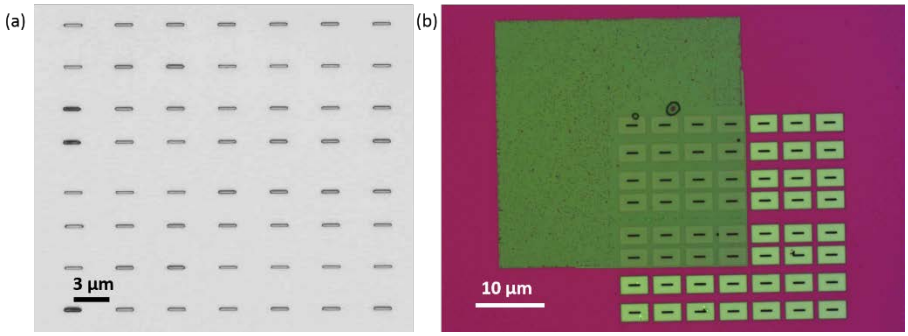

Figure 3.4.(a) The membrane area of the chip after the definition of the slits via laser lithography. (b) Membrane area after definition of slits with a small rotation of the wafer with respect to the axis of the lithography setup.

3.2.5. Etching the membranes, cleave lines and slits with KOH

At this point the Si_3N_4 and SiO_2 layers have been removed at the desired places: membrane features and cleave lines on the backside (and slits on the front side if that step was performed). A KOH wet etching step is then performed to etch the Si which is not protected by Si_3N_4 layers. To do so, a KOH bath is prepared by adding two components: 756 g KOH (≥ 85 %, Ph.Eur., in pellets) and 950 ml DIW. This solution is heated to and then maintained at 80°C. The wafer is added into it with the help of an appropriate holder. Ideally, only the outside edges are held. The etching takes around 8 hours in total. It is very helpful to add a dummy sample into the same KOH bath in order to determine the precise etching rate of Si of the prepared solution. It is typically around 70 µm/h. Around one extra hour should be allocated for etching the SiO_2 of the front side. The reuse of a KOH bath for another sample is not advised. Besides a significantly lower etching rate it is also possible to obtain recrystallizations of Si that had formerly dissolved in it. Careful as well not to leave the wafer too long in the solution as it is obviously possible to dissolve the entre Si wafer and be left with KOH resistant flappy sheets of SiN. Taking the wafer out of the solution before the etching has finished, should likewise be avoided. It may, however, be necessary to reintroduce it to the KOH bath (checking the improvement every half an hour) if the membrane feature on the front side of the sample have not been established clearly yet. After the successful KOH bath, the wafer is extensively rinsed with DIW and cleaned for 1 hour in HNO_3 (65%) at 80°C. In figure 3.5. the result of insufficiently long KOH etch durations can be seen as observed by visible light microscopy.

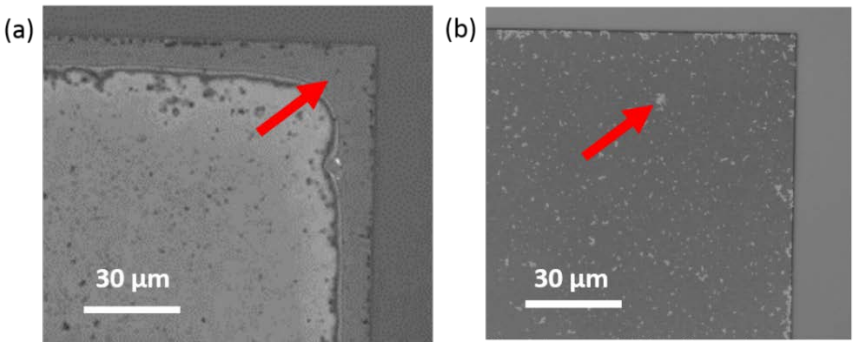

Figure 3.5. Visible light microscope images of the top right quadrant of a membrane with etching problems: (a) A rim of remaining SiO_2 on the edges of the membrane can be seen. (Careful not to mistake these for remaining solvents in the process of drying.) (b) Remaining SiO_2 particles on the backside of the membrane.

3.2.6. Defining Metal Contacts by Laser Lithography

The last steps of the fabrication of in-situ TEM membranes are defining of metal features on the front side of the wafer with laser lithography, doing a metal evaporation and lift-off. The following features are designed (given in blue in figure 3.3.): contact pads which are compatible with the in-situ TEM holder (e.g. double tilt DensSolutions 6 contact holder for FEI/ Thermo Fischer TEMs), markers which will be used for alignment in an electron beam lithography step contacting the desired nano-object and any kind of other markers that might be useful during characterization (e.g. labeling the contact pads, labeling the contact leads on the membrane, markers on the membrane, marker lines indicating the position of cleave lines on the back side…). In preparation for the laser lithography two positive photoresists are spun onto the wafer. The first is LOR 3A (6000 rpm, 4000 r/s^2, 30 s) baked for 2 min at 200°C, followed by S1805 (6000 rpm, 4000 r/s^2, 30 s) baked for 1 min at 115°C. Including the LOR 3A layer was found to help lifting off the metal after evaporation. The wafer is aligned on the back side (as described above). The laser lithography is done employing two filters (30%, 10%) to reduce the total laser power to 3%. Additionally, a dose of 75 is employed resulting in a total output power of 2.25%. The sample is developed in MF26A for 1 min and then rinsed with DIW.

The metal deposition should be done within a couple of hours of the development of the photoresist. That way the undercut in the LOR 3A layer does not cave in by the weight of the S1805 layer which leads to a broadening of the final shapes of features and lift-off problems. In the Plassys metal depositon system a 10 s Ar plasma at 250 V is performed first. The metal deposition itself consists of two processes. The first deposits 5 nm Ti to ensure a good mechanical contact between the Si_3N_4 layer and the actual contact. The second step is the deposition of 35 nm Au. Pt can also be used with the same results. The lift-off of the metal (at the undesired places) is done by putting the wafer in PG remover at 80°C at least 2 hours (can be left over night without problems). It is helpful to put the wafer upside down on a watch glass. That way any detaching metal can already fall off and separate from the wafer. After having left the wafer an appropriate amount of time it is taken out, cleaned with IPA, rinsed with acetone and then put into an acetone bath. A pipette can be employed to help lift off the metal. This should go relatively easily. Care has to be taken to not create too much pressure which will break the membranes. The pipetting can also be done in DIW and under a visible light microscope. That way checking on the membrane sites is possible. It is important to keep the wafer in a solution as long as the lift-off is not completed as drying it leads to a definite attachment of the metal to the wafer. After rinsing the wafer with DIW and carefully blow drying it with a standard N gun (low pressure, low angle with membrane surface) the membranes are ready to use. SEM images of a finished chip are depicted in figure 3.6.

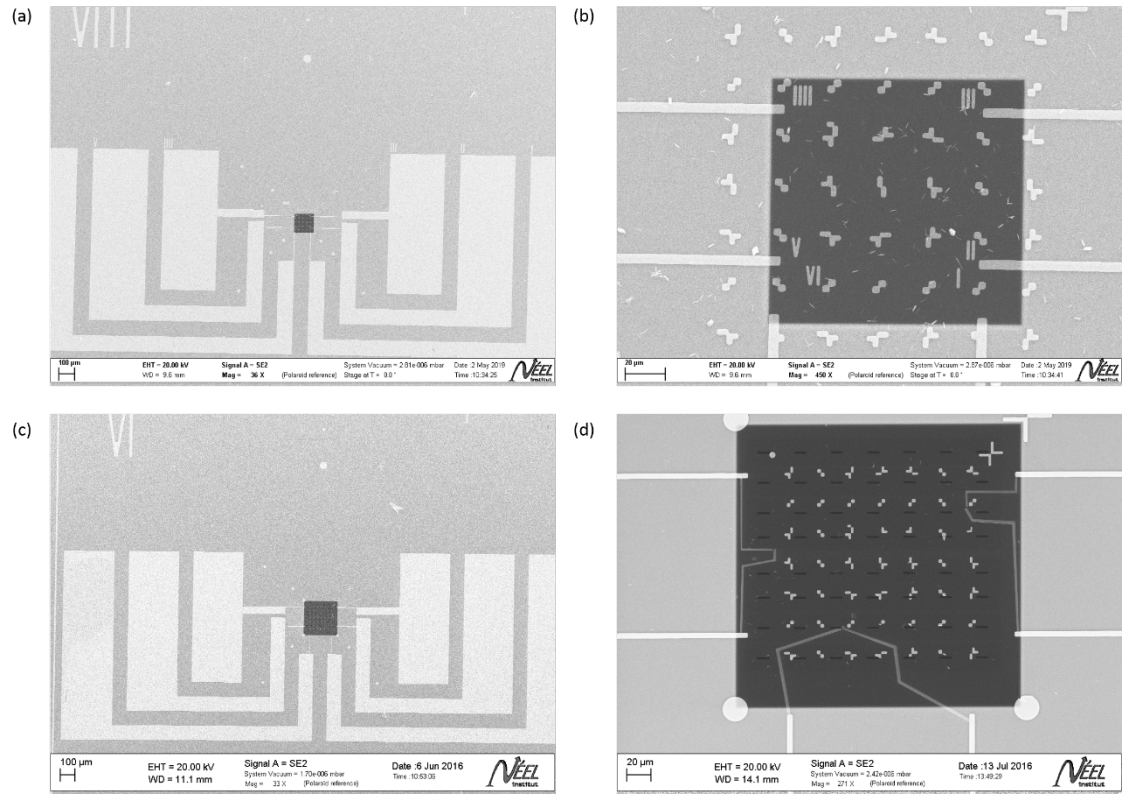

Figure 3.6. SEM images of chip with 100x100 µm² membrane: (a) the full chip and (b) the membrane area including markers, contact leads, labels and drop casted NWs. SEM images of a 220x220 µm² membrane with slits: (c) the full chip and (d) the membrane area which is here shown after contacting three NWs (one suspended, two on flat areas) between the contacts.

3.2.7. Dispersing and Contacting of Nanowires

In top view SEM imaging of the as grown NW ensemble it is verified that single NWs are present and the coalescence is low.

A piece of the as grown sample is cleaved. It should come from the suitable area of the as grown sample and be a couple of mm in length. This piece is then put into an Eppendorf tube. Drops of ethanol or isopropanol are added. Three usually cover the entire sample and suffice for the dispersion. The Eppendorf tube undergoes a short sonication of a couple of seconds. The NWs are considered to break off from their substrate by the first ultrasonic waves. The solution therefore then contains NWs. This solution is dropped onto a 4×4 chip ensemble with a pipette. While one drop may cover the whole surface, the density of the dispersed NWs can be heightened by dispersing a few drops onto the chips. The solution is left to dry at ambient temperature. Putting it on a hot plate accelerates the drying process yet may also lead to droplet formation. This leads to unwanted rings of high NWs densities at the outskirts of the drying droplets. It is therefore advisable to, if at all, only briefly hold it over the hot plate until the height of the deposited droplet of solution is gone down, yet only to the point that dry surfaces start appearing on the chips. It is furthermore possible to find the optimum temperature of ethanol where drops of it disperse in an even, pearly fashion on the chip leading to an even distribution of NWs on the surface.

With the use of a visible light microscope the density of NWs on the membranes is then checked. Note here, that the dimensions of NWs (1.5 µm length, 40–200 nm diameter) are at the limit of visible light microscopy. Most observables are large bundles of NWs which are not interesting for this study. Two techniques help to select single NWs. One is observation in dark field mode. As this technique uses the scattered light smaller NW bundles are observable than in bright field. They are mostly still bundles, however. The more useful technique is using a filter, such as an orange filter, to render the light monochromatic. Comparing with SEM images it was

shown that NWs of diameters below 100 nm appear systematically as bright contrast whereas bigger ones, stacked NWs and bundles appear as dark contrast (see Annex D). This can be explained through interference effects. All NWs (down to 40 nm thickness in the given studies) are observable that way in visible light microscopy.

If the density of single NWs is considered high enough, the next processing step is mapping the exact locations of the single NWs with the SEM. These images will be used subsequently to design the contacts for the single NWs in KLayout. An overview image of the chip is taken with around 30× magnification to check contact pad quality, contact leads, labeling and marker quality. This is typically done at a large working distance (8–10 mm) to be able to view the whole chip. High acceleration voltages (10–20 kV) and the secondary electron detector are employed for the best image contrast between NWs and the membrane itself. Then a second image at around 400x magnification is taken of the of membrane area itself. This is useful to have the positions of all the bigger NW bundles in order to avoid these locations when drawing the contacts. Thirdly, an image of around 2500× magnification is taken comprising a square with four markers. These markers are later used in KLayout in order to align the drawing with the SEM image. Often it is only at this point that single NWs can faintly be observed. In a last step using around 24000× magnification the nature of the apparent single NW is verified. It is often at this point that coalescences and bundles are discovered. The images taken are then used to design the contacts in KLayout.

A nomenclature for contacted NWs was developed. The growth number is given followed by "_dX_mY_cZ_1Z_2" where *d* stands for dispersion and is followed by the number of the dispersion, *m* stands for membrane and is followed by the number of the membrane of the used 4×4 chip ensemble, and *c* stands for contacts which is followed by the two numbers of the contact pads that contact the NW.

3.3. Electron Microscopy

The Nobel Prize winning development of electron optical lens systems starting in the 1930s allowed for the emergence of a new group of microscopes which employ a beam of accelerated electrons as illumination source. With these the limitations of visible light microscopy of maximum resolution of 200 nm could be overcome. Nowadays ultimate resolution of electron microscopy may go to the sub-nm range. A variety of electron beam techniques have been developed, several of which were employed during this project and are briefly described in the following. The starting point is always the beam of accelerated electrons. It gives rise to a variety of signals which can be collected and analyzed, giving information on different aspects of the probed specimen. A schematic overview can be seen in figure 3.7.

The effect of the electron beam is limited to a pear-shaped interaction volume (indicated in green in figure 3.7.) as can be demonstrated using Monte Carlo simulations, for example CASINO[239–241]. The interaction depth depends on the acceleration voltage of the electron beam, the atomic number Z of the material and the density of the probed material. As a result of the interaction, a number of signals are emitted and can be detected. These may be of different type (light radiation, electron radiation, electric current) and originate from different interactions within the specimen. There are two main kinds of electron microscopes (EM), namely scanning (SEM) and transmission electron microscopes (TEM).

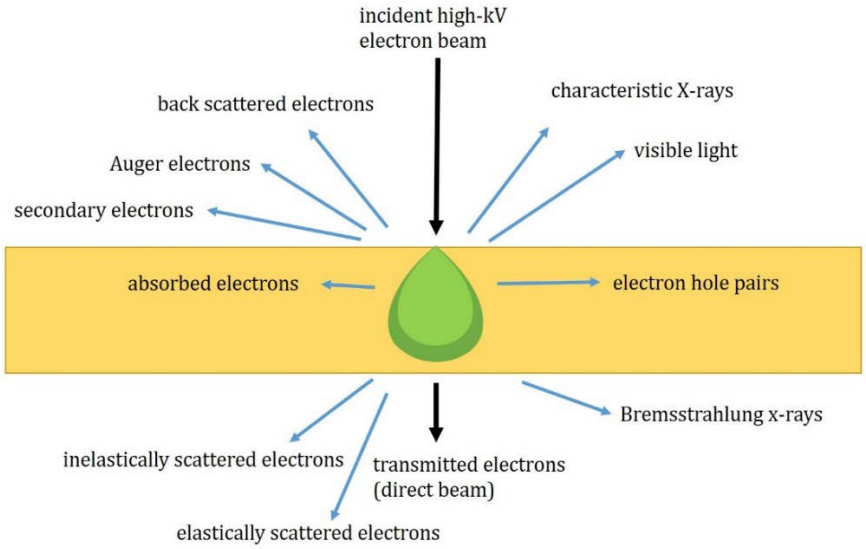

Figure 3.7. Schematic illustrating the interaction of highly accelerated electrons with matter.

3.3.1. Scanning Electron Microscopy

An SEM uses electron beam acceleration voltages of 1–30 kV. A focused electron beam is raster scanned over the sample surface generating different types of signals, e.g. secondary electrons, backscattered electrons and electron beam induced current (used for EBIC measurements) that can be detected using a suitable detector. The output value of the used detector at each scan point is then used to create an image.

Secondary electrons originate from the conduction or valence band of the specimen due to impact with the impinging electron beam. Through inelastic scattering they obtain enough energy to become free electrons. Due to their comparatively low energy of up to 50 meV only electrons emitted close to the surface can leave the specimen and be detected. Secondary electrons from deeper in the specimen are reabsorbed by surrounding atoms. The angle of incidence of the electron beam on the specimen influences the amount of electrons emitted. The interaction volume of the beam is deep compared to path of the generated secondary electrons before reabsorption, therefore more secondary electrons can leave the surface at the edges than at the flat surfaces, called the edge effect. It makes the analysis of secondary electrons sensitive to the topography of the surface.

Backscattered electrons are electrons of the incident beam that are reflected, i.e. scattered through Coulomb repulsion with the electron cloud of the atoms. They lose only little energy in the scattering process and leave the specimen with nearly the same energy as the incident beam. Backscattered electrons therefore possess higher energies than secondary electrons (see figure 3.8.) and can originate from deeper within the specimen with respect to secondary electrons. At the scattering site they are scattered in arbitrary directions within the specimen. Those that are sent backwards are collected by the detector. As the scattering event involves the atomic core, the resulting collected signal is sensitive to the atomic number Z of the encountered atoms: higher atomic number leads to higher backscattering and therefore higher counts. Information on the specimen's morphology, chemistry and even crystal orientations in large grains can be gathered.

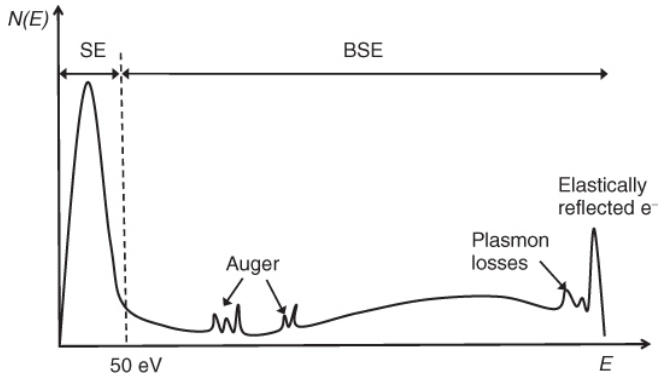

Figure 3.8. Schematic energy distribution of electrons emitted from the specimen after low-kV electron bombardment. Number of electrons N is given as a function of their energy E. SE abbreviates secondary electrons, BSE abbreviates backscattered electrons. Taken from ref. 242.

When an inner shell electron is removed from the atom by the incoming electron beam, it may lead to an outer shell electron from the same atom filling the newly created hole. The released energy may be emitted as a photon, or it can be transferred to another electron of the same atom which may therewith have gathered enough energy to leave the atom. These latter electrons are called Auger electrons. Auger electrons are likewise detectable in SEM imaging but occur in fewer numbers than backscattered and secondary electrons.

For the imaging of the surface of the specimen of this manuscript the Zeiss ultra + and Zeiss Leo 1530 SEMs in Institut Néel, Grenoble, France, were used. The scanning mode with an acceleration voltage of 1–20 kV can be used to extract morphological information. In these SEM systems, there are different electron detectors. The two employed ones are the secondary electron detectors: Everhart-Thornley or lateral secondary electron detector (ETD) and the in-lens secondary electron detector. The ETD is in the chamber and typically mounted horizontally between specimen and the pole piece. Electrons emitted from the surface are attracted to it by a voltage applied to a grid in front of the detector (the collector). The collected electrons are in a large part secondary electrons (and a few backscattered electrons that arrive directly on it). The in-lense detector is situated in the column between condenser and objective lense. It collects first generation secondary electrons produced by the beam hitting the sample. Best spatial resolution is achieved with this one, about 1 nm at 15 kV and 1.7 nm at 1 kV. Both SEMs also contain a backscattered electron detector (BSE), mounted next to the column, useful starting from 5 kV, for imaging contrast in chemical compositions. The ultra + likewise has a BSE In-lense (EsB: energy selective BSE) for the detection of low kV backscattered electrons.

Best contrasts between dispersed NWs and the surrounding membrane can be obtained for high acceleration voltages of 20 kV using the ETD.

3.3.1.1. Electron Beam Induced Current

A beam of accelerated electrons incident on a semiconducting specimen generates electron-hole pairs. Through inelastic scattering, electrons from the valence band gain energy and get promoted to the conduction band. These electron-hole pairs diffuse through the sample until trapped or recombined.

In the presence of an electric field in the specimen the electron-hole pairs will get separated by drift. Contacting the sample and connecting an ammeter allows charge carrier collection, i.e. detection of electric current. Such an experiment is called Electron Beam Induced Current (EBIC). Typically, the collection of a secondary electron image is done simultaneously while collecting an EBIC signal of the region of interest. That way information on the electric field,

the positioning and extend of depletion regions, such as p-n junctions, heterointerfaces, Schottky contacts, and depleted surface regions can be collected. A schematic can be seen in figure 3.9.

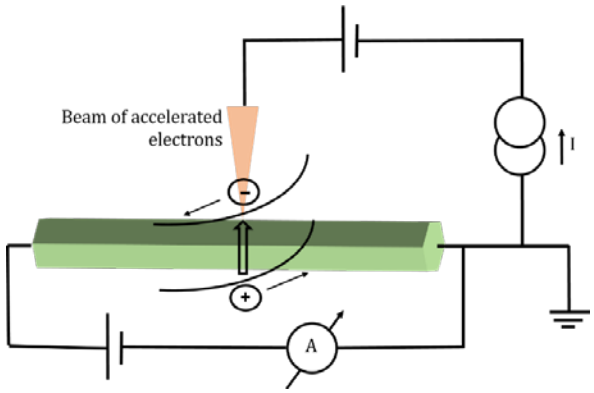

Figure 3.9. Schematic of electron beam induced current set up. The NW is depicted in green, the beam of accelerated electrons from the SEM in orange. Elements of a simplified electronic circuit and the simplified band diagram are depicted for better understanding.

The measurements carried out in this manuscript were done using two different setups. One is a Zeiss Ultra 55 SEM at PDI Berlin, Germany, equipped with a Gatan SmartEBIC system which was operated by Jonas Lähneman at 20 kV with a beam current of 1.7 nA. The current is amplified with a SR570 current-to-voltage preamplifier. The other is a FEI Inspect F50 at Institut Néel, Grenoble, France, with a home-made EBIC system operated by Fabrice Donatini and myself.

An overview of different SEM systems employed in this project is given in table 3.2.

Type of SEM	**Institut**	**Operator**	**Employment**
Zeiss Ultra +	Néel, Grenoble	Myself	Observation
Zeiss LEO 1530	Néel, Grenoble	Myself	Observation, Electron Beam Lithography
Zeiss Ultra 55	PDI Berlin	Jonas Lähnemann	EBIC
FEI Inspect F50	Néel, Grenoble	Fabrice Donatini, myself	EBIC
JEOL JSM-7001F	CEA, Grenoble	Akhil Ajay	Observation

Table 3.2. Overview of Scanning Electron Microscopy equipment employed throughout the project.

3.3.2. Transmission Electron Microscopy

A TEM extracts information from transmitted, elastically and inelastically scattered electrons. To detect transmitted electrons, the specimen to probe must be sufficiently thin. That is generally achieved by making a thin lamella of the sample with the focused ion beam technique or using mechanical polishing (potentially combined with ion milling). In this PhD project all the investigated specimen are NWs, which by definition already meet the requirements of small thickness. These however have to be dispersed on a grid, e.g. made of SiN.

A TEM is typically operated at 200–300 kV but can also be used at lower acceleration voltage. The incident electron beam of a TEM is (nearly) parallel. It traverses the specimen and is generally recorded with a camera. There, either the image plane (real space) or the back focal plane (reciprocal space) of the objective lens is projected in order to record an image or diffraction pattern, respectively. The resulting image is a bright field image. At the locations where the beam interacted with the specimen less electrons are collected. A heavier material (increased atomic number Z) or a thicker specimen absorb more electrons. That leads to materials with higher atomic number Z and thicker regions to be represented by a darker contrast. By inserting an aperture, dark field (DF) imaging is possible as well. In TEM imaging the precise location of atomic columns is difficult to extract from the high-resolution (HR) lattice image. A lattice-like image is

an indication of a crystalline structure but not a direct representation of that lattice. The image is constructed by interference of different diffracted beams, and therefore depends on many parameters: mainly the present aberrations and defocus of the objective lens and the sample orientation. A more quantitative interpretation of HR TEM images is possible, but requires doing simulations to allow a better interpretation of the obtained bright field image.

In the diffraction plane below the sample, a diffraction pattern characteristic of the crystal structure of the specimen can be collected. An analyses of the diffraction pattern allows quantification of crystal orientations and lattice types through comparison with simulations or a crystallographic database.

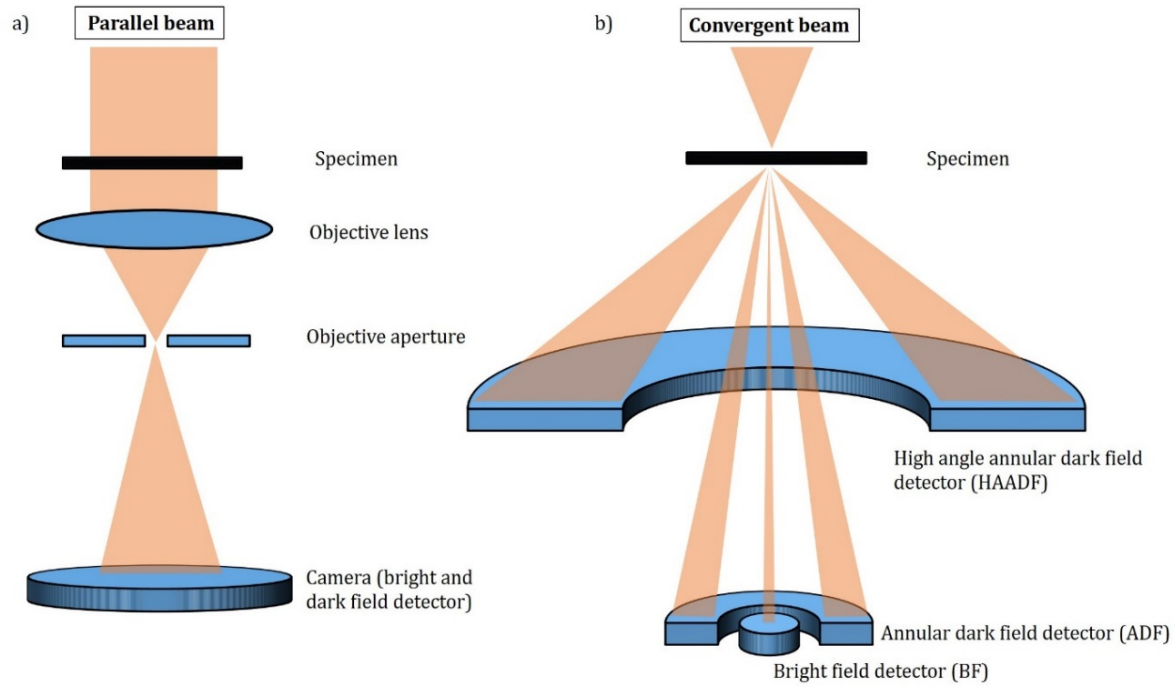

Figure 3.10. Schematics of the beam paths in (a) TEM and (b) STEM between the specimen and the detectors.

Most TEM equipment can also be operated as a scanning transmission electron microscope (STEM), see figure 3.10. In that case, the electron beam is not parallel but focused to one point and is scanned over the specimen. At each scanning point a value of counts on a detector is recorded from which subsequently an image is reconstructed (just like in SEM). In this operation mode, a very useful detector is the high angle annular dark field detector (HAADF). It has an annular shape and is mounted in a plane conjugated to the back focal plane (diffraction plane) of the objective lens. As a result of this positioning, the impinging electrons stem almost exclusively from scattering events in the specimen over high angles with respect to the direct beam. A qualitative interpretation of HR HAADF STEM images is more straightforward than for HR TEM images, as atomic columns can be observed directly. They appear as a bright contrast as an increased number of electrons is collected on the detector due to the scattering event on the atomic column. The contrast can be related to different chemical components where the relation $Z^{1.7}$ is a good approximation[243,244]. The image contrast in BF TEM and BF STEM is comparable and the contrast between BF and DF is reversed. A comparison between BF TEM, BF STEM and HAADF STEM on the same specimen can be seen in figure 3.11. Ultimate spatial resolutions in (aberration corrected) TEM and STEM are around 50 pm.

In the present work, a probe corrected FEI TITAN Themis of CEA-IRIG, Grenoble, France, equipped with a field emission gun working at 200 kV was employed for (HAADF) STEM. It was operated by Martien den Hertog. A CM 300 TEM at Institut Néel, Grenoble, France, working at 300 kV was employed for TEM and operated by myself. We use TEM and STEM techniques to verify

that the contacted NW is indeed a single one, its state of coalescence, if any, to determine its diameter, length, thicknesses of AlN barriers, QD insertions and to observe the potential presence of AlN or GaN shells surrounding the structures as well as detecting regions of strain-induced chemical interdiffusion.

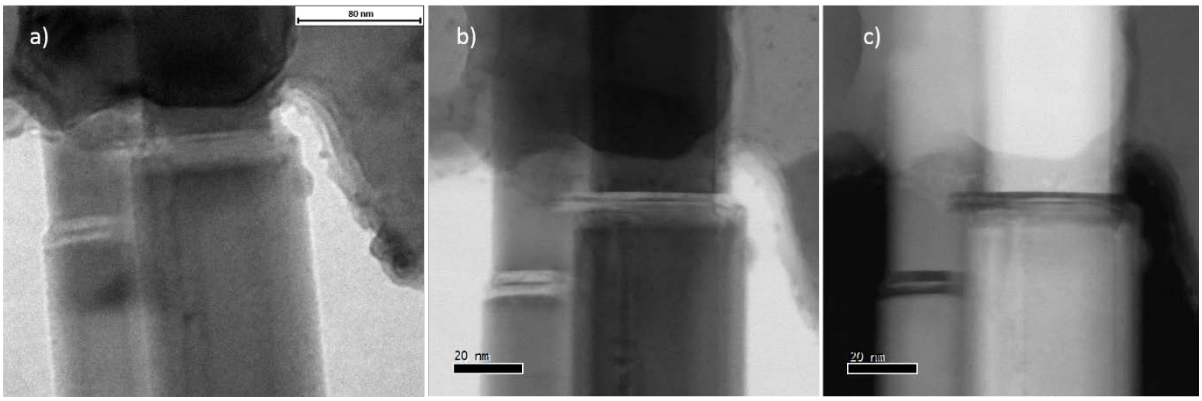

Figure 3.11. Different transmission electron microscopy micrographs of the same specimen (E3605_d5_m4_c23). (a) BF-TEM, (b) BF-STEM and (c) HAADF-STEM where (b) and (c) are acquired simultaneously.

DENS Solutions 6 contact double tilt holders were used. These are in-situ double-tilt holders that allow for application of electric bias during the imaging process. They require specific grids. We used home-made membranes of SiN.

3.4. Electrical and Photocurrent Characterization

Measurements characterizing the current-voltage dependence (IV curves) were done with the use of an Agilent 4155C Semiconductor parameter analyzer.

Photocurrent measurements were carried out as a function of impinging optical power, chopping frequency and wavelength. To probe the photocurrent in the specimen presented in this manuscript two setups were used. One of the setups employs an unfocused continuous-wave HeCd laser emitting at 325 nm with a spot diameter of around 1 mm as excitation source. The signal is typically chopped at 73 Hz and the NW is directly connected to a 10^6 A/V transimpedance amplifier integrated in the lock-in amplifier Stanford Research Systems SR 830. For the spectral response measurements, the illumination source is replaced by a 450 W Xe lamp. Here the emission is passed through a Gemini 180 Jobin-Yvon grating monochromator. Both set-ups are in CEA-IRIG, Grenoble, France.

Photocurrent measurements were performed using a home-made sample holder and switch box developed by Jonas Lähnemann. A schematic is given in figure 3.12. Based on the home-made in-situ chips integrating a TEM-grid described in section 3.2.1, they allow setting up three contacted NWs for electrical measurements. The chip is slid into its predetermined place and held by a clamp on one side and 6 contact needles on the other. The needles get in contact with the gold pads of the chip, and transmit the electrical signals via copper cabling to a six-pin connector. A 6-cable bundle connects the holder to the switch box. On the switch box, the desired NW can be selected by pulling up (p1) the switch for one of the contacts and pushing down (p2) the switch for the other one. In “IV”-mode the top position of contact switches connects to the center of the p1-BNC socket and the bottom position to the center of the p2-BNC socket. In “lock-in”-mode the top position of contact switches connects to the center of the lock-in-BNC socket and the bottom position to the center of the bias-BNC socket. The remaining switches corresponding to the remaining contact pads are grounded. It is important to ground the switches while connecting other electrical equipment such as a power supply or parameter analyzer, since these can introduce tension spikes into the circuit that exceed the maximum current that a NW can withstand. The holder is compatible with the Oxford Optistat CF-V cryostat and therewith allows

measurements in vacuum and at low temperatures. The detailed design of the switch box can be seen in Annex B.

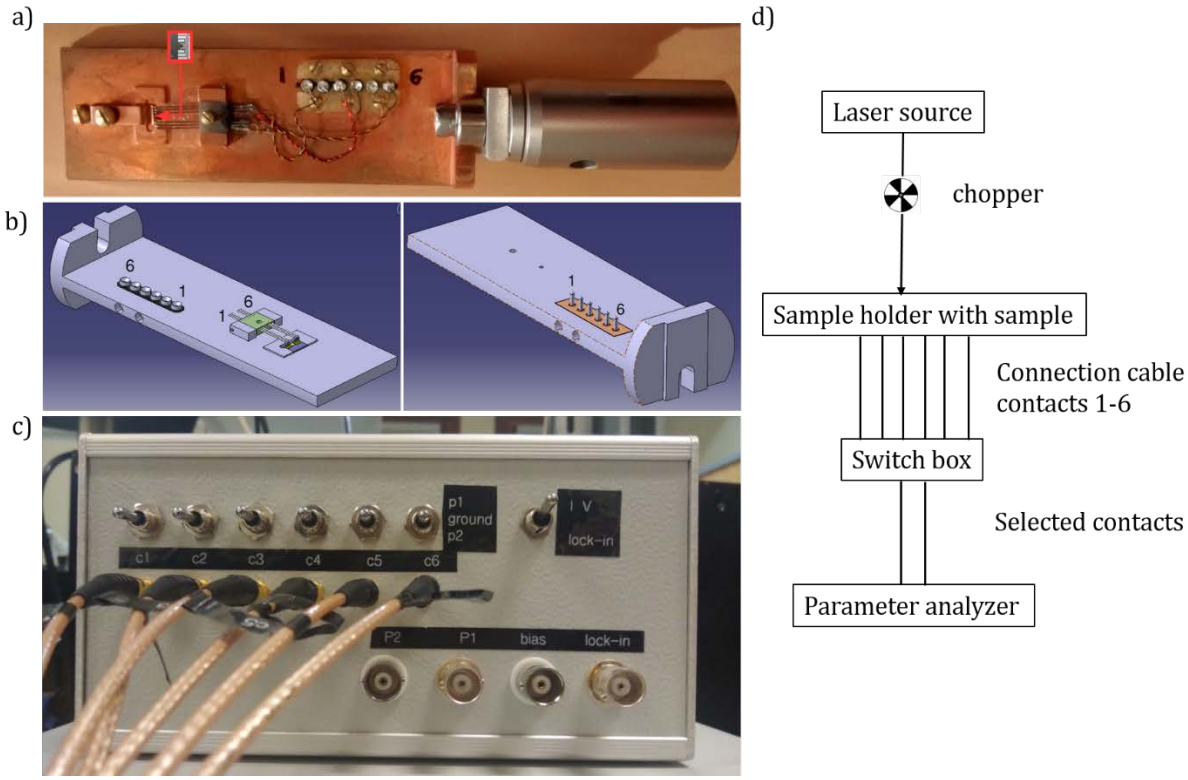

Figure 3.12. (a) Top-view of the home-made sample holder. The place for mounting the sample is indicated in red. (b) Top- and bottom-view schematics of the sample holder indicating the place for the sample, the contact needles and the 6-pin connector bar. (c) Photo of the home-made switch box. (d) A simplified schematic of the set up for measuring IV curves and photocurrent including the sample holder and switch box.

3.5. Photoluminescence

The working principle of photoluminescence (PL) is based on the radiative recombination of electron-hole pairs generated through absorption of incident photons. The energy of the incident photon needs to be larger than the bandgap of the semiconducting material under study, in order to promote an electron from the valence to the conduction band. These electron-hole pairs can recombine in different ways, one of which is radiative recombination. The simplest radiative recombination path is the band-to-band transition between a free electron and a free hole as depicted in figure 3.13(a). Furthermore, the electron can get trapped in donor states and the hole in acceptor states within the bandgap, which gives rise to different radiative recombination paths such as the donor electron to free hole, free electron to acceptor hole and donor electron to acceptor hole recombinations (figure 3.13(b)-(d)). The energetic location of acceptor and donors within the bandgap are characteristic to the semiconductor material and the involved impurity. In addition to these, excitonic recombinations occur. These have a lower energy because the electron and the hole are linked by Coulomb attraction which also makes the exciton be a quasi-particle. All emissions are specific to their recombination paths and they carry a characteristic energy. Probing at liquid helium temperatures (4 K) has the advantage of limiting the influence of phonons, temperature-induced line broadening and the probability of thermally activated non-radiative processes.

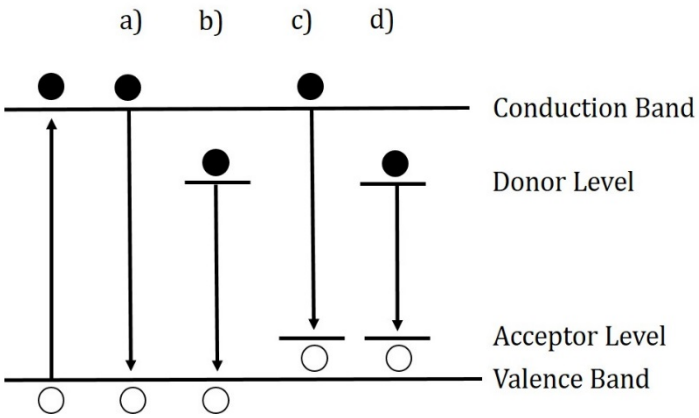

Figure 3.13. Recombination processes between (a) free electron and free hole, (b) donor electron to free hole, (c) free electron to acceptor hole and (d) donor electron to acceptor hole. Modified from ref. 245. Additionally, excitonic recombinations occur whose quasi-particle nature, however, can not be represented in a single particle band diagram.

A schematic of the setup used in this manuscript is depicted in figure 3.14. The illumination source is a frequency doubled solid-state laser emitting at 244 nm (488 nm). Excitation powers up to 1 mW are employed. The laser spot is focused through a NA=0.4 refractive microscope objective and has a size of about 1 µm. A Jobin-Yvon tri-axe 550 monochromator and a liquid nitrogen cooled UV enhanced charge-coupled device (CCD) are used. The sample is mounted onto a cold finger of an Oxford He flow cryostat. The navigation on the sample is done through employment of an UV LED emitting at 365 nm that illuminates the specimen and a UV- enhanced camera (pco.ultraviolet, 190–1100 nm, 1392×1040 pixel^2) for visualization of the specimen.

PL measurements can be performed under bias using a specific sample holder made by Jonas Lähnemann and is depicted in figure 3.15. It allows setting up three contacted NWs for measurements. Based on the home-made TEM-grid described in section 3.2.1. a bundle cable connects the holder and a switch box. On the switch box the desired NW can be selected by pulling up the switch for one of the contacts (p1) and pushing down the switch for the other one (p2). The remaining switches corresponding to the remaining contact pads are grounded. Depending on the selected mode, “analyzer” or “bias/ lock-in”, the selected contacts are then connected to floating ground, common ground or a NW contact pad. In “analyzer” mode the floating ground configuration is used. The top position of the switches corresponds to the center of the p1-BNC socket and the bottom position to the center of the p2-BNC socket. The p1 or p2 socket can be connected to the power supply to apply a bias. The box can be grounded connecting it either to the shield of p1 or the core/shield of lock-in sockets to the ground-terminal of the power supply. In “bias/ lock-in” mode all the connected NWs share a common ground. In this configuration the top position of the switches corresponds to the center of the lock-in BNC socket and the bottom position to the center of the bias BNC socket. This holder is compatible with the Oxford MicrostatHiResII cryostat and therefore allows measurements at low temperatures and in vacuum. The detailed design of the switch box can be seen in Annex B.

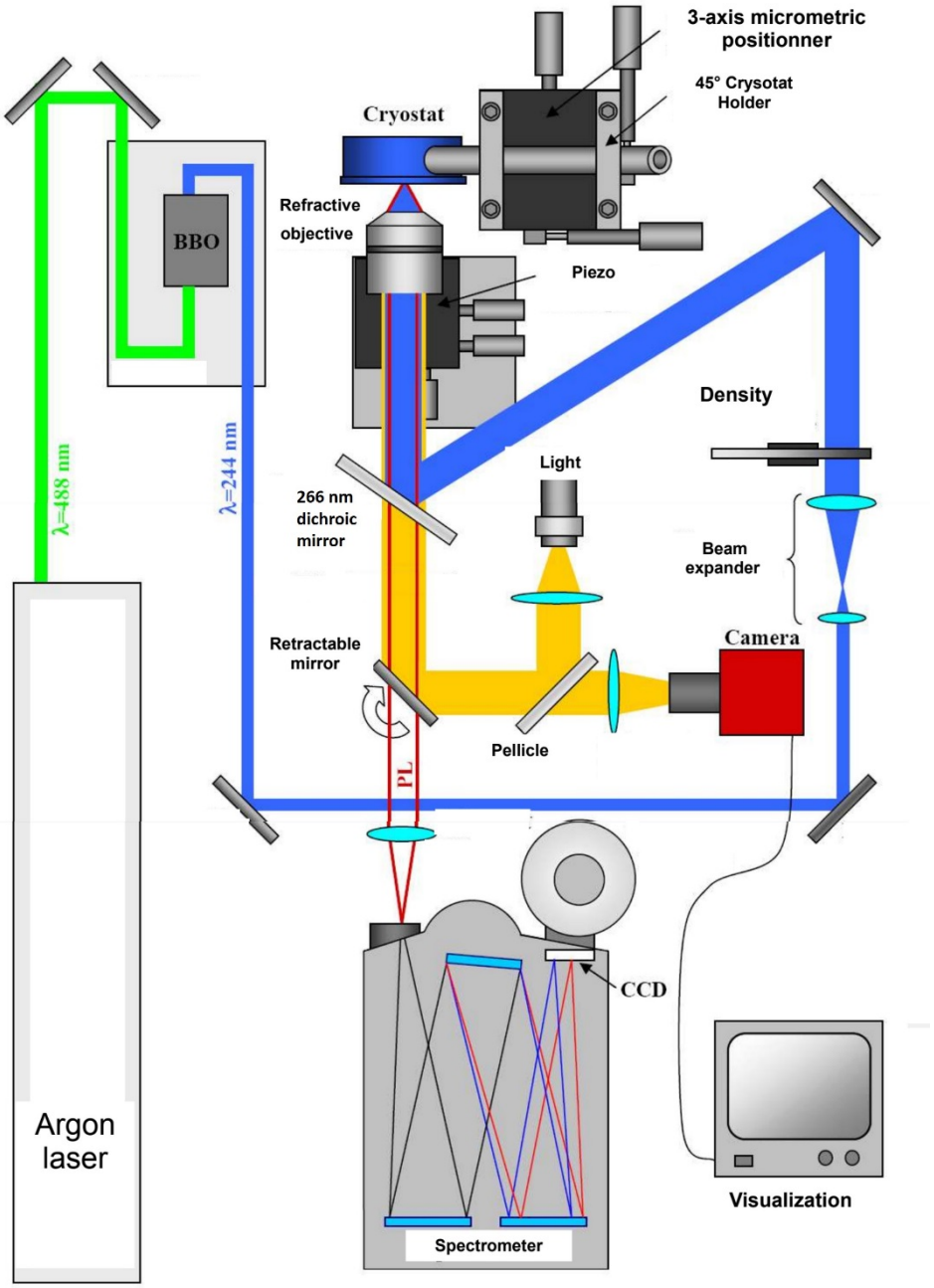

Figure 3.14. PL setup used during the project. Modified from ref. 27.

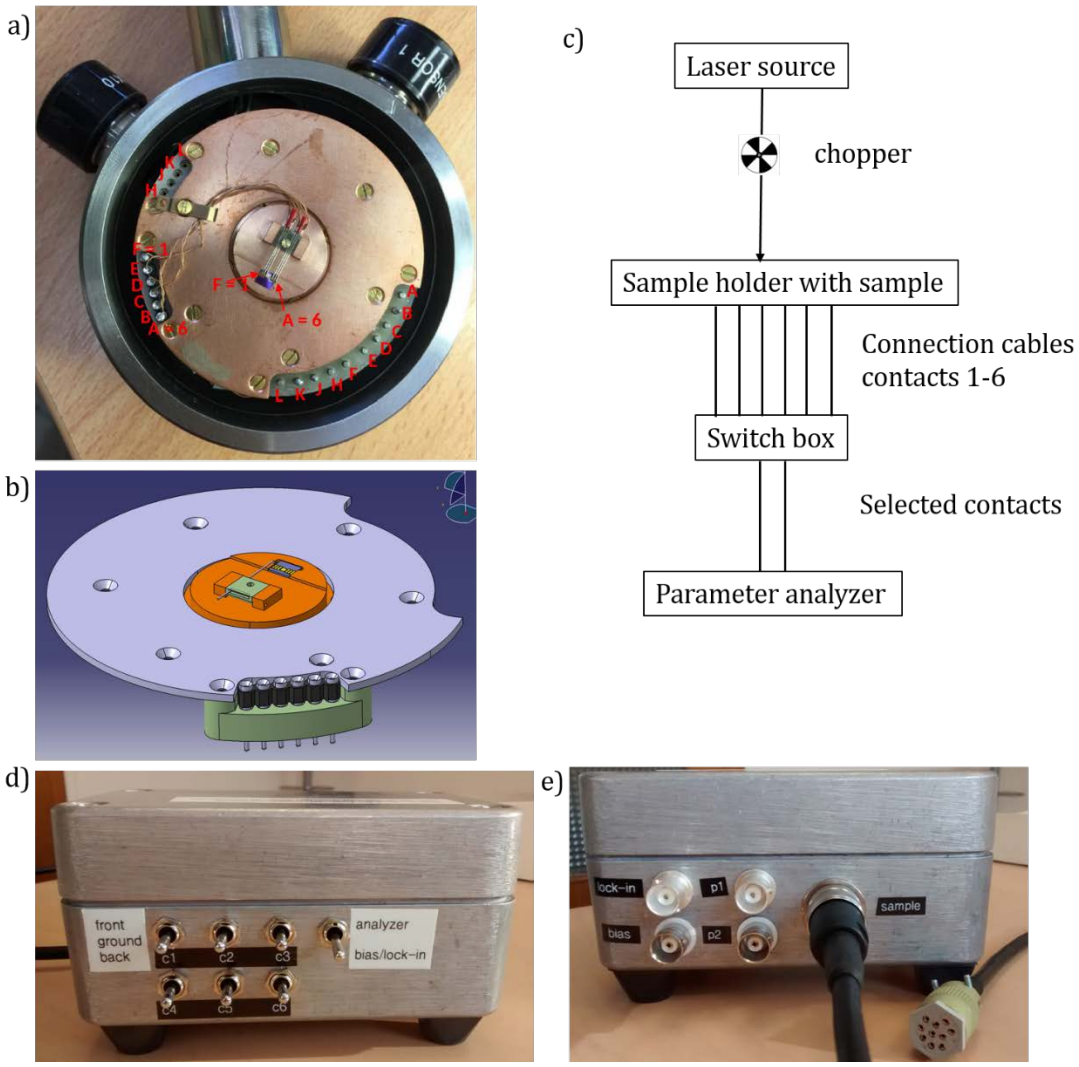

Figure 3.15. (a) Photo of the home-made sample holder mounted inside the cryostat. The place for the sample is in the center in purple. The sample connectors are indicated in red numbers and the cryostat connectors in red letters. The holder contact needles, connecting copper cables and the 6-pin connector (A-F) are visible. (b) Schematic of the sample holder mounted onto the Oxford He flow cryostat sample holder. The sample holder is indicated in orange. The contact needles as well as the 6-pin contact is shown. (c) A simplified schematic of the in-situ PL measurement setup including sample holder and switch box. (d) Front- and (e) back-side of the home-made switch box used for in-situ PL measurements. The selector switches and connector sockets are visible.

3.6. Simulations

Simulations of the strain distribution and electronic structure of the samples were carried out with the nextnano[3] software which is a commercial self-consistent Schrödinger-Poisson equation solver. We used a model based on the **k·p** perturbation theory for calculating the quantum levels. For a detailed description of the models used, the interested reader is referred to the PhD thesis of Stefan Birner[246]. For the work presented in this manuscript the strain distribution, electronic band structure, quantum levels and recombination probabilities of given nanostructures are simulated in one and three dimensions. Note that the Coulomb interactions are not taken into account.

The material parameters given in the software can be modified. The input parameters for GaN and AlN are taken from Kandaswamy et al.[221] and given in table 3.3. To model the ternary alloy AlGaN the bowing parameters have likewise been modified and set to zero.

Parameters (units)	Symbol	GaN	AlN
Lattice constants (nm)	a	0.3189 [28]	0.3112 [28]
	c	0.5185 [28]	0.4982 [28]
Spontaneous polarization (C.m^{-2})	P_{SP}	-0.029	-0.081
Piezoelectric constants (C.m^{-2})	e_{31}	-0.49 [30]	-0.60 [30]
	e_{33}	0.73 [30]	1.46 [30]
Elastic constants (GPa)	c_{11}	390 [32]	396 [33]
	c_{12}	145 [32]	140 [33]
	c_{13}	106 [32]	108 [33]
	c_{33}	398 [32]	373 [33]
Dielectric constant		10 [247]	8.5 [247]
Luttinger parameters	A_1	-5.947 [248]	-3.991 [248]
	A_2	-0.528 [248]	-0.311 [248]
	A_3	5.414 [248]	3.671 [248]
	A_4	-2.512 [248]	-1.147 [248]
	A_5	-2.510 [248]	-1.329 [248]
	A_6	-3.202 [248]	-1.952 [248]
	A_7	0 [248]	0 [248]
(eV)	$E_P^{\parallel}$	14 [248]	17.3 [248]
(eV)	$E_P^{\perp}$	14 [248]	16.3 [248]
Deformation potential	a_{c1}	-4.6 [247]	-4.5 [247]
	a_{c2}	-4.6 [247]	-4.5 [247]
	D_1	-1.70 [247]	-2.89 [247]
	D_2	6.30 [247]	4.89 [247]
	D_3	8.00 [247]	7.78 [247]
	D_4	-4.00 [247]	-3.89 [247]
	D_5	-4.00 [247]	-3.34 [247]
	D_6	-5.66 [247]	-3.94 [247]

Table 3.3. Input parameters used for the calculations with the nextnano³ software.

In the case of 3D calculations, the NW is modelled as a hexagonal prism. It is embedded in a cuboid of air to allow for a proper modelling of the elastic strain relaxation. It is modeled onto a GaN substrate in order to have an in-plane lattice parameter reference. Typically, the 3D strain distribution is calculated first. It is done by minimization of the elastic energy assuming zero stress at the NW surface. Subsequently, the calculation of bands is done taking into account the piezoelectric fields resulting from the strain distribution obtained from the 3D calculation. Then the wave functions and related eigenenergies of the electron and hole states within a QD or SL structure can then be calculated. This is done by solving the Schrödinger-Poisson equations with the 8-band **k·p** model. To model the influence of bias, 1D simulations are done where bias is modeled as an electric field across the structure.

Modeling the surface states is not obvious. In the absence of consistent experimental values, different methods for accounting for surface states were used.

i. introducing a negative 2D charge density of 2×10^{12} cm^{-2} at the surfaces. This is the density of states reported from m-plane GaN[249] and we assume here that those states are not located within the bandgap.
ii. pinning the Fermi level in the middle of the AlN conduction band (if the structure is assumed to have an AlN shell) which is 3.1 eV below the conduction band edge of AlN
iii. pinning the Fermi level in the middle of the GaN conduction band (if the structure is assumed to have an interface with air) which is 1.7 eV below the conduction band edge of GaN
iv. pinning the Fermi level 0.6 eV below the conduction band edge of GaN as predicted in ref. [250].

Note that in the cases (ii) – (iv) the surface pinning is making a Schottky-type interface with air. The experimental values of ref. [251] place the Fermi level pinning of GaN at the m-plane AlN 2.1 eV below conduction band of AlN. That corresponds to a version between the modeled cases (ii) and (iii).

4. Bias-dependent Spectral Response in Superlattice Single Nanowire Photodetectors

In this chapter a GaN single NW structure including an AlN/GaN superlattice (SL) insertion is studied in terms of its photodetector capabilities. A bias-dependent spectral response is observed and attributed to preferential active regions for the charge carrier collection when applying bias. We present a study of GaN single-NW ultraviolet photodetectors with an embedded GaN/AlN SL. The heterostructure dimensions and doping profile were designed in such a way that the application of positive or negative bias leads to an enhancement of the collection of photogenerated carriers from the GaN/AlN SL or from the GaN base, respectively, as confirmed by electron beam-induced current measurements. The devices display enhanced response in the ultraviolet A (≈330–360 nm) / B (≈280–330 nm) spectral windows under positive/ negative bias. The result is explained by correlation of the photocurrent measurements with scanning transmission electron microscopy observations of the same single NW, and semi-classical simulations of the strain and band structure in one and three dimensions.

In this study the fabrication (dispersion, lithography, metallization…) and electrical characterization were carried out by myself. For some of the measurements and processing steps I was assisted by Jakub Polaczyński and Jonas Lähnemann. The theoretical calculations were done by myself and Jonas Lähnemann with support from Eva Monroy. STEM observations were carried out by Martien den Hertog. EBIC measurements have been done by Jonas Lähnemann at Paul-Drude Institut in Berlin, Germany. Characterization by HRXRD and the MBE growth were carried out by Pascal Hille and Jörg Schörmann in the group of Prof. Martin Eickhoff at Justus-Liebig University in Gießen, Germany.

Results were published in Spies et al., Nano Lett. 2017, 17 (7), 4231–4239[252]*.*

4.1. Motivation and State of the Art

The internal electric field in polar GaN/AlN NW heterostructures opens interesting possibilities for band profile engineering in order to modulate the spectral response, and even render it bias-dependent. The feasibility of single NW photodetectors based on GaN/AlN SLs embedded in GaN NWs was demonstrated by Rigutti et al.[20]. In their case, the presence of the SL reduced the dark current, but also decreased the responsivity by around two orders of magnitude. Their SL was designed to have a band-to-band transition (transition between the first confined electron and hole levels, e_1–h_1) around 430 nm (≈ 2.9 eV). Temperature-dependent studies of the photocurrent, presented in ref. [20], showed that such large GaN nanodiscs (room-temperature photoluminescence measured at 2.8–3.2 eV, which corresponds to a nanodisk thickness of ≈ 3–5 nm) present problems for the collection of photogenerated carriers, which explains the low responsivity. Despite that handicap, the response from the SL was observed around 415 nm (≈ 3 eV) in the photocurrent spectrum. Yet it was approximately three orders of magnitude weaker than the response of the GaN cap/stem. With positive bias applied to the stem of the NW, the responsivity decreased by one order of magnitude, and the response of the SL was masked by the background noise.

In this chapter, an improved structural design is presented, more adapted for its use as a photodetector, which exploits the advantages associated with the internal electric field generated by the SL. First, the width of the GaN nanodisks is reduced to 2.5 nm to facilitate the carrier extraction. Secondly, an asymmetry is introduced in the doping profile: The stem and the SL are undoped, whereas the cap is heavily n-type doped. This avoids the pinning of the Fermi level at the conduction band in the stem, and enlarges the regions with internal electric field in the structure. With this new architecture, enhancement of the responsivity by more than two orders of magnitude is envisioned. Furthermore, the application of positive or negative bias should lead

to an enhancement of the collection of photogenerated carriers from the GaN/AlN SL or from the GaN base, respectively.

4.2. Sample Design and Device Fabrication

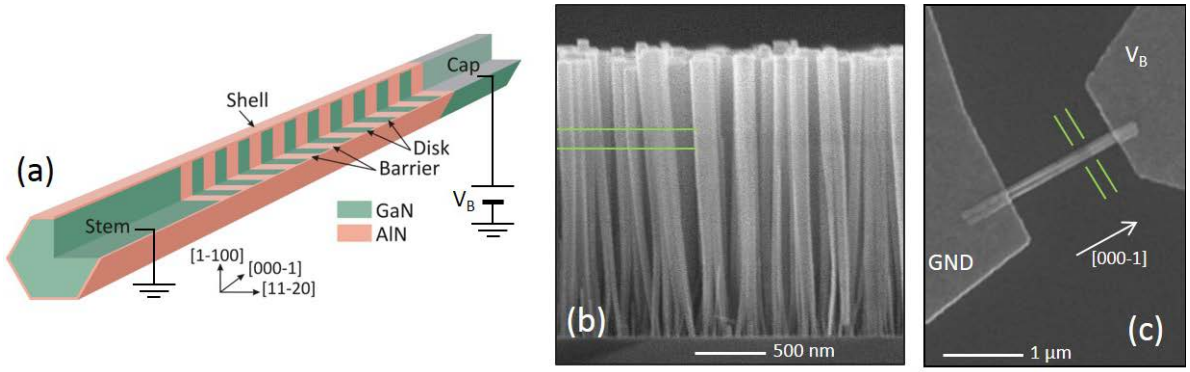

Figure 4.1.(a) Schematic description of the NW heterostructure. The voltage convention is indicated with bias applied to the GaN cap (V_B) whereas the GaN stem is grounded (GND). (b) Cross-sectional SEM image of the as-grown NW ensemble. The GaN/AlN SL, indicated by green horizontal lines, appears with a darker contrast. (c) SEM image of a contacted NW. The GaN/AlN SL, between the green parallel lines, appears with a darker contrast. The voltage convention is indicated with bias applied to the GaN cap (V_B) whereas the GaN stem is grounded (GND).

The structure of the NWs under study is depicted in figure 4.1.(a). The growth sample is called N1604200. The NWs are grown along the $[000\bar{1}]$ axis, and present $\{1\bar{1}00\}$ m-plane sidewalls. The NWs were grown on Si(111) substrates by PAMBE performed under nitrogen-rich conditions at a substrate temperature of 790°C[253]. Aluminum, gallium and germanium were supplied from standard effusion cells with beam equivalent pressures of 7×10^{-8} mbar, 1.5×10^{-7} mbar and 1×10^{-10} mbar, respectively. The source of atomic nitrogen was operated at a power of 300 W using a nitrogen flux of 1 sccm. After the deposition of the 1600-nm-long GaN stem, a 30-period GaN/AlN SL is formed by periodic switching of Ga and Al fluxes. During the growth of the AlN segments, the low mobility of the impinging Al atoms gives rise to the formation of an AlN shell that envelops the GaN/AlN SL and the GaN stem. On the contrary, the high mobility of Ga at the high substrate temperature inhibits the formation of an additional GaN shell around the SL. Finally, the structure is capped with a 600-nm-long Ge-doped GaN segment ($[Ge] \approx 3\times10^{19}$ cm^{-3}), leading to an n/n+ junction encompassing the SL along the NW axis. The choice of Ge as dopant instead of the more common Si is based on previous studies demonstrating its efficiency as n-type dopant in GaN NWs[254,255]. At high doping levels, germanium should reduce the tensile strain induced by doping[256] and prevent the radial segregation and deformation of the NW induced by silicon[73]. However, recent studies[257] show that the behavior of both Si and Ge is quite similar at the doping levels used in this work. The Ge concentration is estimated from time-of-flight secondary ion mass spectrometry on reference samples performed in reference GaN NW samples grown in the same conditions (same substrate temperature and growth rate) and with the same beam equivalent pressure of germanium[254]. The Ge calibration was further validated by comparison with energy dispersive x-ray spectroscopy carried out in a transmission electron microscope[254]. The structural asymmetry of the NW, with a stem significantly longer than the cap, was designed with the aim to obtain a homogeneous height of the GaN stems in the NW ensemble before the growth of the SL[258], which helps to prevent the coalescence of NWs with displaced SLs[128]. Figure 4.1.(b) presents a cross-section scanning electron microscope (SEM) view of the as-grown NWs.

The NWs are subsequently dispersed and contacted as described in section 3.2.7. Figure 4.1.(c) is an SEM image showing a single contacted NW of growth N1604200 used for this study.

4.3. Structural Characterization

The as-grown NW ensemble of N1604200 was characterized with high-resolution x-ray diffraction (HRXRD) in order to obtain a first validation of the existence of the SL. Subsequently photodetector characterization followed by HAADF-STEM imaging was carried out on the individual contacted NWs used for this study. In order to minimize beam damage, (S)TEM observations were done after the photodetector characterization had already been carried out.

HRXRD measurements were performed using a PANalytical X'Pert PRO MRD system with a 4-bounce Ge(220) monochromator. Figure 4.2. shows the θ-2θ x-ray scan around the (0002) reflection of the as-grown NW ensemble, together with a theoretical calculation performed with the X'Pert Epitaxy software from PANalytical. HRXRD measurements of NWs are challenging because of the variation of tilt and twist among the wires, which broadens the x-ray reflections. Nevertheless, it is possible to identify the GaN reflection at 34.58°, with a shoulder at higher angles due to the different strain state of the stem and cap segments induced by the presence or not of the AlN shell around the stem. It is also possible to resolve unambiguously the SL reflection and one of its satellites. The SL period can hence be estimated to be 5.1±0.2 nm from the inter-satellite distance.

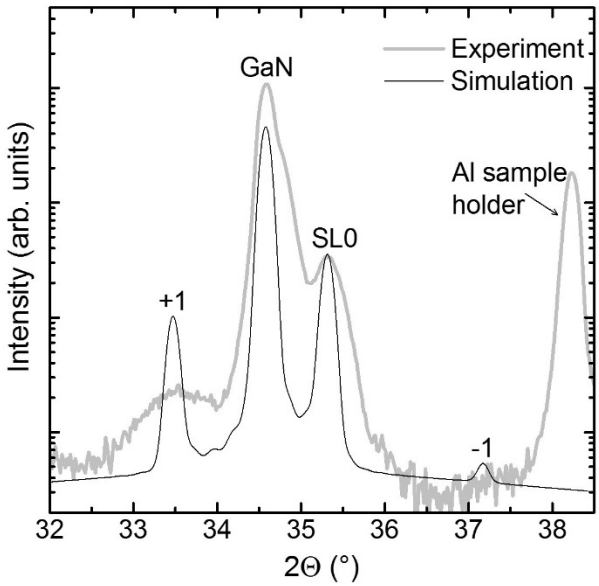

Figure 4.2. Representation of the θ-2 θ x-ray scan around the (0002) reflection of the as-grown NW ensemble (gray) of growth N1604200, and the corresponding theoretical calculation (black) performed with the X'Pert Epitaxy software from PANalytical.

Carrying out a microscopy study and correlating it with the photodetector performance is important to confirm that it is indeed a single object, and to use its real dimensions in the band-structure simulations. Figure 4.3.(a)-(b) and (c)-(d) show HAADF-STEM images of the investigated samples NW4 and NW3 (N1604200_d1_m6_c45 and _c23), respectively. From these micrographs, both of the NWs presented here are a single NW resulting from the coalescence of two NW stems, which takes place before the growth of the SL. (The second orientation of the lower SL layers in micrograph (b) is due to a truncated surface of the top of the NW at the moment of switching on the Al flux, which is an effect of coalescence.) As a result of these early coalescences, the active region is relatively large, with a diameter of ≈ 150 nm for NW4 and ≈ 130 nm for NW3. In the active region, the GaN nanodisk and AlN barrier thicknesses of NW4 are 2.5±0.3 nm and 2.6±0.3 nm, respectively, which is in good agreement with the data extracted from HRXRD measurements. The SL of NW3 is likewise easily discernable with layer thicknesses comparable to those of NW4.

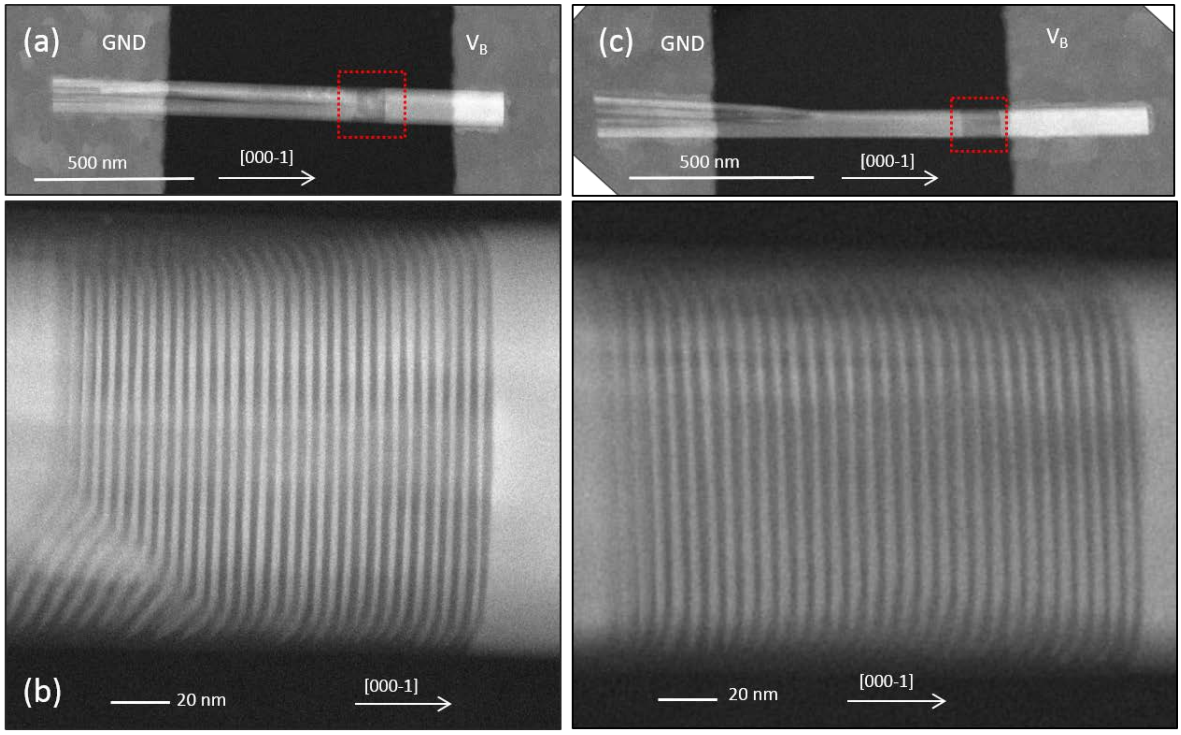

Figure 4.3.(a),(c) HAADF-STEM image of contacted NW4 and NW3 respectively. The GaN/AlN SL, indicated by a red square, appears with a darker contrast. The voltage convention is indicated with bias applied to the GaN cap (V_B) whereas the GaN stem is grounded (GND). These NWs result from the coalescence of a bundle of NWs in the early stages of the growth, well before the deposition of the SL. (b),(d) Zoomed HAADF STEM image revealing the SL structure. Bright areas correspond to GaN, darker contrast to AlN. The active regions have diameters of ≈ 150 nm and ≈ 130 nm, respectively. The second orientation of the lower SL layers in micrograph (b) is due to a truncated surface of the top of the NW at the moment of switching on the Al flux (an effect of coalescence).

4.4. Opto-electrical Characterization

Current-voltage characteristics were measured on individual single NWs. The influence of the impinging optical power and the chopping frequency were measured and compared between the samples. Subsequently spectral response measurements were carried out.

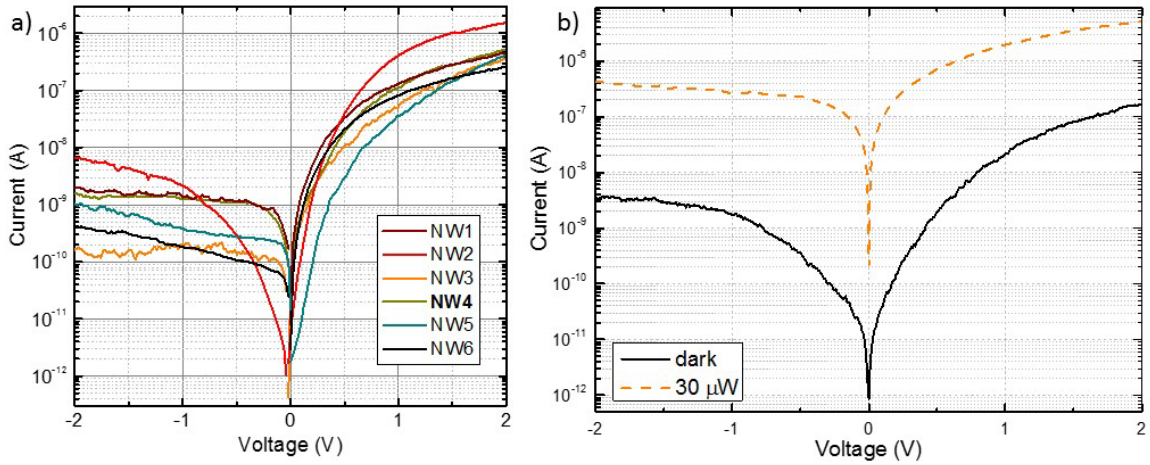

Figure 4.4.(a) Dark current of various NWs of growth N1604200. They systematically display a rectifying behavior with the current blocked under negative bias. (b) Current-voltage characteristic of N1604200_d1_m6_c45 (NW4), recorded in the dark (solid line) and under continuous illumination (dashed line) with a HeCd laser (325 nm, power = 30 µW, spot diameter of 1.5 mm).

The study presented here was validated by the observation of similar results in various NWs with the same structure. However, it was possible to carry out the complete characterization as a photodetector as well as HAADF-STEM and EBIC on NW4 (N1604200_d1_m6_c45) only. Whenever available, the data of other NWs is shown as well. A semi-logarithmic plot of the IV characteristics in the dark of NWs 1−6 is displayed in figure 4.4.(a).

The combination of the internal electric fields induced by the heterostructure and by the n/n+ doping profile along the polar axis results in a strongly rectifying behavior. To give an idea of the homogeneity of the sample, the dark current values at –2 V and +2 V bias were in the range of 0.2−1.6 nA and 0.4−1.5 μA, respectively, for all the NWs under study, in contrast to the up to five orders of magnitude in dispersion of these values found in ref.[128] for a less homogeneous sample. A summary can be seen in table 4.1.

NW	N1604200_d1_	I_{dark} (1 V)	I_{ph} (1 V)	I_{ph} (0 V)
NW1	m2_c23	130 nA	4.9 μA	0.34 nA
NW2	m6_c16	410 nA	3.2 μA	0.48 nA
NW3	m6_c23	51 nA	3.4 μA	3.4 nA
NW4	**m6_c45**	**110 nA**	**4.7 μA**	**0.31 nA**
NW5	m11_c16	36 nA	2.9 μA	0.35 nA
NW6	m11_c13	82 nA	3.8 μA	4.44 nA

Table 4.1. Experimental measurements in the various NWs under study: dark current (I_{dark}) at 1 V bias, and photocurrent (I_{ph}) at 1 V bias and at zero bias. Photocurrent measurements were performed under continuous-wave illumination with a HeCd laser (325 nm, power = 1 mW, spot diameter 2 mm).

In measurements under ultraviolet (325 nm) continuous-wave illumination, we observe an enhancement of the current by several orders of magnitude (dashed line of figure 4.4.(b), NW4, optical power = 5 μW, spot diameter = 2 mm). Note that the ratio between photocurrent and dark current is higher under negative bias (due to the low dark current value), but the photocurrent itself is about one order of magnitude higher under positive bias conditions. Considering the NW surface exposed to the laser as the active photodetector area, the responsivity is as high as 150±30 kA/W at +1 V (optical power = 160 μW, spot diameter = 2 mm, the error bars account for the measurement dispersion in the various wires under study). This value is roughly 2−3 orders of magnitude larger than those in ref.[20] (0.1−2 kA/W, measured at the same irradiance, namely 5 mW/cm^2). However, a word of caution concerning this definition of responsivity needs to be added. First, the responsivity of NW photodetectors is known to depend significantly on the irradiance[18]. In our case, when decreasing the laser power to 1 μW, the responsivity increases even more, up to 3.1±0.8 MA/W at +1 V and 12±3 MA/W at +2 V bias. And secondly, the responsivity is overestimated because the detecting cross-section of a NW is known to be larger than the exposed surface[100,103,155]. The geometry of the NW leads to an antenna effect. Much like a concentrator lens on modern photovoltaics it leads to an increased absorption (see chapter 2.5. NW Photodetectors). Attending to these issues, we mostly focus on photocurrent values instead of responsivities in the remainder of this manuscript and have given these values only for comparison with previous works using the same definition.

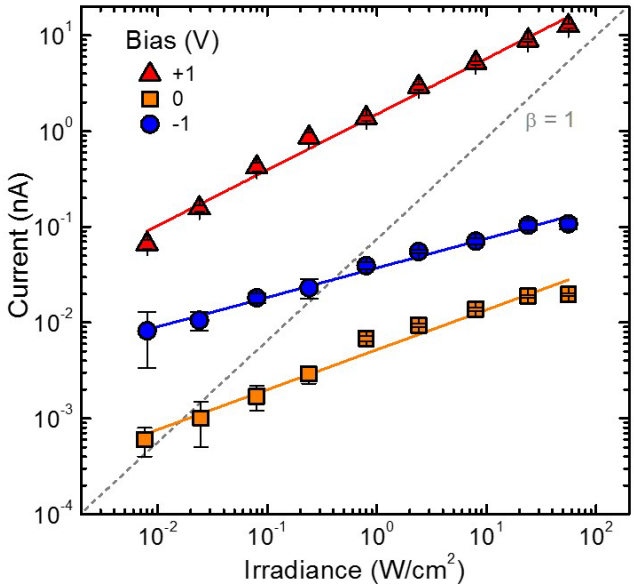

Figure 4.5. Variation of the photocurrent (I) as a function of the impinging optical power (P) in N1604200_d1_m6_c45 (NW4). Measured under chopped illumination (73 Hz) with a HeCd laser (325 nm, power = 5 μW, spot diameter 2 mm). Results for V_B = +1 V, 0 V and −1 V are presented. The error bars in the diagram represent the noise in the measurements. The photocurrent follows an $I \sim P^{\beta}$ power law (solid lines) with $\beta = 0.58 \pm 0.02$ under positive bias and $\beta = 0.31 \pm 0.02$ under negative bias. At zero bias, the response is still sublinear, with $\beta = 0.42 \pm 0.03$. The gray dashed line represents the slope for $\beta = 1$, i.e. linear behavior.

The variation of the photocurrent as a function of the impinging optical power was studied under chopped (73 Hz) excitation at 325 nm. Note that for GaN NWs, the chopped illumination generally leads to a reduction of the photocurrent in comparison with continuous-wave excitation[18,128], and the time response of the NWs described in this section is similar to ref.[128]. Measurements were systematically carried out from low to high excitation power, to prevent artefacts related to persistence or temperature transients.

N1604200_d1_m6_c45 (NW4) was found to be a typical specimen. As shown in figure 4.5., the photocurrent (I_{ph}) increases sublinearly with the optical power (P) following approximately a power law $I_{ph} \sim P^{\beta}$ with $\beta < 1$ for all the measurement bias. This behavior was qualitatively the same for all the NWs under study, with values of β in the range of 0.3−0.6, and a slight difference between positive and negative bias. Such a sublinear response with the optical power was observed in many material systems (GaN[18,21,81], Si[259], Ge[260], ZnO[114,115], SnO_2[261], ZnTe[262]), and it is generally associated to surface-related phenomena[18,79] and comparatively large NW diameters[132] as outlined in chapter 5. The photocurrent is significantly enhanced under positive bias. Note that the photocurrent presented in figure 4.5. is about 50 times higher than previous measurements in NWs with a doped GaN/AlN SL and undoped cap/stem[128].

There is also a photoresponse at zero bias, although it is an order of magnitude lower than at −1 V. This photovoltaic signal is a confirmation of the presence of an internal electric field in the structure at zero bias. It had already been observed that the insertion of a single AlN barrier in a GaN NW leads to a potential asymmetry that manifests in a zero-bias photoresponse[21,204], which can be significantly enhanced through the insertion of a GaN/AlN SL (photocurrent = 0.2 pA, corresponding to a responsivity of 0.1 A/W in ref.[20] under continuous-wave ultraviolet excitation). In the case of the GaN/AlN SL embedded in an n/n+ junction under study, the signal is further enhanced in comparison to refs.[20,21,128,204]. In this study, the photocurrent obtained for the undoped sample under 1 mW of continuous-wave excitation with the HeCd laser (spot diameter = 2 mm) is in the 0.5−3.4 nA range, which corresponds to a responsivity in the 8−60 A/W range. Such an enhancement of the photoresponse makes it possible to observe the sublinear behavior of this photovoltaic signal depicted in figure 4.5. In contrast to

GaN photoconductors, whose photocurrent scales sublinearly with the incident optical power, the photovoltaic response in GaN p-n or Schottky photodiodes are generally linear[263], for values of irradiance that do not introduce an important distortion of the potential profile. The linearity is associated to the different detection mechanisms: in photoconductors, light absorption induces a change in the resistance/mobility of the material, which results in a modulation of the current traversing the device. In contrast, in photovoltaic devices operated at zero-bias the dark current is negligible, and photogenerated electrons and holes are separated by the internal electric field and collected at the contacts. For the NWs under study, the maximum photon flux used in our experiments is estimated at $\approx 7\times10^{17}$ $cm^{-2}s^{-1}$, which implies a generation of carriers lower than 2×10^{15} cm^{-3} (note that this number is an estimation that takes into account the exposed NW surface and a carrier lifetime of ≈ 50 ns, which is the photoluminescence decay time measured at 5 K), so that photogeneration should take place in a linear regime. The sublinear behavior experimentally observed in all the NWs under study means that, once the photogenerated carriers are separated by the internal electric field, the collection process is sensitive to illumination. In other words, the device is sensitive to the photo-induced modulation of the resistance of the GaN stem/cap, which can be explained by the role of the surface states, the large surface-to-volume ratio and the comparatively large diameters.

Raising the chopping frequency from 23 Hz to 1 kHz in the photocurrent measurements of N1604200_d1_m6_c45 (NW4) results in a decrease of the photocurrent (see figure 4.6.). This behavior is independent of bias, being observed at positive, negative and zero bias. This behavior may be explained with the presence of surface phenomena which slow down the charge evacuation processes, with thermal phenomena warming the device under longer illumination or the limited system response time.

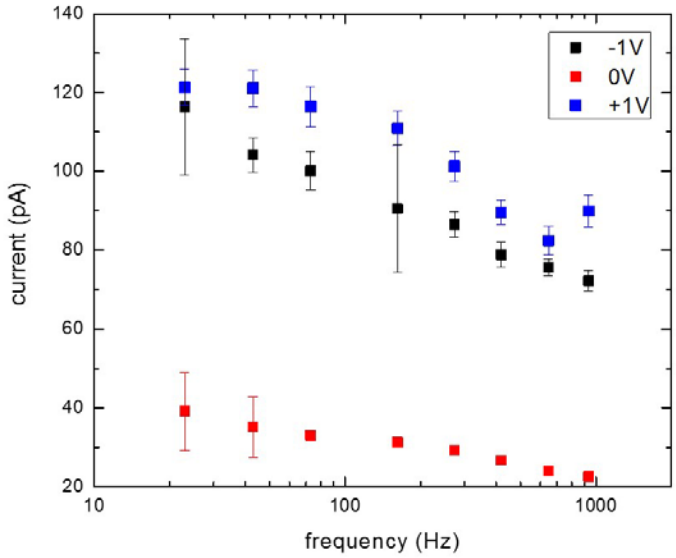

Figure 4.6. Photocurrent under varying bias as a function of chopping frequency.

The above-described study of the variation of the photocurrent as a function of the incident optical power is a prerequisite for a correct interpretation of spectral response measurements of photocurrent. The recorded photocurrent spectra are modulated by the spectral intensity of the lamp, and the correction must take into account the sublinearity of the devices. Corrected photocurrent spectra for various bias values are presented in figure 4.7. for NWs 1–5. Figure 4.7.(a) shows the spectra of NW4 which are normalized and vertically shifted for clarity (the response under positive bias is always at least one order of magnitude higher than under negative bias).

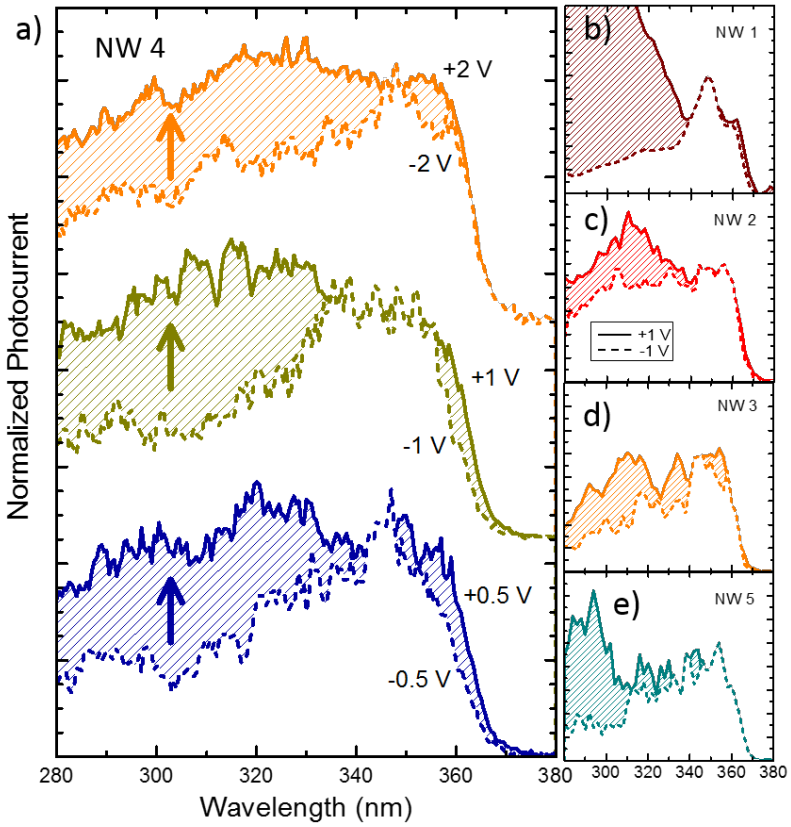

Figure 4.7.(a) Spectral response of a single NW (NW4) at various values of bias voltages (±0.5, ±1, and ±2 V). Data are corrected for the Xe-lamp emission spectrum taking the sublinear power dependence of the NW into account. Measurements are normalized and vertically shifted for clarity. Solid (dashed) lines correspond to positive (negative) bias. Shadowed areas outline the difference in the response between positive and negative bias. (b)-(e)Normalized spectral responses of various NWs measured at ±1 V bias.

Under negative bias, the spectral response is maximum in the range of 330–360 nm. In contrast, under positive bias, the maximum response is obtained in the 310–330 nm band. Note that the spectral response is presented here in a linear scale. Above 400 nm, the response of all the devices is below the detection limit of our measurement system, whatever the bias. To give a quantitative value of the UV/ultraviolet contrast, we illuminated a NW biased at +1 V with a solid-state laser emitting at 488 nm, in the same conditions used for the power dependent measurements in figure 4.5. (laser chopped at 73 Hz, spot diameter = 2 mm, synchronous detection). Under 30 mW of excitation power at 488 nm (irradiance = 0.95 W/cm^2), the photocurrent is below our detection limit of 100 fA, several orders of magnitude below the photocurrent values in figure 4.5. Measurements of NWs 1, 2, 3 and 5 display similar preferential spectral region for the charge carrier generation.

The bias modulated change in the contributions to the photocurrent agrees with the trend in the power law coefficient β observed in figure 4.5. The sub-linear behavior of the photocurrent with optical power is most pronounced for negative bias (β = 0.32), intermediate for zero bias (β = 0.42) and significantly reduced for positive bias (β = 0.58). In other words, when the SL contributes to the photocurrent, the influence of the surface states on the conductivity is not as pronounced.

4.5. Electric Field Profiles and Bias-Dependence

In order to understand the different behavior of the structure under positive and negative bias an analysis of the potential profile along the NW growth axis was done. Figure 4.8. shows the band diagram in the NW calculated using the Nextnano[3] software in one dimension, for a nanodisk/barrier thickness of 2.5 nm / 2.6 nm, considering a residual doping of 5×10^{17} cm^{-3} and a cap layer doped at [Ge] = 3×10^{19} cm^{-3}. The figure presents the band diagram under negative bias ($-V_B$, top image), at zero bias (in the center), and under positive bias ($+V_B$, bottom image).

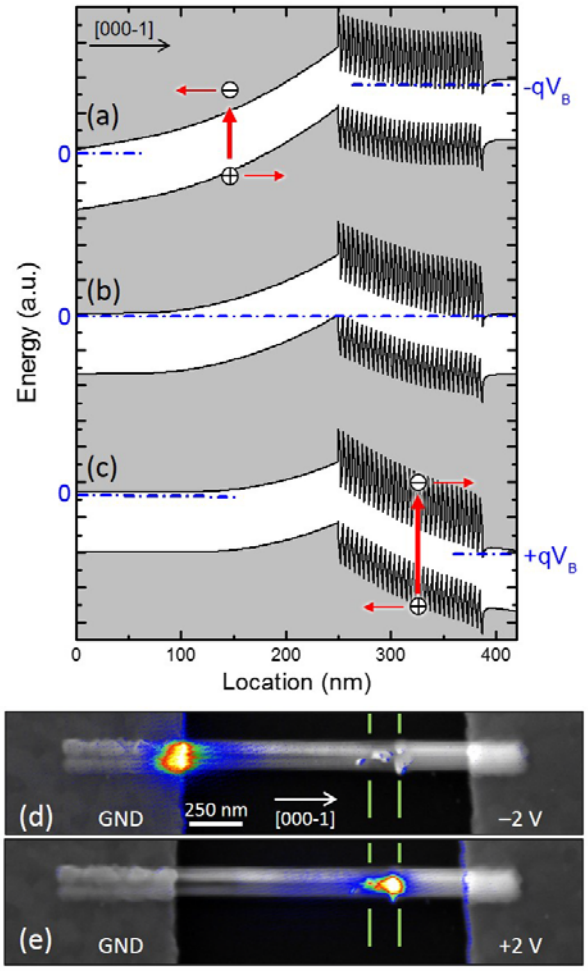

Figure 4.8. Description of the evolution of the band diagram under bias: (a) negative bias, (b) zero bias, and (c) positive bias. The data is the result of one-dimensional calculations of the NW heterostructure, in presence of an external electric field. As the model is one-dimensional, surface states are not taken into account in these calculations. The Fermi level(s) is (are) indicated by a dash-dotted blue line in each diagram. EBIC maps at (d) –2 V bias and (e) +2 V bias superimposed on an SEM image of the NW under study. The location of the GaN/AlN SL is outlined with green vertical lines.

At zero bias, the band profile presents a triangular shape induced by the negative charge sheet at the interface between the GaN stem and the SL. This fixed charge is due to the difference in polarization between GaN and the SL. It creates a large depletion region (≈ 100 nm) in the GaN stem and an internal electric field along the whole SL, which is almost fully depleted. At the interface between the SL and the GaN cap, on the contrary, the difference in polarization generates a positively charged sheet, which pins the Fermi level at the conduction band. The fact that the cap is heavily doped leads to flat bands all along the cap section. In summary, the sample contains two areas with internal electric field: the SL, with electric field pointing towards [0001], and the depletion region in the stem, with electric field pointing towards [000$\bar{1}$]. The application of bias determines the dominant electric field. Under negative bias (figure 4.8.(a)), the bands flatten along

the SL, and predominantly electrons absorbed in the GaN stem are collected. Under positive bias (figure 4.8.(c)), the depletion region in the stem shrinks and collection of carriers absorbed in the SL is favored. At the same time, the barrier for carriers injected from the contacts is higher for negative bias (figure 4.8.(a)) than for positive bias (figure 4.8.(c)), which explains the asymmetry of the dark currents in figure 4.4.(b).

The response from different regions of the NWs under reverse and forward bias should be directly visible in maps of the EBIC signal. Such maps recorded on the investigated NW are presented in figures 4.8.(d) and (e), respectively. In EBIC, electron-hole pairs separated by the internal or applied electric fields are collected through the contacts. Scanning the electron beam as excitation source over the sample results in a map of the origin of the photocurrent. As expected from the spectral response measurements together with the band structure simulations, the signal for positive bias in figure 4.8.(e) largely coincides with the location of the SL. This means that the voltage drops across the heterostructure, and photocurrent is hence generated in that area of the NW. Under negative bias (figure 4.8.(d)), the signal originates from the stem of the NW, below and close to the metal contact. The location and shape of the EBIC signal in this case, points to the stem contact being rather a Schottky contact, which is reasonable since the stem is non-intentionally doped. Photocurrent is hence generated in the depletion region of the Schottky contact, and within a distance corresponding to the carrier diffusion length. Looking at the image, carrier collection is limited to the ≈ 300 nm closer to the contact, and it does not reach the location of the SL. Some additional weak signal components correlate with morphological features in the SEM image, notably with the edge of the metal contacts.

Note that these EBIC maps were taken after STEM observations at 200 kV were made. Contrary to expectations a signal could be detected. This suggests that the effect of the electron beam in the STEM system is not destructive for the device.

The band diagram at zero bias presented in figure 4.8.(b) is rather symmetric with respect to the heterointerface between the GaN stem and the SL. Therefore, it is in contradiction with the significant photoresponse observed at zero bias. A possible explanation of the zero-bias photoresponse is the asymmetry of the contacts, with an Ohmic contact on the cap layer and a Schottky contact on the stem, as demonstrated by the EBIC measurements.

An additional source of asymmetry could be found by analyzing the three-dimensional nature of the NWs considering the surface states and the asymmetry induced by the AlN shell. To study the potential effect of these issues, we performed three-dimensional calculations of the band diagram using the nextnano[3] software, with the results presented in figure 4.9., where (a) is the structure used for the calculation, (b) is a cross-section of the band diagram in the center of the wire viewed along $<1\bar{1}00>$, and figure 4.10.(a) showing the band diagram along the central axis of the wire. The effect of the sidewalls on the potential profile along the NW is studied by comparing calculations obtained with different treatments of the surface states. Thus, figure 4.10.(a) presents the band diagram in the case of

(i) surface states simulated by introducing a negative charge density of 2×10^{12} cm^{-2} at the air/NW side-interface,
(ii) Fermi level pinned in the middle of the bandgap of the AlN shell,
(iii) Fermi level pinned in the middle of the bandgap of the GaN cap, and
(iv) Fermi level pinned 0.6 eV below the conduction band.

In the case of the GaN cap, the doping level is high enough to screen surface effects for the four situations that are considered. For the SL, the potential profile is mostly dominated by the polarization-induced internal electric fields, and the effect of the sidewall surface plays only a secondary role. In contrast, the effect of the sidewalls becomes relevant in the NW stem. There, the axial depletion induced by the presence of the SL extends along around 50 nm (region between 50 and 100 nm in figure 4.10.(a)). Below that (region between 0 and 50 nm) and all along the stem (location < 0 nm, not simulated), the presence of the sidewalls leads to a rearrangement of the free

charges, with the Fermi level getting deep into the bandgap (see red arrow in figure 4.10.(a)). The depth of the Fermi level in the middle of the stem depends on the location of the Fermi level at the sidewalls. Note that the Fermi level pinning 2.1 eV below the conduction band of m-AlN reported by Reddy et al.[251] would lead to a situation halfway between (ii) and (iii). Looking at figure 4.10., this would lead to an asymmetric band profile at zero bias, which would contribute to the zero-bias photoresponse. Indeed, comparing with figure 4.8., we could say that surface states introduce a "bias offset", i.e. at zero bias the bands resemble the positive bias configuration in planar structures (figure 4.8.(c)).

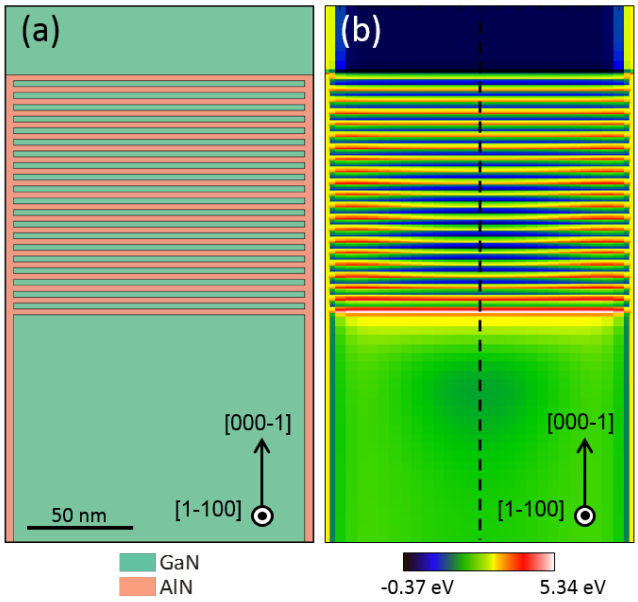

Figure 4.9. Calculation of the band diagram of the NW heterostructure. (a) Schematic structure of the wire. (b) Color-coded cross-section of the conduction band edge viewed along <1–100>, assuming that the Fermi level is pinned in the middle of the AlN bandgap at the NW sidewalls.

To understand the photoresponse of the SL in the 280–330 nm band, we performed one-dimensional and three-dimensional calculations of the electronic levels in the GaN nanodisks, using the nextnano[3] 8-band **k·p** solver. Three dimensional calculations are important to visualize the in-plane separation of the electron and the hole due to the shear component of the strain[264]. Figure 4.10.(c) represents the location of the wave functions of the first electron (e_1) and hole (h_1) levels in a nanodisk located in the center of the GaN/AlN stack (cross-section view along $<1\bar{1}00>$). Even if the wave functions would present a certain overlap along <0001>, their in-plane separation renders the transition extremely improbable. Therefore, the absorption should be associated to higher energy transitions, whose observation is also favored by the higher density of states, and the higher collection probability for the photoexcited electron to contribute to the photocurrent.

A precise calculation of the high energy transitions in three dimensions is difficult due to the high amount of laterally confined levels in GaN nanodisks with such a large diameter, which leads to enormous computation time. However, as excited levels are higher in energy, they also experience a reduced radial confinement, and one-dimensional calculations should provide a reasonable approach. Figure 4.10.(b) presents the confined levels resulting from a one-dimensional simulation. The lower energy transitions are e_1–h_{hh1} = 2.94 eV (= 421 nm) and e_1–h_{hl1} = 2.97 eV (= 418 nm). However, as shown in the following, the interband transition probability is maximum for transitions in the spectral range between 320 nm and 250 nm, which correlates well with the photocurrent enhancement in the 280–330 nm spectral region.

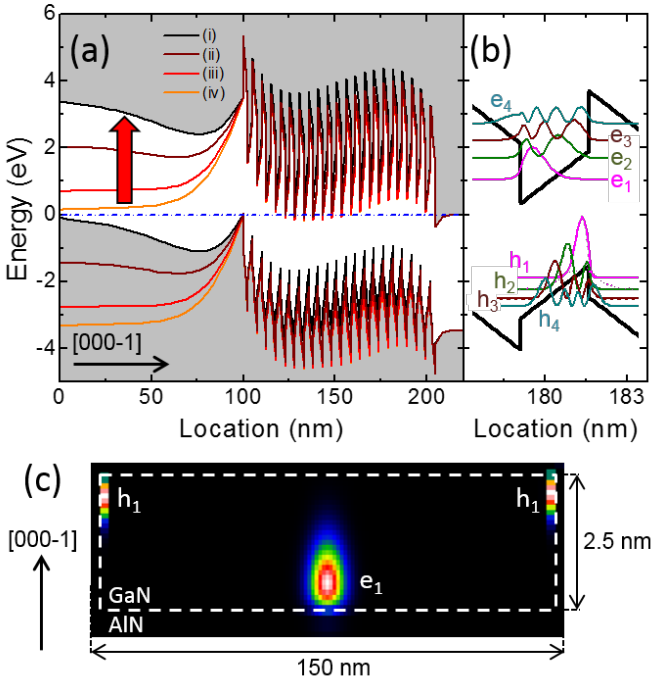

Figure 4.10. (a) Band diagram along the center of the NW (dashed line in (4.9.(b)). The Fermi level is at zero energy (dash-dotted blue line). The red arrow outlines the shift of the Fermi level due to the presence of surface states in the three-dimensional object. Surface states were simulated by assuming: (i) a negative charge density of 2×10¹² cm⁻² at the air/NW side-interface, (ii) Fermi level pinned in the middle of the bandgap of the AlN shell, (iii) Fermi level pinned in the middle of the bandgap of the GaN cap, and (iv) Fermi level pinned 0.6 eV below the conduction band. (b) One-dimensional, zero-bias calculation of the band diagram along <0001> of a nanodisk in the center of the stack, with the squared wave functions of the first, second and third electron and hole levels. (c) Three-dimensional, zero-bias calculation of the location of the first electron and hole levels (e_1, h_1) in a GaN nanodisk. Dashed white lines mark the GaN contour. The disk, located in the center of the stack, is viewed along <1–100>. In this case, the surface is modelled assuming that the Fermi level is pinned in the middle of the AlN bandgap at the NW sidewalls.

The probability of interband transitions in the quantum wells was studied. The photon absorption probability per unit of time, ω_{ij}, from an initial state in the valence band $|i\rangle$ to a final state in the conduction band $|j\rangle$ is given by Fermi's golden rule, $\omega_{ij} \propto \left|\langle\psi_j|e\cdot\hat{p}|\psi_i\rangle\right|^2 = \left|M_{ji}\right|^2$, where e is the unity light polarization vector, $\hat{p}$ is the momentum operator, $\psi_{i,j}$ are the wave functions of the initial and final states, and M_{ji} is the matrix element. Thus, the square of the absolute value of M_{ji} is proportional to the photon absorption probability. Figure 4.11. presents the calculated values of $|M|^2$ for the band-to-band transitions in the quantum well obtained from one-dimensional simulations using the nextnano software. The levels considered in the calculations are the first four electron levels in the conduction band (e_1 to e_4), and the uppermost levels of the valence band that are represented in figure 4.10.(b). Results are depicted as a function of the absorption wavelength associated to the transitions. The squared matrix element is maximum for transitions in the spectral range between 320 nm and 250 nm, which correlates well with the photocurrent spectral response of the SL.

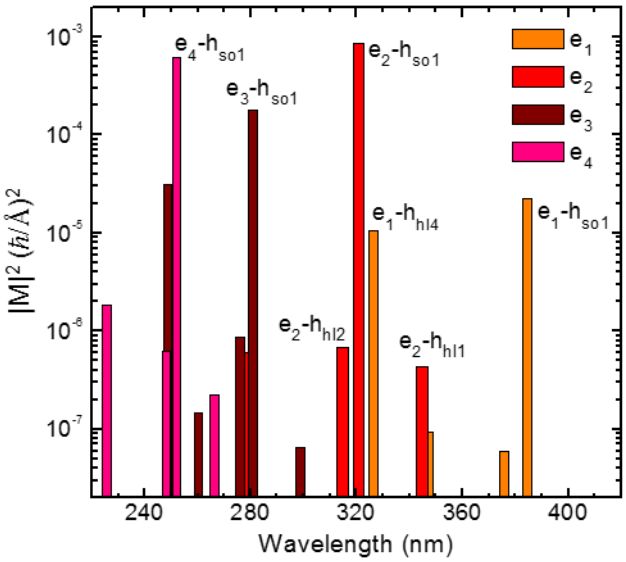

Figure 4.11. Calculated values of $|M|^2$ for the different electron-hole transitions in the quantum wells. Transitions involving different levels of the conduction band (e_1 to e_4) are represented with different colors. The calculations consider heavy holes (h_{hh1} to h_{hh4}), light holes (h_{hl1} to h_{hl4}), and spin-orbit holes (only h_{so1} since h_{so2} is lower in energy than h_{hl4}). Excitonic effects were not taken into account.

For the calculations shown so far, it was conventionally decided to consider a non-intentional doping level of 10^{17} cm^{-3}. However, it is known that the residual doping in the MBE system can vary from run to run. From the typical linewidth of the photoluminescence spectra of our non-intentionally doped GaN NWs (< 1 meV), we can confirm that the residual doping density is well below 10^{18} cm^{-3} (which would correspond to a broadening around 1.5 meV). To assess the effect of this parameter on the potential profile in the NW, we reproduced the three-dimensional calculations leading to figure 4.10.(a) varying the residual doping level in the range of 1×10^{16} to 5×10^{17} cm^{-3}, with the results presented in figure 4.12. Note that the asymmetry of the potential profile is significantly reduced for doping levels beyond 2×10^{17} cm^{-3}. However, these levels of doping have a negligible effect on the potential profile of the nanodisks (see zoomed graphs on the right side of the figure).

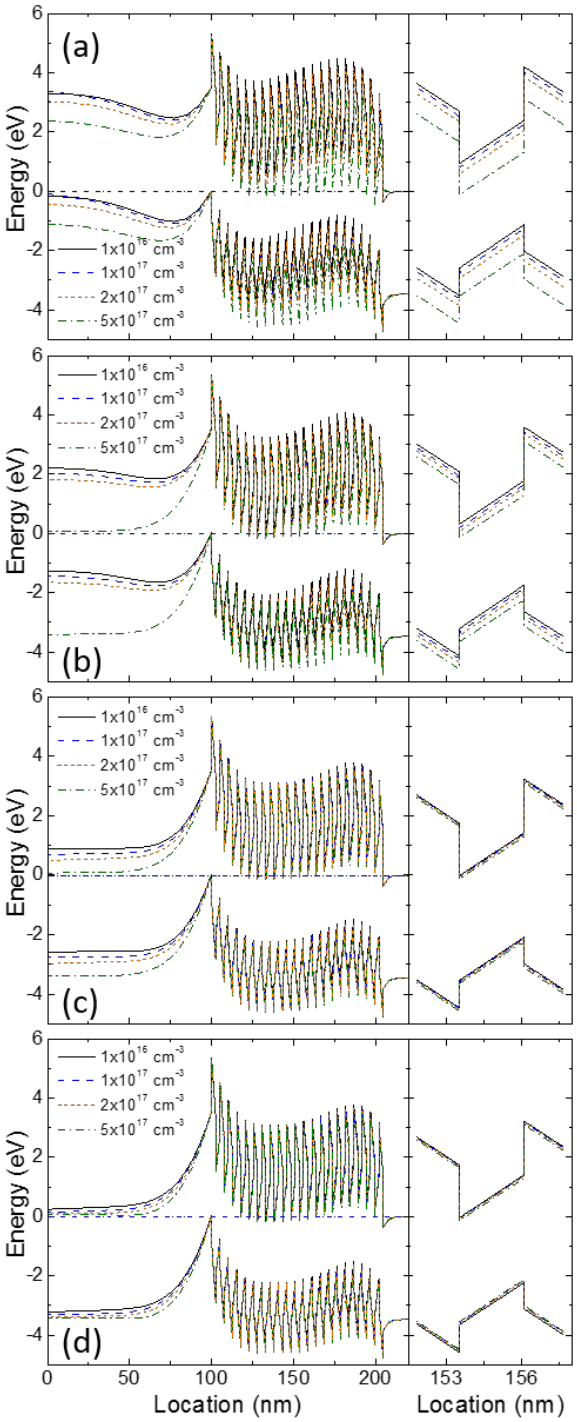

Figure 4.12. Band diagram along the center of the NW obtained from three-dimensional calculations. The Fermi level is at zero energy (horizontal dash-dotted blue line). Surface states were simulated assuming: (a) a negative charge density of 2×10^{12} cm^{-2} at the air/NW side-interface, (b) Fermi level pinned in the middle of the bandgap of the AlN shell, (c) Fermi level pinned in the middle of the bandgap of the GaN cap, and (d) Fermi level pinned 0.6 eV below the conduction band. On the left side, we present a general view of the SL, and on the right side a zoom of one nanodisk in the middle of the SL.

4.6. Conclusions and Prospects

In summary, we performed a study of GaN single NW photodetectors with an embedded SL consisting of 30 periods of GaN/AlN. The stem is undoped, the cap is heavily doped n-type and the SL is undoped. The heterostructure dimensions and doping profile were designed to exploit the advantages associated with the internal electric field generated by the SL. With this architecture, we obtain a significant enhancement of both the response under positive bias and the photovoltaic (zero-bias) response with respect to previous results. Under negative bias, the structure behaves like a GaN metal-semiconductor-metal photodetector, with photocurrent being generated mostly in the GaN stem (in the $\approx 330–360$ nm spectral range). In contrast, under positive bias, the most important potential drop occurs along the SL, and it is hence mostly carriers photogenerated within the SL that are collected (photodetection in the $\approx 280–330$ nm range). EBIC measurements point out that the contact on the NW stem is rectifying, which does not affect the general operation of the device, but partially explains the zero-bias response. Three-dimensional calculations of the band diagram phenomena are investigated to assess the relevance of surface states. From the results, the role of the surface is negligible in the cap and in the SL, but it should induce a partial depletion of the stem. The resulting asymmetry of the potential profile along the NW might contribute to the strong response at zero bias.

5. Linear Photocurrent Dependence on Laser Power in GaN/AlN Nanowire photodetectors

In this chapter a GaN NW structure including an AlN/GaN/AlN insertion is studied in terms of its photodetector capabilities. The activity of the heterostructure is confirmed by the rectifying behavior of the current–voltage characteristics in the dark, as well as by the asymmetry of the photoresponse in magnitude and linearity. Under reverse bias (negative bias on the GaN cap segment), the detectors behave linearly with the impinging optical power when the NW diameter is below a certain threshold (≈80 nm), which corresponds to the total depletion of the NW stem due to the Fermi level pinning at the sidewalls. In the case of NWs that are only partially depleted, their nonlinearity is explained by a nonlinear variation of the diameter of their central conducting channel under illumination.

In this study the device fabrication (dispersion, lithography, metallization…) and electrical characterization were carried out by myself. For some of the measurements and processing steps I was assisted by Jakub Polaczyński, Jonas Lähnemann and Minh Anh Luong. (S)TEM observations were carried out by myself, Martien den Hertog and Dipankar Kalita. The theoretical calculations were done by myself with support from Eva Monroy. The NW sample was grown by plasma-assisted MBE by Akhil Ajay.

The results presented in this chapter were published in Spies et al., Nanotechnology 29, 255204 (2018)[132]*.*

5.1. Motivation and State of the Art

As a reminder, NW photoconductors are characterized by high photocurrent gain, which can reach 10^6, and strong spectral contrast above and below the bandgap. A general disadvantage, however, is the fact that the photocurrent scales sublinearly with the impinging laser power, which was shown for single GaN NWs regardless of the presence of heterostructures[18,80,81,128,265], as also shown in the previous chapter, as well as for NWs of other material systems such as ZnTe[265], ZnO[114,124], InP[266], CuO[123], and GaAs[267]. The sublinearity observed in the photoresponse of NWs hampers the use of such devices for quantification of the radiant fluence, and restricts their application domain to digital detection. The high photocurrent gain and the sublinearity were related to the light-induced reduction of the depletion layer at the NW sidewalls[18,80,114,129,145]. Indeed, the large surface to volume ratio in NWs makes them very sensitive to surface effects (presence of charge traps or Fermi level pinning, which can be modified by adsorbed species). In the case of undoped GaN NWs, Sanford et al. reported an improvement of the linearity in NWs with small diameter (≈ 100 nm), which they attributed to the total depletion of the NWs associated with the axial electric field generated by asymmetric Schottky-like contacts[80].

In the previous chapter, where large diameter (130–150 nm) GaN NWs with and AlN/GaN SL where characterized, we observed that the power dependent photoresponse was non-linear and getting more linear for positive bias to the NW cap. In this chapter, we systematically investigate GaN NW photodetectors with an embedded AlN/GaN/AlN heterostructure, which is responsible for creating an axial electric field within the NW. We demonstrate that for reverse-biased (negative bias on the GaN cap segment) NWs with diameters < 80 nm, the response to ultraviolet illumination is in fact linear, which is consistent with the total depletion of the NW stem due to the Fermi level pinning at the sidewalls. On the contrary, in large NWs (diameter > 80 nm), which are only partially depleted, illumination results in a variation of the lateral electric field and a nonlinear increase of the conducting section in the center of the wires. Therefore, we show here that the depletion of the NW due to surface effects can be beneficial for the photodetector performance since it allows the fabrication of linear devices if the NW heterostructure is properly designed.

5.2. Sample Design and Device Fabrication

The samples under study are GaN NWs incorporating an AlN/GaN/AlN heterostructure. The heterostructure insertion enhances the responsivity at low bias, as a consequence of the internal electric field generated by the large difference in spontaneous and piezoelectric polarization between GaN and AlN. A schematic description of the structure is presented in figure 5.1.(a) The band profile was calculated using the Nextnano^3 8×8 **k·p** self-consistent Schrödinger-Poisson solver[268] using the parameters listed in ref.[221]. The result is illustrated in figure 5.1.(c). The heterostructure consists of two 10-nm-thick AlN insertions, separated by 2.3 nm of GaN. The heterostructure is surrounded by segments of undoped GaN (each 130 nm long), while the ends of the NWs are doped at 8×10^{17} cm^{-3} with Ge to facilitate Ohmic contacts. Therefore, the depletion region induced by the internal electric field is maximized. As self-assembled NWs grow along the [000$\bar{1}$] crystallographic axis[21], the polarization-induced depletion region is located below the heterostructure. In turn, accumulation of free electrons occurs on top of the heterostructure. To avoid the risk of covering the depletion region when depositing the contacts, the wire is asymmetric, with the heterostructure located towards the top of the NW. Under illumination, the depletion region is expected to separate charge carriers, as illustrated in figure 5.1.(c).

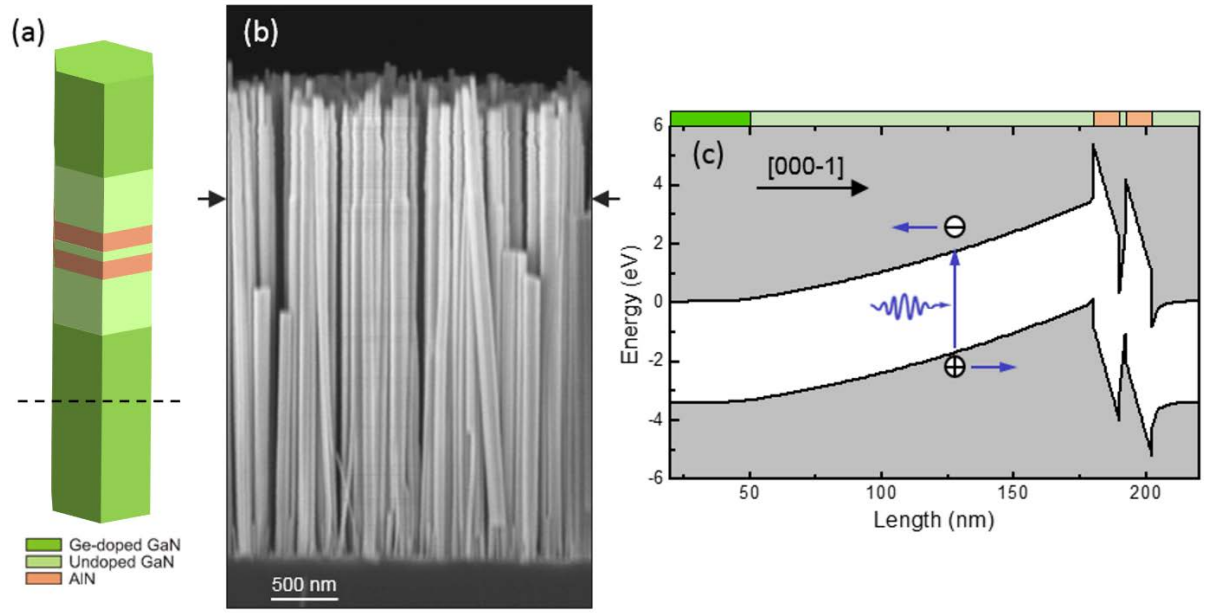

Figure 5.1. (a) Schematic of the NWs under study. (b) SEM image of the as-grown NW ensemble. The position of the insertion can be identified in the top quarter of the NWs as the growth of the strained GaN on the AlN insertion results in a slight reduction of the NW diameter as indicated by the arrows. (c) One-dimensional simulation of the photoactive part of the NW showing the band bending due to the AlN insertions. Electron-hole pairs photogenerated in the space charge region will get separated by the internal electric field, as depicted schematically.

The presence of the GaN/AlN heterostructure favors the collection of photogenerated electrons, but it is an obstacle for hole transport. The field-emission transport through such a barrier should be negligible. However, transport through relatively thick AlN barriers was experimentally observed[269,270], and is explained by the fact that the strong band bending in the heterostructure favors a generation-recombination current that involves holes from the stem and electrons from the cap region. In the case of a single barrier, transport proceeds via interband Zener tunneling[269]. In our case, where two barriers are involved, the states in the intermediate GaN section should play a role as intermediate states in the transport process.

Note that the thickness of the layers in the AlN/GaN/AlN heterostructure is not critical for the photodetector performance, within certain limits. Increasing the size of the AlN barriers would

have the positive impact of decreasing the dark current, but it would lead to problems for the collection of photogenerated holes. Therefore, if a larger heterostructure were desired, it should be implemented as an AlN/GaN multi-quantum-well structure. However, if several periods were added, the heterostructure would start showing its own contribution to the spectral response, particularly when positive bias is applied to the cap. On the other hand, a thinner heterostructure would result in a reduction of the electric field in the stem. This would decrease the extension of the depletion region where the charge carrier separation takes place.

These GaN NWs were synthesized by plasma-assisted molecular beam epitaxy (PAMBE) on Si(111) substrates. The growth rate of the GaN NWs was ≈ 0.11 nm/s and the substrate temperature was T_S = 810°C. Prior to the growth of the NWs, an AlN buffer layer was deposited using the 2-step growth procedure described in ref.[218]. In the sample under study, the NW base consists of a 2.5-μm-long GaN stem doped with Ge ([Ge] = 8×10^{17} cm^{-3}), and a 130-nm-long undoped GaN segment. This was followed by the AlN/GaN/AlN (10 nm/2.3 nm/10 nm) heterostructure and by a 130-nm-thick undoped GaN segment, which is finally capped with a Ge-doped ([Ge] = 8×10^{17} cm^{-3}) GaN segment with a length of about 410 nm. The choice of Ge as n-type dopant was motivated by previous reports indicating that Si has a tendency to migrate to the NW surface[73], whereas Ge incorporates efficiently without deformation of the NW geometry[217,254]. During the growth of the AlN barriers, a thin AlN shell forms around the GaN stem and the AlN/GaN/AlN heterostructure (not indicated in the schematic in figure 5.1.(a)). A scanning electron microscopy (SEM) image of the as-grown NW ensemble can be seen in figure 5.1.(b), where the arrows on the side of the SEM image mark the location of the heterostructure. The NWs exhibit diameters of ≈ 80 nm.

The NWs are subsequently dispersed and contacted as described in sections 3.2.2 and 3.2.3 respectively. An example of a contacted NW can be seen in figure 5.2.(c). In that manner, a large number of NWs were fabricated into devices. The study considers single NWs (figure 5.2.(b)) and coalesced multiple NWs (figure 5.2.(a)).

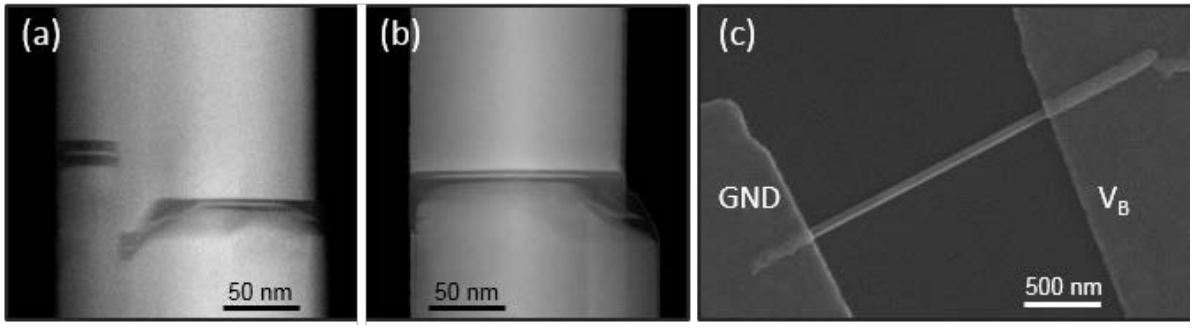

Figure 5.2. (a)-(b) HAADF STEM images of a coalesced and a single NW, respectively. (c) SEM image of a contacted NW.

5.3. Opto-electrical Characterizations

5.3.1. Current-Voltage Characteristics vs. Diameter

A number of NWs were tested for their electrical properties. It was observed that currents larger than 10 μA can thermally detach the NWs from their position, leaving the contact ends deteriorated. An example of this can be seen in figure 5.3.(f). (A significant number of contacted NWs did not withstand the whole range of characterization techniques.) As a result, a safety measure of a 1 μA compliance was introduced. It was possible to group the current-voltage (IV) characteristics of the NWs in the dark into five categories as represented in figure 5.3. The five categories are the following:

- Group I: NWs whose IV characteristic saturates at the compliance for both positive and negative bias, being in the μA range at 1 V; the following NWs display such behavior:
    - M2_B16, M15_A34
- Group II: NWs whose IV characteristic saturates at the positive bias, being in the μA range at 1 V; the following NWs display such behavior:
    - M2_A45, M4_B23, M6_B16, M8_B12, M16_B23
- Group III: NWs whose IV characteristic is seemingly linear, being in the pA range, suggesting the NWs are not contacted or not there (anymore); the following NWs display such behavior:
    - M2_C23, M4_C16, M8_A34, M8_C56, M10_A45, M15_C16, M15_B25
- Group IV: NWs whose IV characteristic is rectifying, being in the nA range at 1 V; the following NWs display such behavior:
    - M12_A45, M10_B23, M4_A45
- Group V: NWs whose IV characteristic is rectifying, being around 1 μA at 1 V; the following NWs display such behavior:
    - M12_B16, M12_C23, M16_A45, E3605_d6_m4_c16

Many NWs were contacted and categorized as indicated above. On all the available NWs, (S)TEM observations were performed with the aim to understand their different behavior. Such measurements allowed a quantification of the NW diameter, barrier thicknesses and total path between the contacts. For the NWs where both (S)TEM observation and IV measurements were possible, a summary is given in Annex A. STEM images of 10 NW bundles (19 NWs) show no correlation of the dark current with the number of NWs that are effectively contacted, or with possible fluctuations in the thickness of the AlN barriers.

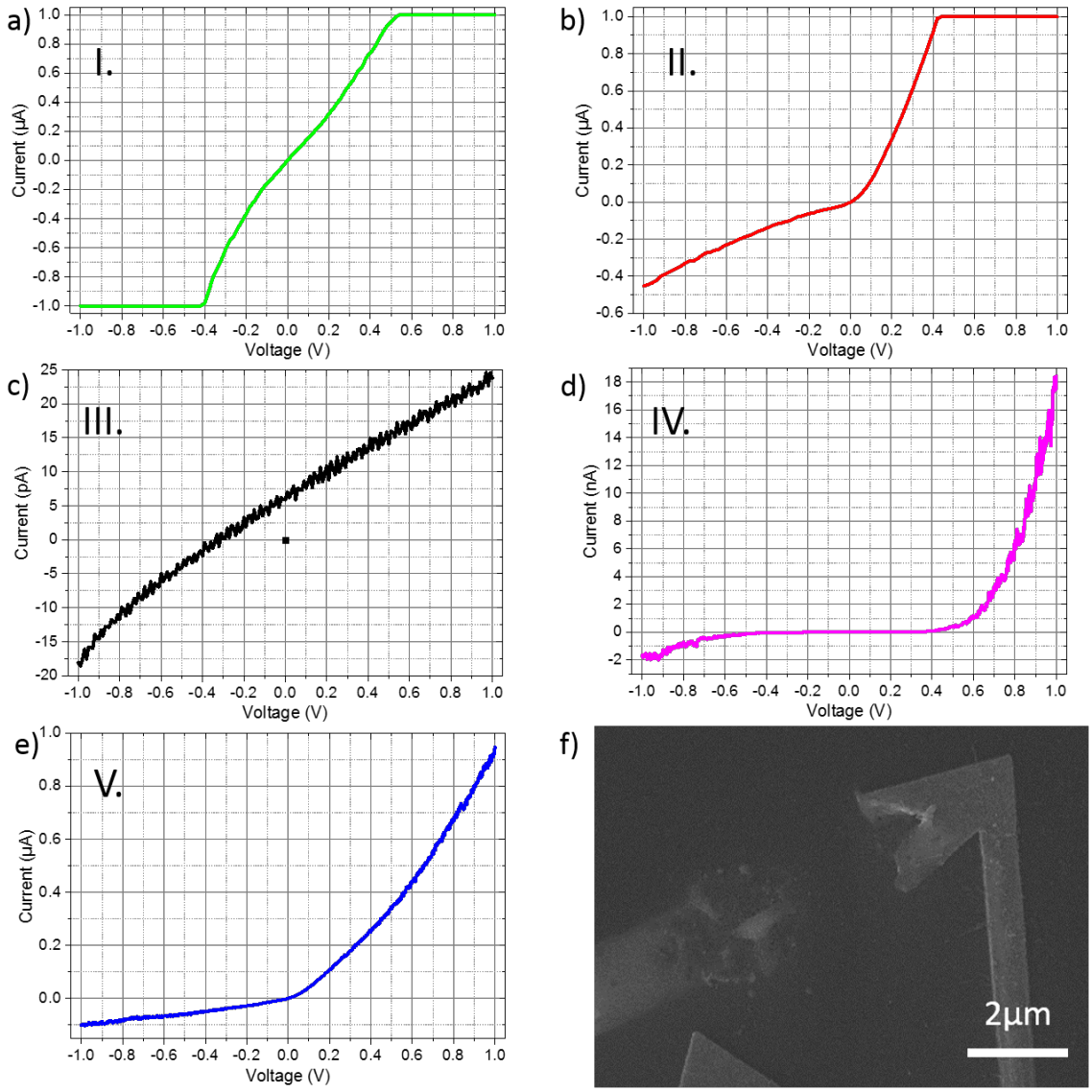

Figure 5.3. (a)-(e) Initial categorization of the NWs according to their IV characteristics in the dark: five categories (I.-V.). (f) SEM image of the location where a NW was contacted: probably due to high currents (>10μA) the NW is gone and the contacts are deteriorated.

However, there is a correlation between the dark current and the NW diameter, as illustrated in figure 5.4.(a). The studied NWs can be divided into two groups: those with dark current in the nA range at +1 V bias (group IV in the initial categorization) – we shall call them group A from here on, and those that display μA-ranged currents at the same bias – we shall call them group B (groups I, II and V in the initial categorization). As shown in figure 5.4.(a), the limit between the two groups is found for a diameter of ≈ 80 nm. The diameter of NW bundles was averaged and is given including an error bar. The NWs for which both IVs and (S)TEM measurements were successfully obtained are indicated.

Figure 5.4.(b) displays typical IV characteristics in the dark for both groups A and B. The asymmetry of the IV curve is explained by the electronic asymmetry presented in figure 5.1.(c), which results from the polarization fields in wurtzite III-nitride heterostructures. The band profile resembles that of a Schottky diode, where the cap layer plays the role of the metal Schottky contact. Consistently, forward bias in figure 5.4. corresponds to a positive voltage being applied to the NW cap with respect to the stem. Following the interpretation for the case of a single AlN insertion[21], the reverse current is associated to a leakage path through the barriers, involving either a GaN shell, surface conduction or the coalescence of multiple wires[128]. Under forward bias,

among the set of NWs under study, we observe a strong dispersion of the dark current, varying from a few nA to µA at +1 V bias.

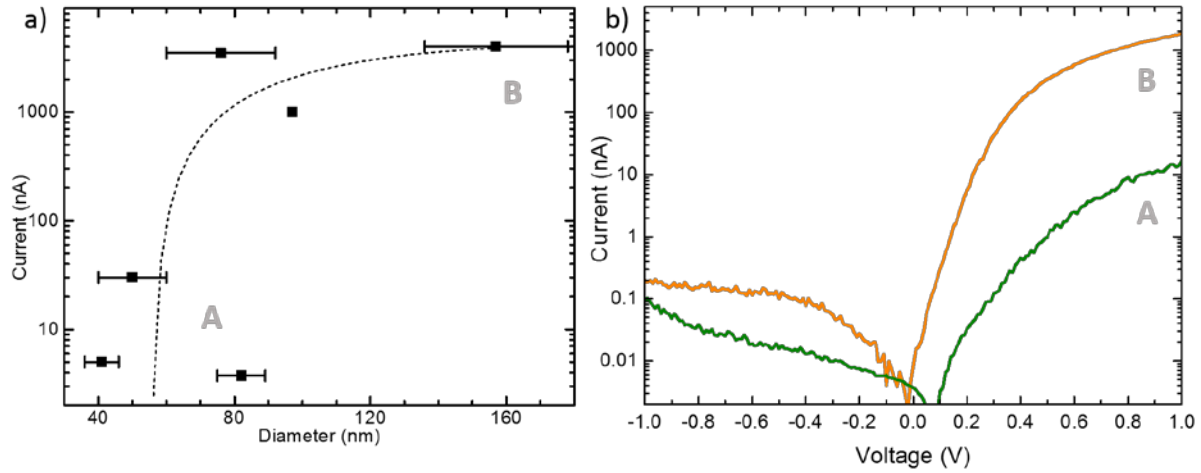

Figure 5.4. (a) Dark current at +1 V bias as a function of the diameter of the NWs measured by STEM in proximity of the AlN/GaN/AlN insertion. The error bars account for the different diameters of NWs in a bundle. The dotted line is a guide to the eye. NWs with diameters <80 nm respond in the nA range (group A), whereas NWs with diameters >80 nm present a dark current in the µA range (group B). (b) IV characteristics of two typical NWs, one with small diameter <80 nm (green) and one with diameter >80 nm (orange).

5.3.2. Photocurrent vs. Dark Current

To further differentiate the behavior of group A and B, measurements under illumination were carried out studying the variation of the photocurrent as a function of the ultraviolet irradiance at 325 nm.

This allowed the following observation:

- Linear photocurrent behavior observed in NWs of group A
- Sublinear photocurrent behavior observed in NWs of group B.

Figures 5.5.(a) and (b) present typical results for specimens in groups A (E3605_M4_A45) and B (E3605_d6_m4_c16), respectively. They were measured at zero and negative bias. Straight lines are fits to $I_{ph} = P_{opt}^{\beta}$, where I_{ph} is the photocurrent, P_{opt} is the impinging optical power and the power law exponent β are fitting parameters. Note that $\beta = 1$ indicates that the photoresponse is linear. In both figures, the photocurrent at zero bias scales sublinearly with the impinging irradiance, which is consistent with previous reports on samples containing GaN/AlN SLs[252]. This behavior differs from the observations in planar photodetectors[111]. Planar photovoltaic devices are systematically linear since the photocurrent is due to the linear generation of electron-hole pairs separated by the internal electric field. The deviation from this trend in the case of NWs reveals the involvement of an additional mechanism such as surface effects in the zero-bias photoresponse.

Under −100 mV bias, NWs groups A and B exhibit different performances. Figure 5.5.(a) displays a linear photocurrent behavior for group A, whereas the photoresponse of group B in figure 5.5.(b) remains sublinear. Additionally, figure 5.5.(a) shows a significant improvement of the linearity for bias voltages as low as −10 mV. Figure 5.6.(a) displays a summary of the values of β (at −100 mV) as a function of the dark current through the NW (at +1 V) for all the NWs in this study. The NWs in group A present $\beta = 1.0 \pm 0.2$, i.e. their photocurrent scales linearly with the optical power within the error bars of the measurement, whereas the NWs in group B clearly show a sublinear behavior, with $\beta = 0.45 \pm 0.11$.

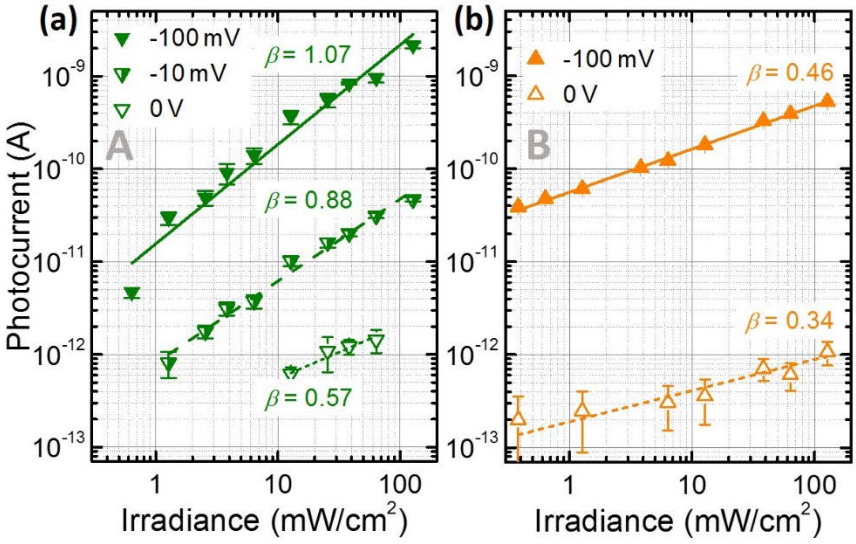

Figure 5.5. Photocurrent measurements as a function of the irradiance (impinging laser power per unit of surface) at 325 nm for (a) a typical group-A NW (diameter <80 nm), and (b) a typical group-B NW (diameter >80 nm). Bias is indicated in the legends. Lines are fits to $I_{ph} = AP_{opt}^{\beta}$, where I_{ph} is the photocurrent, P_{opt} is the impinging optical power and A and β are fitting parameters. The values of β are indicated in the figure.

Note that for the linearity measurements the range of bias voltage applied to the NWs was chosen to keep the maximum photocurrent lower than 10 μA, to prevent device failure. This implies that the maximum applied voltage was in the range of −1 V (lower for some of the specimens). In the devices where a linear behavior is observed (group A), the linearity improves with bias, without any indication of degradation at higher bias.

To verify that the photocurrent induced by ultraviolet illumination stems from the GaN NWs, we recorded the spectral response for both sets of devices. The results are presented in figure 5.6.(b). In both cases (groups A (E3605_M16_A45) and B (E3605_M10_B23)), the absorption exhibits a sharp cutoff around 365 nm, which corresponds well to the bandgap of GaN at room temperature. This experiment confirms that in both cases a potential leakage photocurrent through the silicon substrate is negligible.

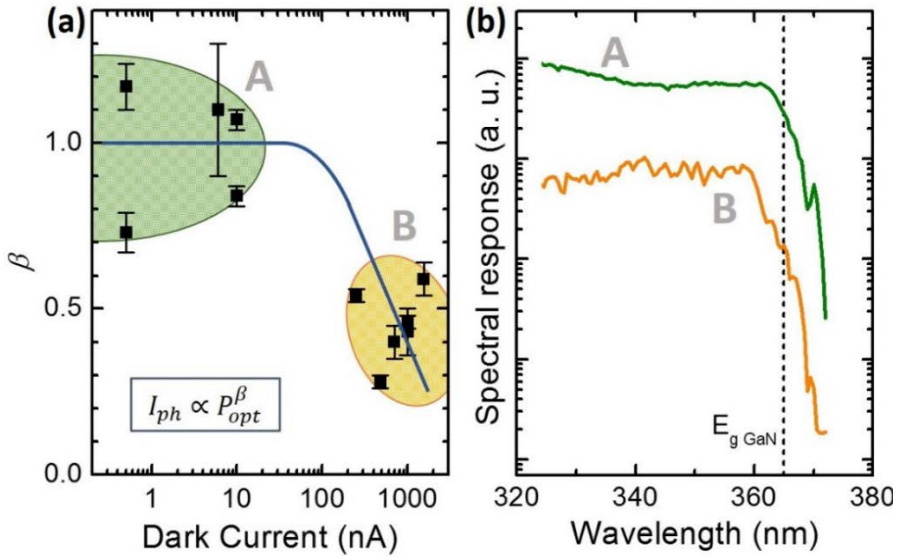

Figure 5.6. (a) Variation of β as a function of the dark current (measured at +1 V). Note, the correlation of almost-linear NWs with dark current in the nA range, and clearly sublinear NWs with dark current in the μA range. The solid line is a guide to the eye. (b) Spectral response measurements for typical group-A and group-B NW specimens. The dashed line marks the wavelength of the GaN bandgap at room temperature.

If we approximate the exposed photodetector area by the in-plane cross-section of the contacted NW (on average, 1.5 μm × 80 nm), we can estimate that the typical responsivity (geometric mean) for an irradiance of 10 mW/cm^2 is around 0.3 A/W at zero bias. (Regarding the calculation of the responsivity, see section 2.4. Photodetectors). At a bias of −100 mV, the typical responsivity, measured under the same conditions and calculated in the same manner, increases to around 20 A/W for NWs in group A, and up to around 700 A/W for NWs in group B. The increase of the responsivity with the NW diameter is consistent with previous reports on GaN NW photodetectors[79,80].

To confirm the role of the heterostructure in the responsivity of the NWs, we compared the photocurrent under forward and reverse bias. Under reverse bias, the response is expected to be dominated by the presence of the space charge region, which separates photogenerated electrons and holes. The response is hence expected to resemble that of a Schottky diode (low dark current and linear response with the optical power)[271]. In contrast, under forward bias, the space charge region disappears and the NW resembles a photoresistor (high dark current and sublinear response)[271]. Figure 5.7. represents the variation of the photocurrent as a function of the ultraviolet irradiance in a specimen from group A (E3605_d4_m8_c45) measured at +1 V and −1 V bias. As expected, the photoresponse scales linearly with the irradiance under reverse bias (β = 0.96±0.06) only, whereas forward bias results in a strongly sublinear behavior (β = 0.61±0.05). This asymmetric behavior is a confirmation of the role of the AlN/GaN/AlN heterostructure in the photoresponse.

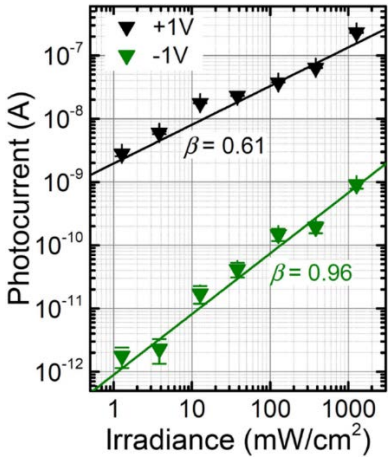

Figure 5.7. Photocurrent measurements as a function of the irradiance at 325 nm for a typical group-A NW measured under forward and reverse bias.

5.4. Time Response and Chopping Frequency

Finally, we assessed the effect of the limited response time of the photodetectors on our measurements. The measurements reported above were recorded using a synchronous detection setup where the light is chopped at a frequency of 33 Hz. In the case of planar structures, it is known that the chopping frequency has dramatic effects on the linearity and spectral response of photoconductors[111,271], whereas Schottky photodiodes are relatively insensitive to the chopping frequency in the typical experimental range (1−1000 Hz). However, in the case of single GaN NWs, we reported that the spectral response does not vary as a function of the chopping frequency[18]. To validate the results of this chapter, we verified that the value of the β exponent as a function of the irradiance is insensitive to the chopping frequency.

The time response of the photodetectors was verified by measuring the photocurrent under chopped illumination with a HeCd laser, with the biased NW connected to an oscilloscope. An example of the resulting signal is presented in figure 5.8.(a). The photocurrent decay exhibits

a fast component with a time constant in the hundreds of μs range, and a slow component with a time constant in the hundreds of ms range. These results are the same for NWs of groups A and B. As a result, increasing the chopping frequency from 3 Hz to 1 kHz results in a decrease of the photocurrent by roughly one order of magnitude (see figure 5.8.(b)). This behavior is independent of bias, being observed at positive and negative bias, and even at zero bias. The result presented in figure 5.8.(b) was recorded at relatively low bias (0 to 10 mV) with a relatively high irradiance (1.3 W/cm^2). Similar attenuation of the response with the chopping frequency is observed at higher bias (1 V) or under much lower irradiance (1.3 mW/cm^2), which suggest that the slow photocurrent component is not associated to a thermal process (neither bias-related nor photo-induced).

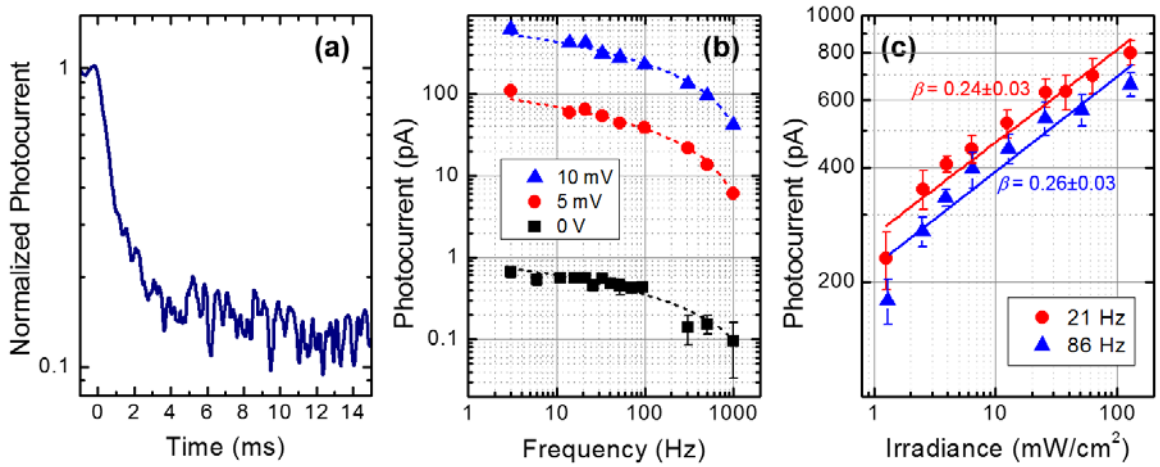

Figure 5.8. (a) Typical decay time of the photocurrent measured in a single NW photodetector at 1 V bias, 3 Hz chopping frequency, and illumination by 3 W/cm² of a HeCd laser (325 nm). (b) Variation of the photocurrent as a function of the chopping frequency measured in a single NW photodetector biased at 0 V, 5 mV and 10 mV, and illumination by 1.3 W/cm² of a HeCd laser (325 nm). (c) Photocurrent of a group B NW as a function of the impinging irradiance (325 nm) measured at different chopping frequencies (21 Hz, 86 Hz). Measurements were performed at 10 mV bias.

To validate the results reported above, we verified that the value of the β exponent of the detectors does not depend on the chopping frequency. Figure 5.8.(c) illustrates the measurement of the photocurrent as a function of the ultraviolet irradiance measured at two different frequencies (21 Hz and 86 Hz). In spite of the decrease of the photoresponse for the higher chopping frequency, the variation of the signal with irradiance remains unchanged within the error bars associated to the measurement.

5.5. Band Profile Simulations

The drastic reduction of the dark current in NWs with a diameter below ≈ 80 nm was observed previously in GaN NWs[79], and it was explained by the presence of a space charge layer extending inwards from the NW sidewalls. In the report by Calarco et al.[79], total depletion of the GaN NWs was obtained for a diameter of 85 nm, when the residual doping level was 6.25×10^{17} cm^{-3}. To confirm that our result is consistent for the doping level in the NWs under study, three-dimensional calculations of the band diagram were carried out. Different diameters, namely 50, 60, 80 and 120 nm, were considered. The results of the simulations are summarized in figure 5.9.(a), which displays the cross-sectional view of the conduction band structure in the doped stem region extracted 200 nm below the first GaN/AlN heterointerface [see dashed line in figure 5.1.(a)]. We note that for NWs with a diameter of 60 nm, the space charge regions extending from opposite sidewalls touch each other, and the location of the conduction band edge in the center of the NW increases by about 100 meV when decreasing the NW diameter from 80 to 50 nm. This confirms the full depletion of the thin NWs and justifies the drastic drop in the dark current.

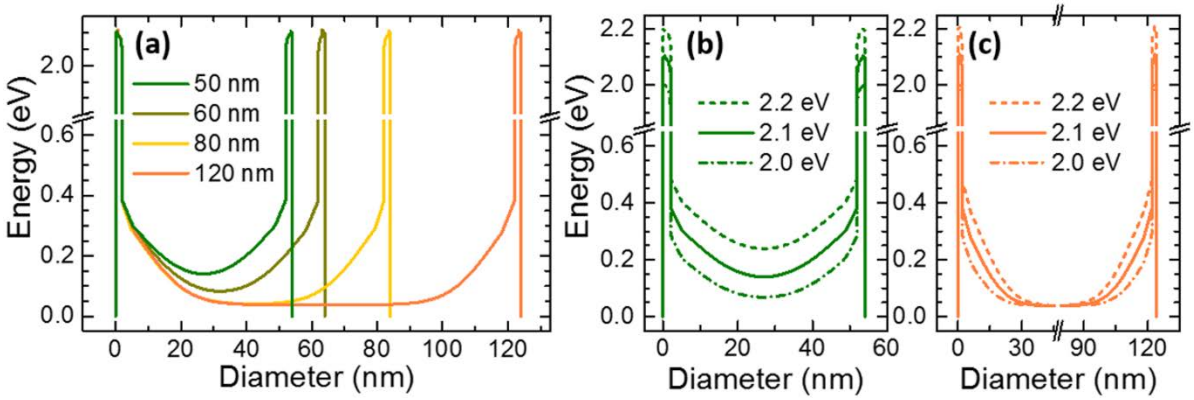

Figure 5.9. Cross-sectional view of the band structure in the doped stem region of the NW, 200 nm below the undoped region (a) for NW diameters of 50, 60, 80, 120 nm, with the Fermi level pinned 2.1 eV below the conduction band edge of AlN. With decreasing diameter, the difference in energy between Fermi level and the lowest point in the conduction band increases from 38 meV to 140 meV. In (b) and (c), the Fermi level pinning is varied between 2.0, 2.1 and 2.2 eV for NWs with diameters of 50 nm and 120 nm, respectively.

Ultraviolet illumination is known to unpin the Fermi level at the NW sidewalls. This phenomenon was experimentally studied by Pfüller et al.[130], and it was attributed to photoinduced desorption of oxygen from the NW sidewalls. Therefore, to simulate the effect of ultraviolet illumination, we analyzed the consequences of changing the position of the Fermi level at the surface in the range of 2.0 eV to 2.2 eV below the conduction band edge of the AlN shell. This is a reasonable assumption of the the position of the Fermi level, as discussed in chapter 4. For the simulations the assumed doping level for the non-intentionally doped sections is 1×10^{17} cm^{-3}, which corresponds approximately to the residual doping of our growth system in the case of N-polar GaN. Simulations assuming residual doping at 1×10^{16}, 3×10^{16}, 1×10^{18} and 3×10^{18} cm^{-3} were carried out for comparison, without relevant differences in the result. Taking a look at the simulations of a NW with a diameter of 50 nm (group A) [figure 5.9.(b)] we observe that changes to the Fermi level pinning shift the radial position of the conduction band as a whole across the NW, but the shape of the potential profile is not modified. In other words, the component of the electric field along the NW diameter seen by photogenerated electrons is approximately the same in all cases, with its maximum value at the GaN/ AlN interface being 210 kV/cm ± 3%. In a NW with diameter of 120 nm (group B) [figure 5.9.(c)] we note a different behavior. When the location of the Fermi level pinning changes from 2.2 eV to 2.0 eV below the conduction band edge of the AlN shell, the maximum radial electric field varies from 360 kV/cm to 240 kV/cm (by more than 30%). At the same time, the space charge region at the sidewalls of the NW shrinks, increasing the extent of the central conducting channel in the NW. Therefore, in thick NWs (group B), light induces not only a linear increase in the carrier concentration, but also a nonlinear variation in the diameter of the conducting channel that such carriers have to cross to be collected.

This explains also the enhancement of the responsivity with the NW diameter. The responsivity is linked to the total number of photogenerated carriers, i.e. it should increase with the square of the NW radius. To this dependence, we have to add the variation of the conductivity due to the change in the diameter of the central conducting channel in the stem. Both phenomena are relatively independent. In small and thus fully depleted NWs, the variation of the responsivity with the diameter will be given by the change in the total amount of photogenerated carriers. In large and thus partially-depleted wires, it is the modulation of the conductive section that dominates, which can lead to huge photocurrent gains. A theoretical analysis of both contributions can be found in ref.[144].

5.6. Conclusions and Prospects

We demonstrated single NW ultraviolet photodetectors consisting of a GaN NW with an embedded AlN/GaN/AlN heterostructure, which generates an electric field along the NW axis as

a result of the difference in polarization between III-nitride compounds with wurtzite crystal structure. The influence of the heterostructure is confirmed by the rectifying behavior of the current-voltage characteristics in the dark, and by the asymmetry of the photoresponse in magnitude and linearity. Under reverse bias (negative bias on the cap segment), the detectors behave linearly with the impinging optical power when the NW diameter remains below a certain threshold (≈ 80 nm). This is explained by the linearity of the photogeneration process, the separation of photogenerated carriers induced by the axial electric field, and the fact that illumination does not have a significant effect on the radial electric field. In the case of NWs that are not fully depleted (diameter > 80 nm), the light-induced change in the Fermi level at the sidewalls results in a variation of the diameter of the central conducting channel in the stem, which leads to an overall nonlinear photoresponse.

In this study, linearity is observed for NWs with a diameter smaller than ≈ 80 nm. For larger NWs, there are two approaches to improve the linearity, namely obtaining a full depletion of the NWs or rendering the band bending at the sidewalls insensitive to light. Full depletion of larger NWs can be achieved by reducing the doping level. Reducing the sensitivity of the band bending to light is more challenging. The use of a thicker AlN shell might help, but there is a risk of generating structural defects due to the lattice mismatch between m-plane AlN and GaN. Alternatively, the use of dielectrics as passivation layer should be explored.

The results presented in chapters 4 and 5 indicate interesting possibilities for NW photodetectors. In chapter 4 we showed a bias dependent preferential absorption using NWs with a GaN/AlN SL. In this case the power dependent photocurrent became more linear with forward bias (associated with absorption in the SL). On the other hand, in chapter 5, we demonstrated that NWs with a single insertion present linear photocurrent characteristics in reverse bias and for small NW diameters, due to the complete depletion of these thin NWs. It may well be possible that linear and spectrally sensitive NW photodetectors are possible both in reverse and forward bias using a GaN/AlN SL in combination with small NW diameters.

Furthermore, the beam damage induced on the NW samples by SEM and (S)TEM observation should be studied and quantified systematically. Deposition of carbon[272] could be a starting point.

6. Electrically tunable Quantum Dot Emissions

In this chapter, a GaN NW structure including an AlN/GaN/AlN quantum dot (QD) insertion is used in order to study the variation of the GaN QD emission as a function of the applied external bias. A shift of the peak wavelength of 11.9 to 25.1 meV per applied Volt is achieved. With increasing applied bias, an evolution of the recombining exciton to different charged states can be observed. The emission intensity scales superlinearly with the impinging optical power, suggesting a saturation of traps, probably point defects in the vicinity of the QD.

In this study, the device fabrication (dispersion, lithography, metallization…) and electrical characterization as well as micro-photoluminescence measurements were carried out by myself. (S)TEM observations were carried out by Martien den Hertog. The theoretical calculations were done by myself with support from Eva Monroy. The NW sample was grown by plasma-assisted MBE by Akhil Ajay.

6.1. Motivation

There is a demand for single photon sources for quantum information technologies[273] which are under development and which open up immense yet unseen possibilities of data treatment. Single photon sources can be implemented using two-level emitters such as a semiconductor quantum dot (QD). However, QDs synthesized following the Stranski-Krastanov (SK) method[274–276] present strong spectral diffusion effects due to point defects in the AlN matrix. Moreover, the location and the density of the QDs is not controlled. The synthesis of single QDs as axial insertions in GaN NWs is regarded as a solution, with the additional advantage of a larger adjustable QD size that can be synthesized without structural defects, thanks to the elastic strain relaxation in these three-dimensional structures. GaN QDs in NWs have demonstrated their capability as single photon emitters at room temperature[17,277], thanks to the large band offsets between GaN and AlN. These nano-objects could set the basis for the introduction of III-nitrides in the domain of quantum technologies

The motivation for this project is to perform a correlated multi-technique study of the same QD under applied external bias in order to get a better understanding of these nano-objects.

GaN/AlN QD emission tuned by application of an external electric field has first been shown by Nakaoka et al in 2006[278]. The dots were self-assembled, grown in the SK method and embedded in 2D layers. They emit at 3.65 eV (≈340 nm). A blueshift of the emission of up to 100 meV was observed with a shift of 5.5 meV per applied Volt of external bias (in the range of −4 V to +14 V). As expected by theory, applying an electric field in the direction of the built-in electric field leads to a redshift in the emission. Likewise applying an external electric field against the built-in electric field compensates the internal electric field, leading to a blueshift of the QD emission. Both cases are illustrated schematically in figure 6.1.

Müßener et al.[26] were the first in 2014 to demonstrate an electrically tuned DQ emission in a single NW of the III-nitride system. Their design of a GaN QD includes an AlGaN/GaN/AlGaN insertion sandwiched by AlN current blocking layers. The emission of the GaN QD at 3.56 eV (≈348 nm) could be shown to shift by 1.3 meV/V[26] (in the range of −10 V to +20 V). An internal electric field strength within the QD of 1.5 MV/cm was calculated. The same group studied a SL structure including multiple GaN QD[279] in a NW observing direct transitions within the QD and indirect transitions to neighboring QDs.

The idea of this project is to improve the sensitivity of the emission to the external bias by employing only AlN barriers, which immediately sandwich the GaN QD. Thus, the total thickness of the heterostructure is significantly reduced. The interfaces with AlN should be sharper than in the case of AlGaN barriers and the band offset is larger, leading to a better confinement.

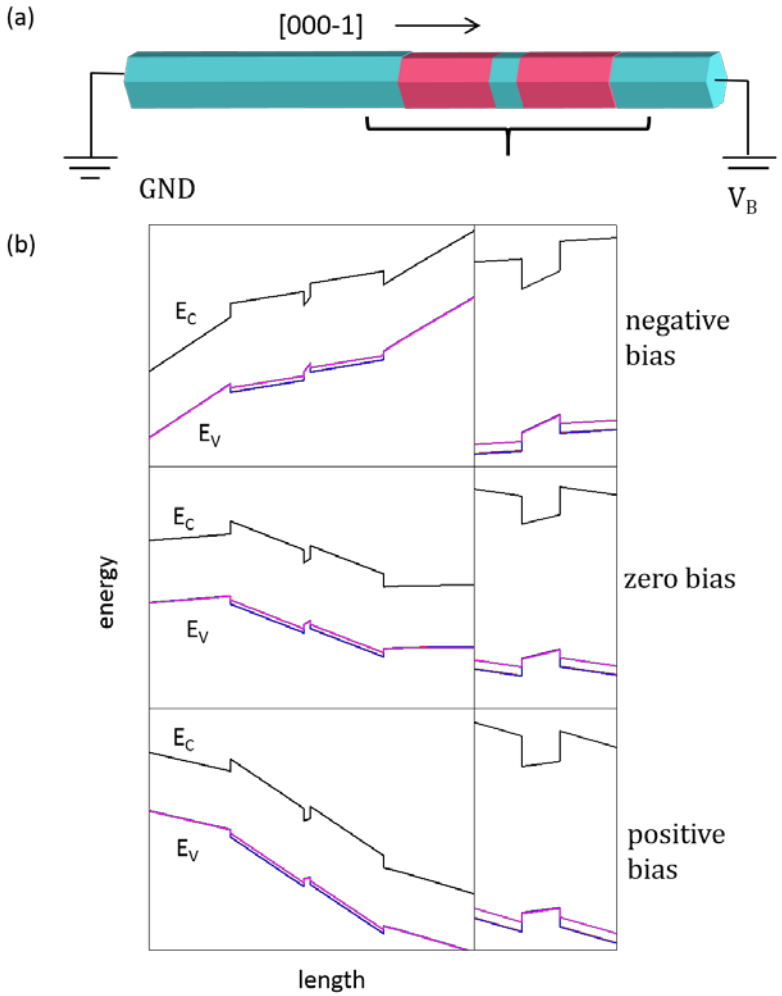

Figure 6.1. (a) Simplified schematic of the NW structure indicating the AlN/GaN/AlN insertion which is indicated by the bracket. The application of bias is indicated: the NW stem is grounded and the bias is applied to the top. (b) 1D nextnano³ simulations of the electric band structure of the NW under bias applied to the cap. On the left: the area around the AlN/GaN/AlN insertion. On the right: in the QD. Applying negative (positive) bias leads to an enhancement (compensation) of the internal electric field within the QD leading to a red (blue) shift of the emission.

6.2. Sample Design and Fabrication

The samples under study in this chapter are GaN NWs incorporating an AlN/GaN/AlN heterostructure. The heterostructure consists of two 10-nm-thick AlN insertions, separated by nominally 0.8 nm of GaN. The heterostructure is surrounded by segments of undoped GaN (each 130 nm long), while the ends of the NWs are doped at 8×10^{17} cm^{-3} with Ge to facilitate Ohmic contacts. As usual, these self-assembled NWs grow along the [000$\bar{1}$] crystallographic axis[21]. A schematic of such a NW can be seen in figure 6.2.(a). An example of a STEM micrograph of a contacted single NW (here NW A) is shown in figure 6.2.(b) where the red square indicates the heterostructure.

The QD size is designed with the aim that their emission is energetically higher than the bulk emission value in order to unambiguously distinguish the QD emission from luminescence involving dopants or defects. 1D nextnano³ simulations of band to band transition energy vs. QD thickness were carried out. They are depicted in figure 6.3. The energetic transition is calculated taking into account the two extreme cases where the lattice of the GaN QD either has the in-plane lattice parameter of GaN (GaN strained) or the in-plane lattice parameter of AlN (AlN strained). An increase of QD height results in a shift to lower energy of the emission. Note that the smallest QD size modeled is 0.5 nm, which corresponds to two monolayers.

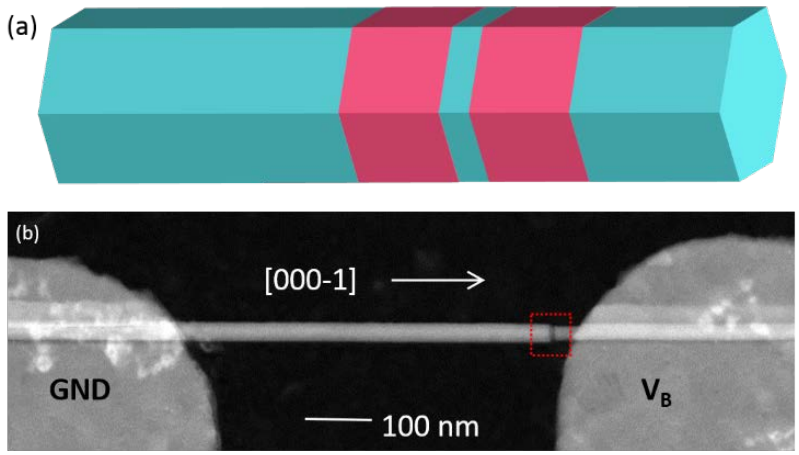

Figure 6.2. (a) Schematic of the NW under study (turquoise: GaN, pink: AlN). (b) HAADF-STEM image of contacted single NW A. The AlN/GaN/AlN insertion is indicated by the red square. In the following the NW stem will be grounded and the cap biased.

We chose to refer to this structure as a QD since 3D confinement as well as nm-sized dimensions are present. Even though lateral confinement is low, the level to level energy separation is larger than kT at 4K (which is ~0.3 meV). Furthermore, a similar structure was tested by Renard et al.[22] demonstrating single photon emission behavior so that this heterostructure behaves as a two-level emitter at low temperature and can thus be considered as a QD.

The GaN NWs analyzed in this chapter were synthesized by plasma-assisted molecular beam epitaxy (PAMBE) on Si(111) substrates. The growth rate of the GaN NWs was ≈ 0.11 nm/s and the substrate temperature was T_S = 810°C. Prior to the growth of the NWs, an AlN buffer layer was deposited using the 2-step growth procedure described in ref.[218]. In the sample under study, the NW base consists of a 2.5-µm-long GaN stem doped with Ge ([Ge] = 8×10^{17} cm^{-3}), and a 130-nm-long undoped GaN segment. This was followed by the AlN/GaN/AlN (10 nm/0.8 nm/10 nm) heterostructure and by a 130-nm-thick undoped GaN segment, which is finally capped with a Ge-doped ([Ge] = 8×10^{17} cm^{-3}) GaN segment with a length of about 410 nm. The choice of Ge as n-type dopant was motivated by previous reports indicating that Si has a tendency to migrate to the NW surface[73], whereas Ge incorporates efficiently without deformation of the NW geometry[217,254]. No formation of an AlN shell was observed in the following. The NWs exhibit diameters of ≈ 60 nm.

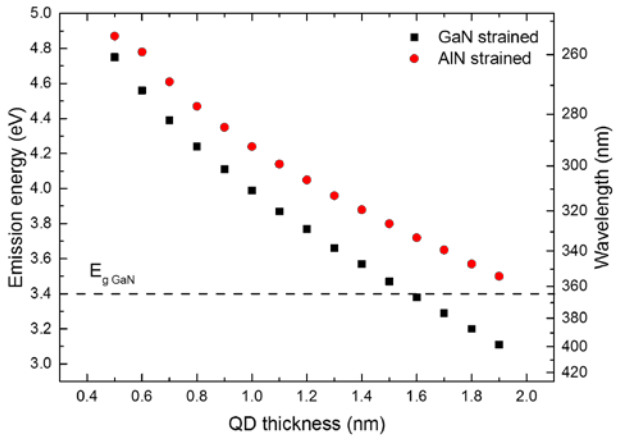

Figure 6.3. Simulated emission wavelengths of a GaN QD surrounded by AlN barriers at 5K for varying QD heights done by 1D nextnano³ simulations. Note that 1 nm corresponds to 4 atomic layers. The bandgap E_{gGaN} of 3.4 eV (~364 nm) at 300 K is indicated. The cases of strained GaN and strained AlN are considered.

The NWs are subsequently dispersed and single NWs are contacted as described in section 3.2.7. The study below considers only single NWs. Results on coalesced NW bundles are given in Annex C.

6.3. Luminescence of the Quantum Dot Structure

The spectrum obtained by μPL of a single dispersed NW (NW A) showing emission lines from the AlN/GaN/AlN QD and the bulk GaN of the stem and cap regions is presented in figure 6.4. The luminescence from contacted NWs shows emission lines in the spectral region from 283 nm to 321 nm, depending on the QD size.

It was observed that the highest number of counts for the emission from the QD peak could be obtained by aligning the piezo controlled stage of the cryostat in a way that maximizes the photocurrent (under illumination and while applying a bias voltage that yields a current of >1 nA). Furthermore, it was useful to mount a filter (300/80 nm BrightLine single-bandpass filter, FF01-300/80-25, transmitting at 260–340nm) that drastically diminishes the GaN bulk emission in order to focus on the QD emission. The linewidth was determined to be around 1 nm or 15 meV for the emission of the QD.

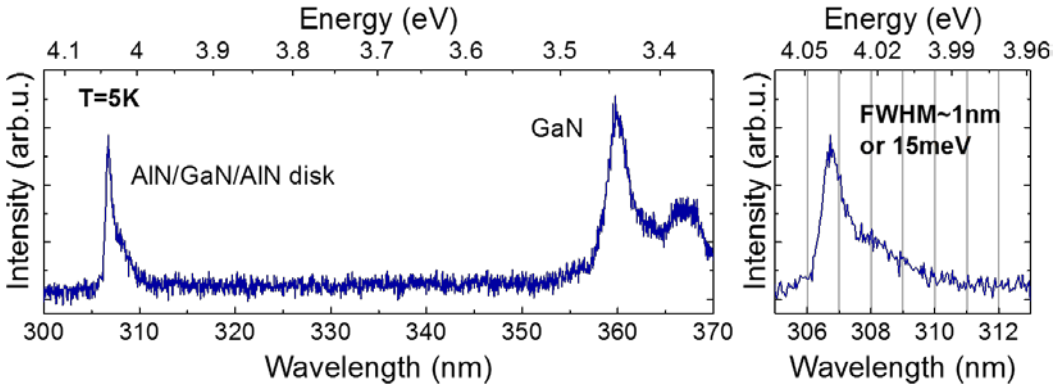

Figure 6.4.(a) Full recorded μPL spectrum of NW A showing the band to band transitions assigned to the GaN stem and cap regions of the NW as well as to the the AlN/GaN/AlN insertion. (b) μPL spectrum of the QD emission with an indicated FWHM of 1 nm or 15 meV.

The studied NWs are summarized in table 6.1. Results from NW A will be discussed in detail. NWs B and C are shown to confirm reproducibility and raise further questions. NW D is a complicated systems of several NWs contacted in parallel and is given in Annex C for completeness for the interested reader. The original sample number, a letter abbreviation for the reader, the nickname obtained during measurements in parenthesis, the number of observed QDs in the NWs and the rate of shifting are indicated in the table.

NW name	Abbreviation	#QDs	rate
E3795_d3_m5_c45	A (the one)	1	11.9 meV/V
E3795_d5_m15_c45	B (the mysterious)	*	25.1 meV/V
E3795_d5_m11_c23	C (the plain)	*	19.9 meV/V
E3795_d3_m12_c45	D (the double)	4	

Table 6.1. Overview of the presented NWs including the original sample number, a letter abbreviation for the reader, the nickname obtained during measurements in parenthesis, the number of observed QDs in the NWs and the rate of shifting. The number of QDs in samples B and C has not yet been determined by (S)TEM, and it is therefore indicated by an asterisk.

6.4. Structural characterization and simulation

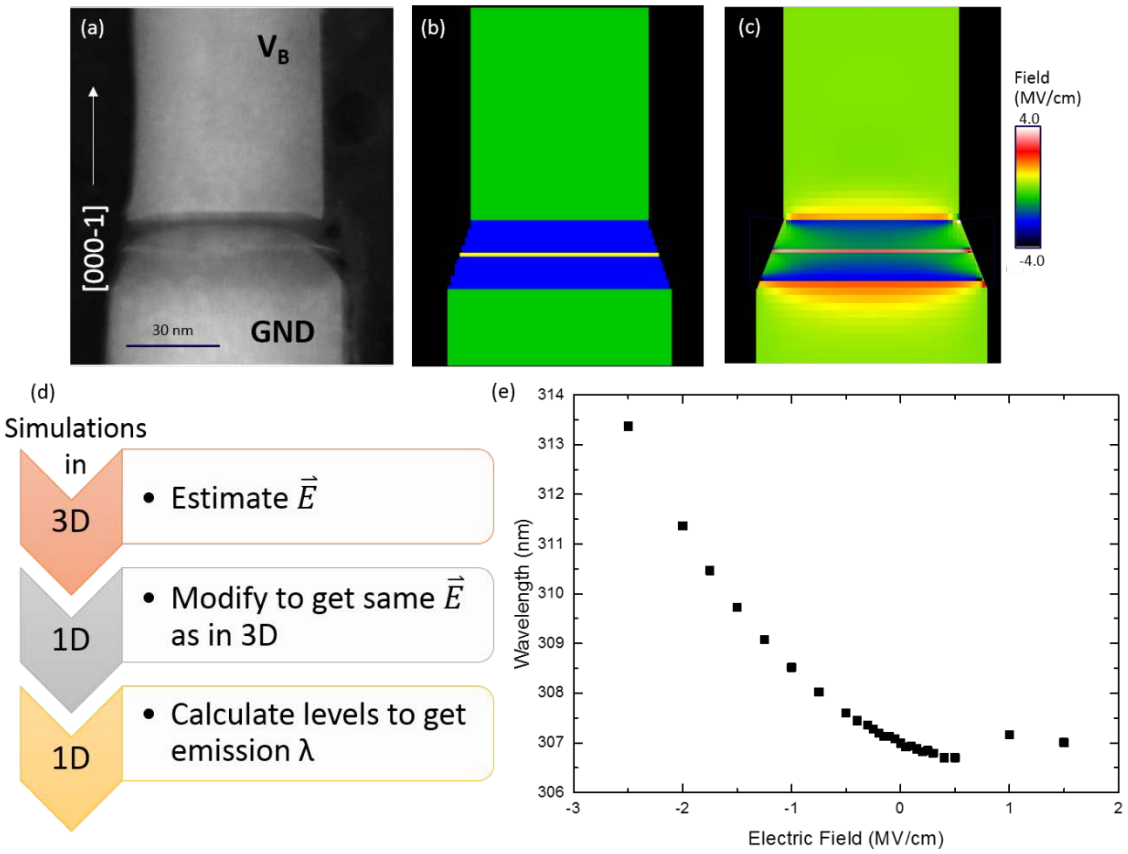

Figure 6.5. (a) High magnification HAADF-STEM micrograph of the insertion section of NW A. (b) Material parameter definition of the three dimensional calculations (green and yellow = GaN, blue = $Al_{0.5}Ga_{0.5}N$, black = air). (c) Component of the electric field along the NW growth axis for the structure of NW A, showing that the expected electric field in the GaN QD is 3 MV/cm assuming $Al_{0.5}Ga_{0.5}N$. (d) Flow chart of the simulation processes. $\vec{E}$ corresponds to the internal electric field in the QD. (e) Simulated emission values of the QD vs. the applied electric field across the QD.

Structural characterization was done by HAADF STEM observation. A micrograph of the insertion region of NW A is given in figure 6.5.(a), which corresponds to the area within the red square in figure 6.2. A strain induced narrowing of the NW diameter after the growth of the insertion region can be observed, and the structural dimensions of the NW and the insertion can be extracted from the image. The QD height is estimated to be 0.8 nm. An interesting observation is that the bottom barrier has a large dome-shaped diffusion region of AlGaN that extends up to the QD and into the second barrier.

In order to simulate the strain in the QD as well as the emission energy and the electric field across the QD, 3D and 1D nextnano[3] simulations were carried out. A flowchart of this process is given in figure 6.5.(d). The starting point are the 3D simulations. The modeled structure is given in figure 6.5.(b). The narrowing of the NW structure is taken into account. Following the results of STEM characterization, the barriers are assumed to be $Al_{0.5}Ga_{0.5}N$ and the QD is assumed to be 0.8 nm high. The electric field distribution taking into account the beforehand calculated strain distribution is depicted in figure 6.5.(c). The electric field across the QD is around 3 MV/cm. This result is further used to approximate the emission wavelength with the help of 1D simulations. The estimated electric field obtained in 3D simulations, given in 6.5.(c), is used as an input for the 1D simulations. The confined electron levels of the structure are then calculated for the QD under externally applied electric field in figure 6.5.(e). Applying an external electric bias, we expect a

blue shift of the emission wavelength with bias, creating an electric field against the built in electric field of the polarized structure.

6.5. Electrical tuning of Quantum Dot Emissions in single Nanowires

In-situ μPL spectra were recorded for varying external bias. The spectra of NW A for bias from −4 V to +4 V are given in figure 6.6. The spectrum acquired at zero bias is indicated in black. A single emission peak can be seen for negative applied bias. It blue shifts with increasingly compensated internal electric field. This behavior is expected as the compensation of the electric field leads to a flattening in the bands and the recombination takes place between bands of higher energetic difference than before.

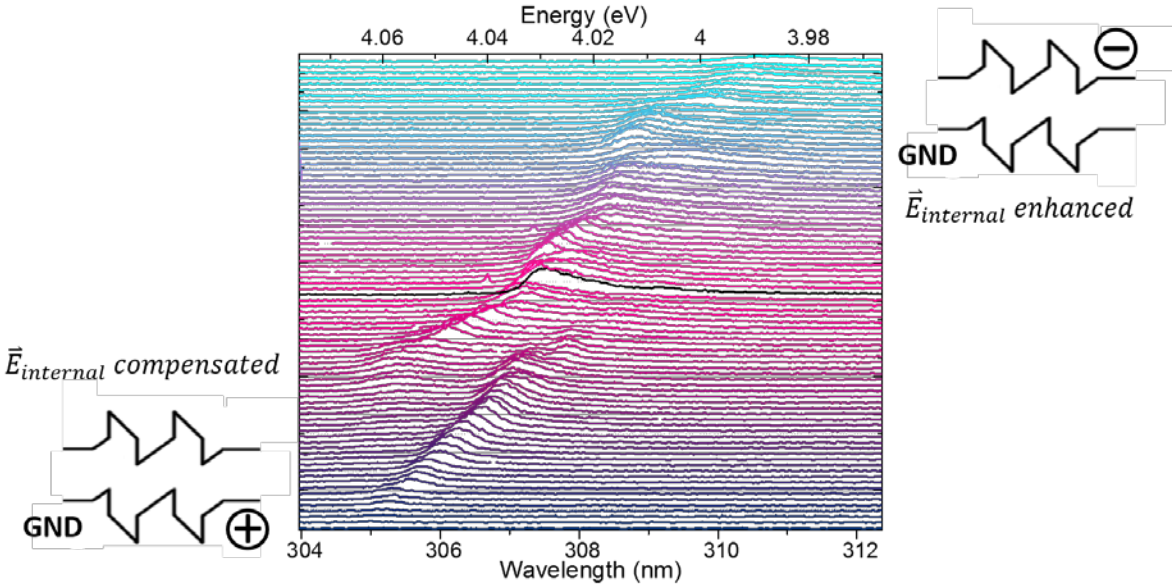

Figure 6.6. Microphotoluminescence spectra applying from −4 V (top) to +4 V (bottom) bias on NW A. The zero bias measurement is indicated in black. The spectra are given without normalization and shifted vertically for clarity. The two schematics indicate the bias polarity. Bottom: the applied bias compensates the internal field, top: the applied bias enhances the internal field.

The shift occurs at an impressive rate of 1.0 nm/V or 11.9 meV/V in the range from −4 V to +2 V. Between +0.6 V and +2.8 V, however, two peaks can be observed which both continue to blue shift with increasing positive bias and increasingly compensated internal electric field. While the first peak disappears when the bias is higher than +2.8 V the second peak also eventually disappears at bias ~+4 V. This behavior is observed only for positive bias. A possible explanation of the second peak occurring is that it is a charged excitonic state. The occurrence of the second peak can be correlated with an increased photocurrent.

At negative bias the peak does not decrease in intensity. In the given series of spectra it may look like the intensity decreases with negative bias, however, the diminishing of the peak for larger negative bias is attributed to a slight misalignment occurring over time while acquiring the spectra. This point was verified in a second measurement series.

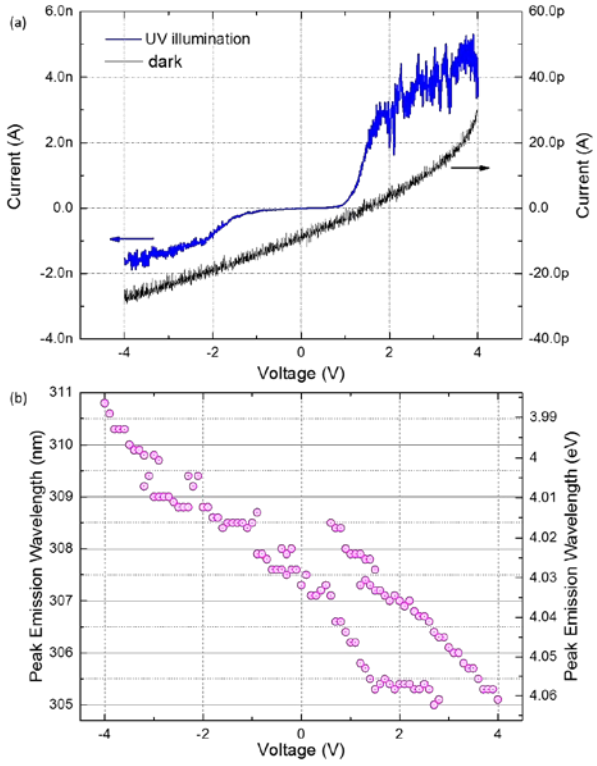

Figure 6.7.(a) IV curve of NW A under UV illumination (blue, left y-axis) and in the dark (black, right y-axis). Note, that the current measured in the dark is the leakage current through the substrate the NW is placed on. (b) Maximum peak wavelength vs. applied bias in NW A. A shift of 6.0 nm over a range of 8 V applied external bias, corresponding to 11.9 meV/V, can be observed as well as a the appearance of a second peak attributed to a charged state.

The NWs have been characterized by their IV curve. Here it was observed that in the dark (without UV illumination) the photocurrent can be approximated as zero for all three single NWs (A,B,C). The curve in the dark for NW A is given in black in figure 6.7.(a). The measured current stays below 30 pA in the −4 V to +4 V range. A similar current is obtained when measuring an IV curve between two contacts on the membrane chip which are not connected by either a contact, a NW or both. Thus, it is considered a leakage current path through the membrane chip. Under UV illumination however the behavior of the NW A in the IV curve becomes rectifying. Starting from around −1.5 V the current increases and reaches +1.5 nA at −4 V. Similarly, starting at the applied voltage of +1 V the current under negative bias decreases and goes up to +4.5 nA at +4 V.

At this point the IV characteristics, the spectral shift, the appearance of a second peak and the 1D simulations can be correlated. In 1D simulations we show that the electric field in the QD is enhanced with negative bias on the cap, see figure 6.1.(b). Therefore, electron and the hole get more separated. With a positive bias on the cap the electric field in the QD is compensated, and electron and hole become closer. This may increase the oscillator strength of the transition. Additionally, the tunnel barrier for the electron towards the cap becomes smaller, so that it is easier for the electron to contribute to the photocurrent. Indeed, we observe higher photocurrent at positive bias (figure 6.7.(a)). The difficulty to confine the electron in the QD might be associated to the observation of the second emission peak, which is assigned to another charged state of the exciton. At that bias range, it seems reasonable to assume that through an additional charge in the QD the exciton can get stabilized. The eventual disappearance of both peaks occurs at a photocurrent of a few nA. At that point, tunneling out of the QD is generally more favorable than radiative recombination, so that the generated electron-hole pairs are collected as current rather than recombining radiatively.

In order to extract where along the NW the applied external electric field drops, the emission shift calculated in 1D simulations taking into account the actual NW geometry (figure 6.5.(e)) has to be compared to the experimentally observed shift. Between 0 V and −4 V applied potential the change in the simulated internal electric field is 1.9 MV/cm leading to a total length of 21 nm (=4V/1.9 MVcm^{-1}) where the potential drop occurs. This result fits well with the insertion in the NW which is 10 nm AlGaN/ 0.8 nm GaN/ 10 nm AlGaN. We can therefore deduce that the GaN stem and cap act highly conductive and the externally applied bias is applied at the ends of the insertion section.

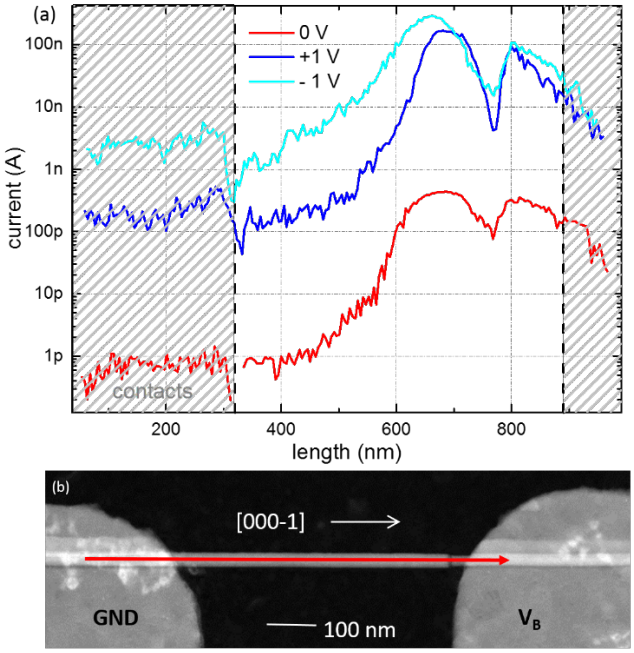

Figure 6.8. (a) EBIC line measurement of NW A scanning along the NW applying 0, +1 and −1 V bias (represented in red, blue and turquoise respectively). We observe Ohmic contacts. The spectra for negative and zero bias are multiplied by −1. The shaded areas correspond to the contacts. (b) STEM image of the NW. The red arrow indicates the position and direction of the line scan.

In order to study the origin of the photocurrent, EBIC measurements have been carried out on NW A. The obtained line scans for 0, +1 and −1 V are given in figure 6.8.(a) in blue, turquoise and red, respectively (note that the spectra for 0 and −1 V are multiplied by −1). The shaded areas correspond to the contacts. Current is generated when exciting the cap and the depletion region below the insertion. Here, the location of the insertion is characterized by a sharp drop of the photocurrent, observed at ~750 nm along the x-position. Close to the insertion, we observe a 3 orders of magnitude increased current collection with applied positive and negative bias, which is slightly lower at zero bias.

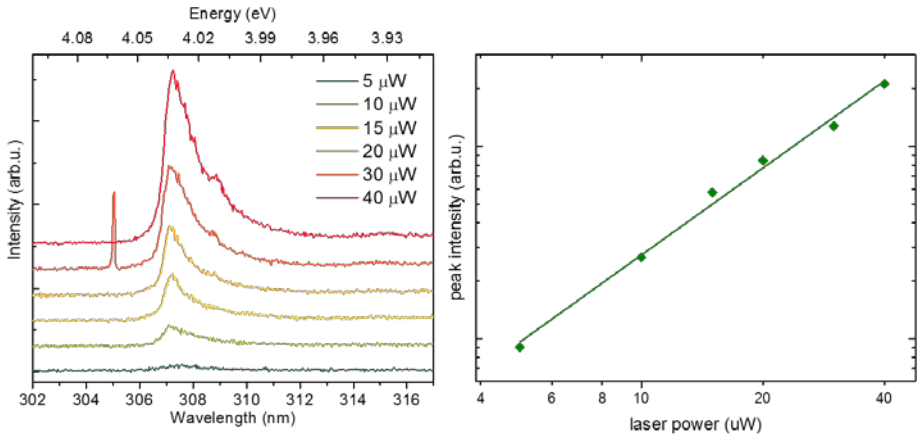

Figure 6.9.(a) Laser power dependence study of NW A at no bias applied (see black line in figure 6.6). The spectra are vertically shifted for visibility. (b) Plot of maximum counts at different values of laser power. The solid line is a fit to Intensity $\propto P^{1.5}$.

In order to determine the nature of the PL emission peaks of NW A, PL measurements as a function of the laser power (varying in the range of 5 to 40 μW) were carried out at zero bias. The result is given in figure 6.9. Plotting the integrated intensity of the QD emission as a function of laser power (P) we find that the intensity scales as $P^{1.5}$. This superlinear power dependence is explained by a saturation of the traps that mask the linear trend expected in an excitonic emission.

The blueshift with increasingly compensated internal electric field through application of external bias was observed as well in NW B and C. The recorded spectra and the variation of the peak emission wavelength with bias of NW B are shown in figure 6.10. The shift occurs between 303 nm and 311 nm. In the range of −1.5 V to +2.5 V the peak shifts 1.9 nm/V, which is 25.1 meV/V. Similarly, for NW C the PL spectra and the peak emission wavelength vs. bias are given in figure 6.11. Here the blue shift occurs between 318 nm and 333 nm in a voltage range of −4.5 V to +4.5 V yielding an average shifting rate of 1.7 nm/V or 19.9 meV/V.

The shifts of all three NWs A, B and C lie almost one order of magnitude above those observed by Müßener et al.[26] in a similar structure. The higher applied voltages in their case can be explained by looking at the thickness of the heterostructure. Müßener et al. have a 50-nm-thick $Al_{0.3}Ga_{0.7}N$ barrier on each side of the QD sandwiched between 16-nm-thick AlN current blocking layers. Therefore, the required external bias to induce a certain electric field in this ~134-nm-thick heterostructure is significantly higher than in our design, where the heterostructure is only ~21 nm thick. The thinner barriers do not open a leakage path as it was verified by the IV measurements in the dark.

The quenching of the emission at highly compensated internal electric field (emission at shorter wavelengths) of NW A has been observed in NW B and C as well, and it is accompanied by comparatively high photocurrents. This behavior can be explained by the charge carriers being collected as photocurrent beyond a critical bias rather than as radiative recombination. This is likewise the reason flatband conditions are not reached in this configuration. The internal electric field in the QD structure by Müßener et al.[26] was determined to be 1.5 MV/cm at zero bias. It was deduced from the voltage where the peak in the PL measurements stops shifting (+20 V) arguing that flatband conditions are reached. In this study, however, the internal electric field was determined to be 3.0 MV/cm by comparison with simulations.

It is interesting to note that during the application of high bias reinforcing the internal electric field of the QD and high currents >250 nA, several emissions were observed in NW B. Besides the main peak at 311 nm, one at 318 nm and one at 324 nm were observed. These additional peaks do not shift with varying bias and are not reproducible. On the contrary, the main peak at 311 nm occurs and shifts in the same way for each sequential measurement.

Effects of ageing have been observed. The QD emission of NW A had dropped between the initial and a second measurement. It could be recovered by a 5 min exposition to an O_2 plasma of 20 W. NW B and C were measured in µPL without any initial O_2 plasma treatment. Likewise the QD emission intensity as well as the photocurrent value of NW B has gone down several orders of magnitude during the measurement processes, which points to a significant ageing effect.

The study of electrically tuned emission in multiple NWs contacted in parallel can be seen in Annex C.

To further understand this QD system it is necessary to systematically study it more. Different barrier compositions, such as AlGaN with less Ga content or even pure AlN should be tested. Thinning the barrier thickness to an optimum point where the electron-hole pair is still confined yet the application of bias is further enhanced is desirable.

The effect of ageing has to be studied in more detail. Most notably, if the application of current or the illumination with laser light is the determining factor and if a universal counter measure is the above mentioned O_2 plasma. If the aging arises due to surface reactions, it may be possible to limit these by depositing an electrically inactive, thin protective shell on the NWs.

It has furthermore been observed that the QD emission peak of NW B decreases from a FWHM of 2 nm to 1 nm before and after the deposition of the contacts. This should be reproduced systematically and explained.

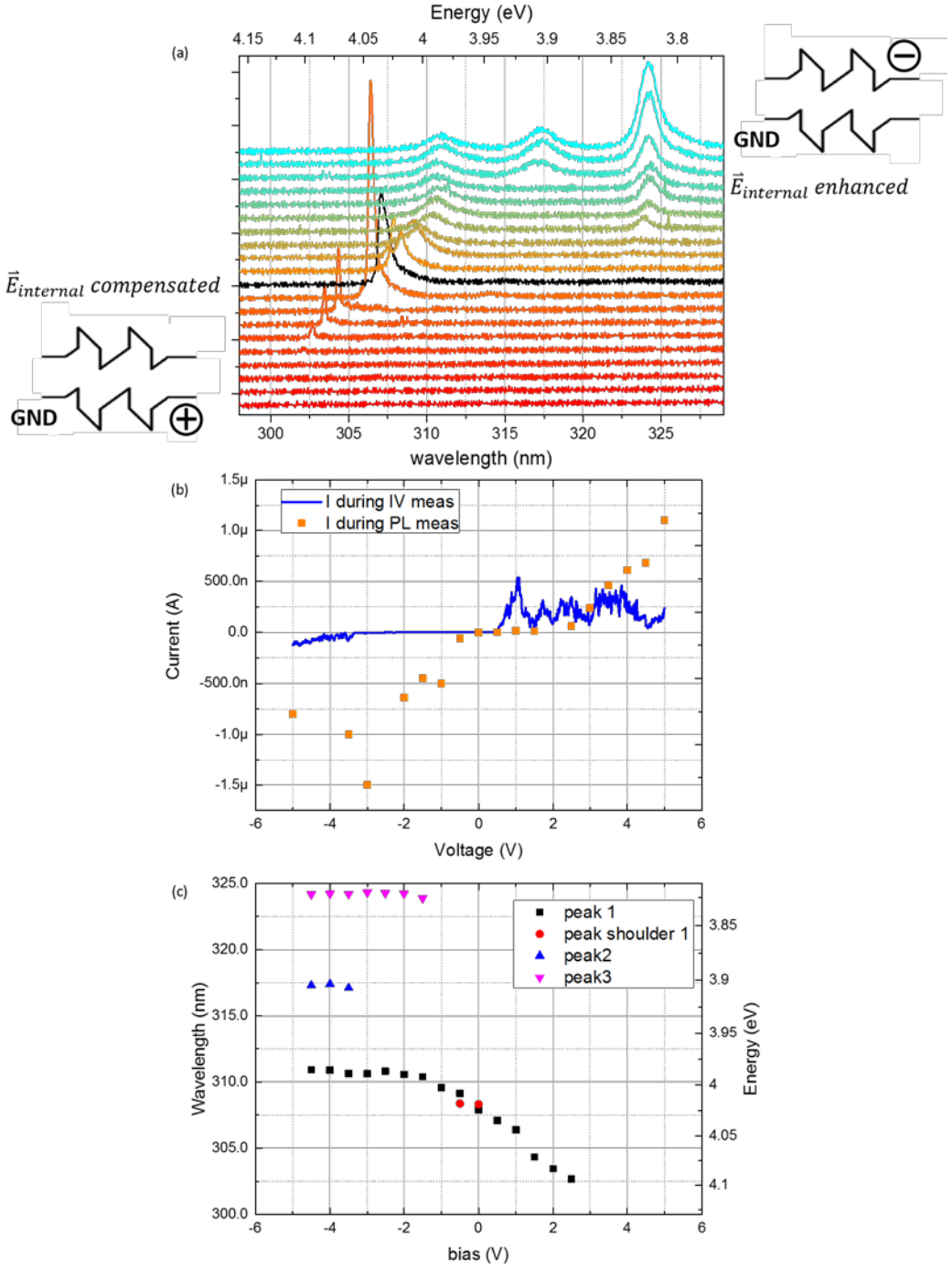

Figure 6.10.(a) Microphotoluminescence spectra applying from −4.5 V to +5 V bias on NW B. The zero bias measurement is indicated in black. The spectra are given without normalization and shifted vertically for clarity. The two schematics indicate the bias polarity. Bottom: the applied bias compensates the internal field, top: the applied bias enhances the internal field. The QD emission disappears at high positive voltages which in the following is explained with an increased photocurrent. (b) IV curve of NW B under UV illumination. Blue: before PL measurement. Orange: during PL measurement. Note, that the current measured in the dark (not shown) is the leakage current through the substrate the NW placed on. (c) Maximum peak wavelength vs. applied bias in NW B. A shift from 311 nm to 303 nm in the range of −1.5 V to +2.5 V is observed which corresponds to a peak shift of 1.9 nm/V which is 25.1 meV/V.

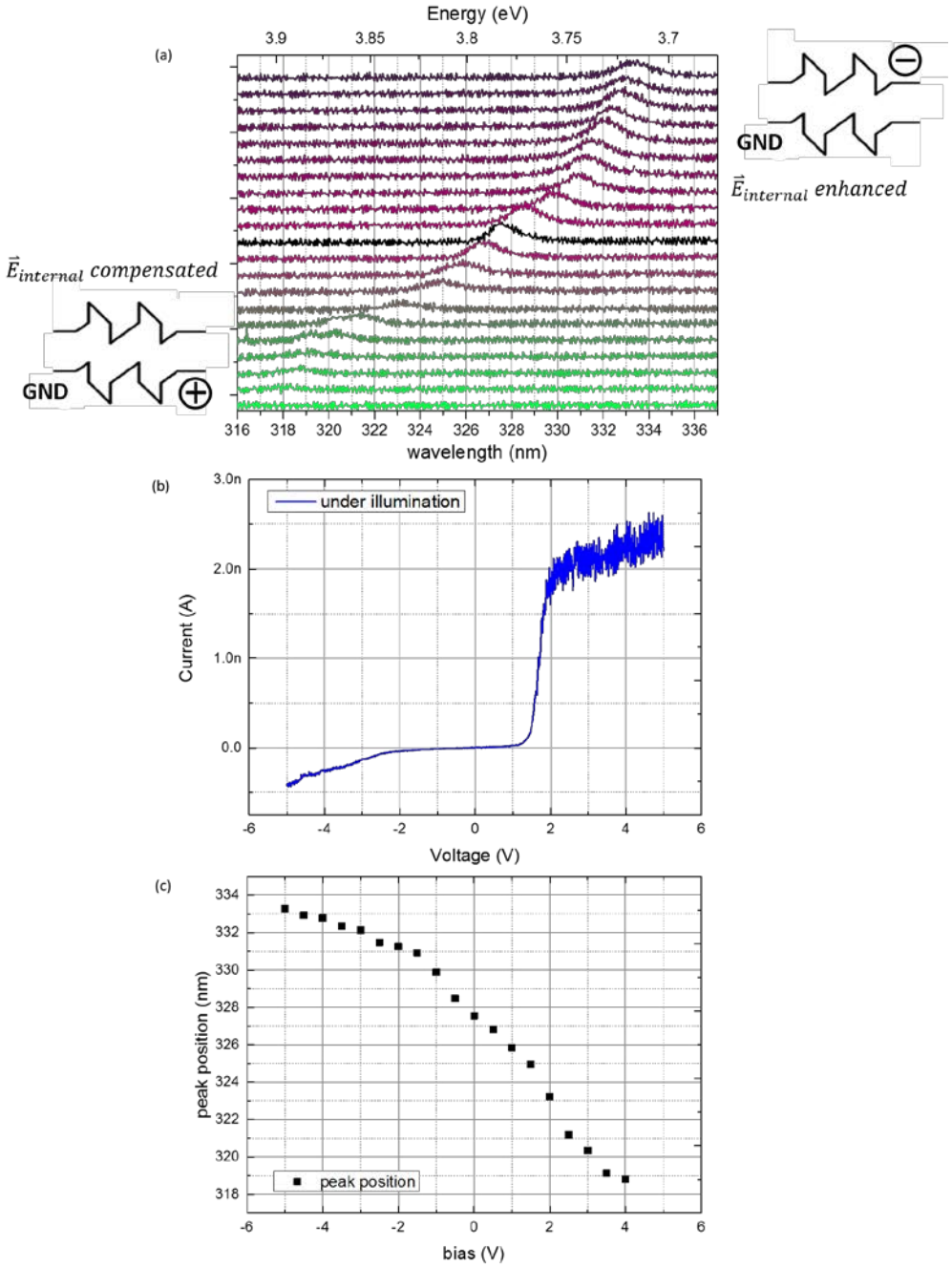

Figure 6.11.(a) Microphotoluminescence spectra applying from −4.5 V to +5 V bias on NW C. The zero bias measurement is indicated in black. The spectra are given without normalization and shifted vertically for clarity. The two schematics indicate the bias polarity. Bottom: the applied bias compensates the internal field, top: the applied bias enhances the internal field. The QD emission disappears at high positive voltages which in the following is explained with an increased photocurrent. (b) IV curve of NW C under UV illumination. Note that the current measured in the dark (not shown) is the leakage current through the substrate the NW placed on. (c) Maximum peak wavelength vs. applied bias in NW C. A shift from 333 nm to 318 nm in a voltage range of −5 V to +5 V yielding an average shifting rate of 1.7 nm/V or 19.9 meV/V is observed.

6.6. Conclusions and Prospects

The tunability of a single NW AlN/GaN/AlN QD structure with a QD height of 0.8 nm was studied. A systematic blue shift is observed in in-situ µPL measurements for the application of an external electric field compensating the internal electric field within the QD structure. Shifts in the range of 11.9 to 25.1 meV/V are observed. Transitions to other charge states are likewise

observed and can be correlated to changes in the photocurrent. At high photocurrents at positive bias compensating the internal electric field the QD emission gets quenched to its full disappearance. The values for the PL shifts are at least one order of magnitude higher than the values obtained previously by Müßener et al.[26] in a similar structure. STEM observations reveal an increased Ga content in the barriers of the studied structure, effectively leading to $Al_{0.5}Ga_{0.5}N$ barriers. The need for less applied external bias compared to Müßener et al. can be explained by a change in the barrier structure. 10 nm $Al_{0.5}Ga_{0.5}N$ barriers around the QD were employed rather than 50 nm $Al_{0.3}Ga_{0.7}N$ and 16 nm AlN. That makes the application of the bias occur on a much shorter section, leading to higer effectively applied field in the QD at the same applied potential to the contacts with respect to Müßener et al.[26]. The thinner barriers do not open a leakage path as was verified by the IV in the dark where only very low current (associated to leakage current) is observed. On the other hand, the thinner barriers do allow for a tunnel current at positive bias quenching the PL. Three-dimensional calculations of the electronic structure taking the STEM-measured morphology into account extract an internal electric field in the QD of around 3 MV/cm. Furthermore, the emission intensity scales superlinearly with the impinging optical power, suggesting a saturation of traps, probably point defects, in the vicinity of the QD. In coalesced NWs, the photoluminescence consists of multiple peaks. Applying an external electric field compensating the internal electric field leads likewise to a blue shift in the emission, which, however, occurs in jumps, suggesting transitions between various charged exciton states.

It is interesting to extend this study to QDs emitting at longer wavelengths, e.g. the visible region, which means synthesizing QDs with larger heights. Here, the influence of the externally applied electric field will be larger as the spatial and energetic differences within the QD are increased. A linear dependence of the wavelength on the applied electric field is imaginable. Technical difficulties for such a study would be two-fold : i) the QD would emit below the GaN bandgap and its emission would have to be distinguished from other below band-gap emission (stacking-fault bound excitons, donor-acceptor pair emission…) and ii) for thick QDs, the QCSE is such that the radiative lifetime can be very long[280] so that the QD emission saturates at low pump power with a quite low emitted signal.

Furthermore, it is interesting to design a QD structure containing 2 QDs separated by the same 10 nm AlN barriers employed in this project (yielding barrier/QD/barrier/QD/barrier) for similar experiments. The expected recombinations include transitions within and across the two QDs. The trans-QD recombination are expected to occur at bias high enough to make such a transition favorable.

Moreover, it would be nice to be able to identify the involved charge carriers as was done in the nice work by Ediger et al in 2007 for InAs/GaAs dots[281] which however would require drastic changes in the structure of the sample and extensive simulations. One of the limitations of the simulations is that the Coulomb interaction is not taken into account. The occurring excitonic effects can be quite strong in these structures with exciton binding energies in the 20 meV range[282]. The occurence of multiple excitonic states or the charging of these states by an additonal charge might herewith be explained.

7. Conclusions and Perspectives

The goal of this project was to study the potential of NW photodetectors containing GaN/AlN heterostructures, and the electrical tunability of the emission of GaN QDs embedded in a NW structure. The idea was to do a consistent correlation of experimental techniques on the same single NW, including TEM, μPL and photocurrent measurements.

7.1. Concerning the Photodetector Studies

A correlated study on single GaN NW ultraviolet photodetectors incorporating a 30 period GaN/AlN SL was presented. The heterostructure dimensions and doping profile were designed to exploit the advantages associated with the internal electric field generated by the SL. With such an architecture, a significant enhancement of both the response under positive bias and the photovoltaic (zero-bias) response can be obtained with respect to previous results. Under negative bias, the structure behaves like a GaN metal-semiconductor-metal photodetector, with photocurrent being generated mostly in the GaN stem. Under positive bias on the other hand, the most important potential drop occurs within the SL. Due to differences in the bandstructure the photogenerated carriers in the stem or in the SL react preferentially to different specific wavelengths ranges. Three-dimensional calculations of the band diagram were carried out to understand the device performance and assess the relevance of surface states. They showed that the role of the surface is negligible in the cap and in the SL, but it should induce a partial depletion of the stem. The resulting asymmetry of the potential profile along the NW might contribute to the strong response at zero bias.

A correlated study on single GaN NW ultraviolet photodetectors incorporating an AlN/GaN/AlN heterostructure was presented. The insertion of the heterostructure leads to an electric field along the NW axis as a result of the difference in polarization between III-nitride compounds with wurtzite crystal structure. Under reverse bias, the detectors behave linearly with the impinging optical power when the NW diameter remains below a certain threshold. This is in contrast to the behavior of larger NWs (diameter above the critical value) and former observations in various NW material systems, where the response is sublinear. The linear behavior of the studied NWs is explained by the linearity of the photogeneration process, the separation of photogenerated carriers induced by the axial electric field, and the fact that illumination does not have a significant effect on the radial electric field. In the case of NWs that are not fully depleted, the light-induced change in the Fermi level at the sidewalls results in a variation of the diameter of the central conducting channel in the stem, which leads to an overall nonlinear photoresponse.

Improving the linearity of NWs with a thicker diameter will be possible by obtaining a full depletion of the NWs via lower doping concentrations or rendering the band bending at the sidewalls insensitive to light via protecting the surfaces with a passivation layer.

The immediate next steps in terms of advanced characterization include correlating results with in-situ TEM techniques such as holography and 4D STEM. With these techniques the spatial distribution of the electric field within the NW photodetector structures can be studied. It may give information on the surface band bending and should allow to measure the electrostatic potential and electric field along the NW and potentially even within SL structures. In terms of device design, literature on architectures containing axial or radial p-n junctions is scarce, and this approach should be explored in more detail. Then, the results presented here describe the performance of single NWs. It would be interesting to compare with photodetectors fabricated with NW ensembles using the same architectures. This would allow identifying problems related to the fabrication process.

7.2. Concerning the Electrical Tunability of Quantum Dot Emissions

The electrical tunability of the optically-pumped emission from a GaN QD embedded in a GaN NW was demonstrated in a correlated study. In μPL measurements, the application of an external electric field compensating the internal electric field within the QD structure results in a blue shift of emission at rates between 11.9 meV/V and 25.1 meV/V. The emission intensity was shown to scale superlinearly with the impinging optical power, suggesting a saturation of traps, probably point defects in the vicinity of the QD. Three-dimensional calculations of the electronic structure were demonstrated in order to extract the internal electric field in the QD taking the STEM-measured morphology into account. The observed spectral shift fits well with theoretical expectations assuming that the applied voltage drops at the edges of the heterostructure.

Extending this study to QDs emitting at longer wavelengths, e.g. the visible region, would be interesting. In that case, the influence of the externally applied electric field should be larger, as the spatial and energetic differences within the QD are increased. Continuing the study with structures containing two QDs would likewise be interesting. If the QDs are separated by a narrow barrier, bias should induce a transition from observation of indirect, inter-QD excitons to direct, intra-QD excitons, with the corresponding change in carrier lifetime.

Introducing a passivation of the NW surfaces is also imaginable to limit the influence of surface effects and gain stability. Furthermore, it would give valuable insights to expand the modelling of such a system to take the Coulomb interaction between charge carriers into account. These should consider the possibility that a given QD can be charged, in order to explain the observation of additional PL lines attributed to other charged states.

Annex A: Correlation TEM vs. IV

The collection of NWs studied for chapter 5, where both the electrical characterization and the structural characterization by (S)TEM were carried out, are given in the following.

E3605_M4_A45

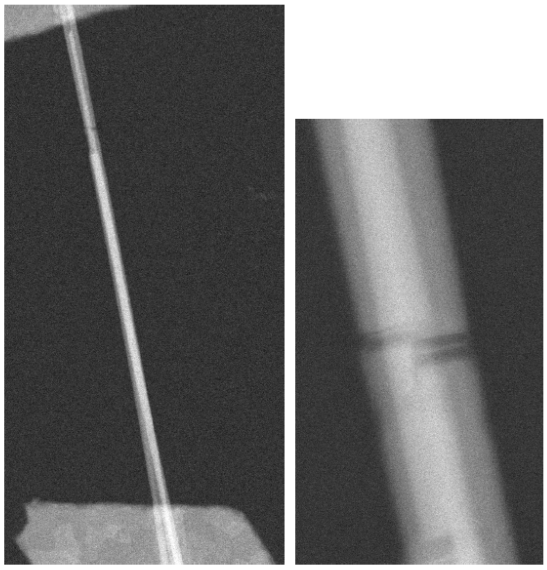

Diameter:
- Left: 46 nm
- Right: 36 nm
- Broken off one: 41 nm

IV:
- @ 1V: nA

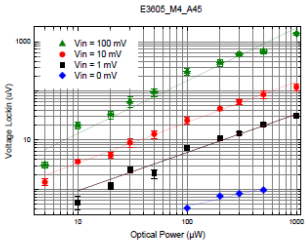

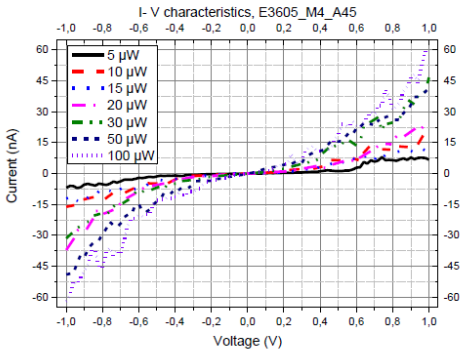

E3605_M4_B23

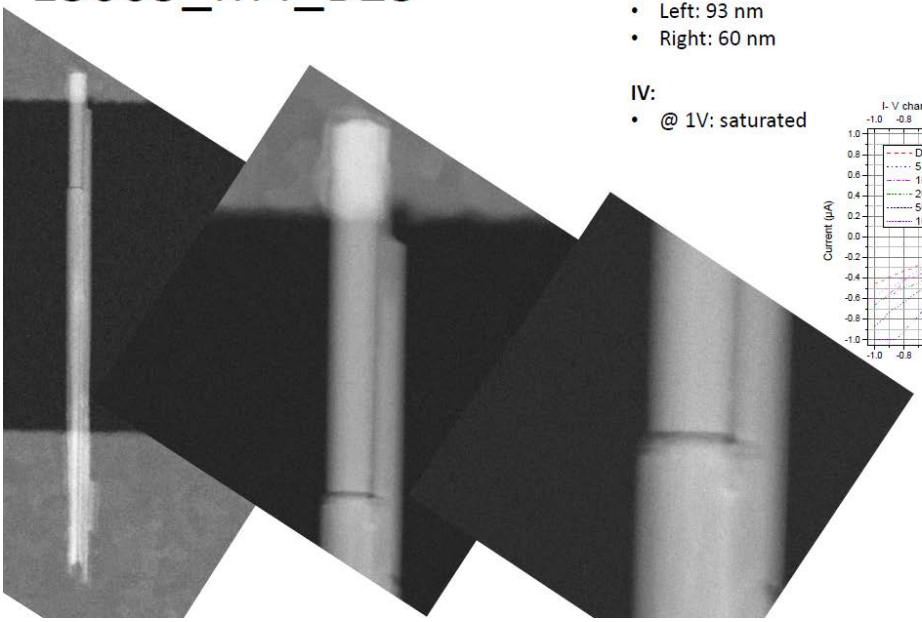

Diameter:
- Left: 93 nm
- Right: 60 nm

IV:
- @ 1V: saturated

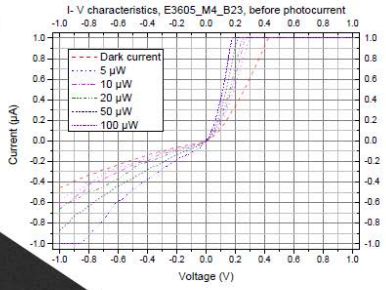

E3605_M4_C16

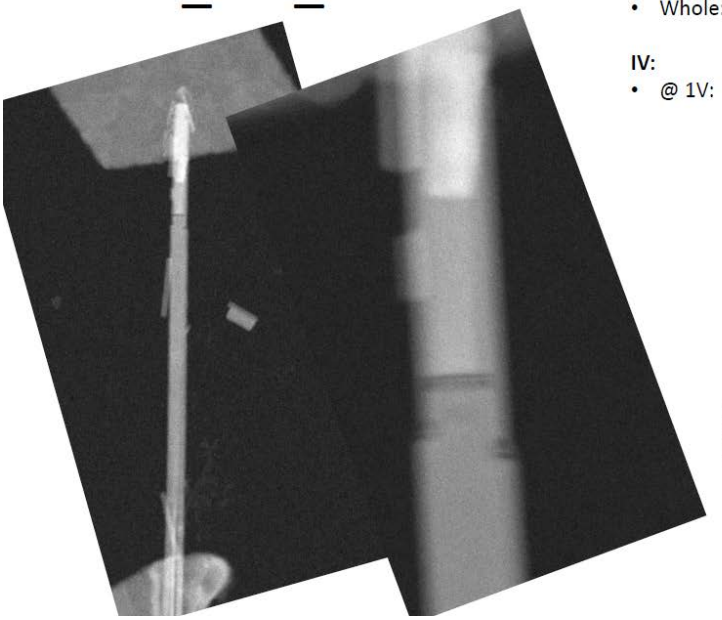

Diameter:
- Whole: 104 nm

IV:
- @ 1V:

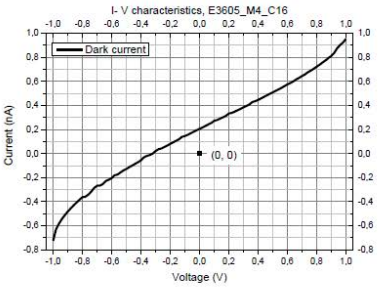

E3605_M12_A45

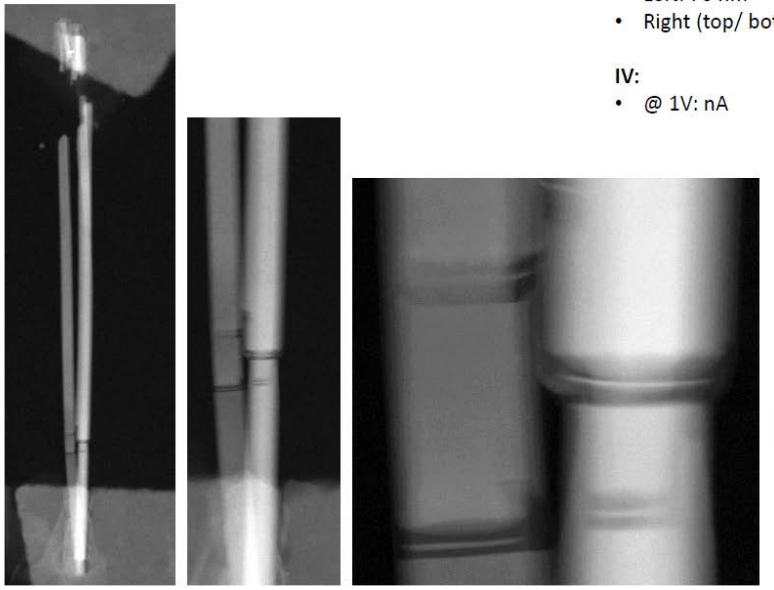

Diameter:
- Left: 76 nm
- Right (top/ bottom): 95/ 74 nm

IV:
- @ 1V: nA

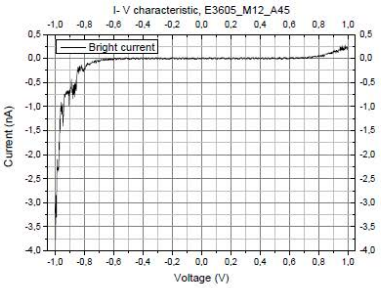

E3605_M12_B16

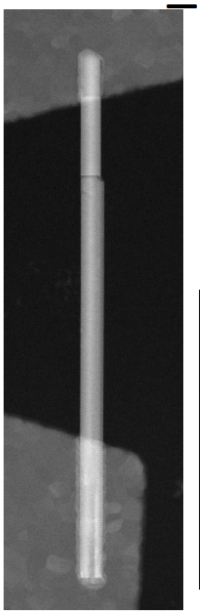

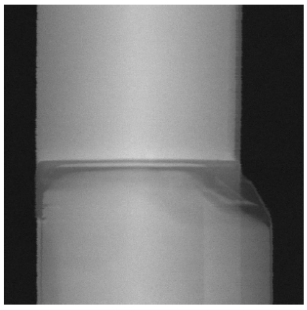

Diameter:
- Bottom: 153 nm
- Top: 140 nm

IV:
- @ 1V: µA

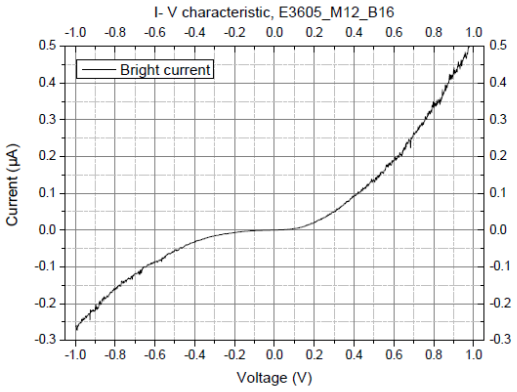

E3605_M10_A45

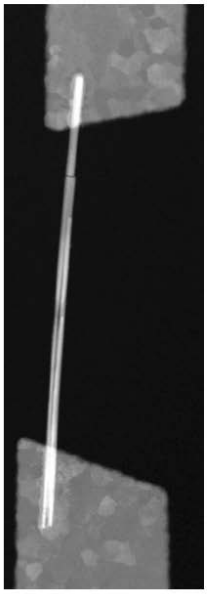

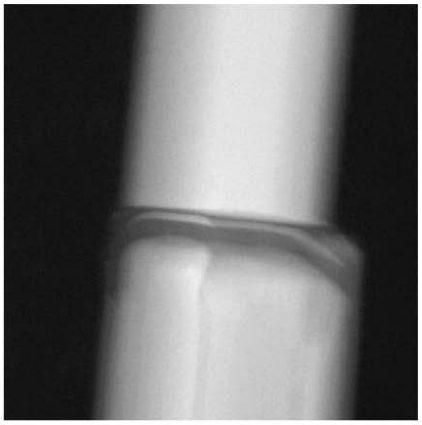

Diameter:
- Top: 72 nm
- Bottom: 89 nm

IV:
- @ 1V:

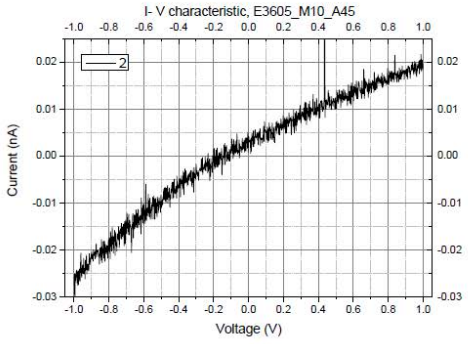

E3605_M10_C16

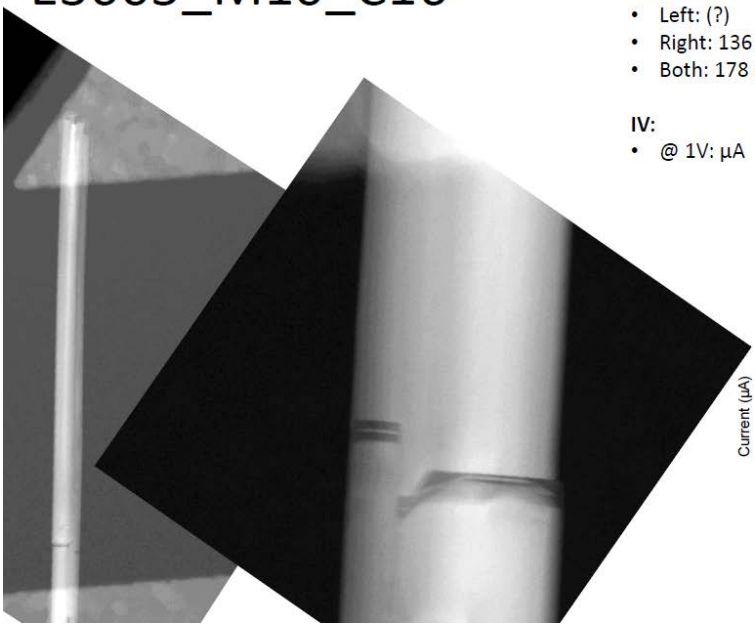

Diameter:
- Left: (?)
- Right: 136 nm
- Both: 178 nm

IV:
- @ 1V: µA

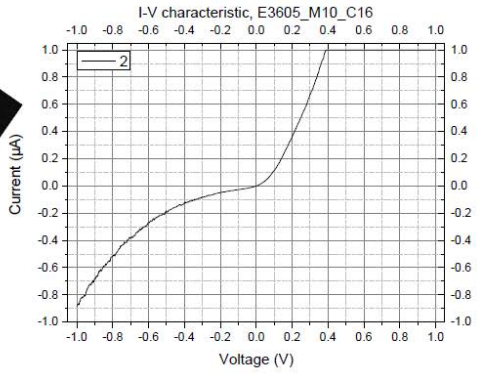

E3605_d7_m10_C23

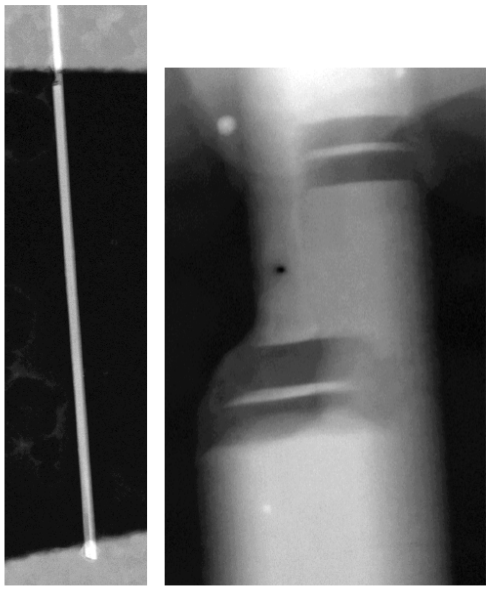

Diameter: (whole)
- Bottom: 48 nm
- Top: 67 nm

IV:
- @ 1V: 48 nA

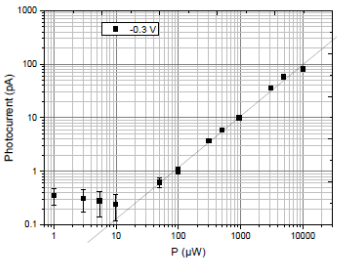

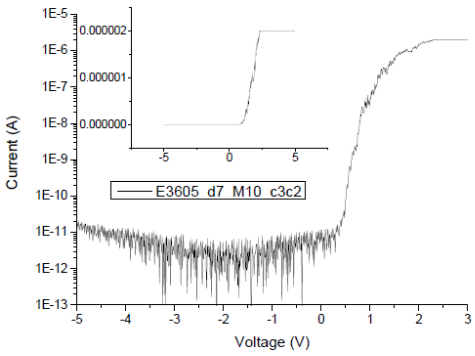

E3605_d7_m10_c16

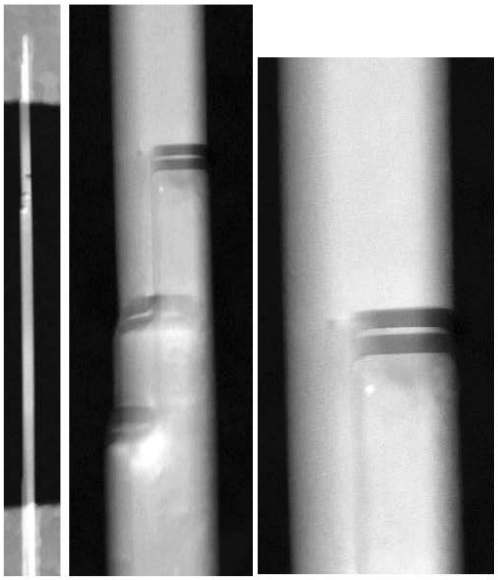

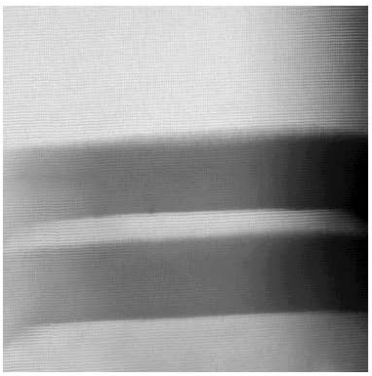

Diameter:
- Left: 27 nm
- Right: 39 nm
- Both top: 65 nm
- Both bottom: 78 nm

IV:
- @ 1V: 75 nA

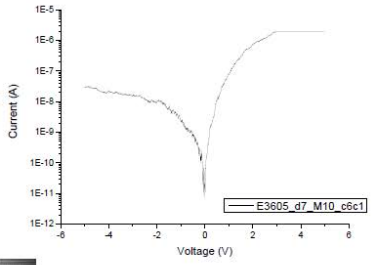

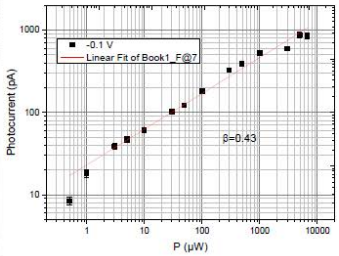

E3605_d7_m10_C45

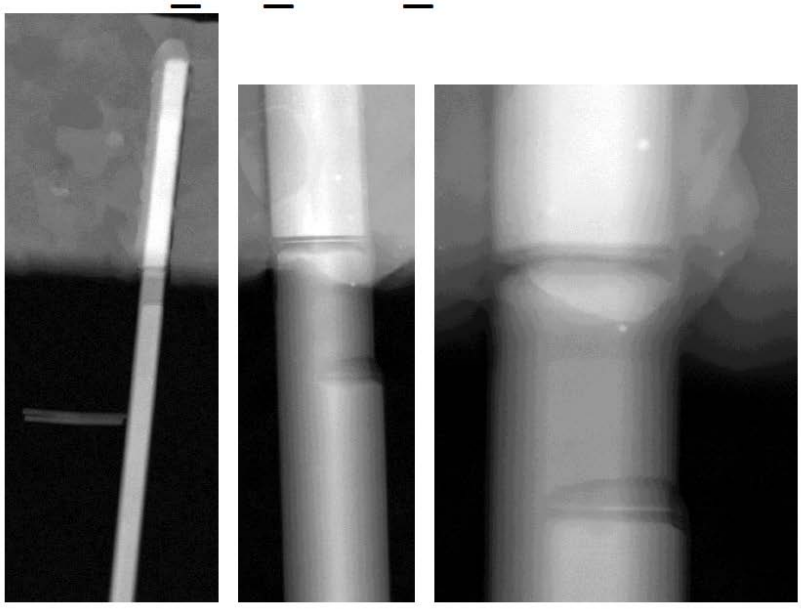

Diameter:
- Top: 102 nm
- Bottom right: 71 nm

IV:
- @ 1V: 1.8 μA

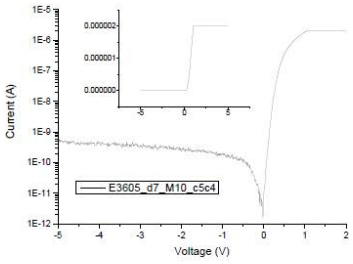

E3605_M15_c34

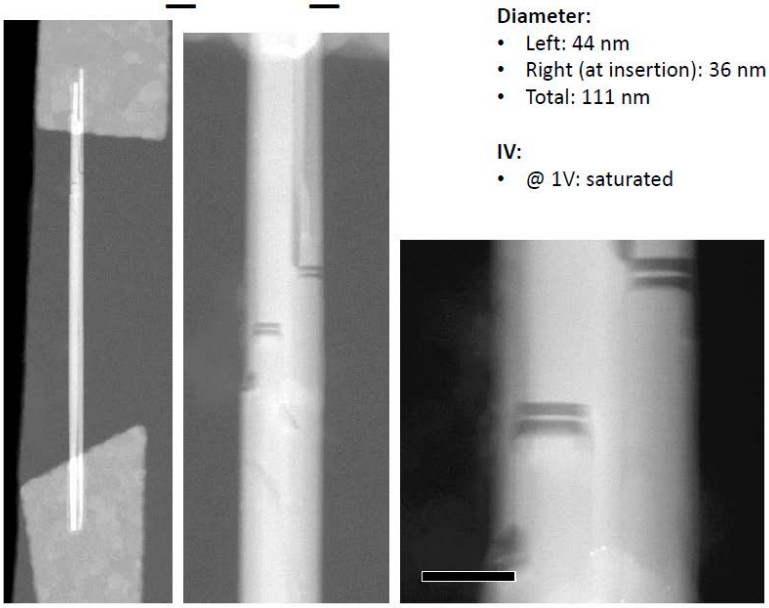

Diameter:
- Left: 44 nm
- Right (at insertion): 36 nm
- Total: 111 nm

IV:
- @ 1V: saturated

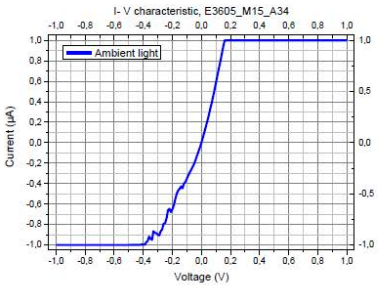

E3605_d4_m8_c45

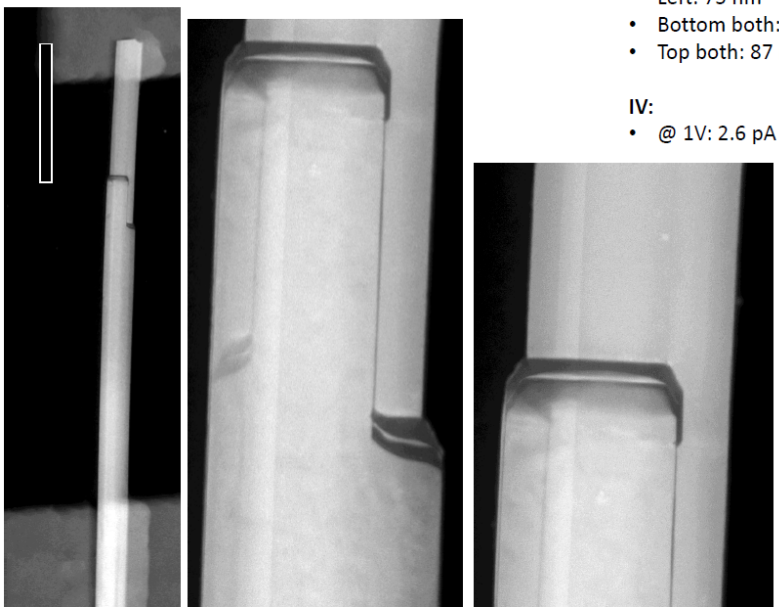

Diameter:
- Left: 75 nm
- Bottom both: 106 nm
- Top both: 87 nm

IV:
- @ 1V: 2.6 pA

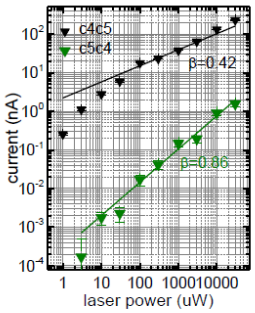

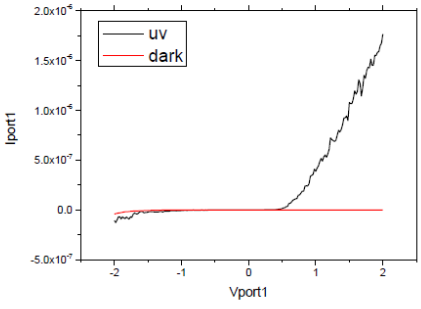

E3605_d5_m4_c23

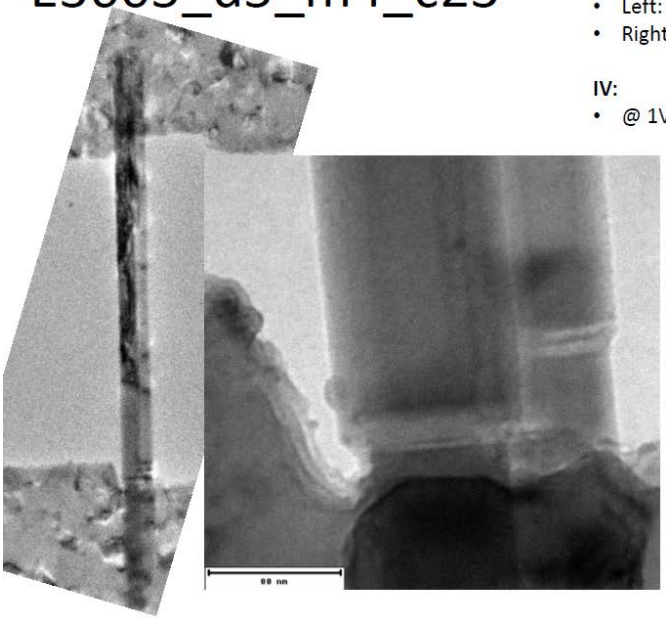

Diameter:
- Left: 122 nm
- Right 144nm

IV:
- @ 1V: µA illu, pA dark

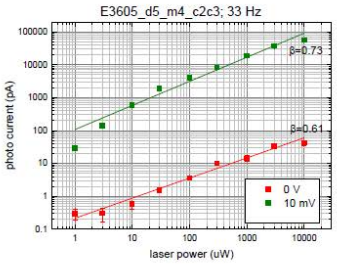

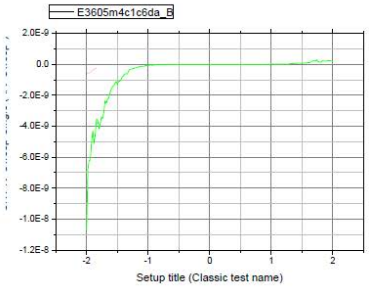

E3605_d5_m4_c23

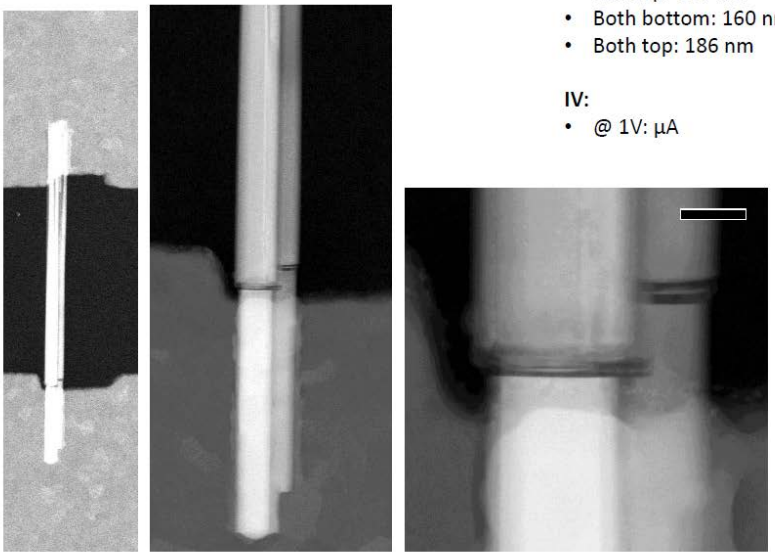

Diameter:
- Left bottom: 89 nm
- Left top: 123 nm
- Both bottom: 160 nm
- Both top: 186 nm

IV:
- @ 1V: µA

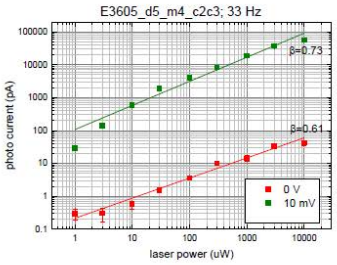

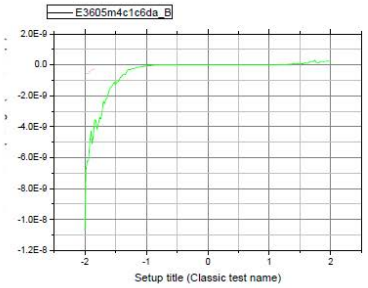

E3605_d5_m8_c45

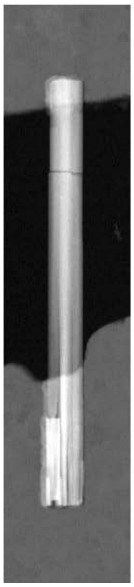

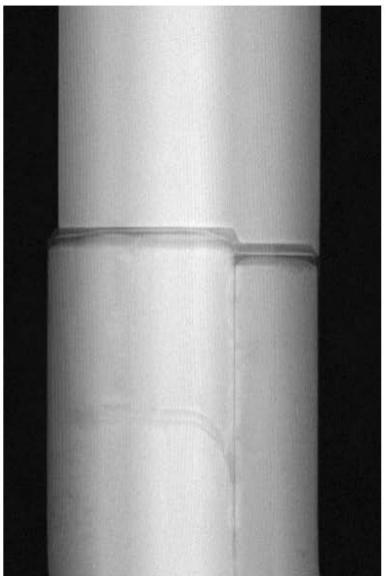

Diameter:
- Left bottom: 174 nm
- Both bottom: 251 nm

IV:
- @ 1V: saturated

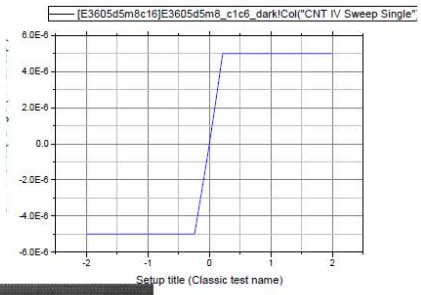

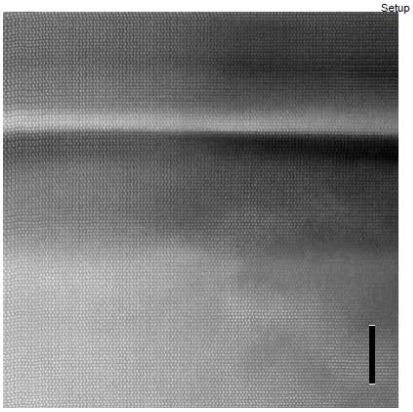

E3605_d6_m4_c16

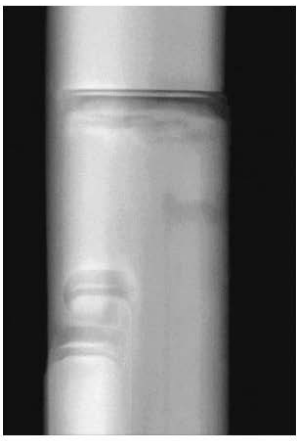

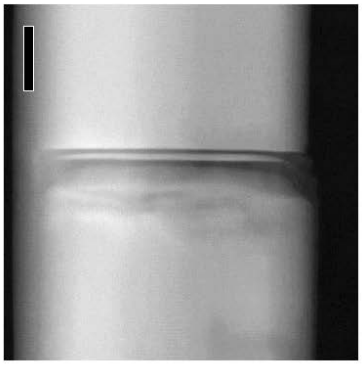

Diameter:
- Both: 120 nm

IV:
- @ 1V: 4.9 uA

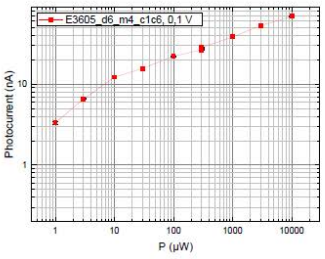

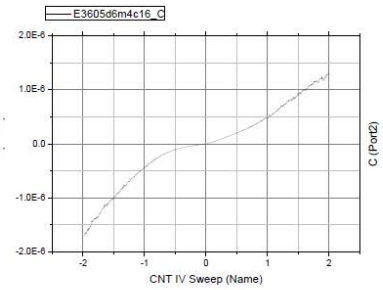

E3605_d6_m4_c23

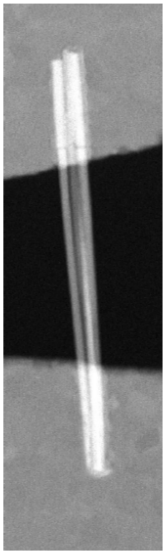

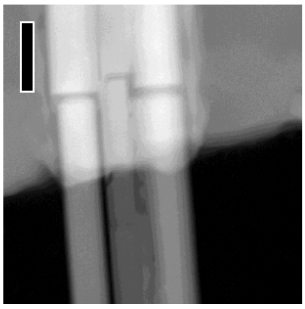

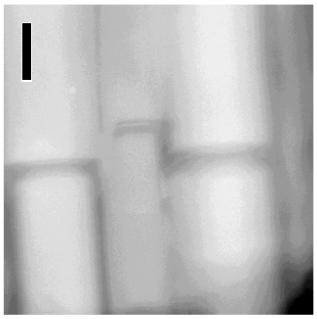

Diameter:
- Left: 82 nm
- Middle: 58 nm
- Right: 91 nm

IV:
- @ 1V: 1.2 uA

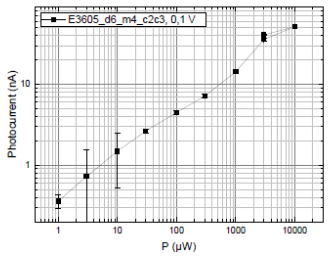

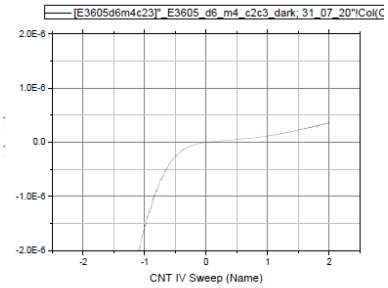

E3605_d6_m4_c45

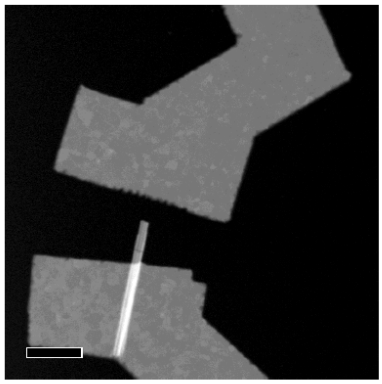

Diameter:
•

IV:
- @ 1V: no information

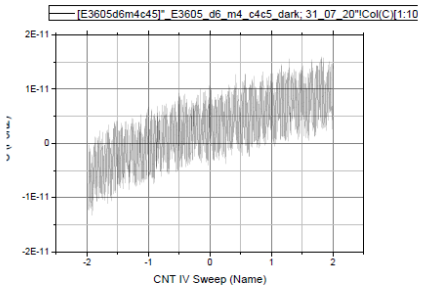

Annex B: Switch box design

The design of the switch boxes used for IV curve measurements and μPL measurements referred to in chapter 3 are given in the following.

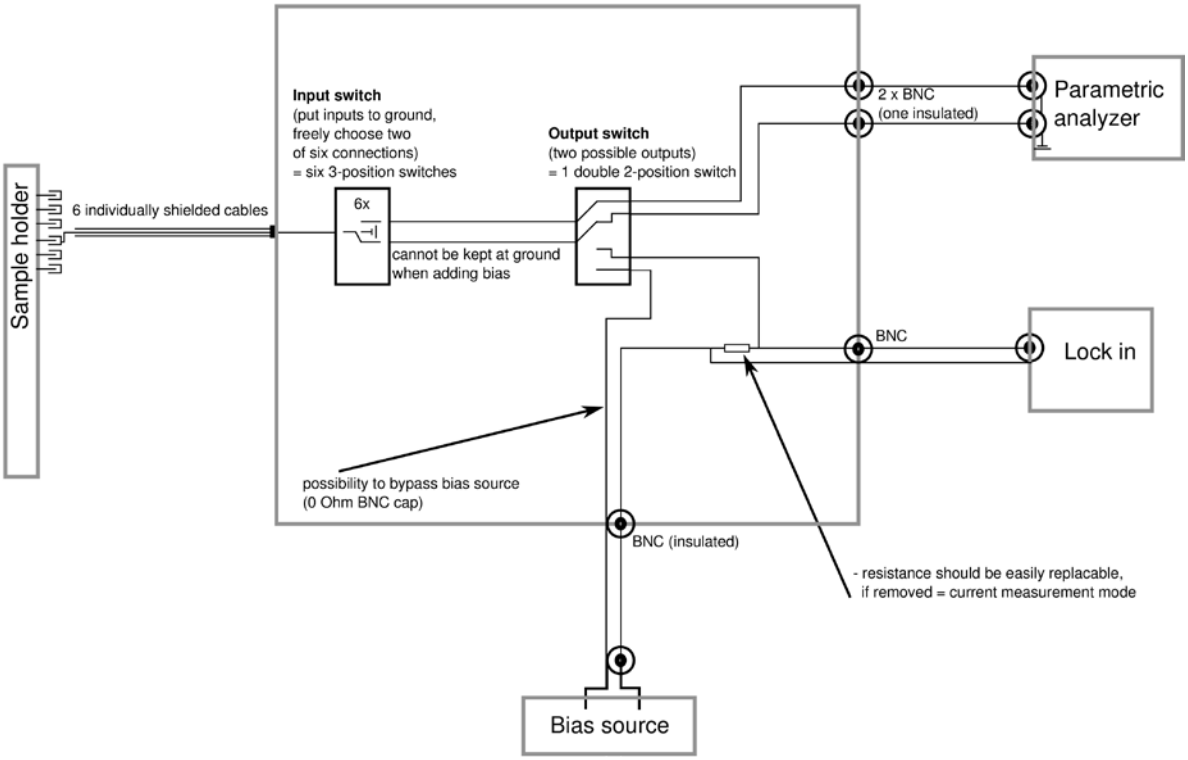

Figure AB.1. Principle of the switch box used for IV and photocurrent measurements.

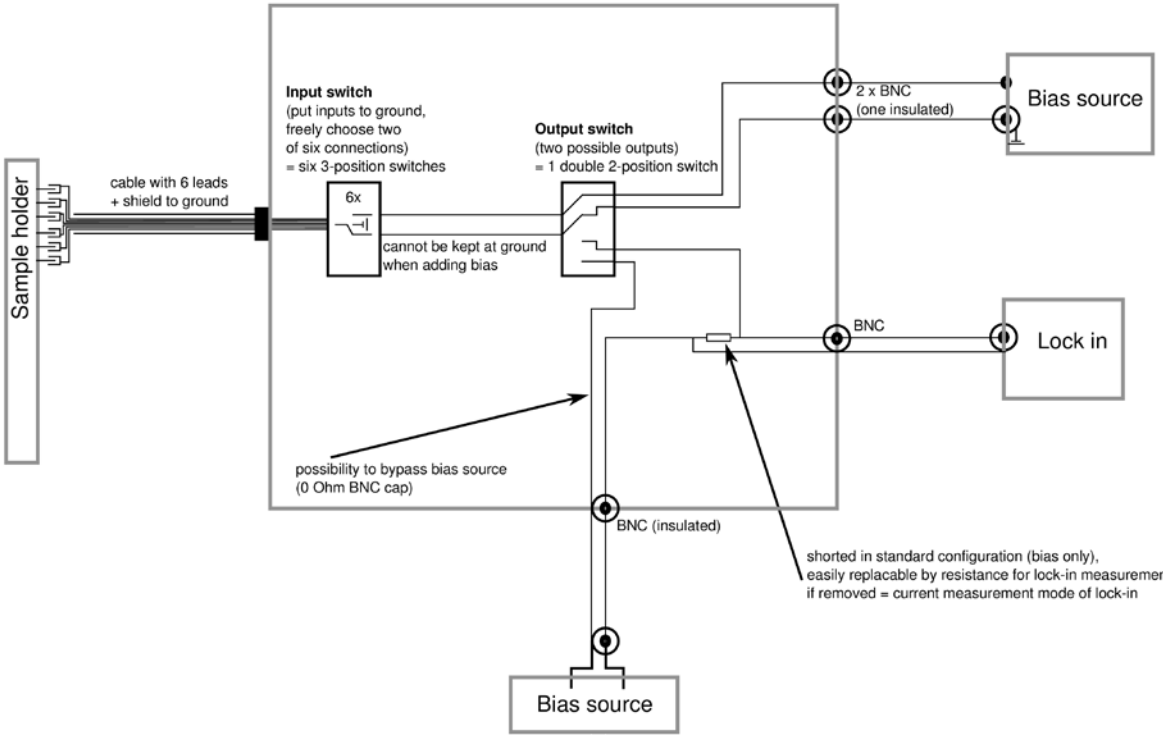

Figure AB.2. Principle of the switch box used for in-situ photoluminescence measurements.

Annex C: Electrically tuned Emission in multiple Nanowires

Complimentarily to single NWs presented in chapter 6, several multiple NW sample were characterized. One exemplary one is given here (NW D). In figure AC.1.(a) a HAADF-STEM micrograph of the insertion section is given. While the NW seems to be a double in SEM observation (not shown here), it is evident in this micrograph that at least four insertions are at play. Similarily, several emission peaks were collected in µPL measurements. At zero bias these peaks occur at 283, 286, 288, 304 and 321 nm. With increasingly compensated internal electric field (here: negative bias applied to the stem) the emission peaks blue shift. It is interesting to note that this blue shift occurs in jumps. That is in contrast to the single NW samples shown in chapter 6 where the emission gradually blueshifts with increasingly compensated internal electric field. As examples in the multiple NW sample: the peak at 281.3 nm jumps to 282.6 nm at +0.4 V and the peak at 287.1 nm jumps to 287.9 nm going from +0.1V to 0V. The peak maximum vs. applied external bias is given in figure AC.2.(b).

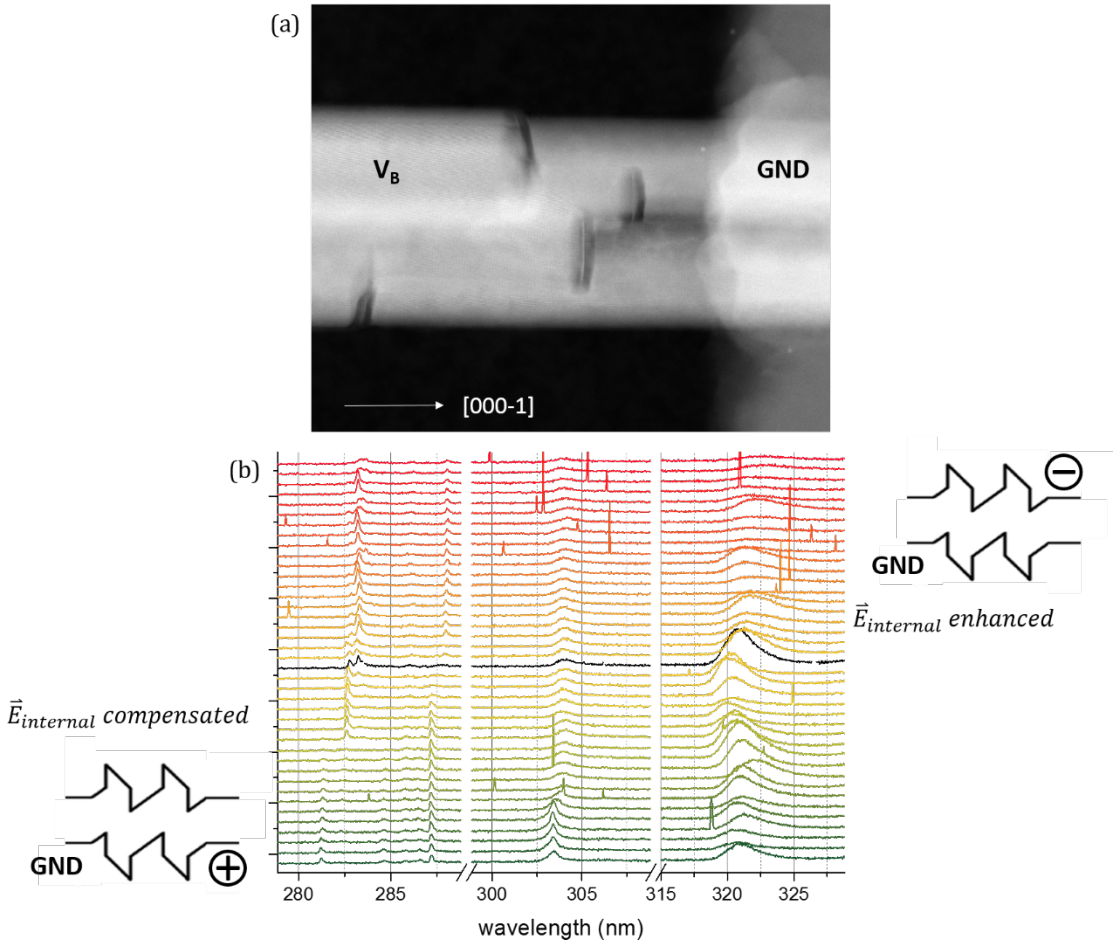

Figure AC.1.(a) HAADF STEM image of the insertion section of NW D. It can be seen that a number of NWs (at least four) are contacted. (b) Microphotoluminescence spectra applying from −1 to +1 V bias on NW D. The spectra are vertically shifted for visibility. The zero bias spectrum is indicated in black. The two schematics indicate the bias polarity: bottom = the bias compensates internal field, top = bias enhances internal field.

It is noteworthy to discuss the IV characteristics of NW D as well. It is different from the samples shown in chapter 6 in several points. In the dark the NW is conducting current whereas the single NWs in the chapter did not (only residual current through chip). This current is as high as a few hundreds of nA (between −1 and −4 V). Even under illumination NW A and C only reach

a few nA, and NW B a few hundred (all at +4V). Under illumination NW D reaches 1 µA at a bias as low as 0.3 V (1 µA is likewise the compliance limit set in order to preserve NWs intact).

Together, it can be concluded that the application of external bias on the QDs in this structure of NW D is difficult due to additional current paths e.g. between the NWs. Due to the complexity of the structure and limited understanding it is at this point not possible to assign the respective peaks to the QD of origin. While it is possible to correlate the emission wavelength with QD dimensions we have at this point no numerical tool, and not the sufficient understanding of the occurrence of multiple emissions, e.g. at high photocurrent values, to predict and assign multiple emissions from the same QD.

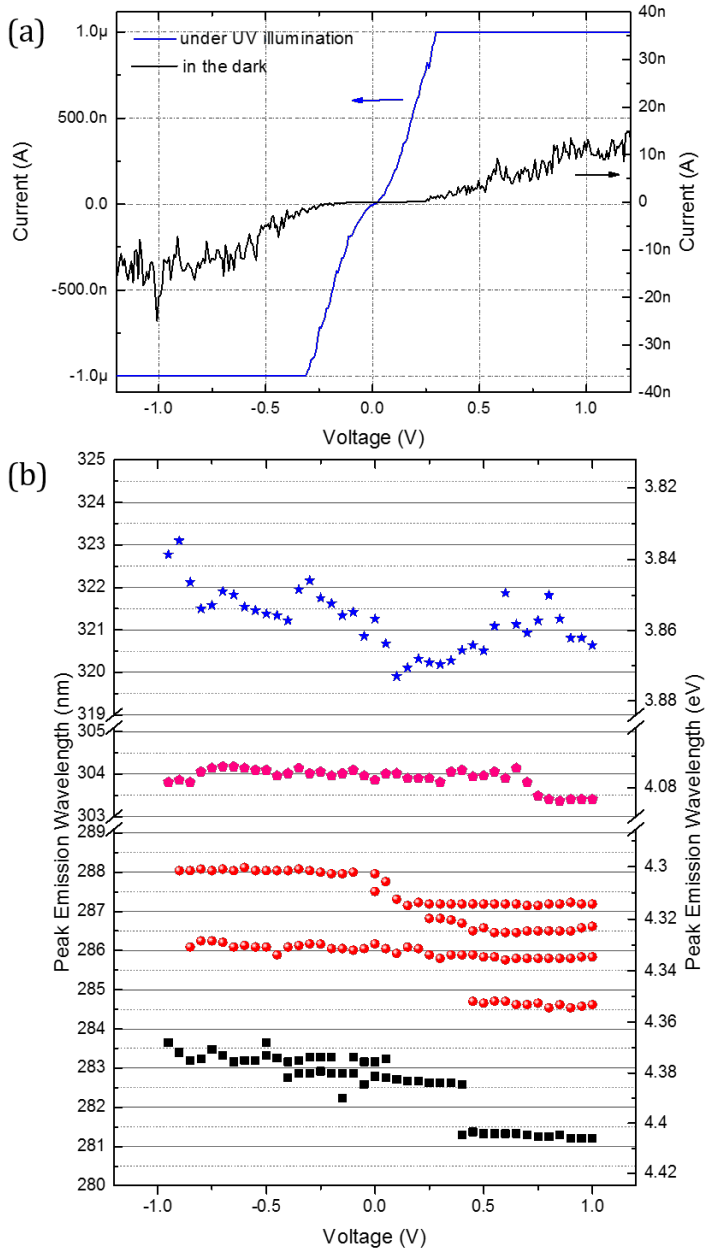

Figure AC.2.(a) IV curve of NW C under UV illumination (blue, left y-axis) and in the dark (black, right y-axis). (b) Maximum peak wavelength vs. applied bias in NW D. It can be observed that peaks are blue shifting, yet they do so abruptly.

Annex D: Observation of dispersed Nanowires

A comparison of visible light microscopy and SEM imaging of dispersed NW samples has been done. It has proven succesful in the identification of single NWs. The use of a filter, such as an orange filter, renders the light monochromatic. Through interference effects NWs of diameters below 100 nm appear systematically as bright contrast whereas bigger ones, stacked NWs and bundles appear as dark contrast. All NWs (down to 40 nm thickness in the given studies) are observable that way in visible light microscopy.

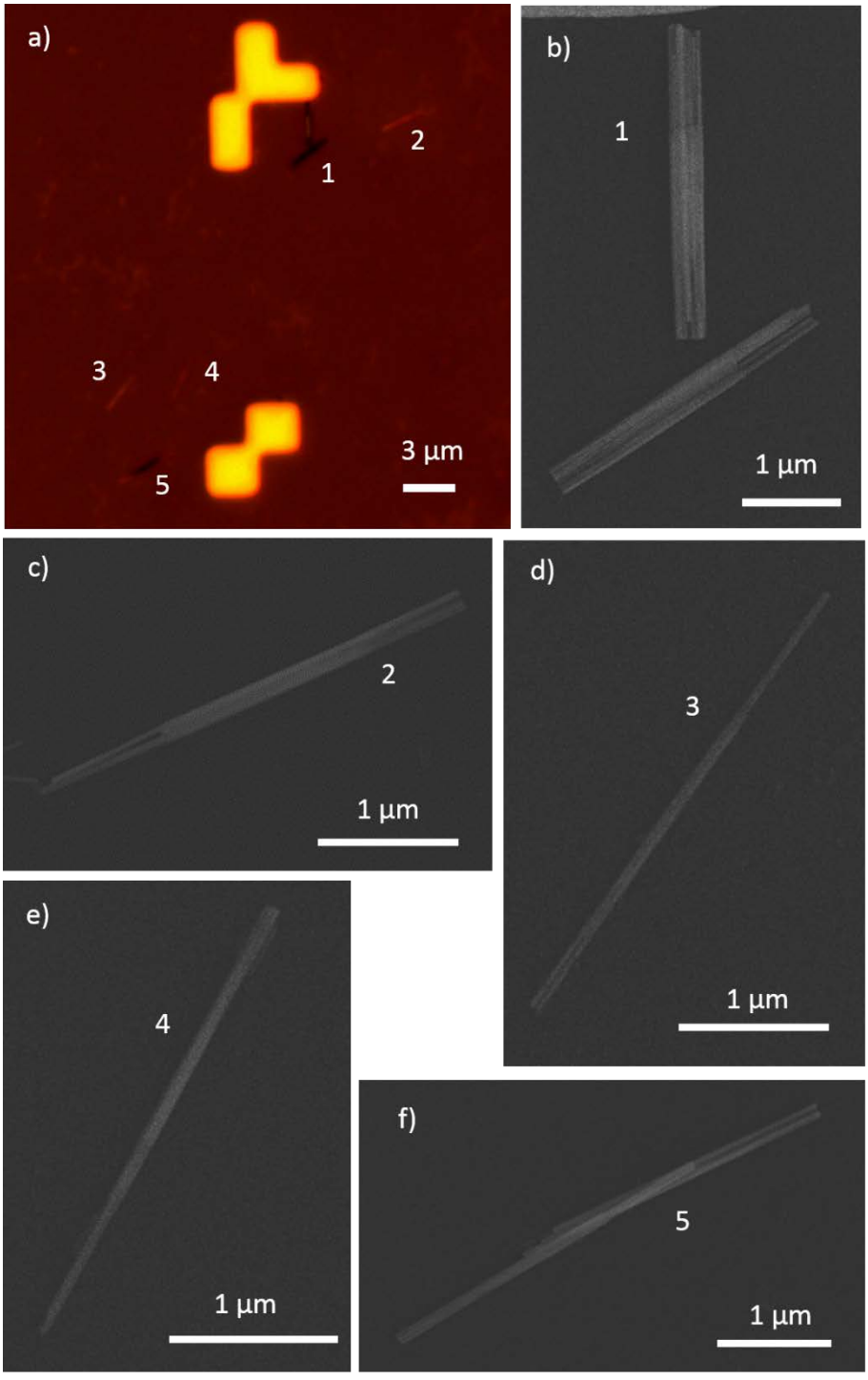

Figure AD.1. Comparison of (a) visible light microscopy employing an orange filter and (b)-(f) SEM images of the same five NW dispered on a 40 nm SiN membrane.

References

(1) Ambacher, O. Growth and Applications of Group III-Nitrides. *J. Phys. Appl. Phys.* **1998**, *31* (20), 2653–2710. https://doi.org/10.1088/0022-3727/31/20/001.

(2) Amano, H.; Kito, M.; Hiramatsu, K.; Akasaki, I. P-Type Conduction in Mg-Doped GaN Treated with Low-Energy Electron Beam Irradiation (LEEBI). *Jpn. J. Appl. Phys.* **1989**, *28* (12A), L2112. https://doi.org/10.1143/JJAP.28.L2112.

(3) Nakamura, S.; Mukai, T.; Senoh, M. High-Power GaN P-N Junction Blue-Light-Emitting Diodes. *Jpn. J. Appl. Phys.* **1991**, *30* (Part 2, No. 12A), L1998–L2001. https://doi.org/10.1143/JJAP.30.L1998.

(4) Nakamura, S. InGaN/AlGaN Blue-light-emitting Diodes. *J. Vac. Sci. Technol. Vac. Surf. Films* **1995**, *13* (3), 705–710. https://doi.org/10.1116/1.579811.

(5) Dingle, R.; Shaklee, K. L.; Leheny, R. F.; Zetterstrom, R. B. Stimulated Emission and Laser Action in Gallium Nitride. *Appl. Phys. Lett.* **1971**, *19* (1), 5–7. https://doi.org/10.1063/1.1653730.

(6) Nakamura, S.; Senoh, M.; Nagahama, S.; Iwasa, N.; Yamada, T.; Matsushita, T.; Kiyoku, H.; Sugimoto, Y. InGaN Multi-quantum-well Structure Laser Diodes Grown on $MgAl_2O_4$ Substrates. *Appl. Phys. Lett.* **1996**, *68* (15), 2105–2107. https://doi.org/10.1063/1.115599.

(7) Nakamura, S.; Senoh, M.; Nagahama, S.; Iwasa, N.; Yamada, T.; Matsushita, T.; Kiyoku, H.; Sugimoto, Y. InGaN Multi-Quantum-Well-Structure Laser Diodes with Cleaved Mirror Cavity Facets. *Jpn. J. Appl. Phys.* **1996**, *35* (Part 2, No. 2B), L217–L220. https://doi.org/10.1143/JJAP.35.L217.

(8) Nakamura, S.; Senoh, M.; Nagahama, S.; Iwasa, N.; Yamada, T.; Matsushita, T.; Sugimoto, Y.; Kiyoku, H. Continuous-wave Operation of InGaN Multi-quantum-well-structure Laser Diodes at 233 K. *Appl. Phys. Lett.* **1996**, *69* (20), 3034–3036. https://doi.org/10.1063/1.116830.

(9) Khan, M. A.; Kuznia, J. N.; Olson, D. T.; Van Hove, J. M.; Blasingame, M.; Reitz, L. F. High-responsivity Photoconductive Ultraviolet Sensors Based on Insulating Single-crystal GaN Epilayers. *Appl. Phys. Lett.* **1992**, *60* (23), 2917–2919. https://doi.org/10.1063/1.106819.

(10) Walker, D.; Zhang, X.; Kung, P.; Saxler, A.; Javadpour, S.; Xu, J.; Razeghi, M. AlGaN Ultraviolet Photoconductors Grown on Sapphire. *Appl. Phys. Lett.* **1996**, *68* (15), 2100–2101. https://doi.org/10.1063/1.115597.

(11) Shur, M. S.; Khan, M. A. GaN/AIGaN Heterostructure Devices: Photodetectors and Field-Effect Transistors. *MRS Bull.* **1997**, *22* (2), 44–50. https://doi.org/10.1557/S0883769400032565.

(12) Xu, G. Y.; Salvador, A.; Kim, W.; Fan, Z.; Lu, C.; Tang, H.; Morkoç, H.; Smith, G.; Estes, M.; Goldenberg, B.; et al. High Speed, Low Noise Ultraviolet Photodetectors Based on GaN p-i-n and AlGaN(p)-GaN(i)-GaN(n)Structures. *Appl. Phys. Lett.* **1997**, *71* (15), 2154–2156. https://doi.org/10.1063/1.119366.

(13) Chen, Q.; Yang, J. W.; Osinsky, A.; Gangopadhyay, S.; Lim, B.; Anwar, M. Z.; Asif Khan, M.; Kuksenkov, D.; Temkin, H. Schottky Barrier Detectors on GaN for Visible–Blind Ultraviolet Detection. *Appl. Phys. Lett.* **1997**, *70* (17), 2277–2279. https://doi.org/10.1063/1.118837.

(14) Van Hove, J. M.; Hickman, R.; Klaassen, J. J.; Chow, P. P.; Ruden, P. P. Ultraviolet-Sensitive, Visible-Blind GaN Photodiodes Fabricated by Molecular Beam Epitaxy. *Appl. Phys. Lett.* **1997**, *70* (17), 2282–2284. https://doi.org/10.1063/1.118838.

(15) Spies, M.; Monroy, E. Nanowire Photodetectors Based on Wurtzite Semiconductor Heterostructures. *Semicond. Sci. Technol.* **2019**, *34* (5), 053002. https://doi.org/10.1088/1361-6641/ab0cb8.

(16) Santori, C.; Pelton, M.; Solomon, G.; Dale, Y.; Yamamoto, Y. Triggered Single Photons from a Quantum Dot. *Phys. Rev. Lett.* **2001**, *86* (8), 1502–1505. https://doi.org/10.1103/PhysRevLett.86.1502.

(17) Holmes, M. J.; Choi, K.; Kako, S.; Arita, M.; Arakawa, Y. Room-Temperature Triggered Single Photon Emission from a III-Nitride Site-Controlled Nanowire Quantum Dot. *Nano Lett.* **2014**, *14* (2), 982–986. https://doi.org/10.1021/nl404400d.
(18) González-Posada, F.; Songmuang, R.; Den Hertog, M.; Monroy, E. Room-Temperature Photodetection Dynamics of Single GaN Nanowires. *Nano Lett.* **2012**, *12* (1), 172–176. https://doi.org/10.1021/nl2032684.
(19) Rigutti, L.; Jacopin, G.; Bugallo, A. D. L.; Tchernycheva, M.; Warde, E.; Julien, F. H.; Songmuang, R.; Galopin, E.; Largeau, L.; Harmand, J.-C. Investigation of the Electronic Transport in GaN Nanowires Containing GaN/AlN Quantum Discs. *Nanotechnology* **2010**, *21* (42), 425206. https://doi.org/10.1088/0957-4484/21/42/425206.
(20) Rigutti, L.; Tchernycheva, M.; De Luna Bugallo, A.; Jacopin, G.; Julien, F. H.; Zagonel, L. F.; March, K.; Stephan, O.; Kociak, M.; Songmuang, R. Ultraviolet Photodetector Based on GaN/AlN Quantum Disks in a Single Nanowire. *Nano Lett.* **2010**, *10* (8), 2939–2943. https://doi.org/10.1021/nl1010977.
(21) den Hertog, M. I.; González-Posada, F.; Songmuang, R.; Rouviere, J. L.; Fournier, T.; Fernandez, B.; Monroy, E. Correlation of Polarity and Crystal Structure with Optoelectronic and Transport Properties of GaN/AlN/GaN Nanowire Sensors. *Nano Lett.* **2012**, *12* (11), 5691–5696. https://doi.org/10.1021/nl302890f.
(22) Renard, J.; Songmuang, R.; Bougerol, C.; Daudin, B.; Gayral, B. Exciton and Biexciton Luminescence from Single GaN/AlN Quantum Dots in Nanowires. *Nano Lett.* **2008**, *8* (7), 2092–2096. https://doi.org/10.1021/nl0800873.
(23) Renard, J.; Kandaswamy, P. K.; Monroy, E.; Gayral, B. Suppression of Nonradiative Processes in Long-Lived Polar GaN/AlN Quantum Dots. *Appl. Phys. Lett.* **2009**, *95* (13), 131903. https://doi.org/10.1063/1.3238311.
(24) Zagonel, L. F.; Mazzucco, S.; Tencé, M.; March, K.; Bernard, R.; Laslier, B.; Jacopin, G.; Tchernycheva, M.; Rigutti, L.; Julien, F. H.; et al. Nanometer Scale Spectral Imaging of Quantum Emitters in Nanowires and Its Correlation to Their Atomically Resolved Structure. *Nano Lett.* **2011**, *11* (2), 568–573. https://doi.org/10.1021/nl103549t.
(25) Arita, M.; Le Roux, F.; Holmes, M. J.; Kako, S.; Arakawa, Y. Ultraclean Single Photon Emission from a GaN Quantum Dot. *Nano Lett.* **2017**, *17* (5), 2902–2907. https://doi.org/10.1021/acs.nanolett.7b00109.
(26) Müßener, J.; Teubert, J.; Hille, P.; Schäfer, M.; Schörmann, J.; de la Mata, M.; Arbiol, J.; Eickhoff, M. Probing the Internal Electric Field in GaN/AlGaN Nanowire Heterostructures. *Nano Lett.* **2014**, *14* (9), 5118–5122. https://doi.org/10.1021/nl501845m.
(27) Renard, J. Optical Properties of GaN Quantum Dots and Nanowires. 2009.
(28) Vurgaftman, I.; Meyer, J. R. Band Parameters for Nitrogen-Containing Semiconductors. *J. Appl. Phys.* **2003**, *94* (6), 3675. https://doi.org/10.1063/1.1600519.
(29) Fiorentini, V.; Bernardini, F.; Ambacher, O. Evidence for Nonlinear Macroscopic Polarization in III–V Nitride Alloy Heterostructures. *Appl. Phys. Lett.* **2002**, *80* (7), 1204–1206. https://doi.org/10.1063/1.1448668.
(30) Bernardini, F.; Fiorentini, V.; Vanderbilt, D. Spontaneous Polarization and Piezoelectric Constants of III-V Nitrides. *Phys. Rev. B* **1997**, *56* (16), R10024–R10027. https://doi.org/10.1103/PhysRevB.56.R10024.
(31) Ambacher, O.; Foutz, B.; Smart, J.; Shealy, J. R.; Weimann, N. G.; Chu, K.; Murphy, M.; Sierakowski, A. J.; Schaff, W. J.; Eastman, L. F.; et al. Two Dimensional Electron Gases Induced by Spontaneous and Piezoelectric Polarization in Undoped and Doped AlGaN/GaN Heterostructures. *J. Appl. Phys.* **2000**, *87* (1), 334–344. https://doi.org/10.1063/1.371866.
(32) Polian, A.; Grimsditch, M.; Grzegory, I. Elastic Constants of Gallium Nitride. *J. Appl. Phys.* **1996**, *79* (6), 3343–3344. https://doi.org/10.1063/1.361236.
(33) Wright, A. F. Elastic Properties of Zinc-Blende and Wurtzite AlN, GaN, and InN. *J. Appl. Phys.* **1997**, *82* (6), 2833–2839. https://doi.org/10.1063/1.366114.

(34) Suzuki, M.; Uenoyama, T.; Yanase, A. First-Principles Calculations of Effective-Mass Parameters of AlN and GaN. *Phys. Rev. B* **1995**, *52* (11), 8132–8139. https://doi.org/10.1103/PhysRevB.52.8132.
(35) Bloom, S.; Harbeke, G.; Meier, E.; Ortenburger, I. B. Band Structure and Reflectivity of GaN. *Phys. Status Solidi B* **1974**, *66* (1), 161–168. https://doi.org/10.1002/pssb.2220660117.
(36) Kobayashi, A.; Sankey, O. F.; Volz, S. M.; Dow, J. D. Semiempirical Tight-Binding Band Structures of Wurtzite Semiconductors: AlN, CdS, CdSe, ZnS, and ZnO. *Phys. Rev. B* **1983**, *28* (2), 935–945. https://doi.org/10.1103/PhysRevB.28.935.
(37) Monroy, E. Development and Characterization of III-Nitride Based Ultraviolet Photodetectors. 1999.
(38) Morkoç, H. *Nitride Semiconductor Devices: Fundamentals and Applications*; John Wiley & Sons, 2013.
(39) Santic, B. On the Hole Effective Mass and the Free Hole Statistics in Wurtzite GaN. *Semicond. Sci. Technol.* **2003**, *18* (4), 219–224. https://doi.org/10.1088/0268-1242/18/4/305.
(40) Ramos, L. E.; Teles, L. K.; Scolfaro, L. M. R.; Castineira, J. L. P.; Rosa, A. L.; Leite, J. R. Structural, Electronic, and Effective-Mass Properties of Silicon and Zinc-Blende Group-III Nitride Semiconductor Compounds. *Phys. Rev. B* **2001**, *63* (16), 165210. https://doi.org/10.1103/PhysRevB.63.165210.
(41) Yan, Q.; Rinke, P.; Janotti, A.; Scheffler, M.; Van de Walle, C. G. Effects of Strain on the Band Structure of Group-III Nitrides. *Phys. Rev. B* **2014**, *90* (12), 125118. https://doi.org/10.1103/PhysRevB.90.125118.
(42) Gorczyca, I.; Suski, T.; Christensen, N. E.; Svane, A. Size Effects in Band Gap Bowing in Nitride Semiconducting Alloys. *Phys. Rev. B* **2011**, *83* (15), 153301. https://doi.org/10.1103/PhysRevB.83.153301.
(43) Tchernycheva, M.; Nevou, L.; Doyennette, L.; Julien, F.; Warde, E.; Guillot, F.; Monroy, E.; Bellet-Amalric, E.; Remmele, T.; Albrecht, M. Systematic Experimental and Theoretical Investigation of Intersubband Absorption in GaN/AlN Quantum Wells. *Phys. Rev. B* **2006**, *73* (12), 125347. https://doi.org/10.1103/PhysRevB.73.125347.
(44) King, P. D. C.; Veal, T. D.; Kendrick, C. E.; Bailey, L. R.; Durbin, S. M.; McConville, C. F. InN/GaN Valence Band Offset: High-Resolution x-Ray Photoemission Spectroscopy Measurements. *Phys. Rev. B* **2008**, *78* (3), 033308. https://doi.org/10.1103/PhysRevB.78.033308.
(45) Grandjean, N.; Damilano, B.; Dalmasso, S.; Leroux, M.; Laügt, M.; Massies, J. Built-in Electric-Field Effects in Wurtzite AlGaN/GaN Quantum Wells. *J. Appl. Phys.* **1999**, *86* (7), 3714. https://doi.org/10.1063/1.371241.
(46) Wagner, R. S.; Ellis, W. C. Vapor-liquid-solid Mechanism of Single Crystal Growth. *Appl. Phys. Lett.* **1964**, *4* (5), 89–90. https://doi.org/10.1063/1.1753975.
(47) Beznasyuk, D. V.; Robin, E.; Hertog, M. D.; Claudon, J.; Hocevar, M. Dislocation-Free Axial InAs-on-GaAs Nanowires on Silicon. *Nanotechnology* **2017**, *28* (36), 365602. https://doi.org/10.1088/1361-6528/aa7d40.
(48) Fontcuberta i Morral, A.; Colombo, C.; Abstreiter, G.; Arbiol, J.; Morante, J. R. Nucleation Mechanism of Gallium-Assisted Molecular Beam Epitaxy Growth of Gallium Arsenide Nanowires. *Appl. Phys. Lett.* **2008**, *92* (6), 063112. https://doi.org/10.1063/1.2837191.
(49) Zi, Y.; Suslov, S.; Yang, C. Understanding Self-Catalyzed Epitaxial Growth of III–V Nanowires toward Controlled Synthesis. *Nano Lett.* **2017**, *17* (2), 1167–1173. https://doi.org/10.1021/acs.nanolett.6b04817.
(50) Yoshizawa, M.; Kikuchi, A.; Mori, M.; Fujita, N.; Kishino, K. Growth of Self-Organized GaN Nanostructures on Al2O3(0001) by RF-Radical Source Molecular Beam Epitaxy. *Jpn. J. Appl. Phys.* **1997**, *36* (Part 2, No. 4B), L459–L462. https://doi.org/10.1143/JJAP.36.L459.
(51) Sanchez-Garcia, M. A.; Calleja, E.; Monroy, E.; Sanchez, F. J.; Calle, F.; Muñoz, E.; Beresford, R. The Effect of the III/V Ratio and Substrate Temperature on the Morphology and Properties of GaN- and AlN-Layers Grown by Molecular Beam Epitaxy on Si(1 1 1). *J. Cryst. Growth* **1998**, *183* (1–2), 23–30. https://doi.org/10.1016/S0022-0248(97)00386-2.

(52) Consonni, V.; Knelangen, M.; Geelhaar, L.; Trampert, A.; Riechert, H. Nucleation Mechanisms of Epitaxial GaN Nanowires: Origin of Their Self-Induced Formation and Initial Radius. *Phys. Rev. B* **2010**, *81* (8), 085310. https://doi.org/10.1103/PhysRevB.81.085310.
(53) Dai, Z. R.; Pan, Z. W.; Wang, Z. L. Novel Nanostructures of Functional Oxides Synthesized by Thermal Evaporation. *Adv. Funct. Mater.* **2003**, *13* (1), 9–24. https://doi.org/10.1002/adfm.200390013.
(54) Noborisaka, J.; Motohisa, J.; Fukui, T. Catalyst-Free Growth of GaAs Nanowires by Selective-Area Metalorganic Vapor-Phase Epitaxy. *Appl. Phys. Lett.* **2005**, *86* (21), 213102. https://doi.org/10.1063/1.1935038.
(55) Tomioka, K.; Mohan, P.; Noborisaka, J.; Hara, S.; Motohisa, J.; Fukui, T. Growth of Highly Uniform InAs Nanowire Arrays by Selective-Area MOVPE. *J. Cryst. Growth* **2007**, *298*, 644–647. https://doi.org/10.1016/j.jcrysgro.2006.10.183.
(56) Kishino, K.; Hoshino, T.; Ishizawa, S.; Kikuchi, A. Selective-Area Growth of GaN Nanocolumns on Titanium-Mask-Patterned Silicon (111) Substrates by RF-Plasma-Assisted Molecular-Beam Epitaxy. *Electron. Lett.* **2008**, *44* (13), 819. https://doi.org/10.1049/el:20081323.
(57) Goto, H.; Nosaki, K.; Tomioka, K.; Hara, S.; Hiruma, K.; Motohisa, J.; Fukui, T. Growth of Core–Shell InP Nanowires for Photovoltaic Application by Selective-Area Metal Organic Vapor Phase Epitaxy. *Appl. Phys. Express* **2009**, *2*, 035004. https://doi.org/10.1143/APEX.2.035004.
(58) Choi, K.; Arita, M.; Arakawa, Y. Selective-Area Growth of Thin GaN Nanowires by MOCVD. *J. Cryst. Growth* **2012**, *357*, 58–61. https://doi.org/10.1016/j.jcrysgro.2012.07.025.
(59) Kishino, K.; Ishizawa, S. Selective-Area Growth of GaN Nanocolumns on Si(111) Substrates for Application to Nanocolumn Emitters with Systematic Analysis of Dislocation Filtering Effect of Nanocolumns. *Nanotechnology* **2015**, *26* (22), 225602. https://doi.org/10.1088/0957-4484/26/22/225602.
(60) Debnath, R.; Ha, J.-Y.; Wen, B.; Paramanik, D.; Motayed, A.; King, M. R.; Davydov, A. V. Top-down Fabrication of Large-Area GaN Micro- and Nanopillars. *J. Vac. Sci. Technol. B Nanotechnol. Microelectron. Mater. Process. Meas. Phenom.* **2014**, *32* (2), 021204. https://doi.org/10.1116/1.4865908.
(61) Wang, H.; Sun, M.; Ding, K.; Hill, M. T.; Ning, C.-Z. A Top-down Approach to Fabrication of High Quality Vertical Heterostructure Nanowire Arrays. *Nano Lett.* **2011**, *11* (4), 1646–1650. https://doi.org/10.1021/nl2001132.
(62) Lähnemann, J.; Browne, D. A.; Ajay, A.; Jeannin, M.; Vasanelli, A.; Thomassin, J.-L.; Bellet-Amalric, E.; Monroy, E. Near- and Mid-Infrared Intersubband Absorption in Top-down GaN/AlN Nano- and Micro-Pillars. *Nanotechnology* **2019**, *30* (5), 054002. https://doi.org/10.1088/1361-6528/aaef72.
(63) Li, Q.; Wright, J. B.; Chow, W. W.; Luk, T. S.; Brener, I.; Lester, L. F.; Wang, G. T. Single-Mode GaN Nanowire Lasers. *Opt. Express* **2012**, *20* (16), 17873. https://doi.org/10.1364/OE.20.017873.
(64) Alloing, B.; Vézian, S.; Tottereau, O.; Vennéguès, P.; Beraudo, E.; Zuniga-Pérez, J. On the Polarity of GaN Micro- and Nanowires Epitaxially Grown on Sapphire (0001) and Si(111) Substrates by Metal Organic Vapor Phase Epitaxy and Ammonia-Molecular Beam Epitaxy. *Appl. Phys. Lett.* **2011**, *98* (1), 011914. https://doi.org/10.1063/1.3525170.
(65) Chen, X. J.; Perillat-Merceroz, G.; Sam-Giao, D.; Durand, C.; Eymery, J. Homoepitaxial Growth of Catalyst-Free GaN Wires on N-Polar Substrates. *Appl. Phys. Lett.* **2010**, *97* (15), 151909. https://doi.org/10.1063/1.3497078.
(66) Bergbauer, W.; Strassburg, M.; Kölper, C.; Linder, N.; Roder, C.; Lähnemann, J.; Trampert, A.; Fündling, S.; Li, S. F.; Wehmann, H.-H.; et al. Continuous-Flux MOVPE Growth of Position-Controlled N-Face GaN Nanorods and Embedded InGaN Quantum Wells. *Nanotechnology* **2010**, *21* (30), 305201. https://doi.org/10.1088/0957-4484/21/30/305201.

(67) Chen, X. J.; Gayral, B.; Sam-Giao, D.; Bougerol, C.; Durand, C.; Eymery, J. Catalyst-Free Growth of High-Optical Quality GaN Nanowires by Metal-Organic Vapor Phase Epitaxy. *Appl. Phys. Lett.* **2011**, *99* (25), 251910. https://doi.org/10.1063/1.3671365.
(68) Foltynski, B.; Garro, N.; Vallo, M.; Finken, M.; Giesen, C.; Kalisch, H.; Vescan, A.; Cantarero, A.; Heuken, M. The Controlled Growth of GaN Microrods on Si(111) Substrates by MOCVD. *J. Cryst. Growth* **2015**, *414*, 200–204. https://doi.org/10.1016/j.jcrysgro.2014.10.047.
(69) Auzelle, T.; Haas, B.; Den Hertog, M.; Rouvière, J.-L.; Daudin, B.; Gayral, B. Attribution of the 3.45 EV GaN Nanowires Luminescence to Inversion Domain Boundaries. *Appl. Phys. Lett.* **2015**, *107* (5), 051904. https://doi.org/10.1063/1.4927826.
(70) Sekiguchi, H.; Kishino, K.; Kikuchi, A. Ti-Mask Selective-Area Growth of GaN by RF-Plasma-Assisted Molecular-Beam Epitaxy for Fabricating Regularly Arranged InGaN/GaN Nanocolumns. *Appl. Phys. Express* **2008**, *1*, 124002. https://doi.org/10.1143/APEX.1.124002.
(71) Huang, Y.; Duan, X.; Cui, Y.; Lieber, C. M. Gallium Nitride Nanowire Nanodevices. *Nano Lett.* **2002**, *2* (2), 101–104. https://doi.org/10.1021/nl015667d.
(72) Kim, J.-R.; So, H. M.; Park, J. W.; Kim, J.-J.; Kim, J.; Lee, C. J.; Lyu, S. C. Electrical Transport Properties of Individual Gallium Nitride Nanowires Synthesized by Chemical-Vapor-Deposition. *Appl. Phys. Lett.* **2002**, *80* (19), 3548–3550. https://doi.org/10.1063/1.1478158.
(73) Fang, Z.; Robin, E.; Rozas-Jiménez, E.; Cros, A.; Donatini, F.; Mollard, N.; Pernot, J.; Daudin, B. Si Donor Incorporation in GaN Nanowires. *Nano Lett.* **2015**, *15* (10), 6794–6801. https://doi.org/10.1021/acs.nanolett.5b02634.
(74) Ajay, A.; Schörmann, J.; Jiménez-Rodriguez, M.; Lim, C. B.; Walther, F.; Rohnke, M.; Mouton, I.; Amichi, L.; Bougerol, C.; Den Hertog, M. I.; et al. Ge Doping of GaN beyond the Mott Transition. *J. Phys. Appl. Phys.* **2016**, *49* (44), 445301. https://doi.org/10.1088/0022-3727/49/44/445301.
(75) Zhong, Z.; Qian, F.; Wang, D.; Lieber, C. M. Synthesis of P-Type Gallium Nitride Nanowires for Electronic and Photonic Nanodevices. *Nano Lett.* **2003**, *3* (3), 343–346. https://doi.org/10.1021/nl034003w.
(76) Zhang, H.; Guan, N.; Piazza, V.; Kapoor, A.; Bougerol, C.; Julien, F. H.; Babichev, A. V.; Cavassilas, N.; Bescond, M.; Michelini, F.; et al. Comprehensive Analyses of Core–Shell InGaN/GaN Single Nanowire Photodiodes. *J. Phys. Appl. Phys.* **2017**, *50* (48), 484001. https://doi.org/10.1088/1361-6463/aa935d.
(77) Son, M. S.; Im, S. I.; Park, Y. S.; Park, C. M.; Kang, T. W.; Yoo, K.-H. Ultraviolet Photodetector Based on Single GaN Nanorod p–n Junctions. *Mater. Sci. Eng. C* **2006**, *26* (5–7), 886–888. https://doi.org/10.1016/j.msec.2005.09.089.
(78) de Luna Bugallo, A.; Tchernycheva, M.; Jacopin, G.; Rigutti, L.; Julien, F. H.; Chou, S.-T.; Lin, Y.-T.; Tseng, P.-H.; Tu, L.-W. Visible-Blind Photodetector Based on p–i–n Junction GaN Nanowire Ensembles. *Nanotechnology* **2010**, *21* (31), 315201. https://doi.org/10.1088/0957-4484/21/31/315201.
(79) Calarco, R.; Marso, M.; Richter, T.; Aykanat, A. I.; Meijers, R.; v.d. Hart, A.; Stoica, T.; Lüth, H. Size-Dependent Photoconductivity in MBE-Grown GaN−Nanowires. *Nano Lett.* **2005**, *5* (5), 981–984. https://doi.org/10.1021/nl0500306.
(80) Sanford, N. A.; Blanchard, P. T.; Bertness, K. A.; Mansfield, L.; Schlager, J. B.; Sanders, A. W.; Roshko, A.; Burton, B. B.; George, S. M. Steady-State and Transient Photoconductivity in c-Axis GaN Nanowires Grown by Nitrogen-Plasma-Assisted Molecular Beam Epitaxy. *J. Appl. Phys.* **2010**, *107* (3), 034318. https://doi.org/10.1063/1.3275888.
(81) González-Posada, F.; Songmuang, R.; Den Hertog, M.; Monroy, E. Environmental Sensitivity of N-i-n and Undoped Single GaN Nanowire Photodetectors. *Appl. Phys. Lett.* **2013**, *102* (21), 213113. https://doi.org/10.1063/1.4808017.
(82) Qian, F.; Li, Y.; Gradečak, S.; Wang, D.; Barrelet, C. J.; Lieber, C. M. Gallium Nitride-Based Nanowire Radial Heterostructures for Nanophotonics. *Nano Lett.* **2004**, *4* (10), 1975–1979. https://doi.org/10.1021/nl0487774.

(83) Dong, Y.; Tian, B.; Kempa, T. J.; Lieber, C. M. Coaxial Group III−Nitride Nanowire Photovoltaics. *Nano Lett.* **2009**, *9* (5), 2183–2187. https://doi.org/10.1021/nl900858v.
(84) Zhao, Z.; Pu, X.; Han, C.; Du, C.; Li, L.; Jiang, C.; Hu, W.; Wang, Z. L. Piezotronic Effect in Polarity-Controlled GaN Nanowires. *ACS Nano* **2015**, *9* (8), 8578–8583. https://doi.org/10.1021/acsnano.5b03737.
(85) Zhang, Y.; Liu, Y.; Wang, Z. L. Fundamental Theory of Piezotronics. *Adv. Mater.* **2011**, *23* (27), 3004–3013. https://doi.org/10.1002/adma.201100906.
(86) Guo, W.; Zhang, M.; Banerjee, A.; Bhattacharya, P. Catalyst-Free InGaN/GaN Nanowire Light Emitting Diodes Grown on (001) Silicon by Molecular Beam Epitaxy. *Nano Lett.* **2010**, *10* (9), 3355–3359. https://doi.org/10.1021/nl101027x.
(87) Prabaswara, A.; Min, J.-W.; Zhao, C.; Janjua, B.; Zhang, D.; Albadri, A. M.; Alyamani, A. Y.; Ng, T. K.; Ooi, B. S. Direct Growth of III-Nitride Nanowire-Based Yellow Light-Emitting Diode on Amorphous Quartz Using Thin Ti Interlayer. *Nanoscale Res. Lett.* **2018**, *13* (1), 41. https://doi.org/10.1186/s11671-018-2453-1.
(88) Johnson, J. C.; Choi, H.-J.; Knutsen, K. P.; Schaller, R. D.; Yang, P.; Saykally, R. J. Single Gallium Nitride Nanowire Lasers. *Nat. Mater.* **2002**, *1* (2), 106–110. https://doi.org/10.1038/nmat728.
(89) Han, S.; Jin, W.; Zhang, D.; Tang, T.; Li, C.; Liu, X.; Liu, Z.; Lei, B.; Zhou, C. Photoconduction Studies on GaN Nanowire Transistors under UV and Polarized UV Illumination. *Chem. Phys. Lett.* **2004**, *389* (1–3), 176–180. https://doi.org/10.1016/j.cplett.2004.03.083.
(90) Wu, H.; Cha, H.-Y.; Chandrashekhar, M.; Spencer, M. G.; Koley, G. High-Yield GaN Nanowire Synthesis and Field-Effect Transistor Fabrication. *J. Electron. Mater.* **2006**, *35* (4), 670–674. https://doi.org/10.1007/s11664-006-0118-9.
(91) Li, Y.; Xiang, J.; Qian, F.; Gradečak, S.; Wu, Y.; Yan, H.; Blom, D. A.; Lieber, C. M. Dopant-Free GaN/AlN/AlGaN Radial Nanowire Heterostructures as High Electron Mobility Transistors. *Nano Lett.* **2006**, *6* (7), 1468–1473. https://doi.org/10.1021/nl060849z.
(92) Duan, X.; Huang, Y.; Lieber, C. M. Nonvolatile Memory and Programmable Logic from Molecule-Gated Nanowires. *Nano Lett.* **2002**, *2* (5), 487–490. https://doi.org/10.1021/nl025532n.
(93) Chou, H. T.; Goldhaber-Gordon, D.; Schmult, S.; Manfra, M. J.; Sergent, A. M.; Molnar, R. J. Single-Electron Transistors in GaN/AlGaN Heterostructures. *Appl. Phys. Lett.* **2006**, *89* (3), 033104. https://doi.org/10.1063/1.2226454.
(94) Kim, J.-R.; Kim, B.-K.; Lee, I. J.; Kim, J.-J.; Kim, J.; Lyu, S. C.; Lee, C. J. Temperature-Dependent Single-Electron Tunneling Effect in Lightly and Heavily Doped GaN Nanowires. *Phys. Rev. B* **2004**, *69* (23), 233303. https://doi.org/10.1103/PhysRevB.69.233303.
(95) Feiginov, M.; Sydlo, C.; Cojocari, O.; Meissner, P. Resonant-Tunnelling-Diode Oscillators Operating at Frequencies above 1.1 THz. *Appl. Phys. Lett.* **2011**, *99* (23), 233506. https://doi.org/10.1063/1.3667191.
(96) Suzuki, S.; Asada, M.; Teranishi, A.; Sugiyama, H.; Yokoyama, H. Fundamental Oscillation of Resonant Tunneling Diodes above 1 THz at Room Temperature. *Appl. Phys. Lett.* **2010**, *97* (24), 242102. https://doi.org/10.1063/1.3525834.
(97) Chen, R. S.; Lu, C. Y.; Chen, K. H.; Chen, L. C. Molecule-Modulated Photoconductivity and Gain-Amplified Selective Gas Sensing in Polar GaN Nanowires. *Appl. Phys. Lett.* **2009**, *95* (23), 233119. https://doi.org/10.1063/1.3264954.
(98) Kishino, K.; Unlu, M. S.; Chyi, J.-I.; Reed, J.; Arsenault, L.; Morkoc, H. Resonant Cavity-Enhanced (RCE) Photodetectors. *IEEE J. Quantum Electron.* **1991**, *27* (8), 2025–2034. https://doi.org/10.1109/3.83412.
(99) Goushcha, A. O.; Tabbert, B. On Response Time of Semiconductor Photodiodes. *Opt. Eng.* **2017**, *56* (09), 1. https://doi.org/10.1117/1.OE.56.9.097101.
(100) Xu, Y.; Gong, T.; Munday, J. N. The Generalized Shockley-Queisser Limit for Nanostructured Solar Cells. *Sci. Rep.* **2015**, *5*, 13536.
(101) Heiss, M.; Russo-Averchi, E.; Dalmau-Mallorquí, A.; Tütüncüoğlu, G.; Matteini, F.; Rüffer, D.; Conesa-Boj, S.; Demichel, O.; Alarcon-Lladó, E.; Fontcuberta i Morral, A. III–V Nanowire

Arrays: Growth and Light Interaction. *Nanotechnology* **2014**, *25* (1), 014015. https://doi.org/10.1088/0957-4484/25/1/014015.
(102) Chen, G.; Wu, J.; Lu, Q.; Gutierrez, H. R.; Xiong, Q.; Pellen, M. E.; Petko, J. S.; Werner, D. H.; Eklund, P. C. Optical Antenna Effect in Semiconducting Nanowires. *Nano Lett.* **2008**, *8* (5), 1341–1346. https://doi.org/10.1021/nl080007v.
(103) Diedenhofen, S. L.; Janssen, O. T. A.; Grzela, G.; Bakkers, E. P. A. M.; Gómez Rivas, J. Strong Geometrical Dependence of the Absorption of Light in Arrays of Semiconductor Nanowires. *ACS Nano* **2011**, *5* (3), 2316–2323. https://doi.org/10.1021/nn103596n.
(104) Heiss, M.; Fontcuberta i Morral, A. Fundamental Limits in the External Quantum Efficiency of Single Nanowire Solar Cells. *Appl. Phys. Lett.* **2011**, *99* (26), 263102. https://doi.org/10.1063/1.3672168.
(105) Cao, L.; White, J. S.; Park, J.-S.; Schuller, J. A.; Clemens, B. M.; Brongersma, M. L. Engineering Light Absorption in Semiconductor Nanowire Devices. *Nat. Mater.* **2009**, *8* (8), 643–647. https://doi.org/10.1038/nmat2477.
(106) Hu, L.; Chen, G. Analysis of Optical Absorption in Silicon Nanowire Arrays for Photovoltaic Applications. *Nano Lett.* **2007**, *7* (11), 3249–3252. https://doi.org/10.1021/nl071018b.
(107) Anttu, N.; Xu, H. Q. Coupling of Light into Nanowire Arrays and Subsequent Absorption. *J. Nanosci. Nanotechnol.* **2010**, *10* (11), 7183–7187. https://doi.org/10.1166/jnn.2010.2907.
(108) Li, J.; Yu, H.; Wong, S. M.; Zhang, G.; Sun, X.; Lo, P. G.-Q.; Kwong, D.-L. Si Nanopillar Array Optimization on Si Thin Films for Solar Energy Harvesting. *Appl. Phys. Lett.* **2009**, *95* (3), 033102. https://doi.org/10.1063/1.3186046.
(109) Narasimhan, V. K.; Cui, Y. Nanostructures for Photon Management in Solar Cells. *Nanophotonics* **2013**, *2* (3), 187–210. https://doi.org/10.1515/nanoph-2013-0001.
(110) Muskens, O. L.; Rivas, J. G.; Algra, R. E.; Bakkers, E. P. A. M.; Lagendijk, A. Design of Light Scattering in Nanowire Materials for Photovoltaic Applications. *Nano Lett.* **2008**, *8* (9), 2638–2642. https://doi.org/10.1021/nl0808076.
(111) Monroy, E.; Omnès, F.; Calle, F. Wide-Bandgap Semiconductor Ultraviolet Photodetectors. *Semicond. Sci. Technol.* **2003**, *18* (4), R33–R51. https://doi.org/10.1088/0268-1242/18/4/201.
(112) Huang, H. M.; Chen, R. S.; Chen, H. Y.; Liu, T. W.; Kuo, C. C.; Chen, C. P.; Hsu, H. C.; Chen, L. C.; Chen, K. H.; Yang, Y. J. Photoconductivity in Single AlN Nanowires by Subband Gap Excitation. *Appl. Phys. Lett.* **2010**, *96* (6), 062104. https://doi.org/10.1063/1.3292211.
(113) Chen, R.-S.; Yang, T.-H.; Chen, H.-Y.; Chen, L.-C.; Chen, K.-H.; Yang, Y.-J.; Su, C.-H.; Lin, C.-R. High-Gain Photoconductivity in Semiconducting InN Nanowires. *Appl. Phys. Lett.* **2009**, *95* (16), 162112. https://doi.org/10.1063/1.3242023.
(114) Soci, C.; Zhang, A.; Xiang, B.; Dayeh, S. A.; Aplin, D. P. R.; Park, J.; Bao, X. Y.; Lo, Y. H.; Wang, D. ZnO Nanowire UV Photodetectors with High Internal Gain. *Nano Lett.* **2007**, *7* (4), 1003–1009. https://doi.org/10.1021/nl070111x.
(115) Chen, M.-W.; Chen, C.-Y.; Lien, D.-H.; Ding, Y.; He, J.-H. Photoconductive Enhancement of Single ZnO Nanowire through Localized Schottky Effects. *Opt. Express* **2010**, *18* (14), 14836. https://doi.org/10.1364/OE.18.014836.
(116) Peng, S.-M.; Su, Y.-K.; Ji, L.-W.; Young, S.-J.; Tsai, C.-N.; Wu, C.-Z.; Chao, W.-C.; Cheng, W.-B.; Huang, C.-J. Photoconductive Gain and Low-Frequency Noise Characteristics of ZnO Nanorods. *Electrochem. Solid-State Lett.* **2011**, *14* (3), J13. https://doi.org/10.1149/1.3521244.
(117) Law, J. B. K.; Thong, J. T. L. Simple Fabrication of a ZnO Nanowire Photodetector with a Fast Photoresponse Time. *Appl. Phys. Lett.* **2006**, *88* (13), 133114. https://doi.org/10.1063/1.2190459.
(118) Nie, B.; Luo, L.-B.; Chen, J.-J.; Hu, J.-G.; Wu, C.-Y.; Wang, L.; Yu, Y.-Q.; Zhu, Z.-F.; Jie, J.-S. Fabrication of P-Type ZnSe:Sb Nanowires for High-Performance Ultraviolet Light Photodetector Application. *Nanotechnology* **2013**, *24* (9), 095603. https://doi.org/10.1088/0957-4484/24/9/095603.

(119) Dai, J.; Song, X.; Zheng, H.; Wu, C. Excitonic Photoluminescence and Photoresponse of ZnS Nanowires. *Mater. Chem. Phys.* **2016**, *174*, 204–208. https://doi.org/10.1016/j.matchemphys.2016.03.006.
(120) Pei, Y.; Pei, R.; Liang, X.; Wang, Y.; Liu, L.; Chen, H.; Liang, J. CdS-Nanowires Flexible Photo-Detector with Ag-Nanowires Electrode Based on Non-Transfer Process. *Sci. Rep.* **2016**, *6* (1). https://doi.org/10.1038/srep21551.
(121) Zhou, W.; Peng, Y.; Yin, Y.; Zhou, Y.; Zhang, Y.; Tang, D. Broad Spectral Response Photodetector Based on Individual Tin-Doped CdS Nanowire. *AIP Adv.* **2014**, *4* (12), 123005. https://doi.org/10.1063/1.4897521.
(122) Maharjan, A.; Pemasiri, K.; Kumar, P.; Wade, A.; Smith, L. M.; Jackson, H. E.; Yarrison-Rice, J. M.; Kogan, A.; Paiman, S.; Gao, Q.; et al. Room Temperature Photocurrent Spectroscopy of Single Zincblende and Wurtzite InP Nanowires. *Appl. Phys. Lett.* **2009**, *94* (19), 193115. https://doi.org/10.1063/1.3138137.
(123) Wang, S. B.; Hsiao, C. H.; Chang, S. J.; Lam, K. T.; Wen, K. H.; Hung, S. C.; Young, S. J.; Huang, B. R. A CuO Nanowire Infrared Photodetector. *Sens. Actuators Phys.* **2011**, *171* (2), 207–211. https://doi.org/10.1016/j.sna.2011.09.011.
(124) Zhang, H.; Babichev, A. V.; Jacopin, G.; Lavenus, P.; Julien, F. H.; Yu. Egorov, A.; Zhang, J.; Pauporté, T.; Tchernycheva, M. Characterization and Modeling of a ZnO Nanowire Ultraviolet Photodetector with Graphene Transparent Contact. *J. Appl. Phys.* **2013**, *114* (23), 234505. https://doi.org/10.1063/1.4854455.
(125) Wang, H. High Gain Single GaAs Nanowire Photodetector. *Appl. Phys. Lett.* **2013**, *103* (9), 093101. https://doi.org/10.1063/1.4816246.
(126) Chen, R.-S.; Chen, H.-Y.; Lu, C.-Y.; Chen, K.-H.; Chen, C.-P.; Chen, L.-C.; Yang, Y.-J. Ultrahigh Photocurrent Gain in M-Axial GaN Nanowires. *Appl. Phys. Lett.* **2007**, *91* (22), 223106. https://doi.org/10.1063/1.2817595.
(127) Kind, H.; Yan, H.; Messer, B.; Law, M.; Yang, P. Nanowire Ultraviolet Photodetectors and Optical Switches. *Adv. Mater.* **2002**, *14* (2), 158–160. https://doi.org/10.1002/1521-4095(20020116)14:2<158::AID-ADMA158>3.0.CO;2-W.
(128) Lähnemann, J.; Den Hertog, M.; Hille, P.; de la Mata, M.; Fournier, T.; Schörmann, J.; Arbiol, J.; Eickhoff, M.; Monroy, E. UV Photosensing Characteristics of Nanowire-Based GaN/AlN Superlattices. *Nano Lett.* **2016**, *16* (5), 3260–3267. https://doi.org/10.1021/acs.nanolett.6b00806.
(129) Soci, C.; Zhang, A.; Bao, X.-Y.; Kim, H.; Lo, Y.; Wang, D. Nanowire Photodetectors. *J. Nanosci. Nanotechnol.* **2010**, *10* (3), 1430–1449. https://doi.org/10.1166/jnn.2010.2157.
(130) Pfüller, C.; Brandt, O.; Grosse, F.; Flissikowski, T.; Chèze, C.; Consonni, V.; Geelhaar, L.; Grahn, H. T.; Riechert, H. Unpinning the Fermi Level of GaN Nanowires by Ultraviolet Radiation. *Phys. Rev. B* **2010**, *82* (4), 045320. https://doi.org/10.1103/PhysRevB.82.045320.
(131) Fang, H.; Hu, W. Photogating in Low Dimensional Photodetectors. *Adv. Sci.* **2017**, *4* (12), 1700323. https://doi.org/10.1002/advs.201700323.
(132) Spies, M.; Polaczyński, J.; Ajay, A.; Kalita, D.; Luong, M. A.; Lähnemann, J.; Gayral, B.; den Hertog, M. I.; Monroy, E. Effect of the Nanowire Diameter on the Linearity of the Response of GaN-Based Heterostructured Nanowire Photodetectors. *Nanotechnology* **2018**, *29* (25), 255204. https://doi.org/10.1088/1361-6528/aab838.
(133) Degtyarev, V. E.; Khazanova, S. V.; Demarina, N. V. Features of Electron Gas in InAs Nanowires Imposed by Interplay between Nanowire Geometry, Doping and Surface States. *Sci. Rep.* **2017**, *7* (1). https://doi.org/10.1038/s41598-017-03415-3.
(134) Alexander-Webber, J. A.; Groschner, C. K.; Sagade, A. A.; Tainter, G.; Gonzalez-Zalba, M. F.; Di Pietro, R.; Wong-Leung, J.; Tan, H. H.; Jagadish, C.; Hofmann, S.; et al. Engineering the Photoresponse of InAs Nanowires. *ACS Appl. Mater. Interfaces* **2017**, *9* (50), 43993–44000. https://doi.org/10.1021/acsami.7b14415.
(135) Olsson, L. Ö.; Andersson, C. B. M.; Håkansson, M. C.; Kanski, J.; Ilver, L.; Karlsson, U. O. Charge Accumulation at InAs Surfaces. *Phys. Rev. Lett.* **1996**, *76* (19), 3626–3629. https://doi.org/10.1103/PhysRevLett.76.3626.

(136) Werner, F.; Limbach, F.; Carsten, M.; Denker, C.; Malindretos, J.; Rizzi, A. Electrical Conductivity of InN Nanowires and the Influence of the Native Indium Oxide Formed at Their Surface. *Nano Lett.* **2009**, *9* (4), 1567–1571. https://doi.org/10.1021/nl8036799.
(137) Chaudhry, A.; Islam, M. S. Examining the Anomalous Electrical Characteristics Observed in InN Nanowires. *J. Nanosci. Nanotechnol.* **2008**, *8* (1), 222–227. https://doi.org/10.1166/jnn.2008.N18.
(138) Barick, B. K.; Rodríguez-Fernández, C.; Cantarero, A.; Dhar, S. Structural and Electronic Properties of InN Nanowire Network Grown by Vapor-Liquid-Solid Method. *AIP Adv.* **2015**, *5* (5), 057162. https://doi.org/10.1063/1.4921946.
(139) Yu, Y.; Jie, J.; Jiang, P.; Wang, L.; Wu, C.; Peng, Q.; Zhang, X.; Wang, Z.; Xie, C.; Wu, D.; et al. High-Gain Visible-Blind UV Photodetectors Based on Chlorine-Doped n-Type ZnS Nanoribbons with Tunable Optoelectronic Properties. *J. Mater. Chem.* **2011**, *21* (34), 12632. https://doi.org/10.1039/c1jm11408e.
(140) Yen, S.-H.; Hung, Y.-C.; Yeh, P.-H.; Su, Y.-W.; Wang, C.-Y. Fabrication of Single Ga-Doped ZnS Nanowires as High-Gain Photosensors by Focused Ion Beam Deposition. *Nanotechnology* **2017**, *28* (39), 395201. https://doi.org/10.1088/1361-6528/aa7d99.
(141) Wang, X.; Zhang, Y.; Chen, X.; He, M.; Liu, C.; Yin, Y.; Zou, X.; Li, S. Ultrafast, Superhigh Gain Visible-Blind UV Detector and Optical Logic Gates Based on Nonpolar a-Axial GaN Nanowire. *Nanoscale* **2014**, *6* (20), 12009–12017. https://doi.org/10.1039/C4NR03581J.
(142) Thunich, S.; Prechtel, L.; Spirkoska, D.; Abstreiter, G.; Fontcuberta i Morral, A.; Holleitner, A. W. Photocurrent and Photoconductance Properties of a GaAs Nanowire. *Appl. Phys. Lett.* **2009**, *95* (8), 083111. https://doi.org/10.1063/1.3193540.
(143) Miao, J.; Hu, W.; Guo, N.; Lu, Z.; Zou, X.; Liao, L.; Shi, S.; Chen, P.; Fan, Z.; Ho, J. C.; et al. Single InAs Nanowire Room-Temperature Near-Infrared Photodetectors. *ACS Nano* **2014**, *8* (4), 3628–3635. https://doi.org/10.1021/nn500201g.
(144) Garrido, J. A.; Monroy, E.; Izpura, I.; Muñoz, E. Photoconductive Gain Modelling of GaN Photodetectors. *Semicond. Sci. Technol.* **1998**, *13* (6), 563–568. https://doi.org/10.1088/0268-1242/13/6/005.
(145) Sanford, N. A.; Robins, L. H.; Blanchard, P. T.; Soria, K.; Klein, B.; Eller, B. S.; Bertness, K. A.; Schlager, J. B.; Sanders, A. W. Studies of Photoconductivity and Field Effect Transistor Behavior in Examining Drift Mobility, Surface Depletion, and Transient Effects in Si-Doped GaN Nanowires in Vacuum and Air. *J. Appl. Phys.* **2013**, *113* (17), 174306. https://doi.org/10.1063/1.4802689.
(146) Hullavarad, S.; Hullavarad, N.; Look, D.; Claflin, B. Persistent Photoconductivity Studies in Nanostructured ZnO UV Sensors. *Nanoscale Res. Lett.* **2009**, *4* (12), 1421–1427. https://doi.org/10.1007/s11671-009-9414-7.
(147) Foussekis, M.; Baski, A. A.; Reshchikov, M. A. Photoadsorption and Photodesorption for GaN. *Appl. Phys. Lett.* **2009**, *94* (16), 162116. https://doi.org/10.1063/1.3122934.
(148) Lefebvre, P.; Albert, S.; Ristić, J.; Fernández-Garrido, S.; Grandal, J.; Sánchez-García, M.-A.; Calleja, E. Oxygen Photo-Adsorption Related Quenching of Photoluminescence in Group-III Nitride Nanocolumns. *Superlattices Microstruct.* **2012**, *52* (2), 165–171. https://doi.org/10.1016/j.spmi.2012.05.001.
(149) Su, L.; Yang, W.; Cai, J.; Chen, H.; Fang, X. Self-Powered Ultraviolet Photodetectors Driven by Built-In Electric Field. *Small* **2017**, *13* (45), 1701687. https://doi.org/10.1002/smll.201701687.
(150) Cheng, G.; Li, Z.; Wang, S.; Gong, H.; Cheng, K.; Jiang, X.; Zhou, S.; Du, Z.; Cui, T.; Zou, G. The Unsaturated Photocurrent Controlled by Two-Dimensional Barrier Geometry of a Single ZnO Nanowire Schottky Photodiode. *Appl. Phys. Lett.* **2008**, *93* (12), 123103. https://doi.org/10.1063/1.2989129.
(151) Zhou, J.; Gu, Y.; Hu, Y.; Mai, W.; Yeh, P.-H.; Bao, G.; Sood, A. K.; Polla, D. L.; Wang, Z. L. Gigantic Enhancement in Response and Reset Time of ZnO UV Nanosensor by Utilizing Schottky Contact and Surface Functionalization. *Appl. Phys. Lett.* **2009**, *94* (19), 191103. https://doi.org/10.1063/1.3133358.

(152) Nakano, M.; Makino, T.; Tsukazaki, A.; Ueno, K.; Ohtomo, A.; Fukumura, T.; Yuji, H.; Akasaka, S.; Tamura, K.; Nakahara, K.; et al. Transparent Polymer Schottky Contact for a High Performance Visible-Blind Ultraviolet Photodiode Based on ZnO. *Appl. Phys. Lett.* **2008**, *93* (12), 123309. https://doi.org/10.1063/1.2989125.
(153) Yang, Y.; Guo, W.; Qi, J.; Zhao, J.; Zhang, Y. Self-Powered Ultraviolet Photodetector Based on a Single Sb-Doped ZnO Nanobelt. *Appl. Phys. Lett.* **2010**, *97* (22), 223113. https://doi.org/10.1063/1.3524231.
(154) Czaban, J. A.; Thompson, D. A.; LaPierre, R. R. GaAs Core−Shell Nanowires for Photovoltaic Applications. *Nano Lett.* **2009**, *9* (1), 148–154. https://doi.org/10.1021/nl802700u.
(155) Krogstrup, P.; Jørgensen, H. I.; Heiss, M.; Demichel, O.; Holm, J. V.; Aagesen, M.; Nygard, J.; Fontcuberta i Morral, A. Single-Nanowire Solar Cells beyond the Shockley–Queisser Limit. *Nat. Photonics* **2013**, *7* (4), 306–310. https://doi.org/10.1038/nphoton.2013.32.
(156) Holm, J. V.; Jørgensen, H. I.; Krogstrup, P.; Nygård, J.; Liu, H.; Aagesen, M. Surface-Passivated GaAsP Single-Nanowire Solar Cells Exceeding 10% Efficiency Grown on Silicon. *Nat. Commun.* **2013**, *4* (1). https://doi.org/10.1038/ncomms2510.
(157) Tchernycheva, M.; Rigutti, L.; Jacopin, G.; de Luna Bugallo, A.; Lavenus, P.; Julien, F. H.; Timofeeva, M.; Bouravleuv, A. D.; Cirlin, G. E.; Dhaka, V.; et al. Photovoltaic Properties of GaAsP Core–Shell Nanowires on Si(001) Substrate. *Nanotechnology* **2012**, *23* (26), 265402. https://doi.org/10.1088/0957-4484/23/26/265402.
(158) Lysov, A.; Vinaji, S.; Offer, M.; Gutsche, C.; Regolin, I.; Mertin, W.; Geller, M.; Prost, W.; Bacher, G.; Tegude, F.-J. Spatially Resolved Photoelectric Performance of Axial GaAs Nanowire Pn-Diodes. *Nano Res.* **2011**, *4* (10), 987–995. https://doi.org/10.1007/s12274-011-0155-4.
(159) Cho, H. D.; Zakirov, A. S.; Yuldashev, S. U.; Ahn, C. W.; Yeo, Y. K.; Kang, T. W. Photovoltaic Device on a Single ZnO Nanowire p–n Homojunction. *Nanotechnology* **2012**, *23* (11), 115401. https://doi.org/10.1088/0957-4484/23/11/115401.
(160) Hayden, O.; Agarwal, R.; Lieber, C. M. Nanoscale Avalanche Photodiodes for Highly Sensitive and Spatially Resolved Photon Detection. *Nat. Mater.* **2006**, *5* (5), 352–356. https://doi.org/10.1038/nmat1635.
(161) Duan, X.; Huang, Y.; Cui, Y.; Wang, J.; Lieber, C. M. Indium Phosphide Nanowires as Building Blocks for Nanoscale Electronic and Optoelectronic Devices. *Nature* **2001**, *409* (6816), 66–69. https://doi.org/10.1038/35051047.
(162) Wang, Y.; Chen, Y.; Zhao, W.; Ding, L.; Wen, L.; Li, H.; Jiang, F.; Su, J.; Li, L.; Liu, N.; et al. A Self-Powered Fast-Response Ultraviolet Detector of p–n Homojunction Assembled from Two ZnO-Based Nanowires. *Nano-Micro Lett.* **2017**, *9* (1). https://doi.org/10.1007/s40820-016-0112-6.
(163) Zhang, H. D.; Yu, M.; Zhang, J. C.; Sheng, C. H.; Yan, X.; Han, W. P.; Liu, Y. C.; Chen, S.; Shen, G. Z.; Long, Y. Z. Fabrication and Photoelectric Properties of La-Doped p-Type ZnO Nanofibers and Crossed p–n Homojunctions by Electrospinning. *Nanoscale* **2015**, *7* (23), 10513–10518. https://doi.org/10.1039/C5NR02191J.
(164) Zhang, Z.; Ning, Y.; Fang, X. From Nanofibers to Ordered ZnO/NiO Heterojunction Arrays for Self-Powered and Transparent UV Photodetectors. *J. Mater. Chem. C* **2019**, *7* (2), 223–229. https://doi.org/10.1039/C8TC05877F.
(165) Wang, D.; Qian, F.; Yang, C.; Zhong, Z.; Lieber, C. M. Rational Growth of Branched and Hyperbranched Nanowire Structures. *Nano Lett.* **2004**, *4* (5), 871–874. https://doi.org/10.1021/nl049728u.
(166) Zhang, C.; Tian, W.; Xu, Z.; Wang, X.; Liu, J.; Li, S.-L.; Tang, D.-M.; Liu, D.; Liao, M.; Bando, Y.; et al. Photosensing Performance of Branched CdS/ZnO Heterostructures as Revealed by in Situ TEM and Photodetector Tests. *Nanoscale* **2014**, *6* (14), 8084. https://doi.org/10.1039/c4nr00963k.
(167) Li, X.; Gao, C.; Duan, H.; Lu, B.; Wang, Y.; Chen, L.; Zhang, Z.; Pan, X.; Xie, E. High-Performance Photoelectrochemical-Type Self-Powered UV Photodetector Using Epitaxial TiO_2 /SnO_2 Branched Heterojunction Nanostructure. *Small* **2013**, *9* (11), 2005–2011. https://doi.org/10.1002/smll.201202408.

(168) Pettersson, H.; Zubritskaya, I.; Nghia, N. T.; Wallentin, J.; Borgström, M. T.; Storm, K.; Landin, L.; Wickert, P.; Capasso, F.; Samuelson, L. Electrical and Optical Properties of InP Nanowire Ensemble p $^{+}$ –i–n $^{+}$ Photodetectors. *Nanotechnology* **2012**, *23* (13), 135201. https://doi.org/10.1088/0957-4484/23/13/135201.
(169) Chen, C.-H.; Chang, S.-J.; Chang, S.-P.; Li, M.-J.; Chen, I.-C.; Hsueh, T.-J.; Hsu, C.-L. Novel Fabrication of UV Photodetector Based on ZnO Nanowire/p-GaN Heterojunction. *Chem. Phys. Lett.* **2009**, *476* (1–3), 69–72. https://doi.org/10.1016/j.cplett.2009.06.007.
(170) Bie, Y.-Q.; Liao, Z.-M.; Zhang, H.-Z.; Li, G.-R.; Ye, Y.; Zhou, Y.-B.; Xu, J.; Qin, Z.-X.; Dai, L.; Yu, D.-P. Self-Powered, Ultrafast, Visible-Blind UV Detection and Optical Logical Operation Based on ZnO/GaN Nanoscale p-n Junctions. *Adv. Mater.* **2011**, *23* (5), 649–653. https://doi.org/10.1002/adma.201003156.
(171) Wang, G.; Chu, S.; Zhan, N.; Lin, Y.; Chernyak, L.; Liu, J. ZnO Homojunction Photodiodes Based on Sb-Doped p-Type Nanowire Array and n-Type Film for Ultraviolet Detection. *Appl. Phys. Lett.* **2011**, *98* (4), 041107. https://doi.org/10.1063/1.3551628.
(172) Senanayake, P.; Hung, C.-H.; Shapiro, J.; Lin, A.; Liang, B.; Williams, B. S.; Huffaker, D. L. Surface Plasmon-Enhanced Nanopillar Photodetectors. *Nano Lett.* **2011**, *11* (12), 5279–5283. https://doi.org/10.1021/nl202732r.
(173) Bulgarini, G.; Reimer, M. E.; Hocevar, M.; Bakkers, E. P. A. M.; Kouwenhoven, L. P.; Zwiller, V. Avalanche Amplification of a Single Exciton in a Semiconductor Nanowire. *Nat. Photonics* **2012**, *6* (7), 455–458. https://doi.org/10.1038/nphoton.2012.110.
(174) Jain, V.; Heurlin, M.; Barrigon, E.; Bosco, L.; Nowzari, A.; Shroff, S.; Boix, V.; Karimi, M.; Jam, R. J.; Berg, A.; et al. InP/InAsP Nanowire-Based Spatially Separate Absorption and Multiplication Avalanche Photodetectors. *ACS Photonics* **2017**, *4* (11), 2693–2698. https://doi.org/10.1021/acsphotonics.7b00389.
(175) Senanayake, P.; Hung, C.-H.; Farrell, A.; Ramirez, D. A.; Shapiro, J.; Li, C.-K.; Wu, Y.-R.; Hayat, M. M.; Huffaker, D. L. Thin 3D Multiplication Regions in Plasmonically Enhanced Nanopillar Avalanche Detectors. *Nano Lett.* **2012**, *12* (12), 6448–6452. https://doi.org/10.1021/nl303837y.
(176) Chuang, L. C.; Sedgwick, F. G.; Chen, R.; Ko, W. S.; Moewe, M.; Ng, K. W.; Tran, T.-T. D.; Chang-Hasnain, C. GaAs-Based Nanoneedle Light Emitting Diode and Avalanche Photodiode Monolithically Integrated on a Silicon Substrate. *Nano Lett.* **2011**, *11* (2), 385–390. https://doi.org/10.1021/nl102988w.
(177) Farrell, A. C.; Meng, X.; Ren, D.; Kim, H.; Senanayake, P.; Hsieh, N. Y.; Rong, Z.; Chang, T.-Y.; Azizur-Rahman, K. M.; Huffaker, D. L. InGaAs–GaAs Nanowire Avalanche Photodiodes Toward Single-Photon Detection in Free-Running Mode. *Nano Lett.* **2019**, *19* (1), 582–590. https://doi.org/10.1021/acs.nanolett.8b04643.
(178) Gallo, E. M.; Chen, G.; Currie, M.; McGuckin, T.; Prete, P.; Lovergine, N.; Nabet, B.; Spanier, J. E. Picosecond Response Times in GaAs/AlGaAs Core/Shell Nanowire-Based Photodetectors. *Appl. Phys. Lett.* **2011**, *98* (24), 241113. https://doi.org/10.1063/1.3600061.
(179) Divitini, G.; Plank, N. O. V.; Snaith, H. J.; Welland, M. E.; Ducati, C. High-Resolution TEM Characterization of ZnO Core-Shell Nanowires for Dye-Sensitized Solar Cells. *J. Phys. Conf. Ser.* **2010**, *241*, 012031. https://doi.org/10.1088/1742-6596/241/1/012031.
(180) Kayes, B. M.; Atwater, H. A.; Lewis, N. S. Comparison of the Device Physics Principles of Planar and Radial P-n Junction Nanorod Solar Cells. *J. Appl. Phys.* **2005**, *97* (11), 114302. https://doi.org/10.1063/1.1901835.
(181) Wang, S.; Yan, X.; Zhang, X.; Li, J.; Ren, X. Axially Connected Nanowire Core-Shell p-n Junctions: A Composite Structure for High-Efficiency Solar Cells. *Nanoscale Res. Lett.* **2015**, *10* (1). https://doi.org/10.1186/s11671-015-0744-3.
(182) Yu, S.; Witzigmann, B. A High Efficiency Dual-Junction Solar Cell Implemented as a Nanowire Array. *Opt. Express* **2013**, *21* (S1), A167. https://doi.org/10.1364/OE.21.00A167.
(183) Zhang, Y.; Wang; Mascarenhas, A. "Quantum Coaxial Cables" for Solar Energy Harvesting. *Nano Lett.* **2007**, *7* (5), 1264–1269. https://doi.org/10.1021/nl070174f.

(184) Lin, Y.; Chen, W.-J.; Lu, J.; Chang, Y.; Liang, C.-T.; Chen, Y.; Lu, J.-Y. Growth and Characterization of ZnO/ZnTe Core/Shell Nanowire Arrays on Transparent Conducting Oxide Glass Substrates. *Nanoscale Res. Lett.* **2012**, *7* (1), 401. https://doi.org/10.1186/1556-276X-7-401.
(185) Chao, H. Y.; Cheng, J. H.; Lu, J. Y.; Chang, Y. H.; Cheng, C. L.; Chen, Y. F. Growth and Characterization of Type-II ZnO/ZnTe Core-Shell Nanowire Arrays for Solar Cell Applications. *Superlattices Microstruct.* **2010**, *47* (1), 160–164. https://doi.org/10.1016/j.spmi.2009.07.005.
(186) Janik, E.; Wachnicka, A.; Guziewicz, E.; Godlewski, M.; Kret, S.; Zaleszczyk, W.; Dynowska, E.; Presz, A.; Karczewski, G.; Wojtowicz, T. ZnTe–ZnO Core–Shell Radial Heterostructures Grown by the Combination of Molecular Beam Epitaxy and Atomic Layer Deposition. *Nanotechnology* **2010**, *21* (1), 015302. https://doi.org/10.1088/0957-4484/21/1/015302.
(187) Park, S.; Kim, S.; Sun, G.-J.; Byeon, D. B.; Hyun, S. K.; Lee, W. I.; Lee, C. ZnO-Core/ZnSe-Shell Nanowire UV Photodetector. *J. Alloys Compd.* **2016**, *658*, 459–464. https://doi.org/10.1016/j.jallcom.2015.10.247.
(188) Zhang, Y.; Wu, Z.; Zheng, J.; Lin, X.; Zhan, H.; Li, S.; Kang, J.; Bleuse, J.; Mariette, H. ZnO/ZnSe Type II Core–Shell Nanowire Array Solar Cell. *Sol. Energy Mater. Sol. Cells* **2012**, *102*, 15–18. https://doi.org/10.1016/j.solmat.2011.12.015.
(189) Wu, Z.; Zhang, Y.; Zheng, J.; Lin, X.; Chen, X.; Huang, B.; Wang, H.; Huang, K.; Li, S.; Kang, J. An All-Inorganic Type-II Heterojunction Array with Nearly Full Solar Spectral Response Based on ZnO/ZnSe Core/Shell Nanowires. *J. Mater. Chem.* **2011**, *21* (16), 6020. https://doi.org/10.1039/c0jm03971c.
(190) Bera, A.; Basak, D. Photoluminescence and Photoconductivity of ZnS-Coated ZnO Nanowires. *ACS Appl. Mater. Interfaces* **2010**, *2* (2), 408–412. https://doi.org/10.1021/am900686c.
(191) Wang, K.; Chen, J. J.; Zeng, Z. M.; Tarr, J.; Zhou, W. L.; Zhang, Y.; Yan, Y. F.; Jiang, C. S.; Pern, J.; Mascarenhas, A. Synthesis and Photovoltaic Effect of Vertically Aligned ZnO/ZnS Core/Shell Nanowire Arrays. *Appl. Phys. Lett.* **2010**, *96* (12), 123105. https://doi.org/10.1063/1.3367706.
(192) Consonni, V.; Renet, S.; Garnier, J.; Gergaud, P.; Artús, L.; Michallon, J.; Rapenne, L.; Appert, E.; Kaminski-Cachopo, A. Improvement of the Physical Properties of ZnO/CdTe Core-Shell Nanowire Arrays by CdCl2 Heat Treatment for Solar Cells. *Nanoscale Res. Lett.* **2014**, *9* (1), 222. https://doi.org/10.1186/1556-276X-9-222.
(193) Consonni, V.; Rey, G.; Bonaimé, J.; Karst, N.; Doisneau, B.; Roussel, H.; Renet, S.; Bellet, D. Synthesis and Physical Properties of ZnO/CdTe Core Shell Nanowires Grown by Low-Cost Deposition Methods. *Appl. Phys. Lett.* **2011**, *98* (11), 111906. https://doi.org/10.1063/1.3567764.
(194) Michallon, J.; Zanuccoli, M.; Kaminski-Cachopo, A.; Consonni, V.; Morand, A.; Bucci, D.; Emieux, F.; Szambolics, H.; Perraud, S.; Semenikhin, I. Comparison of Optical Properties of Si and ZnO/CdTe Core/Shell Nanowire Arrays. *Mater. Sci. Eng. B* **2013**, *178* (9), 665–669. https://doi.org/10.1016/j.mseb.2012.10.037.
(195) Wang, X.; Zhu, H.; Xu, Y.; Wang, H.; Tao, Y.; Hark, S.; Xiao, X.; Li, Q. Aligned ZnO/CdTe Core−Shell Nanocable Arrays on Indium Tin Oxide: Synthesis and Photoelectrochemical Properties. *ACS Nano* **2010**, *4* (6), 3302–3308. https://doi.org/10.1021/nn1001547.
(196) Flores, E. M.; Gouvea, R. A.; Piotrowski, M. J.; Moreira, M. L. Band Alignment and Charge Transfer Predictions of ZnO/ZnX (X = S, Se or Te) Interfaces Applied to Solar Cells: A PBE+U Theoretical Study. *Phys. Chem. Chem. Phys.* **2018**, *20* (7), 4953–4961. https://doi.org/10.1039/C7CP08177D.
(197) Brandt, R. E.; Young, M.; Park, H. H.; Dameron, A.; Chua, D.; Lee, Y. S.; Teeter, G.; Gordon, R. G.; Buonassisi, T. Band Offsets of N-Type Electron-Selective Contacts on Cuprous Oxide (Cu2O) for Photovoltaics. *Appl. Phys. Lett.* **2014**, *105* (26), 263901. https://doi.org/10.1063/1.4905180.

(198) Klein, A. Energy Band Alignment in Chalcogenide Thin Film Solar Cells from Photoelectron Spectroscopy. *J. Phys. Condens. Matter* **2015**, *27* (13), 134201. https://doi.org/10.1088/0953-8984/27/13/134201.
(199) Schrier, J.; Demchenko, D. O.; Lin-Wang; Alivisatos, A. P. Optical Properties of ZnO/ZnS and ZnO/ZnTe Heterostructures for Photovoltaic Applications. *Nano Lett.* **2007**, *7* (8), 2377–2382. https://doi.org/10.1021/nl071027k.
(200) Pettersson, H.; Trägårdh, J.; Persson, A. I.; Landin, L.; Hessman, D.; Samuelson, L. Infrared Photodetectors in Heterostructure Nanowires. *Nano Lett.* **2006**, *6* (2), 229–232. https://doi.org/10.1021/nl052170l.
(201) van Kouwen, M. P.; van Weert, M. H. M.; Reimer, M. E.; Akopian, N.; Perinetti, U.; Algra, R. E.; Bakkers, E. P. A. M.; Kouwenhoven, L. P.; Zwiller, V. Single Quantum Dot Nanowire Photodetectors. *Appl. Phys. Lett.* **2010**, *97* (11), 113108. https://doi.org/10.1063/1.3484962.
(202) Kuyanov, P.; LaPierre, R. R. Photoluminescence and Photocurrent from InP Nanowires with InAsP Quantum Dots Grown on Si by Molecular Beam Epitaxy. *Nanotechnology* **2015**, *26* (31), 315202. https://doi.org/10.1088/0957-4484/26/31/315202.
(203) Kuyanov, P.; McNamee, S. A.; LaPierre, R. R. GaAs Quantum Dots in a GaP Nanowire Photodetector. *Nanotechnology* **2018**, *29* (12), 124003. https://doi.org/10.1088/1361-6528/aaa92e.
(204) den Hertog, M. I.; Songmuang, R.; Gonzalez-Posada, F.; Monroy, E. Single GaN-Based Nanowires for Photodetection and Sensing Applications. *Jpn. J. Appl. Phys.* **2013**, *52* (11S), 11NG01. https://doi.org/10.7567/JJAP.52.11NG01.
(205) Bastard, G. *Wave Mechanics Applied to Semiconductor Heterostructures*; Les Editions de Physique ; Halsted Press: Les Ulis Cedex, France; New York, N.Y., 1988.
(206) Liu; Capasso. *Intersubband Transitions in Quantum Wells: Physics and Device Applications II*; Academic Press, 1999.
(207) Faist, J.; Capasso, F.; Sivco, D. L.; Sirtori, C.; Hutchinson, A. L.; Cho, A. Y. Quantum Cascade Laser. *Science* **1994**, *264* (5158), 553–556. https://doi.org/10.1126/science.264.5158.553.
(208) Levine, B. F. Quantum-Well Infrared Photodetectors. *J. Appl. Phys.* **1993**, *74* (8), R1–R81. https://doi.org/10.1063/1.354252.
(209) Beeler, M.; Trichas, E.; Monroy, E. III-Nitride Semiconductors for Intersubband Optoelectronics: A Review. *Semicond. Sci. Technol.* **2013**, *28* (7), 074022. https://doi.org/10.1088/0268-1242/28/7/074022.
(210) Montes Bajo, M.; Tamayo-Arriola, J.; Hugues, M.; Ulloa, J. M.; Le Biavan, N.; Peretti, R.; Julien, F. H.; Faist, J.; Chauveau, J.-M.; Hierro, A. Multisubband Plasmons in Doped Zn O Quantum Wells. *Phys. Rev. Appl.* **2018**, *10* (2). https://doi.org/10.1103/PhysRevApplied.10.024005.
(211) Björk, M. T.; Ohlsson, B. J.; Thelander, C.; Persson, A. I.; Deppert, K.; Wallenberg, L. R.; Samuelson, L. Nanowire Resonant Tunneling Diodes. *Appl. Phys. Lett.* **2002**, *81* (23), 4458–4460. https://doi.org/10.1063/1.1527995.
(212) Karimi, M.; Jain, V.; Heurlin, M.; Nowzari, A.; Hussain, L.; Lindgren, D.; Stehr, J. E.; Buyanova, I. A.; Gustafsson, A.; Samuelson, L.; et al. Room-Temperature InP/InAsP Quantum Discs-in-Nanowire Infrared Photodetectors. *Nano Lett.* **2017**, *17* (6), 3356–3362. https://doi.org/10.1021/acs.nanolett.6b05114.
(213) Karimi, M.; Heurlin, M.; Limpert, S.; Jain, V.; Zeng, X.; Geijselaers, I.; Nowzari, A.; Fu, Y.; Samuelson, L.; Linke, H.; et al. Intersubband Quantum Disc-in-Nanowire Photodetectors with Normal-Incidence Response in the Long-Wavelength Infrared. *Nano Lett.* **2018**, *18* (1), 365–372. https://doi.org/10.1021/acs.nanolett.7b04217.
(214) Karimi, M.; Heurlin, M.; Limpert, S.; Jain, V.; Mansouri, E.; Zeng, X.; Samuelson, L.; Linke, H.; Borgström, M. T.; Pettersson, H. Nanowire Photodetectors with Embedded Quantum Heterostructures for Infrared Detection. *Infrared Phys. Technol.* **2019**, *96*, 209–212. https://doi.org/10.1016/j.infrared.2018.11.009.

(215) Tanaka, K.; Ikuno, K.; Kasai, Y.; Fukunaga, K.; Kunugita, H.; Ema, K.; Kikuchi, A.; Kishino, K. Ultrafast Intersubband Relaxation Dynamics at 1.55 Mm in GaN/AlN Multiple Quantum Disk Nanocolumns. *J. Lumin.* **2008**, *128* (5–6), 1084–1086. https://doi.org/10.1016/j.jlumin.2007.11.062.
(216) Beeler, M.; Hille, P.; Schörmann, J.; Teubert, J.; de la Mata, M.; Arbiol, J.; Eickhoff, M.; Monroy, E. Intraband Absorption in Self-Assembled Ge-Doped GaN/AlN Nanowire Heterostructures. *Nano Lett.* **2014**, *14* (3), 1665–1673. https://doi.org/10.1021/nl5002247.
(217) Ajay, A.; Lim, C. B.; Browne, D. A.; Polaczyński, J.; Bellet-Amalric, E.; Bleuse, J.; den Hertog, M. I.; Monroy, E. Effect of Doping on the Intersubband Absorption in Si- and Ge-Doped GaN/AlN Heterostructures. *Nanotechnology* **2017**, *28* (40), 405204. https://doi.org/10.1088/1361-6528/aa8504.
(218) Ajay, A.; Lim, C. B.; Browne, D. A.; Polaczynski, J.; Bellet-Amalric, E.; den Hertog, M. I.; Monroy, E. Intersubband Absorption in Si- and Ge-Doped GaN/AlN Heterostructures in Self-Assembled Nanowire and 2D Layers. *Phys. Status Solidi B* **2017**, *254* (8), 1600734. https://doi.org/10.1002/pssb.201600734.
(219) Ajay, A.; Blasco, R.; Polaczynski, J.; Spies, M.; den Hertog, M.; Monroy, E. Intersubband Absorption in GaN Nanowire Heterostructures at Mid-Infrared Wavelengths. *Nanotechnology* **2018**, *29* (38), 385201. https://doi.org/10.1088/1361-6528/aacf55.
(220) Tchernycheva, M.; Nevou, L.; Doyennette, L.; Julien, F.; Warde, E.; Guillot, F.; Monroy, E.; Bellet-Amalric, E.; Remmele, T.; Albrecht, M. Systematic Experimental and Theoretical Investigation of Intersubband Absorption in GaN/AlN Quantum Wells. *Phys. Rev. B* **2006**, *73* (12), 125347. https://doi.org/10.1103/PhysRevB.73.125347.
(221) Kandaswamy, P. K.; Guillot, F.; Bellet-Amalric, E.; Monroy, E.; Nevou, L.; Tchernycheva, M.; Michon, A.; Julien, F. H.; Baumann, E.; Giorgetta, F. R.; et al. GaN/AlN Short-Period Superlattices for Intersubband Optoelectronics: A Systematic Study of Their Epitaxial Growth, Design, and Performance. *J. Appl. Phys.* **2008**, *104* (9), 093501. https://doi.org/10.1063/1.3003507.
(222) Lim, C. B.; Ajay, A.; Bougerol, C.; Lähnemann, J.; Donatini, F.; Schörmann, J.; Bellet-Amalric, E.; Browne, D. A.; Jiménez-Rodríguez, M.; Monroy, E. Effect of Doping on the Far-Infrared Intersubband Transitions in Nonpolar m-Plane GaN/AlGaN Heterostructures. *Nanotechnology* **2016**, *27* (14), 145201. https://doi.org/10.1088/0957-4484/27/14/145201.
(223) Guillot, F.; Bellet-Amalric, E.; Monroy, E.; Tchernycheva, M.; Nevou, L.; Doyennette, L.; Julien, F. H.; Dang, L. S.; Remmele, T.; Albrecht, M.; et al. Si-Doped GaN/AlN Quantum Dot Superlattices for Optoelectronics at Telecommunication Wavelengths. *J. Appl. Phys.* **2006**, *100* (4), 044326. https://doi.org/10.1063/1.2335400.
(224) Songmuang, R.; Katsaros, G.; Monroy, E.; Spathis, P.; Bougerol, C.; Mongillo, M.; De Franceschi, S. Quantum Transport in GaN/AlN Double-Barrier Heterostructure Nanowires. *Nano Lett.* **2010**, *10* (9), 3545–3550. https://doi.org/10.1021/nl1017578.
(225) Lähnemann, J.; Ajay, A.; Den Hertog, M. I.; Monroy, E. Near-Infrared Intersubband Photodetection in GaN/AlN Nanowires. *Nano Lett.* **2017**, *17* (11), 6954–6960. https://doi.org/10.1021/acs.nanolett.7b03414.
(226) Shockley, W.; Queisser, H. J. Detailed Balance Limit of Efficiency of P-n Junction Solar Cells. *J. Appl. Phys.* **1961**, *32* (3), 510–519. https://doi.org/10.1063/1.1736034.
(227) Queisser, H. J. Detailed Balance Limit for Solar Cell Efficiency. *Mater. Sci. Eng. B* **2009**, *159–160*, 322–328. https://doi.org/10.1016/j.mseb.2008.06.033.
(228) Otnes, G.; Borgström, M. T. Towards High Efficiency Nanowire Solar Cells. *Nano Today* **2017**, *12*, 31–45. https://doi.org/10.1016/j.nantod.2016.10.007.
(229) Jia, G.; Steglich, M.; Sill, I.; Falk, F. Core–Shell Heterojunction Solar Cells on Silicon Nanowire Arrays. *Sol. Energy Mater. Sol. Cells* **2012**, *96*, 226–230. https://doi.org/10.1016/j.solmat.2011.09.062.

(230) Haverkort, J. E. M.; Garnett, E. C.; Bakkers, E. P. A. M. Fundamentals of the Nanowire Solar Cell: Optimization of the Open Circuit Voltage. *Appl. Phys. Rev.* **2018**, *5* (3), 031106. https://doi.org/10.1063/1.5028049.
(231) Cui, Y.; Wang, J.; Plissard, S. R.; Cavalli, A.; Vu, T. T. T.; van Veldhoven, R. P. J.; Gao, L.; Trainor, M.; Verheijen, M. A.; Haverkort, J. E. M.; et al. Efficiency Enhancement of InP Nanowire Solar Cells by Surface Cleaning. *Nano Lett.* **2013**, *13* (9), 4113–4117. https://doi.org/10.1021/nl4016182.
(232) Wallentin, J.; Anttu, N.; Asoli, D.; Huffman, M.; Aberg, I.; Magnusson, M. H.; Siefer, G.; Fuss-Kailuweit, P.; Dimroth, F.; Witzigmann, B.; et al. InP Nanowire Array Solar Cells Achieving 13.8% Efficiency by Exceeding the Ray Optics Limit. *Science* **2013**, *339* (6123), 1057–1060. https://doi.org/10.1126/science.1230969.
(233) Aberg, I.; Vescovi, G.; Asoli, D.; Naseem, U.; Gilboy, J. P.; Sundvall, C.; Dahlgren, A.; Svensson, K. E.; Anttu, N.; Bjork, M. T.; et al. A GaAs Nanowire Array Solar Cell With 15.3% Efficiency at 1 Sun. *IEEE J. Photovolt.* **2016**, *6* (1), 185–190. https://doi.org/10.1109/JPHOTOV.2015.2484967.
(234) van Dam, D.; van Hoof, N. J. J.; Cui, Y.; van Veldhoven, P. J.; Bakkers, E. P. A. M.; Gómez Rivas, J.; Haverkort, J. E. M. High-Efficiency Nanowire Solar Cells with Omnidirectionally Enhanced Absorption Due to Self-Aligned Indium–Tin–Oxide Mie Scatterers. *ACS Nano* **2016**, *10* (12), 11414–11419. https://doi.org/10.1021/acsnano.6b06874.
(235) Yao, M.; Cong, S.; Arab, S.; Huang, N.; Povinelli, M. L.; Cronin, S. B.; Dapkus, P. D.; Zhou, C. Tandem Solar Cells Using GaAs Nanowires on Si: Design, Fabrication, and Observation of Voltage Addition. *Nano Lett.* **2015**, *15* (11), 7217–7224. https://doi.org/10.1021/acs.nanolett.5b03890.
(236) Lim, C. B. Hétérostructures GaN/Al(Ga)N Pour l'optoélectronique Infrarouge : Orientations Polaires et Non-Polaires. PhD Thesis, Université Grenoble Alpes: Grenoble, 2017.
(237) Musolino, M.; Tahraoui, A.; Fernández-Garrido, S.; Brandt, O.; Trampert, A.; Geelhaar, L.; Riechert, H. Compatibility of the Selective Area Growth of GaN Nanowires on AlN-Buffered Si Substrates with the Operation of Light Emitting Diodes. *Nanotechnology* **2015**, *26* (8), 085605. https://doi.org/10.1088/0957-4484/26/8/085605.
(238) Schenk, H. P. D.; Kipshidze, G. D.; Kaiser, U.; Fissel, A.; Kräußlich, J.; Schulze, J.; Richter, W. Investigation of Two-Dimensional Growth of AlN(0001) on Si(111) by Plasma-Assisted Molecular Beam Epitaxy. *J. Cryst. Growth* **1999**, *200* (1–2), 45–54. https://doi.org/10.1016/S0022-0248(98)01245-7.
(239) Hovington, P.; Drouin, D.; Gauvin, R. CASINO: A New Monte Carlo Code in C Language for Electron Beam Interaction -Part I: Description of the Program. *Scanning* **2006**, *19* (1), 1–14. https://doi.org/10.1002/sca.4950190101.
(240) Demers, H.; Poirier-Demers, N.; Couture, A. R.; Joly, D.; Guilmain, M.; de Jonge, N.; Drouin, D. Three-Dimensional Electron Microscopy Simulation with the CASINO Monte Carlo Software. *Scanning* **2011**, *33* (3), 135–146. https://doi.org/10.1002/sca.20262.
(241) Drouin, D.; Couture, A. R.; Joly, D.; Tastet, X.; Aimez, V.; Gauvin, R. CASINO V2.42—A Fast and Easy-to-Use Modeling Tool for Scanning Electron Microscopy and Microanalysis Users. *Scanning* **2007**, *29* (3), 92–101. https://doi.org/10.1002/sca.20000.
(242) *Low Voltage Electron Microscopy: Principles and Applications*; Bell, D. C., Erdman, N., Eds.; John Wiley & Sons, Ltd: Chichester, UK, 2012. https://doi.org/10.1002/9781118498514.
(243) Hillyard, S.; Silcox, J. Detector Geometry, Thermal Diffuse Scattering and Strain Effects in ADF STEM Imaging. *Ultramicroscopy* **1995**, *58* (1), 6–17. https://doi.org/10.1016/0304-3991(94)00173-K.
(244) Kirkland, E. J.; Loane, R. F.; Silcox, J. Simulation of Annular Dark Field Stem Images Using a Modified Multislice Method. *Ultramicroscopy* **1987**, *23* (1), 77–96. https://doi.org/10.1016/0304-3991(87)90229-4.
(245) Smith, K. K. Photoluminescence of Semiconductor Materials. *Thin Solid Films*. 1981, pp 171–182.

(246) Birner, S. Modeling of Semiconductor Nanostructures and Semiconductor–Electrolyte Interfaces. PhD Thesis, Technische Universität München: Garching b. München, 2011.
(247) Park, S.-H. Crystal Orientation Effects on Electronic Properties of Wurtzite GaN/AlGaN Quantum Wells with Spontaneous and Piezoelectric Polarization. *Jpn. J. Appl. Phys.* **2000**, *39* (Part 1, No. 6A), 3478–3482. https://doi.org/10.1143/JJAP.39.3478.
(248) Rinke, P.; Winkelnkemper, M.; Qteish, A.; Bimberg, D.; Neugebauer, J.; Scheffler, M. Consistent Set of Band Parameters for the Group-III Nitrides AlN, GaN, and InN. *Phys. Rev. B* **2008**, *77* (7), 075202. https://doi.org/10.1103/PhysRevB.77.075202.
(249) Bertelli, M.; Löptien, P.; Wenderoth, M.; Rizzi, A.; Ulbrich, R.; Righi, M.; Ferretti, A.; Martin-Samos, L.; Bertoni, C.; Catellani, A. Atomic and Electronic Structure of the Nonpolar GaN(1-100) Surface. *Phys. Rev. B* **2009**, *80* (11), 115324. https://doi.org/10.1103/PhysRevB.80.115324.
(250) Lymperakis, L.; Weidlich, P. H.; Eisele, H.; Schnedler, M.; Nys, J.-P.; Grandidier, B.; Stiévenard, D.; Dunin-Borkowski, R. E.; Neugebauer, J.; Ebert, Ph. Hidden Surface States at Non-Polar GaN (10-10) Facets: Intrinsic Pinning of Nanowires. *Appl. Phys. Lett.* **2013**, *103* (15), 152101. https://doi.org/10.1063/1.4823723.
(251) Reddy, P.; Bryan, I.; Bryan, Z.; Guo, W.; Hussey, L.; Collazo, R.; Sitar, Z. The Effect of Polarity and Surface States on the Fermi Level at III-Nitride Surfaces. *J. Appl. Phys.* **2014**, *116* (12), 123701. https://doi.org/10.1063/1.4896377.
(252) Spies, M.; den Hertog, M. I.; Hille, P.; Schörmann, J.; Polaczyński, J.; Gayral, B.; Eickhoff, M.; Monroy, E.; Lähnemann, J. Bias-Controlled Spectral Response in GaN/AlN Single-Nanowire Ultraviolet Photodetectors. *Nano Lett.* **2017**, *17* (7), 4231–4239. https://doi.org/10.1021/acs.nanolett.7b01118.
(253) Furtmayr, F.; Teubert, J.; Becker, P.; Conesa-Boj, S.; Morante, J. R.; Chernikov, A.; Schäfer, S.; Chatterjee, S.; Arbiol, J.; Eickhoff, M. Carrier Confinement in GaN/AlxGa1−xN Nanowire Heterostructures (0<x≤1). *Phys. Rev. B* **2011**, *84* (20), 205303. https://doi.org/10.1103/PhysRevB.84.205303.
(254) Schörmann, J.; Hille, P.; Schäfer, M.; Müßener, J.; Becker, P.; Klar, P. J.; Kleine-Boymann, M.; Rohnke, M.; de la Mata, M.; Arbiol, J.; et al. Germanium Doping of Self-Assembled GaN Nanowires Grown by Plasma-Assisted Molecular Beam Epitaxy. *J. Appl. Phys.* **2013**, *114* (10), 103505. https://doi.org/10.1063/1.4820264.
(255) Schäfer, M.; Günther, M.; Länger, C.; Müßener, J.; Feneberg, M.; Uredat, P.; Elm, M. T.; Hille, P.; Schörmann, J.; Teubert, J.; et al. Electrical Transport Properties of Ge-Doped GaN Nanowires. *Nanotechnology* **2015**, *26* (13), 135704. https://doi.org/10.1088/0957-4484/26/13/135704.
(256) Nenstiel, C.; Bügler, M.; Callsen, G.; Nippert, F.; Kure, T.; Fritze, S.; Dadgar, A.; Witte, H.; Bläsing, J.; Krost, A.; et al. Germanium - the Superior Dopant in n-Type GaN. *Phys. Status Solidi RRL - Rapid Res. Lett.* **2015**, *9* (12), 716–721. https://doi.org/10.1002/pssr.201510278.
(257) Ajay, A.; Lim, C. B.; Browne, D. A.; Polaczynski, J.; Bellet-Amalric, E.; Bleuse, J.; Den Hertog, M. I.; Monroy, E. Effect of Doping on the Intersubband Absorption in Si- and Ge-Doped GaN/AlN Heterostructures. **2017**, arXiv:1705.04096.
(258) Fernández-Garrido, S.; Zettler, J. K.; Geelhaar, L.; Brandt, O. Monitoring the Formation of Nanowires by Line-of-Sight Quadrupole Mass Spectrometry: A Comprehensive Description of the Temporal Evolution of GaN Nanowire Ensembles. *Nano Lett.* **2015**, *15* (3), 1930–1937. https://doi.org/10.1021/nl504778s.
(259) Zhang, A.; You, S.; Soci, C.; Liu, Y.; Wang, D.; Lo, Y.-H. Silicon Nanowire Detectors Showing Phototransistive Gain. *Appl. Phys. Lett.* **2008**, *93* (12), 121110. https://doi.org/10.1063/1.2990639.
(260) Kim, C.-J.; Lee, H.-S.; Cho, Y.-J.; Kang, K.; Jo, M.-H. Diameter-Dependent Internal Gain in Ohmic Ge Nanowire Photodetectors. *Nano Lett.* **2010**, *10* (6), 2043–2048. https://doi.org/10.1021/nl100136b.

(261) Hu, L.; Yan, J.; Liao, M.; Wu, L.; Fang, X. Ultrahigh External Quantum Efficiency from Thin SnO2 Nanowire Ultraviolet Photodetectors. *Small* **2011**, *7* (8), 1012–1017. https://doi.org/10.1002/smll.201002379.
(262) Cao, Y. L.; Liu, Z. T.; Chen, L. M.; Tang, Y. B.; Luo, L. B.; Jie, J. S.; Zhang, W. J.; Lee, S. T.; Lee, C. S. Single-Crystalline ZnTe Nanowires for Application as High-Performance Green/Ultraviolet Photodetector. *Opt. Express* **2011**, *19* (7), 6100–6108. https://doi.org/10.1364/OE.19.006100.
(263) Monroy, E.; Omn s, F.; Calle, F. Wide-Bandgap Semiconductor Ultraviolet Photodetectors. *Semicond. Sci. Technol.* **2003**, *18* (4), R33–R51. https://doi.org/10.1088/0268-1242/18/4/201.
(264) Long-Lived Excitons in GaN/AlN Nanowire Heterostructures. https://doi.org/10.1103/PhysRevB.91.205440.
(265) Chen, R. S.; Tsai, H. Y.; Chan, C. H.; Huang, Y. S.; Chen, Y. T.; Chen, K. H.; Chen, L. C. Comparison of CVD- and MBE-Grown GaN Nanowires: Crystallinity, Photoluminescence, and Photoconductivity. *J. Electron. Mater.* **2014**, *44* (1), 177–187. https://doi.org/10.1007/s11664-014-3457-y.
(266) Yan, X.; Li, B.; Wu, Y.; Zhang, X.; Ren, X. A Single Crystalline InP Nanowire Photodetector. *Appl. Phys. Lett.* **2016**, *109* (5), 053109. https://doi.org/10.1063/1.4960713.
(267) Wang, H. High Gain Single GaAs Nanowire Photodetector. *Appl. Phys. Lett.* **2013**, *103* (9), 093101. https://doi.org/10.1063/1.4816246.
(268) Birner, S.; Zibold, T.; Andlauer, T.; Kubis, T.; Sabathil, M.; Trellakis, A.; Vogl, P. Nextnano: General Purpose 3-D Simulations. *IEEE Trans. Electron Devices* **2007**, *54* (9), 2137–2142. https://doi.org/10.1109/TED.2007.902871.
(269) Simon, J.; Zhang, Z.; Goodman, K.; Xing, H.; Kosel, T.; Fay, P.; Jena, D. Polarization-Induced Zener Tunnel Junctions in Wide-Band-Gap Heterostructures. *Phys. Rev. Lett.* **2009**, *103* (2), 026801. https://doi.org/10.1103/PhysRevLett.103.026801.
(270) Leconte, S.; Guillot, F.; Sarigiannidou, E.; Monroy, E. Charge Distribution and Vertical Electron Transport through GaN/AlN/GaN Single-Barrier Structures. *Semicond. Sci. Technol.* **2007**, *22* (2), 107–112. https://doi.org/10.1088/0268-1242/22/2/018.
(271) Monroy, E.; Calle, F.; Muñoz, E.; Omnès, F.; Beaumont, B.; Gibart, P. Visible-Blindness in Photoconductive and Photovoltaic AlGaN Ultraviolet Detectors. *J. Electron. Mater.* **1999**, *28* (3), 240–245. https://doi.org/10.1007/s11664-999-0021-2.
(272) Lähnemann, J.; Flissikowski, T.; Wölz, M.; Geelhaar, L.; Grahn, H. T.; Brandt, O.; Jahn, U. Quenching of the Luminescence Intensity of GaN Nanowires under Electron Beam Exposure: Impact of C Adsorption on the Exciton Lifetime. *Nanotechnology* **2016**, *27* (45), 455706. https://doi.org/10.1088/0957-4484/27/45/455706.
(273) Aharonovich, I.; Englund, D.; Toth, M. Solid-State Single-Photon Emitters. *Nat. Photonics* **2016**, *10* (10), 631–641. https://doi.org/10.1038/nphoton.2016.186.
(274) Kako, S.; Hoshino, K.; Iwamoto, S.; Ishida, S.; Arakawa, Y. Exciton and Biexciton Luminescence from Single Hexagonal GaN⁄AlN Self-Assembled Quantum Dots. *Appl. Phys. Lett.* **2004**, *85* (1), 64–66. https://doi.org/10.1063/1.1769586.
(275) Bardoux, R.; Guillet, T.; Lefebvre, P.; Taliercio, T.; Bretagnon, T.; Rousset, S.; Gil, B.; Semond, F. Photoluminescence of Single GaN/AlN Hexagonal Quantum Dots on Si (111) : Spectral Diffusion Effects. *Phys. Rev. B* **2006**, *74* (19), 195319. https://doi.org/10.1103/PhysRevB.74.195319.
(276) Rol, F.; Founta, S.; Mariette, H.; Daudin, B.; Dang, L. S.; Bleuse, J.; Peyrade, D.; Gérard, J.-M.; Gayral, B. Probing Exciton Localization in Nonpolar Ga N/Al N Quantum Dots by Single-Dot Optical Spectroscopy. *Phys. Rev. B* **2007**, *75* (12), 125306. https://doi.org/10.1103/PhysRevB.75.125306.
(277) Kako, S.; Santori, C.; Hoshino, K.; Götzinger, S.; Yamamoto, Y.; Arakawa, Y. A Gallium Nitride Single-Photon Source Operating at 200 K. *Nat. Mater.* **2006**, *5* (11), 887–892. https://doi.org/10.1038/nmat1763.

(278) Nakaoka, T.; Kako, S.; Arakawa, Y. Quantum Confined Stark Effect in Single Self-Assembled GaN/AlN Quantum Dots. *Phys. E Low-Dimens. Syst. Nanostructures* **2006**, *32* (1–2), 148–151. https://doi.org/10.1016/j.physe.2005.12.028.
(279) Müßener, J.; Hille, P.; Grieb, T.; Schörmann, J.; Teubert, J.; Monroy, E.; Rosenauer, A.; Eickhoff, M. Bias-Controlled Optical Transitions in GaN/AlN Nanowire Heterostructures. *ACS Nano* **2017**, *11* (9), 8758–8767. https://doi.org/10.1021/acsnano.7b02419.
(280) Bretagnon, T.; Lefebvre, P.; Valvin, P.; Bardoux, R.; Guillet, T.; Taliercio, T.; Gil, B.; Grandjean, N.; Semond, F.; Damilano, B.; et al. Radiative Lifetime of a Single Electron-Hole Pair in Ga N/Al N Quantum Dots. *Phys. Rev. B* **2006**, *73* (11). https://doi.org/10.1103/PhysRevB.73.113304.
(281) Ediger, M.; Bester, G.; Badolato, A.; Petroff, P. M.; Karrai, K.; Zunger, A.; Warburton, R. J. Peculiar Many-Body Effects Revealed in the Spectroscopy of Highly Charged Quantum Dots. *Nat. Phys.* **2007**, *3*, 774.
(282) Chen, G. D.; Smith, M.; Lin, J. Y.; Jiang, H. X.; Wei, S.; Asif Khan, M.; Sun, C. J. Fundamental Optical Transitions in GaN. *Appl. Phys. Lett.* **1996**, *68* (20), 2784–2786. https://doi.org/10.1063/1.116606.

Publications and Conference Contributions

Journal Articles

(1) (invited review) **Spies M.**; Monroy, E. Nanowire Photodetectors based on wurtzite semiconductor heterostructures. *Semicond Sci Tech* **2019**, *34* (5), 053002. http://doi.org/10.1088/1361-6641/ab0cb8.

(2) **Spies, M.**; Polaczyński, J.; Ajay, A.; Kalita, D.; Luong, M. A.; Lähnemann, J.; Gayral, B.; den Hertog, M. I.; Monroy, E. Effect of the Nanowire Diameter on the Linearity of the Response of GaN-Based heterostructured NW Photodetectors. *Nanotechnology* **2018**, *29* (25), 255204. https://doi.org/10.1088/1361-6528/aab838.

(3) Sistani, M.; Luong, M. A.; den Hertog, M. I.; Robin, E.; **Spies, M.**; Fernandez, B.; Yao, J.; Bertagnolli, E.; Lugstein, A. Monolithic Axial and Radial Metal–Semiconductor Nanowire heterostructures. *Nano Lett.* **2018**, *18* (12), 7692–7697. https://doi.org/10.1021/acs.nanolett.8b03366.

(4) Ajay, A.; Blasco, R.; Polaczynski, J.; **Spies, M.**; den Hertog, M.; Monroy, E. Intersubband Absorption in GaN Nanowire heterostructures at Mid-Infrared Wavelengths. *Nanotechnology* **2018**, *29* (38), 385201. https://doi.org/10.1088/1361-6528/aacf55.

(5) **Spies, M.**; den Hertog, M. I.; Hille, P.; Schörmann, J.; Polaczyński, J.; Gayral, B.; Eickhoff, M.; Monroy, E.; Lähnemann, J. Bias-Controlled Spectral Response in GaN/AlN Single Nanowire Ultraviolet Photodetectors. *Nano Lett.* **2017**, *17* (7), 4231–4239. https://doi.org/10.1021/acs.nanolett.7b01118.

Conference Contributions

(1) (oral) **Maria Spies**, Akhil Ajay, Fabrice Donatini, Martien I. den Hertog, Eva Monroy, and Bruno Gayral. "Tunable single quantum dot emission in GaN/AlN Nanowires" *International Conference on Nitride Semiconductors,* Bellevue, WA, USA, july 7-12, 2019

(2) (invited) Akhil Ajay, **Maria Spies**, Jonas Lähnemann, Martien I. den Hertog, and Eva Monroy. "GaN/AlN Nanowire photodetectors: from UV to the IR" *MRS Fall Meeting*, Boston, USA, november 25-30, 2018

(3) (oral) **Maria Spies**, Jakub Polaczyński, Akhil Ajay, Dipankar Kalita, Jonas Lähnemann, Bruno Gayral, Martien I. den Hertog, and Eva Monroy. "Linear photoresponse in Nanowires with GaN/AlN heterostructure". *Journées de la Matière Condensées*, Grenoble, France, august 27-31, 2018

(4) (invited) Akhil Ajay, Jonas Lähnemann, **Maria Spies,** Jakub Polaczyński, Martien I. den Hertog and Eva Monroy. "III-Nitride Nanowire photodetectors: from linear UV sensors to NW-QWIP", *SPIE Optics + Photonics, San Diego, USA,* august 19-23, 2018

(5) (poster) **Maria Spies**, Jakub Polaczyński, Akhil Ajay, Dipankar Kalita, Jonas Lähnemann, Bruno Gayral, Martien I. den Hertog, and Eva Monroy. "Heterostructured GaN/AlN Nanowires with linear photoresponse". *International Conference on Superlattices, Nanostructures and Nanodevices*, Madrid, Spain, july 23-27, 2018

(6) (oral) **Maria Spies**, Jakub Polaczyński, Akhil Ajay, Dipankar Kalita, Jonas Lähnemann, Bruno Gayral, Martien I. den Hertog, and Eva Monroy. "Linearity of the photoresponse in heterostructured GaN/AlN Nanowires". *Nanowire Week*, Hamilton, Canada, june 11-15, 2018

(7) (invited) Akhil Ajay, **Maria Spies**, Jonas Lähnemann, Martien I. den Hertog, Bruno Gayral, and Eva Monroy. "GaN/AlN dots-in-a-wire photodetectors" *10th Biannual Conf. on Quantum Dots (QD2018),* Toronto, Canada, june 25-29, 2018

(8) (oral) Akhil Ajay, Rodrigo Blasco, Jakub Polaczynski, **Maria Spies**, Martien I. den Hertog, and Eva Monroy "GaN/AlGaN Nanowire heterostructures for mid-infrared

intersubband technology" *Compound Semiconductor Week*, Boston, USA, may 29 – june 1, 2018

(9) (oral) **Maria Spies**, Jonas Lähnemann, Martien I. Den Hertog, Pascal Hille, Jörg Schörmann, Jakub Polaczyński, Bruno Gayral, Martin Eickhoff, and Eva Monroy. "Single Nanowire Photodetectors with GaN/AlN Superlattice and bias-dependent spectral response" *EMRS Fall Meeting*, Varsovie, Poland, september 18-21, 2017

(10) (poster) **Maria Spies**, Jonas Lähnemann, Pacal Hille, Jörg Schörmann, Jakub Polaczyński, Martien I. den Hertog, Bruno Gayral, Martin Eickhoff, and Eva Monroy. "Bias-controlled spectral response in GaN/AlN Nanowire photodetectors" *International Conference on Nitride Semiconductors,* Strasbourg, France, july 24-28, 2017

(11) (poster) **Maria Spies**, Jonas Lähnemann, Pacal Hille, Jörg Schörmann, Jakub Polaczyński, Martien I. den Hertog, Bruno Gayral, Martin Eickhoff, and Eva Monroy. "Bias-controlled spectral response in GaN/AlN Nanowire photodetectors"*17th TEM-UCA Workshop*, Cadiz, Spain, july 17-21, 2017

(12) (oral) **Maria Spies**, Jonas Lähnemann, Pascal Hille, Jörg Schörmann, Jakub Polaczynski, Martien I. Den Hertog, Bruno Gayral, Martin Eickhoff, and Eva Monroy „GaN/AlN Nanowire photodetectors with bias-controlled spectral response" *Nanowire Week,* Lund, Sweden, may 29 – june 2, 2017

Glossary

1-,2-,3,-4D	1-,2-,3-,4-dimensional
a_i	Conduction Band Deformation Potentials
α_V	Varshni coefficient
β_D	Debye coefficient
BF	Bright Field
BSE	Backscattered Electron Detector
BW_{3dB}	3 dB Bandwidth
CCD	Charge Coupled Device
CH	Crystal Field Hole
CVD	Chemical Vapor Deposition
CW	Continuous Wave
D	Detectivity
D*	Specific Detectivity
DF	Dark Field
D_i	Valence Band Deformation Potentials
DIW	Deionized Water
EBIC	Electron Beam Induced Current
E_F	Fermi Level
E_g	Bandgap
EL	Electron Beam Lithography
EQE	External Quantum Efficiency
EsB	Energy Selective Backscattered Electron Detector
ETD	Everhart-Thornley Detector
FWHM	Full Width Half Maximum
GND	Grounded (electrical contact)
(HA)ADF	(High Angle) Annular Dark Field
HEMT	High Electron Mobility Transistor
HF	Hydroflouric Acid
HH	Heavy Hole
HR	High Resolution
HRXRD	High Resolution X-Ray Diffraction

ICP	Inductively Coupled Plasma Etching
IQE	Internal Quantum Efficiency
IR	Infrared
ISB	Intersubband
IV	Current Voltage Characteristic
KOH	Potassium Hydroxide
LED	Light Emitting Diode
LH	Light Hole
MBE	Molecular Beam Epitaxy
m_e*	Effective Electron Mass
m_{e0}	Electron Mass
m_h*	Effective Hole Mass
m_{h0}	Hole Mass
MOVPE	Metalorganic Vapor Phase Epitaxy
MQW	Multi Quantum Well
(μ)PL	(Micro-)Photoluminescence
NDR	Negative Differential Resistance
NEP	Noise Equivalent Power
NW	NW
PAMBE	Plasma Assisted Molecular Beam Epitaxy
QCSE	Quantum Confined Stark Effect
QD	Quantum Dot
QW	Quantum Well
QWIP	Quantum Well Infrared Photodetectors
RHEED	Reflection High Energy Electron Diffraction
RIE	Reactive Ion Etching
SEM	Scanning Electron Microscopy
SK	Stranksi Krastanov
SL	Super Lattice
SPAD	Single Photon Avalanche Photodetector
(S)TEM	(Scanning) Transmission Electron Microscopy
TE	Transverse Electric Polarized Light
TM	Transverse Magnetic Polarized Light

UV	Ultraviolet
V_B	Bias Potential
VLS	Vapor-Liquid-Solid Growth Technique